# Synthesis of Molybdenum-Based Nanomaterials with High Photothermal Conversion Efficiencies by Femtosecond Laser Ablation in Liquid

by

Fan Ye

A thesis

presented to the University of Waterloo

in fulfillment of the

thesis requirement for the degree of

Doctor of Philosophy

in

Mechanical and Mechatronics Engineering (Nanotechnology)

Waterloo, Ontario, Canada, 2023

## Examining Committee Membership

The following served on the Examining Committee for this thesis. The decision of the Examining Committee is by majority vote.

External Examiner: Dr. Arnaud Weck
Professor
Department of Mechanical Engineering
University of Ottawa

Supervisor(s): Dr. Kevin Musselman
Associate Professor
Department of Mechanical and Mechatronics Engineering
University of Waterloo

Dr. Joseph Sanderson
Associate Professor
Department of Physics and Astronomy
University of Waterloo

Internal Members: Dr. Yimin Wu
Assistant Professor
Department of Mechanical and Mechatronics Engineering
University of Waterloo

Dr. Xiaoyu Wu
Assistant Professor
Department of Mechanical and Mechatronics Engineering
University of Waterloo

Internal-external Member: Dr. Shawn Wettig
Professor
School of Pharmacy
University of Waterloo

## Author's Declaration

This thesis consists of material all of which I authored or co-authored: see Statement of Contributions included in the thesis. This is a true copy of the thesis, including any required final revisions, as accepted by my examiners.

I understand that my thesis may be made electronically available to the public.

## Statement of Contributions

A version of Chapter 4 has been published as Ye, F.; Chang, D.; Ayub, A.; Ibrahim, K.; Shahin, A.; Karimi, R.; Wettig, S.; Sanderson, J.; Musselman, K. P. Synthesis of Two-Dimensional Plasmonic Molybdenum Oxide Nanomaterials by Femtosecond Laser Irradiation. *Chem. Mater.* **2021**, *33*(12), 4510-4521. I was responsible for the design of the experiment, synthesis and characterization of the nanomaterials, collection and analysis of the data, and manuscript drafting and revision. D. Chang performed the measurement of photothermal conversion efficiencies (PTCEs) of the nanomaterials and assisted in the manuscript drafting and revision. A. Ayub measured the particle size distributions of the nanomaterials. K. Ibrahim, A. Shahin and R. Karimi assisted in the synthesis of the nanomaterials. K.P. Musselman, J. Sanderson and S. Wettig provided support in the manuscript revision and supervision of this work. All the authors contributed to the discussion of the results.

A version of Chapter 5 has been published as Ye, F.; Ayub, A.; Chang, D.; Chernikov, R.; Chen, Q.; Karimi, R.; Wettig, S.; Sanderson, J.; Musselman, K. P. Molybdenum Blues with Tunable Light Absorption Synthesized by Femtosecond Laser Irradiation of Molybdenum Trioxide in Water/Ethanol Mixtures. *Adv. Opt. Mater.* **2022**, *10*(23), 2201304. I was responsible for the design of the experiment, synthesis and characterization of the nanomaterials, measurement of the PTCEs of the nanomaterials, collection and analysis of the data, and manuscript drafting and revision. A. Ayub measured the particle size distributions of the nanomaterials, conducted freeze drying of the nanomaterials and assisted in the manuscript drafting and revision. D. Chang assisted in the measurement of the PTCEs of the nanomaterials. R. Chernikov performed the measurement of X-ray Absorption Spectra of the nanomaterials. Q. Chen assisted in the analysis of the data. R. Karimi assisted in the synthesis of the nanomaterials. K.P. Musselman, J. Sanderson and S. Wettig provided support in the manuscript revision and supervision of this work. All the authors contributed to the discussion of the results.

A version of Chapter 6 has been published as Ye, F.; Ayub, A.; Karimi, R.; Wettig, S.; Sanderson, J.; Musselman, K. P. Defect Rich $MoSe_2$ 2H/1T Hybrid Nanoparticles Prepared from Femtosecond Laser Ablation in Liquid and Their Enhanced Photothermal Conversion Efficiencies. *Adv. Mater.* **2023**, 2301129. I was responsible for the design of the experiment, synthesis and characterization of the nanoparticles, measurement of the PTCEs of the nanoparticles, collection and analysis of the data, and manuscript drafting and revision. A. Ayub assisted in the drying of the nanoparticles and manuscript revision, R. Karimi assisted in the synthesis of the nanoparticles. K.P. Musselman, J. Sanderson and S. Wettig provided support in the manuscript revision and supervision of this work. All the authors contributed to the discussion of the results.

A version of Chapter 7 is in preparation for publication as Ye F.; Fruehwald H.; Tian K.; Zandieh M.; Liu J.; Smith, R.; Sanderson, J.; Musselman, K. P. One-Pot Synthesis of PEGylated $MoSe_2$ Nanomaterials with Suppression of Oxidation by Femtosecond Laser Ablation in Water. I was responsible for the design of the experiment, synthesis and characterization of the nanomaterials, measurement of the PTCEs of the nanomaterials, collection and analysis of the data, and manuscript drafting and revision. H. Fruehwald measured the Raman spectra of the nanomaterials. K. Tian assisted in the synthesis of the nanomaterials. M. Zandieh performed freeze drying of the nanomaterials. K.P. Musselman, J. Sanderson, R. Smith and J. Liu provided supervision of this work.

Chapter 1, 2, 3 and 8 are originally written by Fan Ye and have never been published before.

My publications during my study at the University of Waterloo are listed below:

[1] **Ye, F.**; Ayub, A.; Karimi, R.; Wettig, S.; Sanderson, J.; Musselman, K. P. Defect Rich $MoSe_2$ 2H/1T Hybrid Nanoparticles Prepared from Femtosecond Laser Ablation in Liquid and Their Enhanced Photothermal Conversion Efficiencies. *Adv. Mater.* **2023**, 2301129.

[2] **Ye, F.**; Ayub, A.; Chang, D.; Chernikov, R.; Chen, Q.; Karimi, R.; Wettig, S.; Sanderson, J.; Musselman, K. P. Molybdenum Blues with Tunable Light Absorption Synthesized by Femtosecond Laser Irradiation of Molybdenum Trioxide in Water/Ethanol Mixtures. *Adv. Opt. Mater.* **2022**, *10*(23), 2201304.

[3] **Ye, F.**; Chang, D.; Ayub, A.; Ibrahim, K.; Shahin, A.; Karimi, R.; Wettig, S.; Sanderson, J.; Musselman, K. P. Synthesis of Two-Dimensional Plasmonic Molybdenum Oxide Nanomaterials by Femtosecond Laser Irradiation. *Chem. Mater.* **2021**,*33*(12), 4510-4521.

[4] Gurbandurdyyev, G.; Mistry, K.; Delumeau, L.; Loke, J. Y.; Teoh, C. H.; Cheon, J.; **Ye, F.**; Tam, K. C.; Musselman, K. P. Robust, Conformal ZnO Coatings on Fabrics *via* Atmospheric-Pressure Spatial Atomic Layer Deposition with In-Situ Thickness Control. *ChemNanoMat* **2023**, *9*, e202200498.

[5] Shahin, A.; Ibrahim, K.; **Ye, F.**; Karimi, R.; Sanderson, J.; Musselman, K. P. Selective sensing of heavy metal ions via fluorescence quenching of femtosecond-laser-synthesized 2D nanoparticles. *Sens. Actuators B: Chem.* **2022**, *359*, 131576.

[6] Ibrahim, K.; Shahin, A.; Jones, A.; Alshehri, A.; Mistry, K.; Singh, M.; **Ye, F.**; Sanderson, J.; Yavuz, M.; Musselman, K. P. Humidity-resistant perovskite solar cells via the incorporation of halogenated graphene particles. *Sol. Energy* **2021** *224*, 787-797.

## Abstract

Photothermal therapy is a novel cancer treatment that can be an alternative or useful supplement to traditional cancer treatments. It relies on nanomaterials which target and accumulate in tumor cells to absorb near infrared light and convert the absorbed light energy into heat to kill tumors. Therefore, it is important to prepare nanomaterials with high photothermal conversion efficiencies (PTCEs). Pulsed laser ablation in liquid is a novel technique to prepare nanomaterials. In this work, this technique is used to prepare molybdenum-based nanomaterials including substoichiometric molybdenum oxide ($MoO_{3-X}$) nanosheets, molybdenum blue (MB) nanorings, and molybdenum selenide ($MoSe_2$) spherical nanoparticles and quantum dots.

$MoO_{3-X}$ and MB nanorings are produced by laser ablation of $MoS_2$ powder and $MoO_3$ powder in water/ethanol mixtures, respectively. The oxidation process of $MoS_2$ and the formation mechanism of MB nanorings are studied. In both ablation processes, ethanol plays a critical role in reducing Mo(VI) which results in the blue color of $MoO_{3-X}$ and MB nanorings. 80-90 vol.% ethanol is the optimum to produce blue-colored $MoO_{3-X}$, while 30 vol.% ethanol is the optimum to produce MB nanorings with the darkest blue color. A higher concentration of ethanol in the solvent results in the formation of $MoO_{3-X}$ instead of MB. The $MoO_{3-X}$ nanosheets show a high PTCE of 33%, and the MB nanorings show a PTCE as high as 45%.

$MoSe_2$ spherical nanoparticles are produced by laser ablation of $MoSe_2$ powder for a short time (10 min) in isopropyl alcohol or in water containing polyethylene glycol (PEG). The spherical nanoparticles are fragmented from ablated powder particles based on two primary approaches. The first one is thermodynamic equilibrium melting and evaporation which usually occurs when the ablation power is low. The second one is explosive boiling when the ablation power is high. Two kinds of spherical nanoparticles, including polycrystalline nanoparticles and onion-structured nanoparticles, are observed. The polycrystalline nanoparticles are primarily formed by the agglomeration of nanocrystals, atoms and ions ejected from the ablated powder. The onion-structured nanoparticles are formed by

nucleation on the surface of melted droplets followed by inward growth of {002} planes of $MoSe_2$ along the radial direction of the droplets layer-by-layer. Additionally, PEGylated $MoSe_2$ nanoparticles can be directly produced by ablating $MoSe_2$ power in aqueous PEG solutions. The surface attachment of PEG to the nanoparticles *via* Mo-O chemical bonds can suppress oxidation of the nanoparticles. The $MoSe_2$ nanoparticles show high PTCEs of around 38-40% thanks to strong sub-bandgap photon absorption.

Smaller PEGylated $MoSe_2$ quantum dots are synthesized by laser ablation with a high power (1.5 W) for a longer time (30 min). The PTCEs of the PEGylated quantum dots are around 42-44%, higher than that of the PEGylated spherical nanoparticles, which is probably due to a larger absorption cross-section, multiple exciton generation and multiple electron-decay channels.

## Acknowledgements

First and foremost, I would like to express my sincere gratitude to my supervisors, Dr. Kevin Musselman and Dr. Joseph Sanderson, for their valuable guidance and advice on my study and research and their support in helping me apply for scholarships. To Dr. Kevin Musselman, thank you for your confidence in me and giving me this opportunity to join your group. Your professionalism in supervising students, managing the lab and research projects let me enjoy my research life here in Waterloo, and will continue inspiring me to be a better person. To Dr. Joseph Sanderson, thank you for bringing me to the world of ultrafast pulse laser and allowing me to operate the world-class femtosecond laser system by myself. I would also like to express my sincere appreciation to my collaborators: Darren Chang, Ahsan Ayub and Dr. Shawn Wettig. Without your insightful suggestions and hard work, I could not have finished this project.

I am also very thankful to all the technicians and research scientists who trained me to use various equipment and helped me analyze my materials, especially Dr. Joseph Jessy, Dr. Lei Zhang and Dr. Nina Heinig in WATLab, Dr. Sandra Gibson in QNC, Dr. Sahar Adnani in G2N, Dr. Natalie Hamada in CCEM, Dr. Roman Chernikov in CLS, Dr. Charles Dal Castel in the analytical lab of chemical engineering, Dr. Holly Fruehwald in Dr. Rodney Smith's group and Dr. Mohamad Zandieh in Dr. Juewen Liu's group. Additionally, I appreciate all the group members in both Dr. Kevin Musselman's group and Dr. Joseph Sanderson's group for their kind assistance in the past four years.

Moreover, I would like to thank the New Frontiers in Research Fund for funding my research, and my financial support sources including Engineering Excellence PhD Fellowship, WIN NanoFellowship, Ontario Graduate Scholarship and W.S. Rickert Graduate Student Fellowship.

Finally, my deep thanks go to my family, especially my parents. I would not go back to school after working for several years without your support and encouragement.

# Table of Contents

# List of Figures

# List of Tables

# List of Abbreviations

AFM: Atomic force microscope

ATR: Attenuated total reflection

BN: Boron nitride

BSA: Bovine serum albumin

CT: X-ray computed tomography

DLS: Dynamic light scattering

DOX: Doxorubicin

EPR: Enhanced permeability and retention

ER: Estrogen receptor

FT-EXAFS: Fourier-transformed extended X-ray absorption fine structure

FTIR: Fourier transform infrared spectroscopy

GIXRD: Grazing incident X-ray diffraction

HAADF: High angle annular dark field

HRTEM: high resolution transmission electron microscopy

IPA: Isopropyl alcohol

LA: Lipoic acid

LSPR: Localized surface plasmon resonance

NIR: Near infrared

NMP: N-methyl-2-pyrrolidone

OS: Onion-structured

PAA: Polyacrylic acid

PDT: Photodynamic therapy

PC: Polycrystalline

PEG: Polyethylene glycol

PEG-SH: Thiolated polyethylene glycol

PGLA: Poly(lactic-Glu-co-glycolic acid)

PLAL: Pulsed laser ablation in liquid

POM: Polyoxometalate

PTA: Photothermal therapy agent

PTCE: Photothermal conversion efficiency

PTT: Photothermal therapy

PVP: Polyvinylpyrrolidone

SDS: Sodium dodecyl sulfate

SEM: Scanning electron microscope

SP: Soybean pentapeptide

STEM: scanning transmission electron microscope

TGA: Thermogravimetric analysis

TMDC: Transition metal dichalcogenide

TMO: Transition metal oxide

XPS: X-ray photoelectron spectroscopy

# Chapter 1
# Introduction

## 1.1 Background Introduction

Cancer has been a major health issue for people in many countries. Early diagnosis, universal access to healthcare and effective treatment are critical to reduce cancer mortality.[1] Conventional cancer treatments include surgery, radiochemistry and chemotherapy. In order to effectively remove tumor cells and minimize the recurrence of the tumors, different treatments are usually carried out together.[1] Chemotherapy has many side effects on healthy cells and radiotherapy which uses high doses of radiation to kill cells needs to be delivered to tumor sites precisely.[2] Therefore, there exists a high demand to develop more advanced treatments that can kill tumor cells effectively and are more friendly to healthy cells. Photothermal therapy (PTT) has attracted much attention recently for its non-invasive treatment based on the administration of photothermal therapy agents (PTAs). The PTAs can target and accumulate in tumor tissues through either passive targeting strategies such as enhanced permeability and retention (EPR) or active targeting strategies which functionalize PTAs with biomolecules that can recognize molecules overexpressed on tumor sites.[3] When near infrared (NIR) light illuminates tumor tissues, the accumulated PTAs absorb the NIR light and convert the energy to heat, leading to the apoptosis of tumor cells. Compared to conventional treatments, PTT has fewer side effects as it only works on the area where the PTAs accumulate. Therefore, the synthesis of PTAs with high photothermal conversion efficiency (PTCE), good biocompatibility and precise targeting at tumors is of critical importance to PTT.

As of today, many inorganic PTAs including gold nanoparticles,[4–6] transition metal dichalcogenide (TMDC) nanomaterials,[7–11] transition metal oxides (TMO),[12,13] MXene nanosheets (two-dimensional carbides or nitrides),[14,15] carbon-based nanomaterials[16,17] and black phosphorus nanomaterials[18–20] have been found to be promising PTA candidates. The synthesis of these nanomaterials usually has two approaches. One is bottom-up methods

involving chemical reactions between precursors; the other is physical top-down methods that apply external forces to fragment bulk materials into nanomaterials; however, these methods usually take a long time and may introduce contaminants. Additionally, these nanomaterials usually need to be surface functionalized with biomolecules to improve their biocompatibility and physiological stability, and to reduce cytotoxicity.

Pulsed laser ablation in liquid (PLAL) is a method to synthesize nanomaterials using a pulsed laser beam. There are two approaches for PLAL. One is to focus a laser beam on a large bulk target immersed in liquid. The laser beam should be well controlled to focus on the surface of the target. It also requires continuous movement of either the container that carries the target or the laser beam along directions that are vertical to the incident laser beam to ablate the whole target. The other is to ablate bulk powder particles that are dispersed in liquid. There are no strict requirements on the position of the focal point of the laser beam as the powder particles are usually stirred by a magnetic stirrer during the laser ablation process such that all the powder particles can be ablated.[21] Even though PLAL aims to fragment bulk materials, chemical reactions between bulk materials with liquid molecules are unavoidable since the high-energy laser pulses can ionize and fragment not only bulk materials but also liquid molecules. Hence PLAL can be used to perform either top-down or bottom-up synthesis methods. As a result, PLAL shows several advantages over conventional methods to synthesize nanomaterials. Firstly, the setup is simple. The whole experiment can be performed at room temperature in atmospheric conditions. Secondly, PLAL is regarded as a "green" synthesis method. It does not necessarily require other chemicals like catalysts besides the initial bulk materials or precursors and produces minimal waste such that it introduces little contamination into the produced nanomaterials. Thirdly, PLAL is a fast method to synthesize nanomaterials.[22] Among all the PLAL methods, ablation with femtosecond laser pulses is more favorable thanks to the minimal heat generated in the whole process, as the pulse duration on the time scale of femtoseconds is much shorter than the thermal relaxation time of most materials.[23]

## 1.2 Objectives

As of today, PLAL has been widely applied to synthesize single-element nanoparticles like noble metals *via* fragmentation of bulk materials or basic oxide nanoparticles *via* ablating corresponding metal oxide targets or metal targets in oxygen containing liquids like water and alcohol solvents. The laser ablation of semiconductors such as TMDC and TMO materials is less studied, including those based on molybdenum. Molybdenum based TMDCs and oxides have promising properties for PTAs and warrant further development. This work aims to use a femtosecond laser to ablate Molybdenum based TMDC and TMO bulk powders in liquids to synthesize molybdenum-based PTA nanomaterials with high PTCEs and explore the interaction between laser pulses and the bulk powders.

The detailed objectives are listed below:

1. To prepare molybdenum oxide nanomaterials including substoichiometric molybdenum oxide ($MoO_{3-X}$) nanosheets and molybdenum blue nanorings by femtosecond laser ablation of molybdenum disulfide ($MoS_2$) and molybdenum trioxide ($MoO_3$) powders in mixed ethanol/water solvents, and research their formation mechanisms and PTCEs.

2. To prepare molybdenum selenide ($MoSe_2$) nanoparticles by femtosecond laser ablation of $MoSe_2$ bulk powder particles in isopropyl alcohol (IPA), and research their formation mechanisms and PTCEs.

3. To develop a one-pot synthesis method to suppress the oxidation of $MoSe_2$ nanoparticles in PLAL and prepare $MoSe_2$ nanoparticles surface functionalized with polyethylene glycol (PEG) by femtosecond laser ablation of $MoSe_2$ bulk powder and PEG in water together.

## 1.3 Chapter Synopses

Chapter 2 Literature Review: Different inorganic PTAs including noble metals, TMO, molybdenum blue, TMDC and other two-dimensional materials such as MXene, black phosphorus, and their mechanisms to absorb NIR light and generate heat are introduced. A

review of the synthesis methods of $MoO_{3-X}$, molybdenum blues and $MoSe_2$ nanomaterials is presented. Additionally, The PLAL technique to prepare nanomaterials and laser-matter interactions are introduced.

Chapter 3 Methodology: The femtosecond laser system and the PLAL setup used in this work are introduced. A customized setup to evaluate the photothermal conversion performance of nanomaterials and the method to calculate PTCE are also presented.

Chapter 4 Synthesis of $MoO_{3-X}$ nanosheets by femtosecond laser ablation: Plasmonic $MoO_{3-X}$ nanosheets are produced by laser ablation of $MoS_2$ bulk powder in ethanol/water mixtures. It is found that both ethanol and water are necessary to produce $MoO_{3-X}$. The oxidation process is also researched. The highest PTCE achieved by the $MoO_{3-X}$ nanosheets is around 33%.

Chapter 5 Synthesis of molybdenum blue nanorings by femtosecond laser ablation: Molybdenum blue nanorings are special giant molybdenum polyoxometalate nanoclusters which have high absorbance of NIR light. MB nanorings are synthesized by laser ablation of $MoO_3$ bulk powder in water/ethanol mixtures. It is found that the optical absorption band of the MBs can be tuned by changing the concentration of ethanol in the solvent. The highest PTCE observed for the MB nanorings is 45%.

Chapter 6 Synthesis of $MoSe_2$ spherical nanoparticles by femtosecond laser ablation: $MoSe_2$ 1T/2H hybrid nanoparticles are synthesized by laser ablation of $MoSe_2$ bulk powder in IPA. Two types of nanoparticles are observed. One is polycrystalline nanoparticles, the other is onion-structured nanoparticles with an amorphous core and a laminated shell. The $MoSe_2$ nanoparticles show high PTCEs with the highest value of 38%. The formation mechanisms of the nanoparticles and the reasons behind their high PTCEs are studied.

Chapter 7 Synthesis of PEGylated $MoSe_2$ nanoparticles and quantum dots by femtosecond laser ablation: PEGylated $MoSe_2$ nanomaterials including quantum dots and larger spherical nanoparticles are prepared by femtosecond laser ablation of $MoSe_2$ bulk powder in aqueous solutions of PEG. It is found that PEG can be attached to the nanoparticles via Mo-O

chemical bonds in laser ablation, which can protect the nanomaterials from severe oxidation. The PEGylated $MoSe_2$ spherical nanoparticles prepared in water show consistent PTCEs. However, the PEGylated $MoSe_2$ quantum dots show a higher PTCE of 44%.

Chapter 8 Conclusions: Several conclusions are summarized, and proposed future work is presented.

# Chapter 2
# Literature Review

## 2.1 Inorganic Photothermal Therapy Agents

Photothermal therapy (PTT) is a hyperthermia cancer treatment, which creates a localized high temperature in tumor tissues to cause the apoptosis of the tumor cells when they are exposed to a laser beam (**Figure 2.1**).[24] Photothermal therapy agents (PTAs) that can selectively target tumor cells and have high photothermal conversion efficiencies (PTCEs) are of importance for PTT. PTCE is the ratio of the heat generated by PTAs to the total absorbed light energy upon laser illumination.[25] Near infrared (NIR) lasers with a wavelength between 750 nm and 1300 nm are usually used for PTT as most biological tissues have the lowest absorption of light in this window.[3] Therefore the PTA nanomaterials should present high absorption of NIR light and high PTCEs in the NIR spectrum.

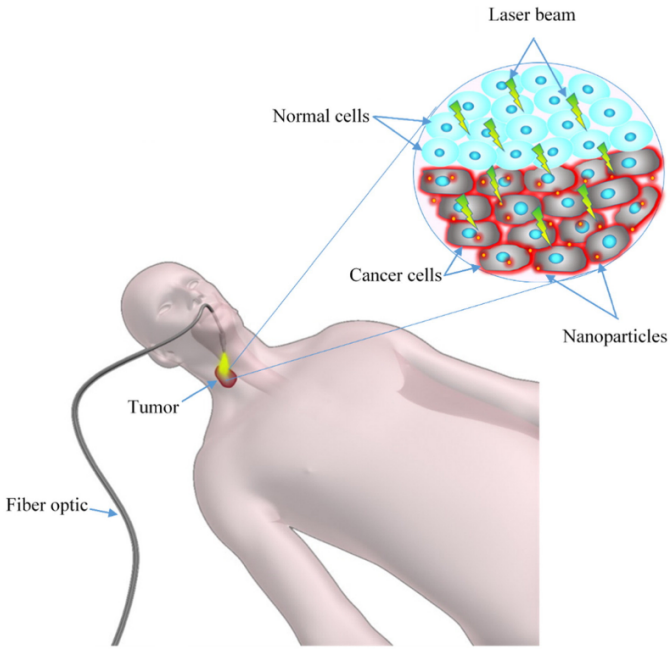


**Figure 2.1**. Schematic illustration of photothermal therapy.[24] Reprinted with permission from *J. Control. Release* 2016, *235,* 205–221. Copyright 2016 Elsevier Inc.

The size of nanomaterials is another critical factor that needs to be considered when designing PTAs. If the nanomaterials are too small, they will face renal clearance by kidneys (< 5 nm) or rapid liver uptake (10 – 20 nm); if the nanomaterials are too big, they will be filtered out from the blood into the spleen (> 200 nm).[3,26] Therefore, nanomaterials with sizes between 20 nm and 200 nm are more favorable for PTT as they can circulate in the bloodstream for enough time to effectively target and get incorporated into tumor cells.

PTA nanomaterials should also possess other features such as low toxicity to healthy cells, easy functionalization for active targeting of tumor cells and synergistic cancer treatments, and good dispersibility in blood for long circulation in the bloodstream.[27] In the past decades, several inorganic nanomaterials have been explored as PTAs, including noble metals, transition metal oxides (TMOs), polyoxometalates, transition metal dichalcogenides (TMDCs) and other nanomaterials such as graphene, MXenes and black phosphorus, thanks to facile synthesis and abundant surface functionalization. The next section will introduce these nanomaterials as PTAs.

### 2.1.1 Noble Metal Nanomaterials

Gold nanomaterials have attracted increasing attention for biomedical applications due to their tunable optical properties affected by their sizes and shapes. Gold nanoparticles can absorb light based on localized surface plasmon resonance (LSPR) which refers to a collective and coherent oscillation of surface electrons along the electric field direction of the light, as shown in **Figure 2.2**.

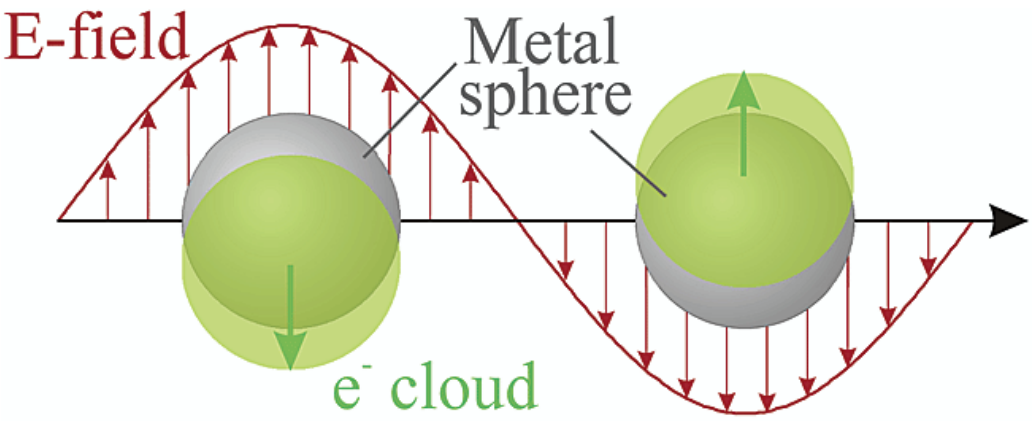


**Figure 2.2**. Schematic diagram of plasmon oscillation of a metal spherical nanoparticle.[28] Reprinted with permission from *J. Phys. Chem. B* 2003, *107*(3), 668-677. Copyright 2003 American Chemical Society.

When gold spherical nanoparticles are monodispersed in a dielectric medium and the particle size is much smaller than the wavelength of the incident light, the extinction cross-section can be estimated by solving Maxwell's equations using Mie's theory and dipole approximation. The extinction cross-section is expressed below[29–31]:

$$C_{ext} \approx \frac{24\pi^2 R^3 \varepsilon_m^{3/2}}{\lambda} \frac{\varepsilon_i}{(\varepsilon_r + 2\varepsilon_m)^2 + \varepsilon_i^2} \tag{2.1}$$

$R$ is the radius of the spherical nanoparticle; $\varepsilon_m$ is the dielectric constant of the surrounding medium; $\tilde{\varepsilon} = \varepsilon_r + i\varepsilon_i$ is the complex dielectric constant of the nanoparticle, and $\lambda$ is the wavelength of the incident light in vacuum. The resonance takes place when $\varepsilon_r = -2\varepsilon_m$. It should be noted that **Equation 2.1** only works for small, discrete spherical nanoparticles (size < 25 nm for gold) with no interactions between each other.[32] **Figure 2.3** shows the normalized absorption spectra of gold nanoparticles with different sizes.[32] The absorption band redshifts with increasing size, especially when the size is larger than 22 nm. When the gold nanoparticle size is larger than 25 nm, the oscillating electric field of the light cannot polarize the nanoparticle homogeneously such that the dipole approximation is not valid.[33] The redshift of the LSPR peak is attributed to the higher-order modes at lower energies.[33] It

should be noted that the increase in gold nanoparticle size can only tune the LSPR peak in the visible light region (up to 600 nm),[27,32] while the PTAs work in NIR region.

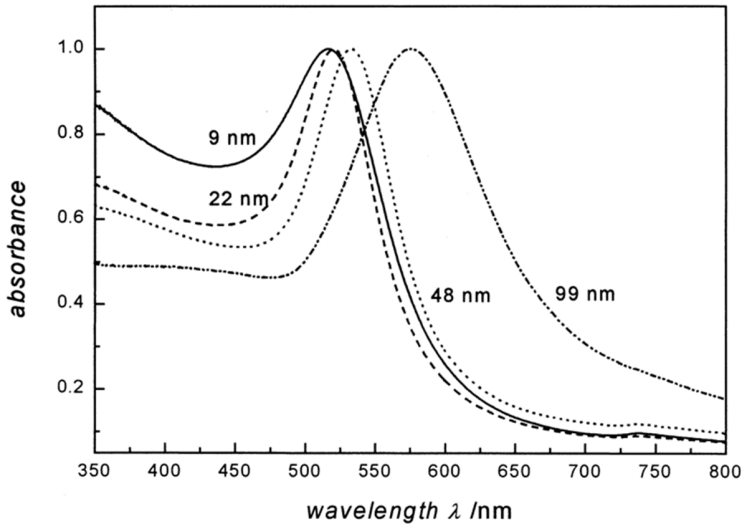


**Figure 2.3**. Normalized UV-vis spectra of gold nanoparticles with difference sizes in water.[32] Reprinted with permission from *J. Phys. Chem. B* 1999*, 103*(21), 4212–4217. Copyright 1999 American Chemical Society.

Fortunately, the LSPR peaks of gold nanomaterials with complex geometries can be tuned into the NIR region of the spectrum by varying shapes. For example, the LSPR peak redshifts with increasing aspect ratio of gold nanorods (**Figure 2.4a**);[34] and it also redshifts with decreasing shell thickness for gold nanoshells outside silica cores (**Figure 2.4b**).[35] Additionally, the LSPR peak of gold nanocages was also found to redshift with increasing thickness of the cage wall (increasing volume of $HAuCl_4$ solution in **Figure 2.4c**, as the thickness is controlled by the volume of $HAuCl_4$ during the synthesis of the gold nanocages)[36]. For more-complex-shaped nanomaterials such as gold nanostars, the LSPR peak redshifts with increasing aspect ratio of branch length to branch base, as shown in **Figure 2.4d**.[37] The PTCE of gold nanorods is usually around 20% when the nanorods are illuminated by an 808 nm laser.[4–6] Ma et al reported that the PTCE was increased to 60% when the gold nanorods were coated with a shell of layered double hydroxides which contributed more electrons to gold nanorods.[6] Additionally, the highest PTCE of gold

nanostars was recently reported to be 78.6% when the nanostars were coated with a 20 nm-thick polyaniline shell which shifted the absorption band from 733 nm to 881 nm.[38]

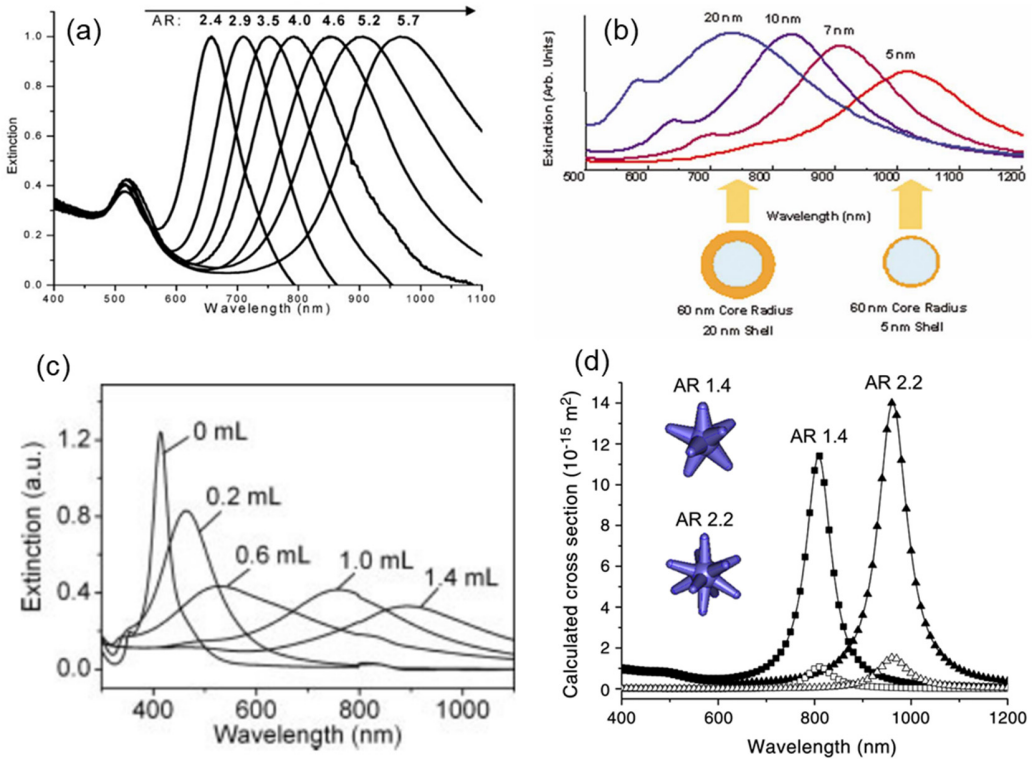


**Figure 2.4.** (a) UV-vis-NIR extinction spectra of gold nanorods with different aspect ratios.[34] Reprinted with permission from *Adv. Mater.* 2009, *21* (48), 4880-4910, Copyright 2009 Wiley-VCH. (b) UV-vis-NIR extinction spectra of gold nanoshells outside silica cores with different shell thicknesses (core radius is 60 nm).[35] Reprinted with permission from *Technol. Cancer Res. Treat.* 2004*, 3,* 33-40, Copyright 2004 SAGE Publications. (c) UV-vis-NIR extinction spectra of gold nanocages titrated with different volumes of a 0.2 mM $HAuCl_4$ solution.[36] Reprinted with permission from *Adv. Mater.* 2005, *17* (18), 2255–2261, Copyright 2005 Wiley-VCH. (d) Calculated absorption cross section and scattering cross section of gold nanostars with different aspect ratios of branch length to branch base.[37] Reprinted with permission from *Nanomedicine Nanotechnology, Biol. Med.* 2012, *8* (8), 1355–1363, Copyright 2012 Elsevier B.V.

Some other noble metal nanomaterials like silver also show LSPR peaks in the NIR region of the spectrum,[39,40] but gold nanomaterials are more favorable as they can form conjugates with other thiolated biomolecules through gold-thiol bonds to realize multifunctionality including active targeting, chemotherapy and improvement of biocompatibility. For example, Dreaden et al. attached thiolated PEG (PEG-SH) and tamoxifen to gold nanoparticles through gold-thiol chemical bonds.[41] In his design, tamoxifen aimed to selectively target breast cancer cells as estrogen receptors (ER) are overexpressed in breast cancers and tamoxifen can bind with ER to target the cancer cells. As shown in **Figure 2.5a**, PEG-SH conjugated gold nanoparticles show no apparent difference of cellular uptake in either ERα(+) or ERα(-) breast cells, while tamoxifen-PEG-SH conjugated gold nanoparticles exhibit higher cellular uptake in ERα(+) breast cells.[41] Similarly, Wang et al. functionalized gold nanorods with poly(L-Glu-co-Lys acid) (SH-PGLA) through gold-thiol bonds and then attached doxorubicin (DOX) to the conjugate through acid sensitive hydrazone bonds for a combination of PTT and chemotherapy.[5] As illustrated in **Figure 2.5b**, when the gold nanorod conjugates circulate in blood where the pH value is 7.4, the surface of the conjugates is negatively charged. When the conjugates reach cancer regions where the pH value drops to 6.5, the surface of the conjugates becomes positively charged, enhancing cellular uptake as the membrane of tumor cells is negatively charged. After cellular internalization, DOX is released by cleavage of the hydrazone bonds in the conjugates as the pH value of the intracellular environment drops to 5.0-5.5.[5] The combination of PTT and chemotherapy can effectively kill tumor cells. Even though gold nanoparticles show great potential as PTAs, the high cost of gold encourages people to look for other nanomaterials for PTT.

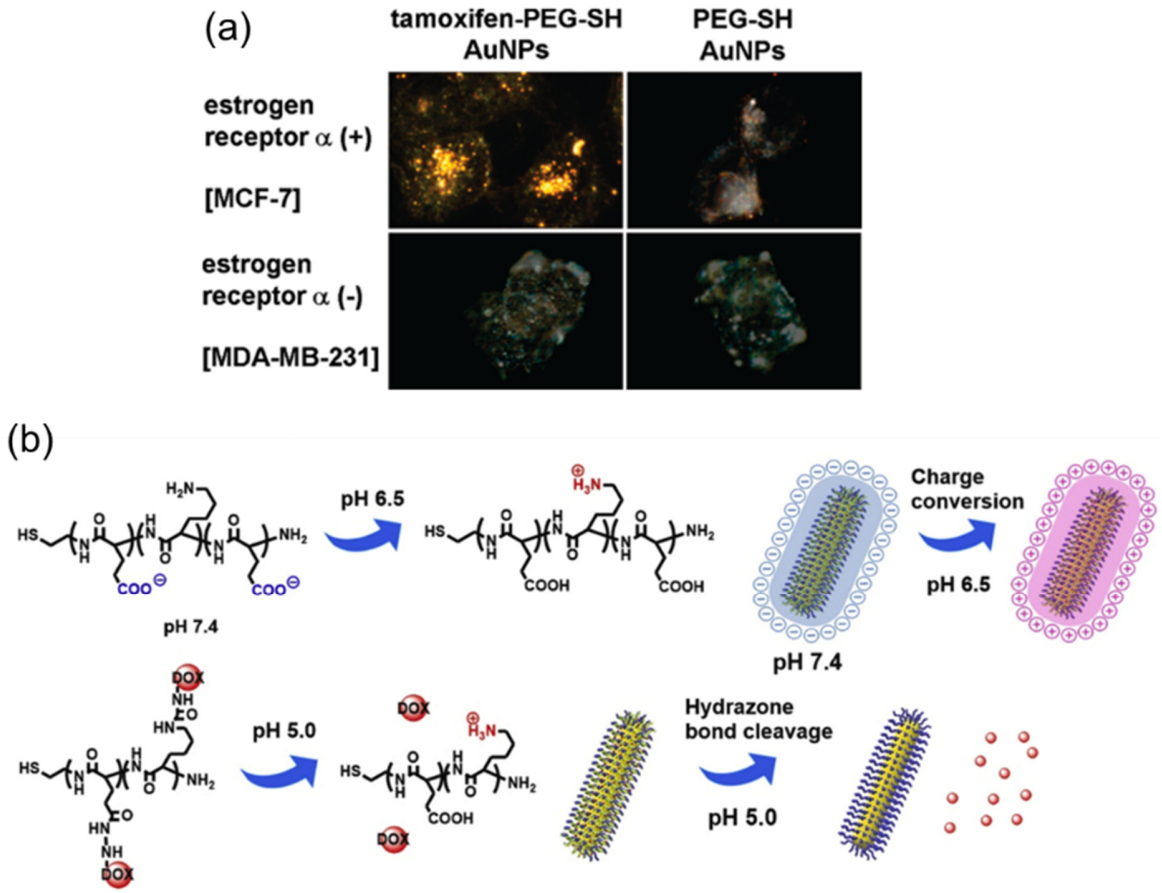


**Figure 2.5.** (a) Dark-field scattering microscopic images showing intracellular localization of different gold nanoparticle conjugates in breast cancer cells with or without rich estrogen receptors.[41] Reprinted with permission from *Bioconjugate Chem.* 2009, *20*(12), 2247-2253, Copyright 2009 American Chemical Society. (b) Schematic illustration of surface charge change and drug release of gold nanorod conjugates in terms of pH values.[5] Reprinted with permission from *Colloids Surfaces B Biointerfaces* 2021, *207*, 112014, Copyright 2021 Elsevier B.V.

### 2.1.2 Transition Metal Oxide Nanomaterials

Substoichiometric transition metal oxides (TMO) such as $MoO_{3-X}$ and $WO_{3-X}$ are another promising group of PTAs due to strong absorbance of NIR light. Even though $MoO_3$ and

$WO_3$ are wide-bandgap semiconductors that have low absorbance of NIR light, $MoO_{3-X}$ ($X > 0.125$) and $WO_{3-X}$ ($X > 0.1$) are semimetals thanks to high free-electron concentrations arising from oxygen vacancies such that they can absorb NIR light and convert the light energy to heat based on the LSPR effect.[42,43]

Ding et al. reported that $MoO_{3-X}$ quantum dots had PTCE of 25.5%.[12] In Ding's work, the $MoO_{3-X}$ quantum dots could also work as photosensitizers for photodynamic therapy (PDT) which generated reactive oxygen species to damage cancer cells.[12] The combination of PTT and PDT can increase the efficacy of cancer treatment. Similarly, Bao et al. reported a synergistic cancer treatment method that used PEGylated $MoO_{3-X}$ hollow nanoparticles to load the anticancer drug Camptothecin and the PTCE of the $MoO_{3-X}$ hollow nanoparticles was 22.64% when illuminated with an 808 nm laser.[13] $MoO_{3-X}$ nanosheets are more attractive than nanoparticles thanks to higher specific surface areas for surface modification. Wu et al. used $MoO_{3-X}$ nanosheets to carry $MnO_2$ nanocubes which facilitated the generation of reactive oxygen species for PDT, and reported a higher PTCE of 37%.[44] Another advantage of $MoO_X$ nanomaterials which contain Mo(V) is that they are degradable under certain pH conditions. They can be oxidized to $[Mo^{VI}O_4]^{2-}$ by oxygen in alkali environments, or kept stable in acidic environments.[45] Song et al. found that PEGylated $MoO_X$ nanosheets degraded very quickly in major organs of tested mice. The content of Mo dropped to a very low level after one day (**Figure 2.6 a and b**).[45] Ultrasound imaging of tumor and muscle areas (**Figure 2.6 c and d**) showed that the intensity of the acoustic signal in the tumor area was much higher than that in the muscle area at 24 hrs post injection. This suggests that PEGylated $MoO_X$ nanosheets accumulating in acidic and oxygen-deficient tumor cells generated heat upon illumination of NIR light to kill the tumor cells, then quickly degraded to $[Mo^{VI}O_4]^{2-}$ and were removed from body to reduce damage to healthy cells.

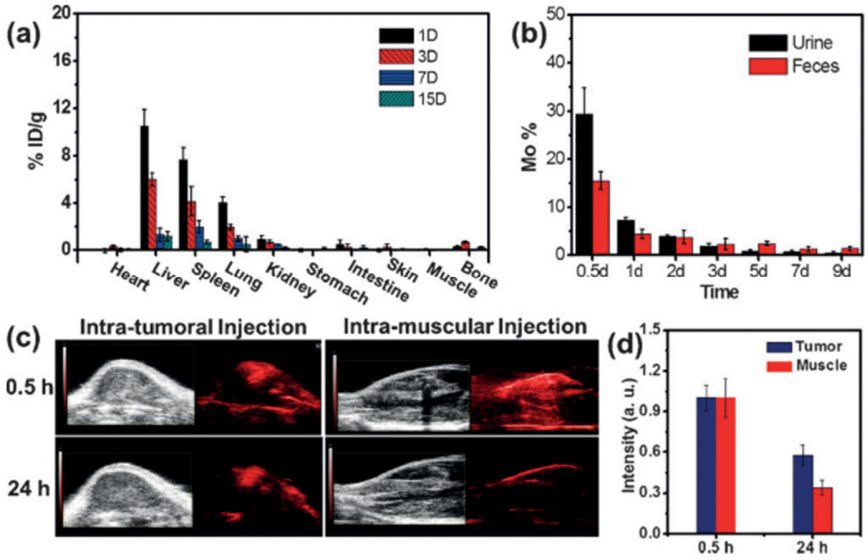


**Figure 2.6.** (a) Time-dependent biodistribution of molybdenum in female mice after intravenous injection of PEGylated $MoO_X$ nanosheets. (b) Content of molybdenum in urine and feces at various times after injection. (c) Ultrasound and photoacoustic imaging of tumor and muscle areas at 0.5 and 24 h post injection. (d) Relative photoacoustic signal intensities in the tumor and muscle areas.[45] Reprinted with permission from *Angew. Chemie - Int. Ed.* 2016, *55*(6), 2122-2126, Copyright 2016 Wiley-VCH.

Like $MoO_{3-X}$ nanomaterials, $WO_{3-X}$ has also been widely tested as a PTA. PEGylated $W_{18}O_{49}$ nanowires (1 mg/mL in water) were reported to increase the temperature to 50 °C after illumination for 2 min by a 960 nm laser with a power density of 0.72 W/cm$^2$ in an *in-vivo* test.[46] The PTCE of PEGylated $WO_{3-X}$ nanoflowers was reported to be 28.1% when illuminated by a 915 nm laser.[47] Sun et al. also reported that $WO_{2.9}$ nanorods showed a high PTCE of 44.9% under the illumination of a 808 nm laser thanks to the LSPR effect.[48]

### 2.1.3 Polyoxometalate clusters

Polyoxometalates (POMs) are inorganic metal oxide clusters which are comprised of group V (V, Ta and Nb) and group VI (Mo and W) transition metals bridged by oxygen atoms. If the POM molecules only contain one metal element, they are called isopolyoxometalates.

When they contain more than one metal element (heteroatoms), they are called heteropolyoxometalates. Additionally, the number of atoms in POM clusters ranges from tens to thousands.[49] The integration of heteroatoms and the diverse sizes make the chemical compositions and structures of POMs highly versatile such that they present variable physicochemical properties.[50] There are three basic forms of small Mo POMs: Lindqvist, Keggin and Wells-Dawson, as shown in **Figure 2.7**.[50] In some POMs, some metal atoms are reduced without changing the overall structure of POMs. The mixed-valent metal atoms make the POMs colored, mostly blue. The blue color arises from a high absorption band in the NIR region of the spectrum due to delocalized electrons and intervalence charge transfer. The intensity and position of the absorption band can be tuned by the degree of reduction.[51] The intervalence charge transfer occurs when electrons in a reduced metal atom move to a neighboring full valent atom through the oxygen bridge upon the absorption of photons. The excited electrons eventually drop back to the ground state and dissipate energy in the form of heat.[51] Therefore, POMs are attractive for PTT.

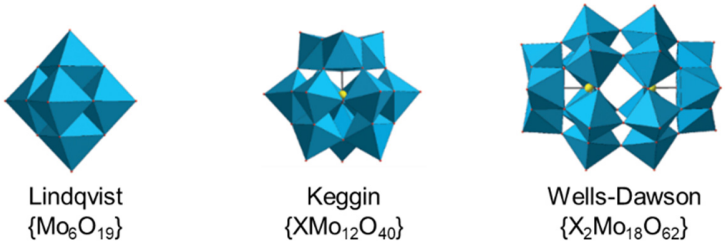


**Figure 2.7** Basic types of small Mo POMs. X refers to heteroatoms.[50] Adapted with permission from *Nat. Rev. Chem.* 2018, *2* (2), 0112, Copyright 2018 Springer Nature.

Zhang et al. synthesized a Keggin-structured Mo POM by using sodium dihydrogen phosphate dodecahydrate ($NaH_2PO_4 \cdot 12H_2O$) to reduce hexaammonium molybdate tetrahydrate ($(NH_4)_6Mo_7O_{24} \cdot 4H_2O$) in acidic solvents.[52] The pH value was controlled by the concentration of L-ascorbic acid in the solvents. It was found that the degree of reduction of the POM was controlled by the pH value of the solvent. A low pH value resulted in more significant reduction and a higher absorbance of NIR light (**Figure 2.8a**).[52] Meanwhile, the small POM molecules were found to self-assemble to larger hollow spheres when the pH

dropped, and disassembled when the pH increased (**Figure 2.8b and c**).[52] Hence the POMs can remain as small molecules when circulating in the blood stream to avoid rapid removal by the mononuclear phagocyte system but self-assemble to larger molecules, which are more likely accumulate in tumors by enhanced permeability and retention (EPR), when activated by acidic tumor microenvironments.[52]

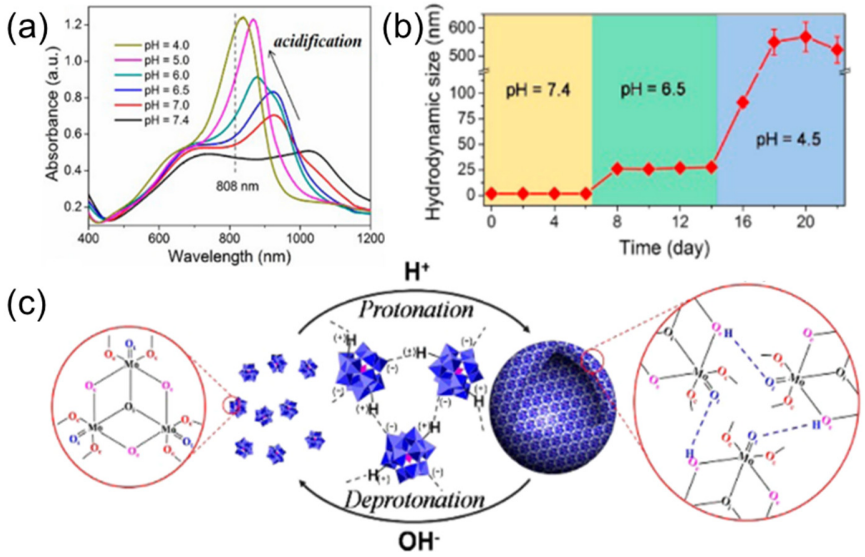


**Figure 2.8.** (a) UV−vis absorption spectra of POM nanoclusters at different pH values. (b) Average hydrodynamic size of POM nanoclusters in the solution with successive acidifications from pH = 7.4 to 6.5 and to 4.5. (c) Schematic illustration of self-assembly of small POM clusters into large hollow spheres through protonation-induced hydrogen bonding in an acidic environment.[52] Reprinted with permission from *J. Am. Chem. Soc.* 2016, *138*(26), 8156-8164. Copyright 2016 American Chemical Society.

The photothermal conversion performance of POMs is sensitive to acidity, and the interaction of bare POMs with peptides and other biomolecules due to negatively charged surfaces might lead to toxicity issues.[51] Therefore, it is necessary to wrap POMs with positively charged biocompatible molecules to increase physiological stability and reduce toxicity to healthy cells. Organic dendrons comprised of cationic heads and triethylene glycol chain tails could be used to encapsulate $Mo_{154}$ nanorings to form core-shell structures

(**Figure 2.9a**).[53] $Mo_{154}$ is one special type of giant blue POMs with 154 Mo atoms in the molecule. The encapsulation of dendritic polymers on $Mo_{154}$ increased its biocompatibility and stability, and efficiency to load drugs. The PTCE of the composite was 30.9% when illuminated with an 808 nm laser.[53] Additionally, soybean pentapeptide (SP) was found to be a good biopolymer to increase the photothermal stability of POMs.[54] As shown in **Figure 2.9b**, a SP-encapsulated reduced POM (rSP) increased the temperature of an aqueous solution quickly after storing in air for 24 hrs. In contrast, the reduced POM (rPOM) without SP encapsulation only increased the temperature of the solvent slightly.[54]

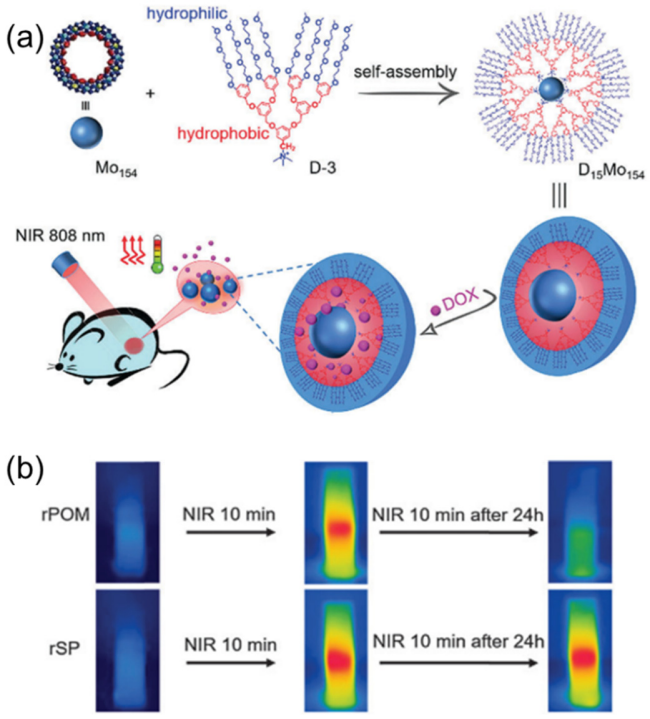


**Figure 2.9.** (a) Schematic illustration of the preparation of $D_{15}Mo_{154}$ composite micelles, and drug loading and release upon 808 nm laser irradiation.[53] Reprinted with permission from *J. Mater. Chem. B* 2018, *6*(2), 241-248. Copyright 2018 Royal Society of Chemistry. (b) IR thermal images of rPOM and rSP in an aqueous solution after 10 min of laser illumination (808 nm, 1 W/cm$^2$) and the same samples tested again after 24 hrs. The sample concentration

was 0.5 mM.[54] Reprinted with permission from *Soft Matter,* 2019*, 15,* 5375. Copyright 2018 Royal Society of Chemistry.

### 2.1.4 Transition Metal Dichalcogenide Nanomaterials

Transition metal dichalcogenides (TMDCs) have a general formula of $MX_2$, where M is a transition metal element from group IV, V or VI (Ti, Nb, Mo, W, etc.) and X is a chalcogen element including S, Se and Te.[55] A plane of M is sandwiched by two planes of X to form layered structures and adjacent layers are stacked by van der Waals forces to form bulk materials such that the layers can be exfoliated to form nanosheets. In 2013, Chou et al. first found that the chemically exfoliated $MoS_2$ nanosheets demonstrated good photothermal conversion performance thanks to their high absorbance of NIR light.[56] Since then many other TMDC nanomaterials including $MoS_2$,[7–11] $WS_2$,[57–60] $MoSe_2$,[61–63], $WSe_2$[64–66] and $MoTe_2$[67] have been used as PTAs for PTT.

One reason that TMDC nanomaterials are favorable for PTT is that the high specific surface area of the 2D structure makes them ideal platforms to carry biomolecules and anti-cancer drugs to achieve a synergy of phototherapy and chemotherapy, which is expected to be more efficient to kill cancer cells; however, TMDC nanomaterials usually need to be surface functionalized with biopolymers to increase biocompatibility and physiological stability and reduce cytotoxicity. Regular PEG physiosorbed by TMDC nanomaterials *via* van der Waals force is one solution, however, the binding is not that strong. Lipoic-acid-terminated PEG (LA-PEG) is an alternative. For example, $MoS_2$ nanosheets were surface functionalized with LA-PEG and carried antitumor drugs (**Figure 2.10a**).[8] Compared to regular PEG, The two sulfur atoms in the lipoic acid terminal can form stronger bonds with $MoS_2$ nanosheets.[8] LA-PEG was also used to attach to $WS_2$ nanosheets.[57] Another way to form strong binding of PEG with TMDC materials is through amide bonds. Chen et al. prepared $MoS_2$ nanosheets surface functionalized with polyacrylic acid ($MoS_2$-PAA) *via* a one-pot hydrothermal method, then $NH_2$ terminated PEG ($NH_2$-PEG) was conjugated to the nanosheets *via* amide bonds, as shown in **Figure 2.10b**.[9] It was found that the conjugates

biodegraded quickly in pH-neutral solutions but slowly in acidic solutions and the major degradation product was $MoO_4^{2-}$ which could be quickly excreted from body after PTT.[9,68]

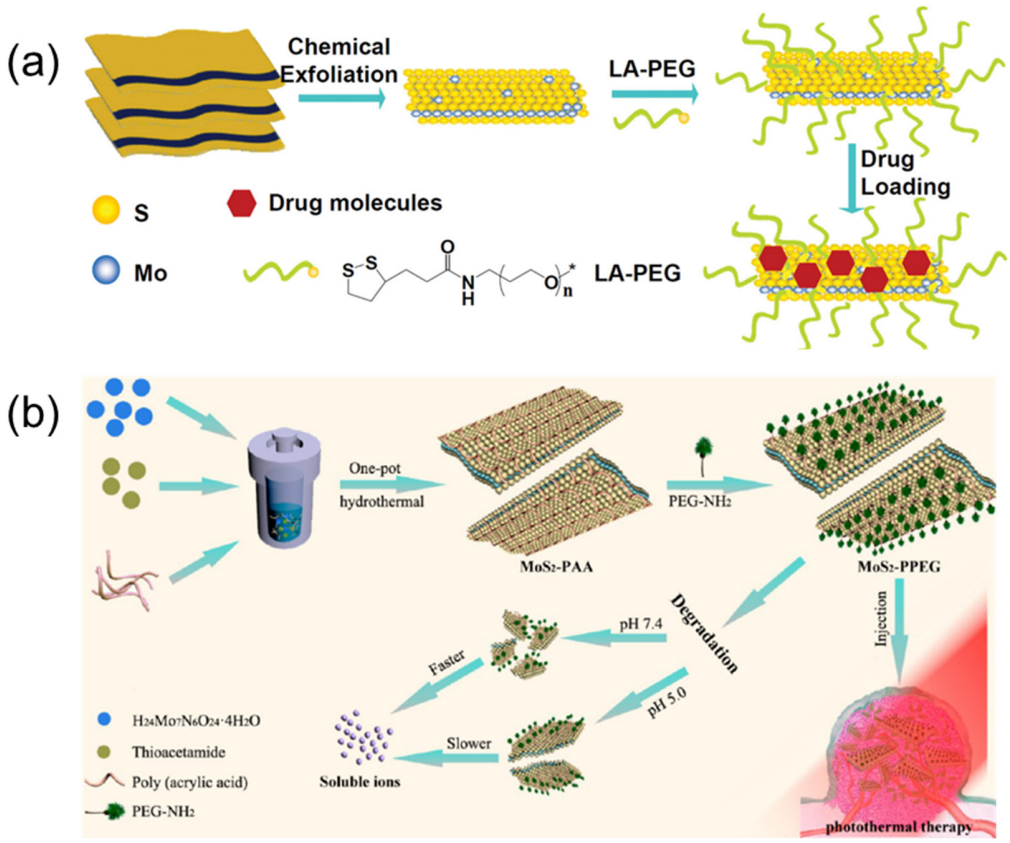


**Figure 2.10.** Schematic illustration of (a) the fabrication process of PEGylated $MoS_2$ and drug loading,[8] and (b) the preparation of $MoS_2$-PAA-PEG conjugate with desirable degradability.[9] (a) is reprinted with permission from *Adv. Mater.* 2014, *26*(21), 3433-3440, Copyright 2014 Wiley-VCH. (b) is reprinted with permission from *ACS Appl. Mater. Interfaces* 2017, *9*(20), 17347-17358. Copyright 2017 American Chemcal Society.

Besides drug loading, TMDC nanosheets can also be platforms to deliver other functional nanomaterials such as photosensitizers for PDT and RNA for gene-thermotherapy. Yong et al. applied $WS_2$ nanosheets functionalized with bovine serum albumin (BSA) as platforms to carry methylene blue for PDT.[59] Like PEG, BSA can also improve the biocompatibility and physiological stability of $WS_2$ nanosheets. Upon illumination with an 808 nm laser, the $WS_2$

conjugates generated heat leading to the release of the methylene blue from the $WS_2$ nanosheets. Then the methylene blue generated reactive oxygen species to kill cancer cells upon illumination with a 665 nm laser.[59] Similarly, $WSe_2$ nanosheets can also carry methylene blue for PDT.[64] Surface functionalization of TMDC nanomaterials with genes is one solution to treat some cancer cells that show thermal resistance as a result of a heat shock response triggered by PTT. For example, $WS_2$ nanodots surface functionalized with small intervening RNA were used to intervene a gene called survivin which could suppress cancer cells apoptosis by blocking caspase activation.[58] The downregulation of survivin reduced thermal resistance of cancer cells and made the cells more sensitive to heat, then a mild temperature increase could kill the cancer cells.[58] An advantage of $WS_2$ over $MoS_2$ is that $WS_2$ has better X-ray attenuation ability such that $WS_2$-based nanoplatforms can also be used for X-ray computed tomography (CT) to diagnose cancers.[57,58,60]

Compared to $MoS_2$ and $WS_2$, $MoSe_2$ and $WSe_2$ nanomaterials display higher absorbance of NIR light as they have excitonic absorption bands around 800 nm, as shown in **Figure 2.11**. The PTCEs of some TMDC nanomaterials upon illumination with 808 nm laser beams are listed in **Table 2.1**.

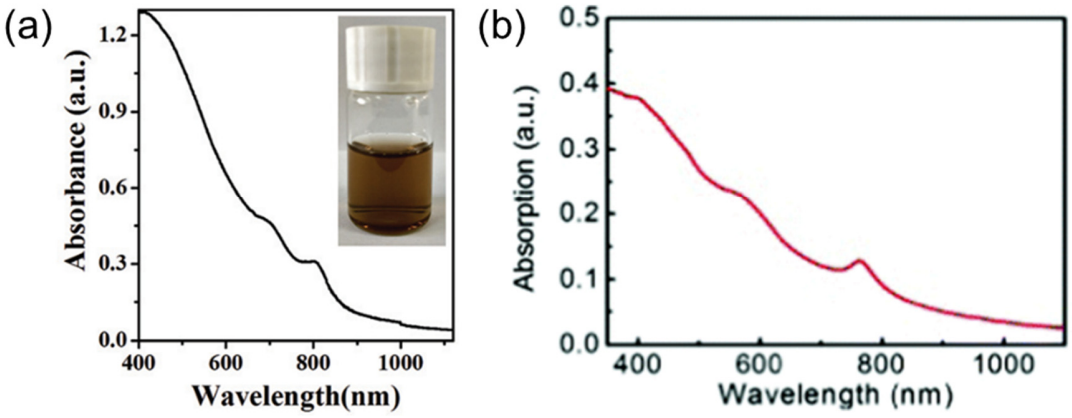


**Figure 2.11.** UV-Vis-NIR spectrum of (a) $MoSe_2$ nanodots surface attached with F127[61] and (b) $WSe_2$ nanosheets surface modified with BSA in water.[64] Inset in (a) is the image of a $MoSe_2$ suspension. (a) is reprinted with permission from *Nanoscale*, 2016, *8*, 2720.

Copyright 2016 Royal Society of Chemistry. (b) is reprinted with permission from *J. Mater. Chem. B*, 2017, *5*, 269. Copyright 2017 Royal Society of Chemistry.

**Table 2.1** Photothermal conversion efficiencies of several TMDC nanomaterials

| Materials | Surface Functionalization | PTCE | Ref. |
|---|---|---|---|
| $MoS_2$ nanosheets | Chitosan and doxorubicin | 24.4% | 7 |
| $MoS_2$ nanoflowers | LA-PEG | 27.6% | 10 |
| $WS_2$ nanosheets | BSA and methylene blue | 32.8% | 59 |
| $WS_2$ nanosheets | Thiol terminated PEG | 35% | 60 |
| $MoSe_2$ nanodots | F-127 | 46.5% | 61 |
| $MoSe_2$ nanosheets | Polyvinylpyrrolidone (PVP) | 57.9% | 62 |
| $WSe_2$ nanosheets | BSA and methylene blue | 35.1% | 64 |
| $WSe_2$ nanosheets | PVP | 38.3% | 65 |
| $MoTe_2$ nanosheets | PEG and doxorubicin | 33.8% | 67 |

### 2.1.5 Other PTAs

Graphene-based nanosheets are another group of 2D nanomaterials for PTT. Liu's group first tested the photothermal conversion performance of PEGylated graphene nanosheets.[16] As shown in **Figure 2.12a**, the temperature of a PEGylated graphene nanosheet solution increased quickly when illuminated with an 808 nm laser (power density: 2 W/cm$^2$).[16] Robinson et al. then researched the photothermal conversion performance of reduced graphene oxide nanosheets.[17] It was found that the reduced graphene oxide nanosheets showed 6.8 fold increase in the absorbance of 808 nm light when compared to graphene oxide nanosheets (**Figure 2.12b**).[17] This is attributed to the degree of π conjugation. In graphene oxide, the π conjugation is disrupted, leading to lower electrical conductivity and optical absorbance of visible and NIR light.[17,69]

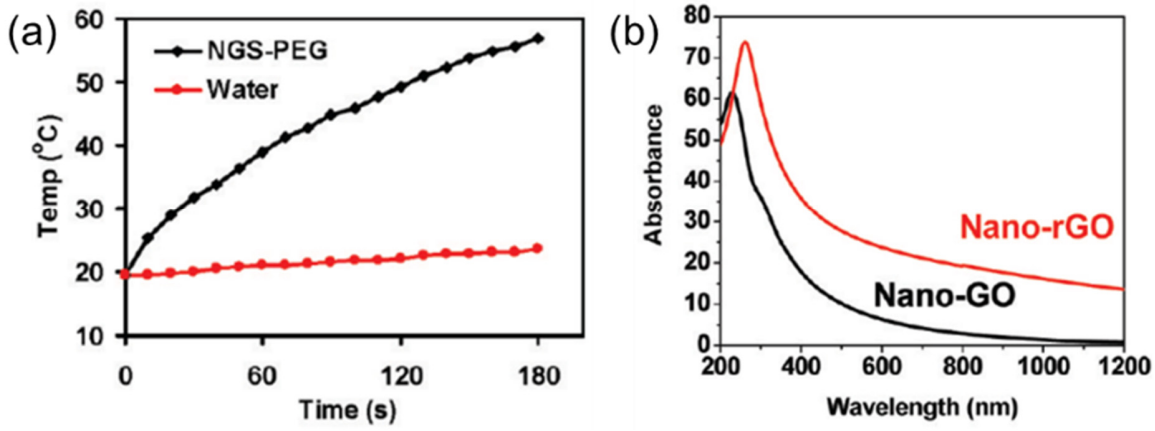


**Figure 2.12.** (a) Temperature increase of a PEGylated graphene nanosheet solution and water when illuminated by an 808 nm laser with power density of 2 W/cm$^2$.[16] Reprinted with permission from *Nano Lett.* 2010, *10*(9), 3318-3323. Copyright 2010 American Chemical Society. (b) UV-vis-NIR absorption spectra of graphene oxide and reduced graphene oxide nanosheets in water.[17] Reprinted with permission from *J. Am. Chem. Soc.* 2011, *133*(17), 6825-6831. Copyright 2010 American Chemical Society.

MXene nanosheets have also attracted much attention as they display strong absorbance of NIR light. MXene is a novel class of 2D nanomaterials discovered in 2011. It has a general form of $M_{n+1}X_n$, where M represents transition metals such as Ti, Nb, Zr, Ta, V, etc., and X refers to C or N.[70] Lin et al. reported that $Ti_3C_2$ nanosheets with SP attached displayed a strong absorption band ranging from 750 to 850 nm due to LSPR, and showed a PTCE of 30.6% upon illumination with an 808 nm laser.[14] Dai et al. tested the photothermal conversion performance of $Ta_4C_3$ nanosheets surface modified with SP and manganese oxide nanoparticles.[15] The high atomic number of Ta endows the $Ta_4C_3$ nanosheets great X-ray attenuation ability for CT imaging. Meanwhile the manganese oxide nanoparticles can be used for magnetic resonance imaging.[15] The PTCE of the $Ta_4C_3$ conjugates was measured to be 34.9%.[15] Moreover, Lin et al. reported that $Nb_2C$ nanosheets surface modified with PVP did not only have a high PTCE of 36.5% when illuminated with an 808 nm laser but also show a high PTCE of 46.65% when illuminated with a 1064 nm laser.[71] The longer-wavelength laser results in less damage to healthy cells.

Black phosphorus (BP) nanomaterials including quantum dots[72,73] and nanosheets[18–20] have also been tested for PTT. When illuminated with an 808 nm laser, PEGylated BP quantum dots had a PTCE of 28.4%,[72] and BP nanosheets surface modified with human serum albumin had a PTCE of 32.7%.[20] In addition, BP nanomaterials have excellent biodegradability as they can be oxidized to $(PO_4)^{3-}$ ions and excreted.[20,74] Other inorganic nanomaterials such as copper sulfide[75–77] and copper selenide[78,79] also demonstrated outstanding photothermal conversion performance with PTCEs of over 40% when exposed to an 808 nm laser.

From this literature review, it is seen that molybdenum-based nanomaterials are promising PTAs for PTT. The next three sections introduce traditional methods to prepare three molybdenum-based nanomaterials, including $MoO_{3-X}$, MB nanorings and $MoSe_2$.

## 2.2 Synthesis of Substoichiometric Molybdenum Oxide

The methods to prepare $MoO_{3-X}$ nanomaterials can be generally classified into two approaches. The first one is bottom-up methods including hydrothermal or solvothermal reactions. Huang et al. reported one way to prepare $MoO_{3-X}$ nanosheets by using oleylamine to reduce ammonium molybdate in an oil/water emulsion.[80] Ammonium molybdate was first dissolved in a mixture of deionized water and hydrochloric acid. Then oleylamine dissolved in cyclohexane was added to form a milky emulsion. After stirring for 1 min, the mixture was transferred into a Teflon-lined autoclave, and then heated at 180 °C for 5 hrs. After cooling down to room temperature, cyclohexane was added to extract blue nanosheets. The blue nanosheets were precipitated by adding ethanol.[80] However, the blue nanosheets would be wrapped by themselves to form white nanotubes if they were not precipitated in time.[80] The color change indicated the $MoO_{3-X}$ nanosheets were oxidized to $MoO_3$ nanotubes.[80] Xiao et al. reported a facile method to prepare $MoO_{3-X}$ quantum dots by using $H_2O_2$ to oxidize $MoS_2$.[81] $MoS_2$ powder was added into a mixture of 30% $H_2O_2$ and $H_2O$. After 30 min, the pH value of the mixture was adjusted to 7.0 with sodium hydroxide. The $MoO_{3-X}$ QDs were finally obtained by centrifugation at 8000 g for 10 min to remove large particles and

followed by dialysis for 48 h to remove byproducts.[81] The reaction could be explained by **Equation 2.2**[81]**:**

$$3MoS_2 + 26H_2O_2 \rightarrow MoO_3 + Mo_2O_5 + 6SO_4{}^{2-} + 12H^+ + 20H_2O \quad (2.2)$$

However, the content of $MoO_{3-X}$ was not high in the mixed molybdenum oxide; the XPS spectrum showed that $MoO_3$ was still the dominant phase (**Figure 2.13a**).[81] Zhan et al. further developed this method to prepare $MoO_X$ nanoparticles and found that the phase of the molybdenum oxide nanoparticles can be controlled by the reaction time when using $H_2O_2$ to oxidize $MoS_2$ at high temperatures.[82] $MoS_2$ powder was added into a mixture of 30% $H_2O_2$ and ethanol. After stirring for 15 min, the mixture was moved into a Teflon-lined autoclave and heated at 180 °C.[82] As shown in **Figure 2.13b**, $MoO_2$ nanoparticles were produced when the mixture was heated for 5 hrs; $MoO_{3-X}$ nanoparticles were produced when heated for 7 hrs and $MoO_3$ nanoparticles were produced when heated for 11 hrs.[82] In addition, Ding et al. proposed to use 30% $H_2O_2$ to oxidize Mo powder for the preparation of $MoO_{3-X}$ quantum dots.[12] In brief, 7.5 mg of Mo powder was added into 7.5 mL of $H_2O_2$ and then diluted to 30 mL. The mixture was transferred to a Teflon-lined autoclave and heated at 80 °C for 24 hrs.[12] These hydrothermal methods usually require high temperatures and long reaction times.

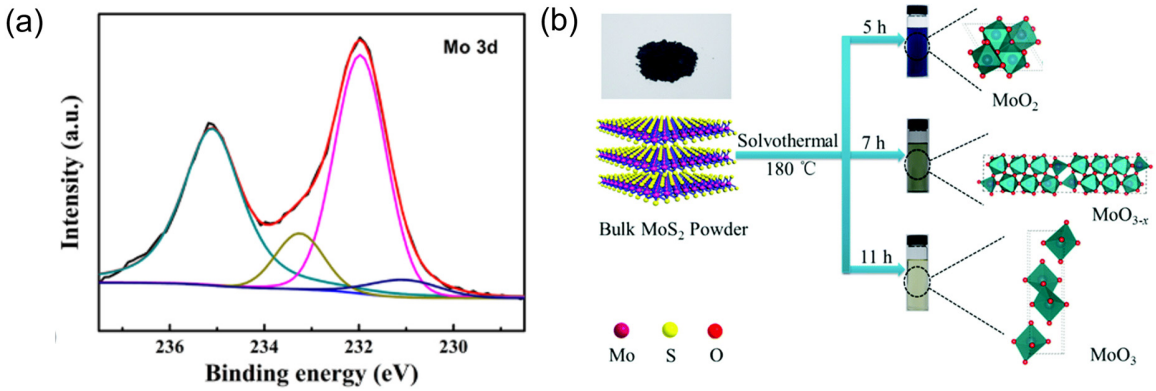


**Figure 2.13.** (a) XPS spectra of Mo3d peaks of molybdenum oxide mixture prepared by Xiao et al.[81] The green and purple peaks belong to Mo(VI) and the brown and blue peaks below to Mo(V). Reprinted with permission from *ACS Appl. Mater. Interfaces* 2016, *8*(12), 8184-8191. Copyright 2016 American Chemical Society**.** (b) Schematic illustration of synthesis of molybdenum oxide nanoparticles with different phases by hydrothermal method.[82] Reprinted with permission from *Nanoscale,* 2018*, 10,* 5997-6004. Copyright 2018 Royal Society of Chemistry.

The second approach to prepare $MoO_{3-X}$ nanomaterials is top-down methods. Alsaif et al. reported a method to use protons to reduce $MoO_3$ with the assistance of solar light.[83] $MoO_3$ bulk powder was first added to a mixture of 50% ethanol and 50% water, followed by probe sonication for 2 hrs to prepare $MoO_3$ nanosheets. After centrifugation to remove extra bulk powder, the exfoliated $MoO_3$ nanosheets were collected and then exposed to solar light from a solar simulator with an intensity of 100 mW/cm$^2$.[83] With increasing exposure time, the color of the solution changed from clear to dark blue and the intensity of a broad absorption band from 550 nm to 950 nm increased (**Figure 2.14a and b**), suggesting the formation of $MoO_{3-X}$.[83] This was attributed to the doping of protons into the $MoO_3$ nanosheets to form $H_XMoO_3$ which was not stable and finally degraded and turned into $MoO_{3-X}$. The formation of $H_XMoO_3$ can be explained by the following equations.[83,84]

$$MoO_3 \xrightarrow{h\nu} MoO_3^* + h^+ + e^- \quad (2.3)$$

$$2h^+ + H_2O \rightarrow 2H^+ + \frac{1}{2}O_2 \quad (2.4)$$

$$MoO_3 + xH^+ + xe^- \rightarrow H_xMoO_3 \quad (2.5)$$

The transformation from $H_XMoO_3$ to $MoO_{3-X}$ is illustrated in **Figure 2.14c**.[85] The proton atoms preferably interact with corner-sharing oxygen atoms in $MoO_3$ and form theoretical -$OH_2$ groups which are not stable and are released from the $MoO_3$ leaving an oxygen vacancy, such that $MoO_{3-X}$ is formed with more and more oxygen vacancies created.[85]

Zu et al. combined the bottom-up and top-down methods together and came up with a facile and quick method to prepare $MoO_{3-X}$ quantum dots, as shown in **Figure 2.14d**.[86] In brief, polyvinyl pyrrolidone K30 as a reductant was added into a mixture of deionized water and hydrochloric acid (1 mol/L) containing 2 mmol of ammonium molybdate. After stirring evenly, the mixture was exposed to UV light (365 nm) and the blue $MoO_{3-X}$ quantum dots were produced after 30 min.[86]

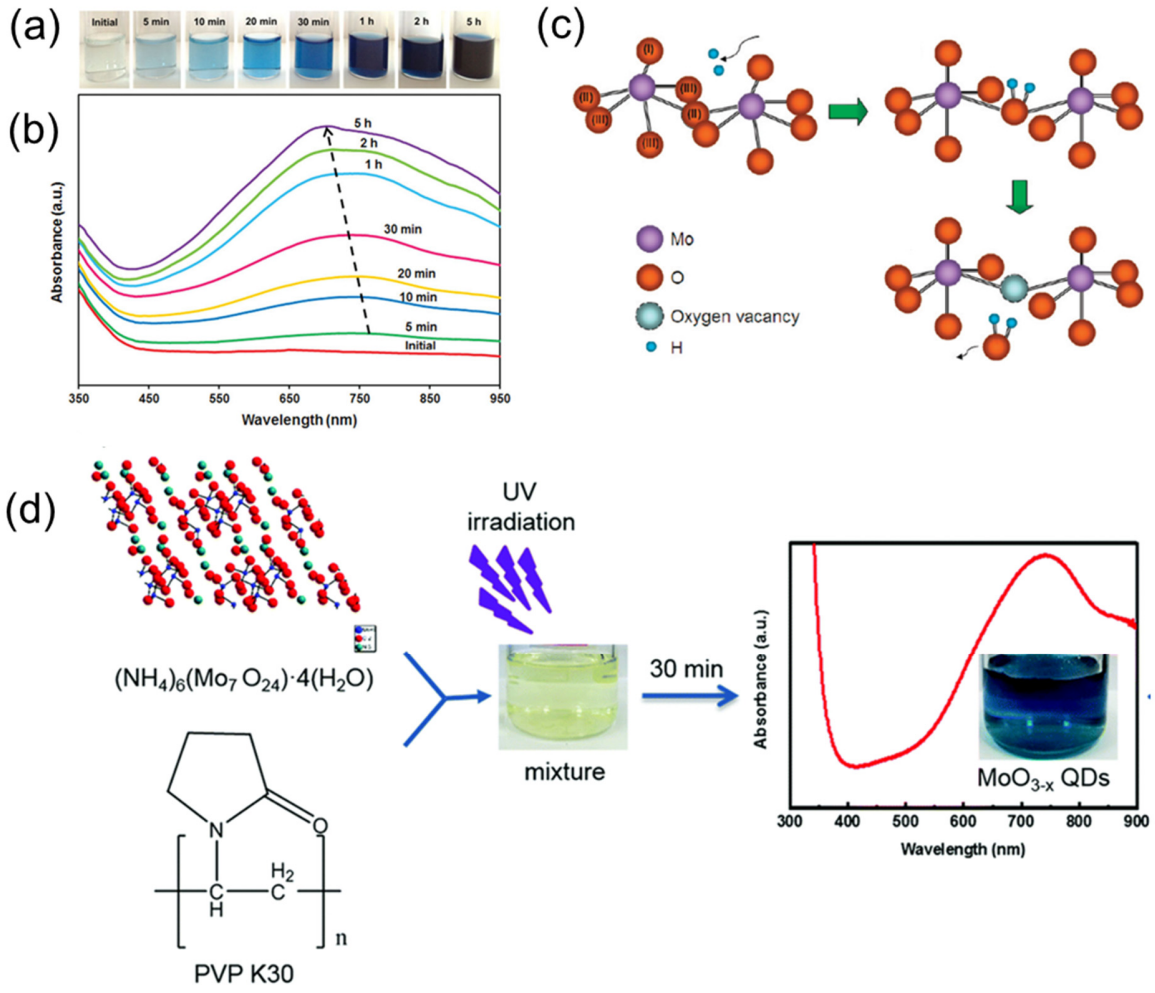


**Figure 2.14.** (a) Optical images and (b) UV-vis absorption spectra of $MoO_X$ solutions with different solar light irradiation times.[83] Reprinted with permission from *Adv. Mater.* 2014, *26*(23), 3931-3937. Copyright 2014 Wiley-VCH. Schematic illustrations of (c) the interaction between protons and $MoO_3$ and the formation of oxygen vacancies,[85] and (d) synthesis of $MoO_{3-X}$ quantum dots *via* ultraviolet light irradiation of ammonium molybdate and PVP K30.[86] (c) is reprinted with permission from *J. Phys. Chem. C* 2011, *115*(21), 10757-10763. Copyright 2011 American Chemical Society. New J. (d) is reprinted with permission from *New J. Chem.* 2018, *42*, 18533 -18540. Copyright 2018 Royal Society of Chemistry

## 2.3 Synthesis of Molybdenum Blue Nanoclusters

Molybdenum Blue (MB), also known as heteropoly blue, is an example of a reduced POM. These reduced POMs usually have the same atomic structures as the oxidized ones. The reduction of POMs can be realized by either chemical, photochemical or electrochemical methods.[50] For example, a blue POM of $(nMe_4)_2(NH_4)_8(Mo_{14}O_{46})\cdot 8H_2O$ can be prepared by irradiating aqueous solutions containing $(NH_4)_6(Mo^{VI}_7O_{24})\cdot 4H_2O$ (0.1 mol/L) and MeOH (2.5 mol/L) with UV light (100 W) for 20 hrs, followed by the addition of $[nMe_4]ClO_4$ (0.3 g) and cooling overnight at 0 °C.[87] In this process, $[Mo^{VI}_7O_{24}]^{6-}$ was reduced by ultraviolet irradiation in aqueous solutions to form blue species of $[Mo_{14}O_{46}]^{10-}$ which equals $2[Mo^{V}Mo^{VI}_6O_{23}]^{5-}$.[50,87,88] The reduction of Mo can be explained by the steps illustrated in **Figure 2.15**.[87,88]

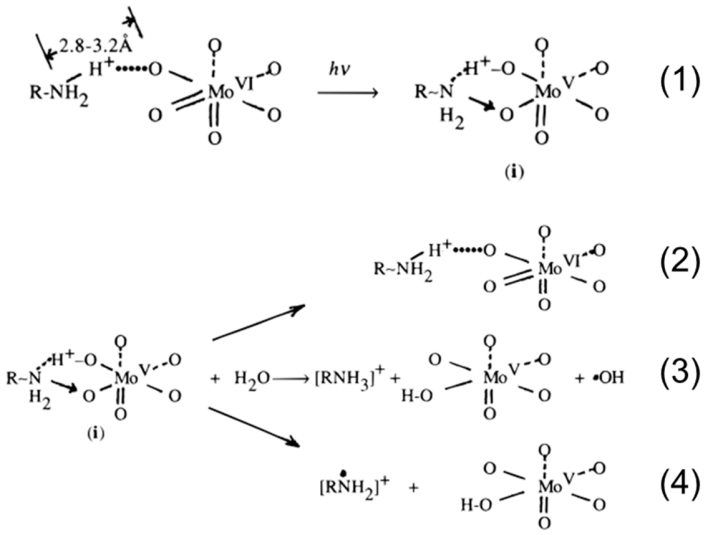


**Figure 2.15.** Schematic illustration of photoreduction of $Mo^{VI}O_6$ octahedra to $Mo^{V}O_5(OH)$.[88] Adapted with permission from *Chem. Rev.* 1998, *98*(1), 307–326. Copyright 1998 American Chemical Society.

Firstly, photoexcitation of alkylammonium polyoxomolybdate after photon absorption due to O→M ligand metal charge transfer (LMCT) results in the transfer of a proton from the nitrogen in an alkylammonium group to a reducible bridging oxygen atom in an edge-shared

$MoO_6$ octahedron, followed by the interaction of the photoexcited electron with the proton.[88] Meanwhile, the photoexcited hole left at the oxygen atom as a result of the O→Mo LMCT transition interacts with the non-bonding electron of the amino nitrogen atom to form a charge-transfer complex (i in **Figure 2.15**).[88] Then the charge-transfer complex (i) can deactivate to original species (process "2"), oxidize water to an ·OH radical (process "3") or lead to decomposition of the alkylammonium cation (Process "4").[88] Processes "3" and "4" lead to the reduction of Mo. Additionally, Keggin-structured reduced Mo POMs can be synthesized by mixing $(NH_4)_6(Mo^{VI}_7O_{24})\cdot 4H_2O$ and $NaH_2PO_4\cdot 12H_2O$ to form heteropoly acid, followed by reduction by L-ascorbic acid.[50,54] Other popular reducing agents that can be used to reduce $Mo^{VI}$ species include metals (Al, Pb, Mo, Cu, Zn, Cd, Hg), $B_2H_6$, $NaBH_4$, $N_2H_4$, $NH_2OH$, $SO_3^{2-}$, $S_2O_4^{2-}$, $S_2O_3^{2-}$, $SnCl_2$, $Mo^VCl5$, $(Mo^VoCl_5)^{2-}$, Mohr's salt, formic acid, tartaric acid, thiourea, hydroquinone, D-glucose, and sucrose.[50,89] Moreover, a Wells-Dawson-structured heteropoly 18-molybdopyrophosphate anion $[(P_2O_7)Mo^{VI}_{18}O_{54}]^{4-}$ can be reduced through electrolytic reduction to form green species of $[(P_2O_7)Mo^VMo^{VI}_{17}O_{54}]^{5-}$ or blue species of $[(P_2O_7)Mo^V_2Mo^{VI}_{16}O_{54}]^{6-}$ at 0.11 V and 0 V (against Ag/AgCl) in acetonitrile, respectively.[90]

One special MB is $\{Mo_{154}\}$-based nanorings. The $\{Mo_{154}\}$ nanoring is made of 14 $\{Mo_8\}$,14$\{Mo_2\}$ and 14$\{Mo_1\}$ moieties (**Figure 2.16a)**.[91] Other $\{Mo_{154}\}$ derivatives are formed when one or more moieties are missing. For example, $\{Mo_{142}\}$ is made of 14$\{Mo_8\}$, 8$\{Mo_2\}$ and 14$\{Mo_1\}$ with 6 missing $\{Mo_2\}$; $\{Mo_{138}\}$ is made of 14$\{Mo_8\}$, 6$\{Mo_2\}$ and 14$\{Mo_1\}$ with 8 missing $\{Mo_2\}$.[92] These blue POMs are usually produced by partial reduction of $Na_2Mo^{VI}O_4$ by $N_2H_4$, $Na_2S_2O_4$ or $NH_2OH$ in acidic solutions.[93–96] For instance, one recipe to prepare $\{Mo_{154}\}$ involves mixing $Na_2MoO_4\cdot 2H_2O$ (30.8 mmol), $NH_2OH\cdot HCl$ (184.6 mmol), HCl(3.5%, 9.5 mL) and water (200 mL) together followed by heating the mixture at 65-70°C for 20 hrs.[94] The collected precipitate is $(NH_4)_{25}[Mo_{154}(NO)_{14}O_{420}(OH)_{28}(H_2O)_{70}]\cdot 350H_2O$.[94] Additionally, it was found that the structure of $\{Mo_{154}\}$-based nanorings highly depended on the pH of the solution during the synthesis.[92,93] Nakamura et al. used sodium dithionite ($Na_2S_2O_4$) to reduce $Na_2MoO_4$ and the

pH was adjusted by addition of hydrochloric acid.[93] As shown in **Figure 2.16b**, {Mo154/152} was prepared when the pH value was 1, {Mo144} was prepared when the pH value was 2 and {Mo138} was prepared when the pH value increased to 3.[93] The pH of the reaction solutions influenced the nuclearity of the MB nanorings but did not change their geometries.[92] Higher pH values increased the number of defect sites in the MB nanorings.[92] The color of the reduced POMs was found to be related to both the structure of the POMs and the reagent ratio (R =[$S_2O_4^{2-}$]/[$MoO_4^{2-}$]).[93] {Mo154/152} was always blue regardless of R, while {Mo144} and {Mo138} changed to brown with increasing R. In addition, Liu et al. reported that MB nanorings can also be produced by mixing $H_2O_2$ and Mo powder and storing the mixture at room temperature overnight.[97] Moreover, MB nanorings in solution can self-assemble into chains, layers or vesicles.[89,98] The assembly occurs when $H_2O$ ligands at {$Mo_2$} on one ring are replaced by oxygen atoms in Mo=O terminal of an {$Mo_2$} on another ring.[89] The assembly of 3D vesicles may be the result of interplay between short-term van der Waals attraction and long-term electrostatic repulsion.[98]

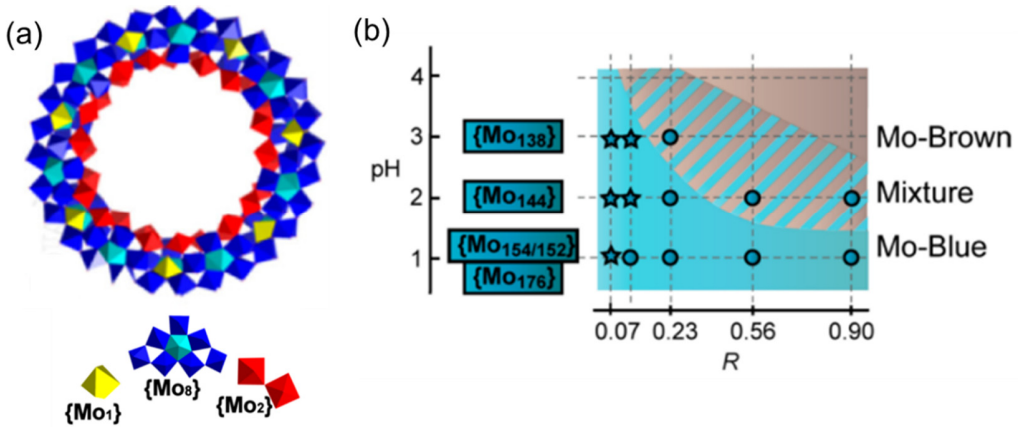


**Figure 2.16.** (a) Building blocks of the {Mo154} nanoring.[91] Reprinted with permission from *J. Am. Chem. Soc.* 2014, *136*(40), 14114-14120. Copyright 2014 American Chemical Society. (b) Diagram of Mo-blue and Mo-brown formed in solution after at least 24 hrs in terms of pH of the solution and reagent ratio. Circles and stars denote the POM nanorings. Single crystals are denoted by the stars.[93] Reprinted with permission from *J. Am. Chem. Soc.* 2015, *137*(20), 6524–6530. Copyright 2015 American Chemical Society.

## 2.4 Synthesis of Molybdenum Selenide Nanomaterials

The synthesis of molybdenum selenide nanomaterials, like other TMDC nanomaterials, has two approaches: top-down and bottom-up methods. The top-down methods are to fragment bulk powder into nanoparticles. Like graphite, $MoSe_2$ bulk material has a layered structure and adjacent layers are stacked together by van der Waals forces. Hence $MoSe_2$ bulk crystals can be mechanically exfoliated by scotch tape in the same way as graphite.[99] A small thin crystal was pressed onto a thick layer of photoresist spun on a glass plate. After baking, the crystal was firmly attached to the photoresist. Then the scotch tape was used to repeatedly peel flakes off the crystal. The flakes left on the photoresist were released in acetone, and finally transferred to a silicon wafer by dip-coating.[100] Even though it is possible to achieve $MoSe_2$ monolayers in this way, the yield is very low. Alternatively, TMDC bulk materials can be exfoliated by sonication in liquid to form monolayer or few-layer nanosheets. This method is also known as liquid exfoliation. Coleman et al. discovered that exfoliation efficiency is governed by the Hansen solubility parameters of the exfoliated materials and the liquid, which should be close enough to minimize the enthalpy of mixing, and found that $MoSe_2$ can be efficiently exfoliated by probe sonication in cyclohexyl-pyrrolidinone.[101] To further improve the yield, intercalation assisted liquid exfoliation was developed, which includes two steps of intercalation and liquid exfoliation. N-butyllithium is the most extensively researched intercalant for TMDC bulk materials.[102,103] As shown in **Figure 2.17**, Li ions from n-butyllithium can be intercalated into interlayer spaces of TMDC materials and form $Li_xMX_2$, where M denotes transition metals and X denotes chalcogens.[104] To ensure enough Li ions intercalate into TMDC materials, the intercalation process usually takes several days. It should be noted that TMDC bulk materials will change from semiconducting 2H phase to semi-metallic 1T phase when they are intercalated with excessive Li ions.[105] Besides $Li^+$, $Na^+$ and $K^+$ can also intercalate into TMDC bulk materials.[106,107] However, $Na^+$ and $K^+$ ions are larger than $Li^+$, making them more difficult to be inserted into TMDC materials. To solve this problem, Zheng et al. added another step before the intercalation.[107] TMDC materials were mixed with hydrazine ($N_2H_4$) first for hydrothermal reactions to

expand interlayer spaces of the TMDC materials, then metallic ions could be inserted into the spaces more easily.[107] After intercalation, the intercalated TMDC materials are usually exfoliated by sonication in water. Intercalants such as Li can react with water to generate $H_2$ and separate layers of TMDC materials.[104] Additionally, $MoSe_2$ powder can be directly fragmented into quantum dots or nanosheets when sonicated in water containing other organic molecules such as F127 or PVP.[61,62] These organic molecules did not only help intercalate $MoSe_2$ but also kept the prepared nanomaterials colloidally stable in water.

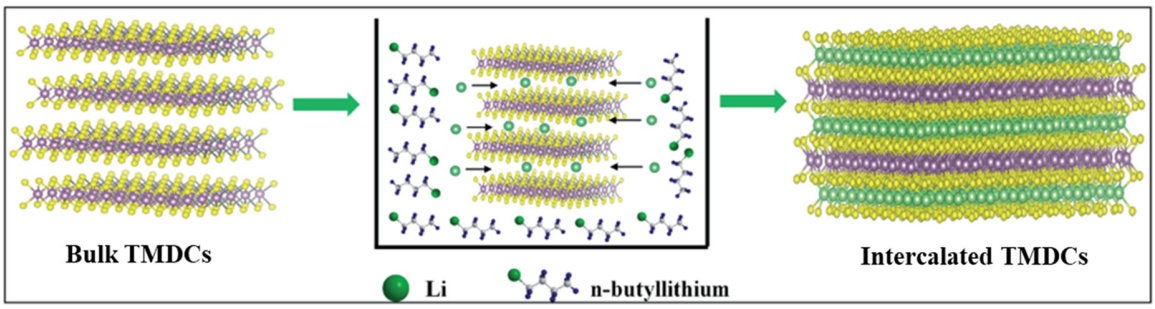


**Figure 2.17.** Schematic illustration of chemical intercalation of TMDC bulk materials with n-butyllithium.[104] Reprinted with permission from *J. Mater. Chem. A*, 2020, 8, 15417-15444. Copyright 2020 Royal Society of Chemistry.

Besides top-down methods, $MoSe_2$ nanomaterials can also be prepared by bottom-up methods. For example, a low-temperature hydrothermal method was proposed to prepare amorphous $MoSe_2$ nanosheets, where $Na_2SeSO_3$ (0.01 mol) and $Na_2MoO_4$ (0.005 mol) were mixed and added into a Teflon-lined autoclave with 15 mL of 50% $N_2H_4$ aqueous solution and heated at 135 °C for 12 hrs.[108] The prepared $MoSe_2$ nanosheets crystallized when annealed at 350 °C in an inert atmosphere.[108] $MoSe_2$ nanosheets can also be produced by other hydrothermal methods such as mixing $NaBH_4$, Se and $Na_2MoO_4$ in water and heating the mixture in an autoclave at 200 °C for 20 hrs;[109] or heating $(NH_4)_6Mo_7O_{24}{\cdot}4H_2O$, $N_2H_4{\cdot}H_2O$ and $SeO_2$ together at 200 °C for 20 hrs.[110] Additionally, the hydrothermal method could also be used to synthesize fullerene-structured $MoSe_2$ nanoparticles, where $H_{24}Mo_7N_6O_{24}{\bullet}4H_2O$ (0.3 mmol) and $Na_2SeO_3$ (10 mmol) dissolved into a mixed solution of

water (15 mL) and ethylene glycol (15 mL) were heated in an autoclave at 250 °C for 12 hrs.[111]

## 2.5 Pulsed Laser Ablation in Liquid

Pulsed laser ablation in Liquid (PLAL) is a novel technique to prepare nanomaterials by using a pulsed laser beam to ablate bulk materials in liquid. Compared to conventional techniques, PLAL has many attractive features such as a simple setup, fast synthesis and eco-friendly. Compared to laser ablation in air or vacuum, PLAL can create extreme conditions of high temperatures, high pressures and high cooling rates which can be used to prepare metastable nanomaterials and induce reactions with liquid. When the laser energy is high, plasma will be generated. The laser-induced plasma confined by the surrounding liquid expands ultrasonically, then a shockwave is generated. The shockwave will add extra pressure to the laser-induced plasma. The increased pressure will increase the temperature of the plasma.[112]

Different pulsed lasers including nanosecond, picosecond and femtosecond lasers can be used for PLAL. Among them, ablation with a femtosecond laser, whose pulse duration is in the range of femtoseconds, is advantageous for several reasons. First, the ultrashort pulse duration can make the peak intensity of the laser pulses higher than $10^{12}$ W/cm$^2$ at the focal point, while the peak intensity of nanosecond laser pulses is less than $10^{10}$ W/cm$^2$.[23] The higher peak intensity increases the ablation efficiency. Second, the temperature and pressure of the plasma plume in femtosecond laser ablation is 2-4 fold higher than that in nanosecond laser ablation,[113] which can create more extreme conditions to explore more structures and metastable phases of nanomaterials. Third, the ultrashort laser period is shorter than electron-lattice coupling times, resulting in reduced heat-affected zones.[114] Therefore, this work focuses on the synthesis of nanomaterials by femtosecond laser ablation in liquid.

The setup of PLAL can be generally classified as one of two ways, as shown in **Figure 2.18**. One is to ablate a bulk target placed at the bottom of a container which is placed on top of a translation stage to ensure the surface of the bulk target is evenly ablated. The other is to

ablate powder particles dispersed in solution. The solution needs to be stirred to ensure each particle has the same chance to be ablated. PLAL can be further classified as regular ablation or reactive ablation depending on whether the materials ejected from ablated targets react with solvents. If the emitted materials react with the solvents, it is called reactive PLAL.

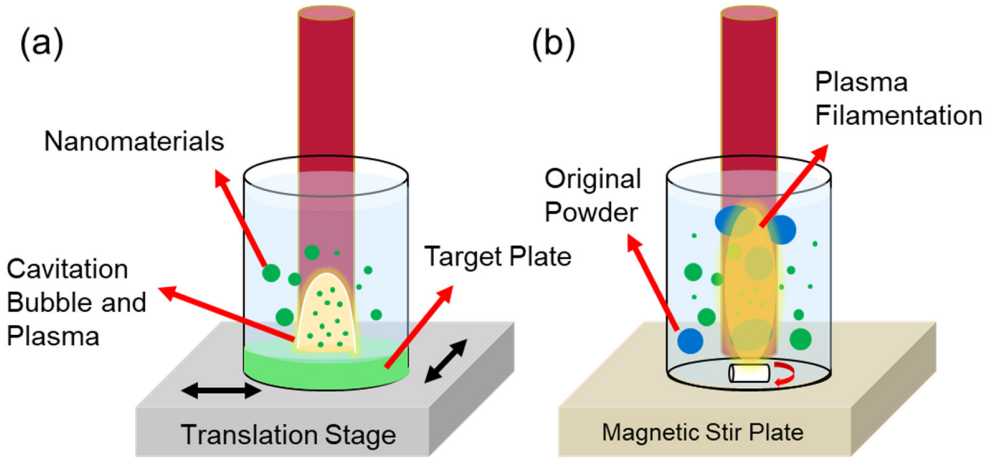


**Figure 2.18.** Schematic illustration of the typical experimental setups of pulsed laser ablation of (a) a bulk target and (b) powder particles in liquid.

This section starts with an introduction to ablation mechanisms of PLAL, followed by an introduction to chemical reactions of solvents (water, alcohol) during pulsed laser irradiation, and finally introduces several nanomaterials prepared by PLAL.

### 2.5.1 Ablation Mechanisms of Femtosecond PLAL

#### 2.5.1.1 Mechanism of Pulsed Laser Ablation of a Bulk Target

Before reaching the ablated target, laser pulses interact with the liquid first. The laser light may experience refraction at the air-liquid boundary, absorption, self-focusing, optical breakdown of the liquid and diffraction by laser-induced plasma, depending on the laser wavelength and energy.[115] In most cases, the energy dissipated from laser-liquid interaction is negligible as the energy delivered to the ablated solid is orders of magnitude higher.[115]

When a laser pulse reaches the bulk target, the absorption of light occurs until the end of the pulse. The absorption of light can be caused by inverse bremsstrahlung absorption for metals, or excitation of electrons from valence bands for semiconductors and dielectric materials.[114] When the intensity of a laser pulse is high enough, the ablated material might directly interact with the electric field of the intense laser and ionize the material *via* tunneling ionization or over-the-barrier ionization.[116]

On timescales of tens of picoseconds after the arrival of the laser pulse, detachment of matter from the ablated target occurs.[115] The mechanism of matter detachment is related to the intensity of the laser pulse. Due to the ultrashort pulse duration, there is little density variation of the ablated target upon heating; isochoric heating is expected to occur after energy deposition ("a→(b, c, d)" in **Figure 2.19a**).[23] If the laser intensity is low, just around the ablation threshold, matter is detached from the ablated target due to photomechanical spallation (region "I" in **Figure 2.19b**). The spallation is caused by isochoric laser heating of the irradiated region leading to a buildup of compressive stresses. As a result, voids nucleate, grow and coalesce in a subsurface region of the irradiated region, and finally lead to the fragmentation and ejection of large chunks of material.[117] When the laser intensity is above the ablation threshold (region "II" in **Figure 2.19b**), the detachment of matter is dominated by phase-explosive ablation which starts with bubble nucleation in a superheated liquid near the spinodal temperature, slightly below the critical temperature.[23] The bubble nucleation can take place homogeneously in the superheated liquid or heterogeneously at the liquid-solid interface. With adiabatic cooling, the superheated liquid enters the spinodal region of the temperature-density (T-ρ) phase diagram ("c→$c_1$" in **Figure 2.19a**) and finally creates a mixture of vapor and liquid droplets with spinodal decomposition. Nanoparticles are formed when the liquid droplets cool down.[23,115] When the laser intensity is higher (region "III" in **Figure 2.19b**), the adiabatic expansion and cooling of homogeneous superheated liquid leads to gas phase formation (vaporization) by direct fragmentation ("d→$d_1$" in **Figure 2.19a**), and then nanomaterials are produced from these vaporized fragments.[23,115,118] When the laser intensity is even higher, above the optical breakdown threshold, the ablated target is directly

photoionized by the intense laser field at the beginning. The hot electrons return to the ablated target after tens of picoseconds, followed by the generation of a plasma plume in the surrounding liquid and emission of a shockwave due to the confinement of liquid.[23,115] After $10^{-10}$ to $10^{-7}$ s, with the expansion of the plasma and shockwave, the plasma cools down and emits energy into the liquid on one side and the ablated target on the other side. In this process, nanomaterials are nucleated and grown through a combination of above-mentioned mechanisms including spallation, phase explosion and direct vaporization of superheated liquid depending on the deposited energy.[23] After $10^{-6}$ to $10^{-4}$ s, with the complete quenching of the plasma, a cavitation bubble is formed and continues expansion until it collapses and generates a secondary shockwave.[115] Additionally, when the ablated target is extremely ionized, non-thermal fragmentation such as Coulomb explosion takes place due to Coulomb repulsion of multiple-charge ionized clusters.[119–121]

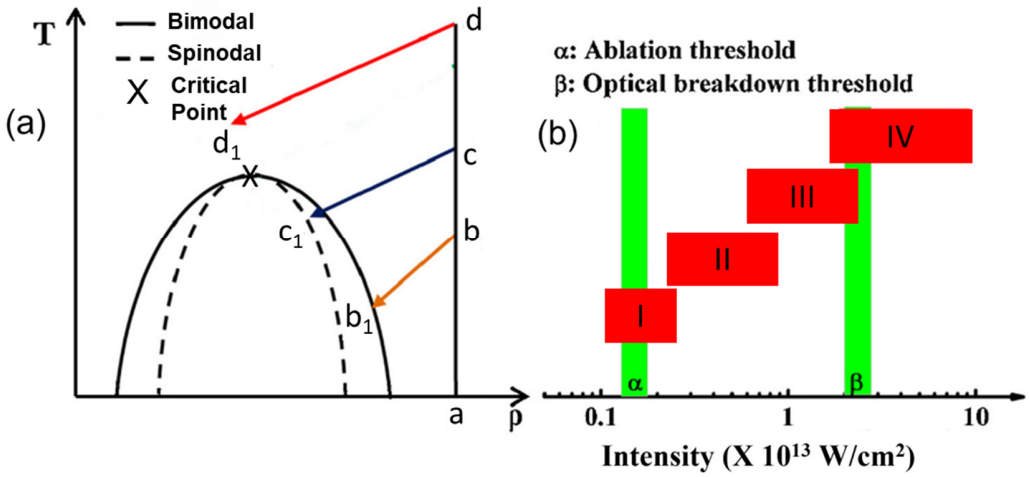


**Figure 2.19.** (a) Temperature (T) – density (ρ) phase diagram and three heating and cooling paths for femtosecond laser ablation in liquid. (b) Possible ablation mechanisms as a function of laser intensity. I: photomechanical spallation; II: phase-explosion ablation, III: vaporization and direct fragmentation, IV: Plasma ablation and Coulomb explosion.[23] Adapted with permission from *J. Photochem. Photobiol. C Photochem. Rev.* 2013, *17*, 50-68. Copyright 2013 Elsevier B.V.

#### 2.5.1.2 Mechanism of Pulsed Laser Ablation of Powder Dispersed in Liquid

Pulsed laser ablation of powder particles dispersed in liquid is mainly caused by photothermal ablation and Coulomb explosion depending on the laser intensity. Photothermal ablation takes place when the laser intensity is relatively low. The absorption of light results in the generation of plasma, heating the ablated powder particles which are then fragmented *via* melting, evaporation, or explosive boiling to form nanoparticles.[122–124] When the laser intensity is high, more electrons are emitted and the ablated powder is multiple-charge ionized; Coulomb explosion is then the dominant mechanism to fragment particles.[125,126] Additionally, Pletch et al. reported the observation of femtosecond laser near-field ablation of gold nanoparticles suspended in water, which takes place below gold's melting temperature.[127]

### 2.5.2 Chemical Reactions of Solvents in Femtosecond PLAL

Thanks to the extreme conditions created in PLAL, it is inevitable for the formed nanomaterials to react with solvent molecules. Therefore, it is critical to understand the products of femtosecond laser irradiation of water and organic solvents.

#### 2.5.2.1 Femtosecond Laser Irradiation of Water

Femtosecond laser irradiation of water may result in self-focusing, filamentation, optical breakdown and supercontinuum generation when the laser intensity is high.[128] When the laser intensity is high, the refractive index of a dielectric medium is linearly related to the intensity. Self-focusing is caused by a nonuniform spatial intensity distribution of a Gaussian beam, which results in the refractive index of the medium in the center of the beam being higher than that at the edges, such that the light is self-focused.[128] Filamentation is caused by the balance between self-focusing and defocusing of a laser induced plasma. The filamentation is accompanied by a broadening of the laser spectrum, expanding from NIR to visible light. The broadening of the spectrum is also called supercontinuum.[128] It was reported that the electron-density threshold for optical breakdown induced plasma in water is $1.8\times10^{20}$ $cm^{-3}$, while the electron-density threshold for supercontinuum induced plasma is

around $1\times10^{18}$ - $3\times10^{18}$ $cm^{-3}$.[129,130] The plasmas caused by either optical breakdown or supercontinuum lead to chemical reactions in water.

Frias Batista et al. summarized the chemical reactions of water under laser irradiation, as shown in **Figure 2.20**.[129] The laser induced chemical reaction of water starts from multiple-photon absorption and excitation of a water molecule ($H_2O^*$).[129,131,132] The excited water molecule is then ionized and emits one electron[131,132]:

$$H_2O^* \rightarrow H_2O^+ + e^- \quad (2.6)$$

Within less than 300 fs, hydration of the emitted electron takes place.[131] The hydrated electron with a lifetime of 1 ns is the main reducing agent in reactive laser ablation.[129]

$$e^- \xrightarrow{H_2O} e_{aq}^- \quad (2.7)$$

The cationic water ion produced in **Equation 2.6** is not stable and will be transformed into a hydrogen ion ($H_3O^+$) after reaction with another water molecule, producing one hydroxyl radical in 100 fs:[131]

$$H_2O^+ + H_2O \rightarrow H_3O^+ + OH^\cdot \quad (2.8)$$

On the other hand, excited water molecules can decompose into hydroxyl radicals, hydrogen atoms or oxygen atoms in 100 fs as well[129,131]:

$$H_2O^* \rightarrow H^\cdot + OH^\cdot \quad (2.9)$$

$$H_2O^* \rightarrow H_2 + O^\cdot \quad (2.10)$$

These free atoms and radicals will eventually recombine to form $O_2$, $H_2$ and $H_2O$.[129]

Additionally, hydroxyl anions are primarily produced from hydrated electrons and other photolysis products in tens of picoseconds, as shown below:[131]

$$2e_{aq}^- + 2H_2O \rightarrow H_2 + 2OH^- \quad (2.11)$$

$$e_{aq}^- + H^\cdot + H_2O \rightarrow H_2 + OH^- \quad (2.12)$$

$$e_{aq}^- + OH^\cdot \rightarrow OH^- \quad (2.13)$$

The hydroxyl anions will eventually combine with hydrogen ions to form water in hundreds of picoseconds.[129] Moreover, hydrogen peroxide is produced by combining hydroxyl radicals in nanoseconds:[129,131]

$$2OH^{\cdot} \rightarrow H_2O_2 \tag{2.14}$$

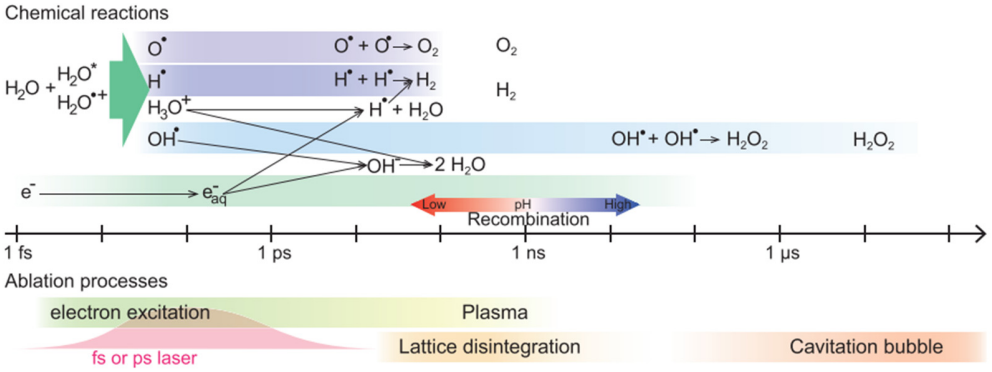


**Figure 2.20.** The timeline of laser induced chemical reactions of water and ablation process.[129] Reprinted with permission from *Sci. China Physics, Mech. Astron.* 2022, *65*(7), 274202. Copyright 2022 Springer Nature.

From **Figure 2.20**, it is clear to see that hydroxyl radicals and anions, hydrogen and oxygen atoms, reactive electrons, as well as oxygen and hydrogen gases are all present on the timescale of picoseconds when ablated targets are heated and plasma is generated, such that they are all available to get involved in reactive laser ablation. After milliseconds, when the cavitation bubbles collapse, hydrogen peroxide is still present together with oxygen and hydrogen gases in the solution.[129]

### 2.5.2.2 Femtosecond Laser Irradiation of Organic Solvents

Similar to water, polar organic molecules such as alcohol can also be ionized after multiple-photon absorption and produce solvated electrons.[133] However, unlike rapidly decaying water cations, the organic cations can last for nanoseconds or longer.[129,133] At the same time, the organic cation will undergo dissociation or Coulomb explosion when the laser intensity is high.[133]

Take ethanol for example, as it is one of the most common organic solvents used in PLAL.[134–136] Under intense laser irradiation, ethanol molecules experience dissociative ionization and Coulomb explosion. **Figure 2.21** shows the time-of-flight (TOF) spectrum of ethanol irradiated by a 810 nm femtosecond laser (130 fs) with the intensity of $3.8\times10^{15}$ W/cm$^2$.[137] There are three types of ions. The first type is $C_2H_nOH^+$ (n = 1-5), which have the C-C-O skeleton. The second type of ions is $CH_2OH^+$ and $C_2H_n^+$ (n = 2, 3, 5), indicating one bond of the C-C-O skeleton has been broken. The third type of ions is $CH_n^+$ (n = 1-3), $CH_2^{2+}$, $H^{n+}$ (n = 1-2), $O^{n+}$ (n = 1-2), $OH^+$ and $C_n^+$ (n = 1-3), which do not have skeletons.[137] The momentum-scaled spectra of the fragmented ions suggests these fragments are dissociated from $C_2H_5OH^+$.[137] Some dissociate paths are listed below[137]:

$$CH_3CH_2OH^+ \rightarrow CH_2OH^+ + CH_3 \quad (2.15)$$

$$CH_3CH_2OH^+ \rightarrow CH_3^+ + CH_2OH \quad (2.16)$$

$$CH_3CH_2OH^+ \rightarrow C_2H_5^+ + OH^{\cdot} \quad (2.17)$$

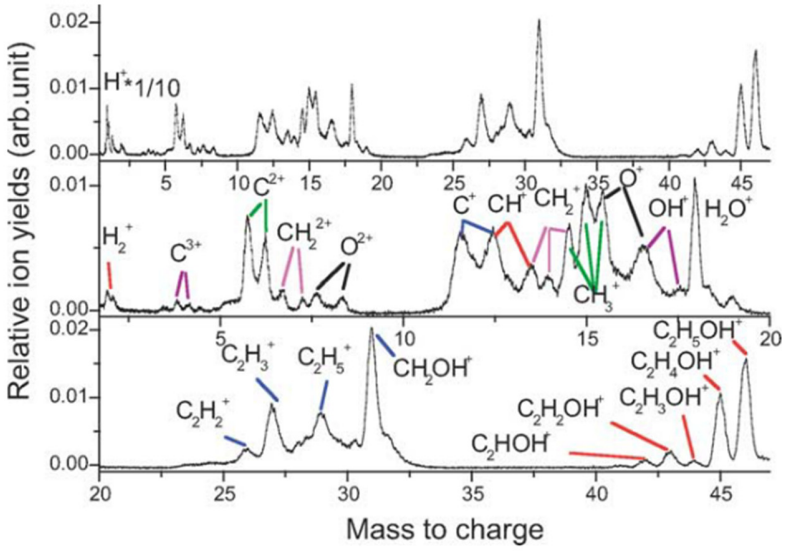


**Figure 2.21.** TOF mass spectrum of ethanol irradiated by 810 nm, 130 fs linearly polarized laser pulses ($3.8\times10^{15}$ W/cm$^2$).[137] Reprinted with permission from *Int. J. Mass Spectrom.* 2005, *241* (1), 25-29. Copyright 2005 Elsevier B.V.

Additionally, it was found that the temporal duration and wavelength of the laser pulse affect the breaking point of the C-C-O skeleton. The C-O bond of $C_2H_5OH^+$ is more likely to be broken when the pulse duration of the femtosecond laser increases, or the wavelength of the pulse decreases.[138] Coulomb explosion of ethanol can also produce $H_3O^+$ which is formed by decomposition of $(C_2H_5OH)H^+$.[139,140] $(C_2H_5OH)H^+$ is formed by migration of H from the ethyl group of one $C_2H_5OH$ molecule to one $C_2H_5OH^+$ ion through hydrogen bonds. The dissociation of $(C_2H_5OH)H^+$ is expressed below[139]:

$$(C_2H_5OH)H^+ \rightarrow H_3O^+ + C_2H_4 \quad (2.18)$$

Moreover, much previous work has unveiled the formation of reactive trihydrogen cations ($H_3^+$) when alcohol solvents are dissociation ionized by intense femtosecond laser irradiation.[141–143] **Figure 2.22** illustrates two primary paths for the formation of $H_3^+$ from methanol and ethanol, which starts from the formation of a roaming $H_2$. When methanol and ethanol molecules are double-charge ionized under strong-field excitation, the C-H bonds on α-C are elongated and the H-C-H angle is narrowed, which results in the formation of a roaming $H_2$ moiety. For methanol, the roaming $H_2$ moiety can abstract another proton from the hydroxyl group, or the proton left on the carbon to form $H_3^+$. For ethanol, the roaming $H_2$ moiety can abstract the third proton from the terminal methyl group in addition to the proton from the hydroxyl group.[142,143] The lifetime of $H_3^+$ is related to the carbon chain length of the alcohol; it increases from 102 fs for methanol, to 235 fs for ethanol, to 260 fs for 1-propanol.[143] The $H_3^+$ can be deactivated by reaction with methanol or ethanol molecules. Take methanol for example[144]:

$$H_3^+ + CH_3OH \rightarrow CH_2OH^+ + 2H_2 \quad (2.19)$$

$$H_3^+ + CH_3OH \rightarrow CH_3OH_2^+ + H_2 \quad (2.20)$$

$CH_3OH_2^+$ is not stable, and will decompose to $CH_2OH^+$ or $CH_3^+$, as shown below.

$$CH_3OH_2^+ \rightarrow CH_2OH^+ + H_2 \quad (2.21)$$

$$CH_3OH_2^+ \rightarrow CH_3^+ + H_2O \quad (2.22)$$

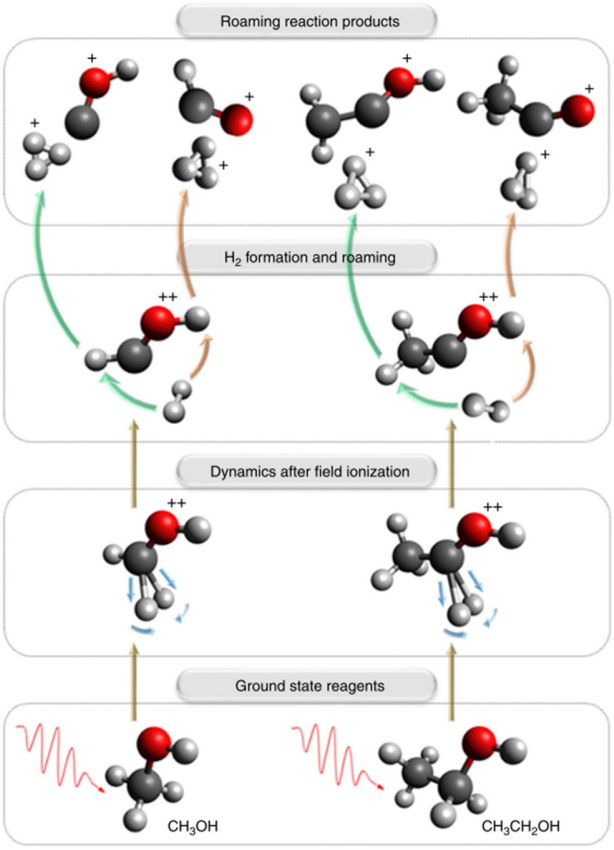


**Figure 2.22.** Primary pathways for the formation of $H_3^+$ from dissociation of methanol and ethanol.[143]

When alcohol in water is irradiated by pulsed laser, the alcohol molecules can also react with products such as hydrogen atoms and hydroxyl radicals dissociated from water at the α-carbon position, as shown below.[145]

$$RCHOH + OH^{\cdot} \rightarrow RC^{\cdot}OH + H_2O \quad (2.23)$$

$$RCHOH + H^{\cdot} \rightarrow RC^{\cdot}OH + H_2 \quad (2.24)$$

$$2RC^{\cdot}OH \rightarrow RCO + H_2O \quad (2.25)$$

$$2RC^{\cdot}OH \rightarrow RC(OH)C(OH)R \quad (2.26)$$

R denotes the rest part of an alcohol molecule other than α-carbon.

### 2.5.3 Synthesis of Metallic Nanomaterials by Femtosecond PLAL

Noble metal nanoparticles especially gold nanoparticles are the most widely researched nanomaterials synthesized by femtosecond PLAL.[125,146–148] The ablation of a gold target is usually conducted in water. The inert property of gold ensures it does not react with the solvent during the ablation process. The sizes of produced gold nanoparticles always follow bimodal distributions, as shown in **Figure 2.23a**. The generation of monodispersed small nanoparticles is usually attributed to non-thermal ablation such as Coulomb explosion and the coalescence of ablated nanoparticles, while the larger and broader distributed nanoparticles are formed due to laser-induced plasma thermal ablation.[146,147] In addition, silver nanoparticles can also be prepared by femtosecond laser ablation of a bulk silver target in water (**Figure 2.23b**).[149]

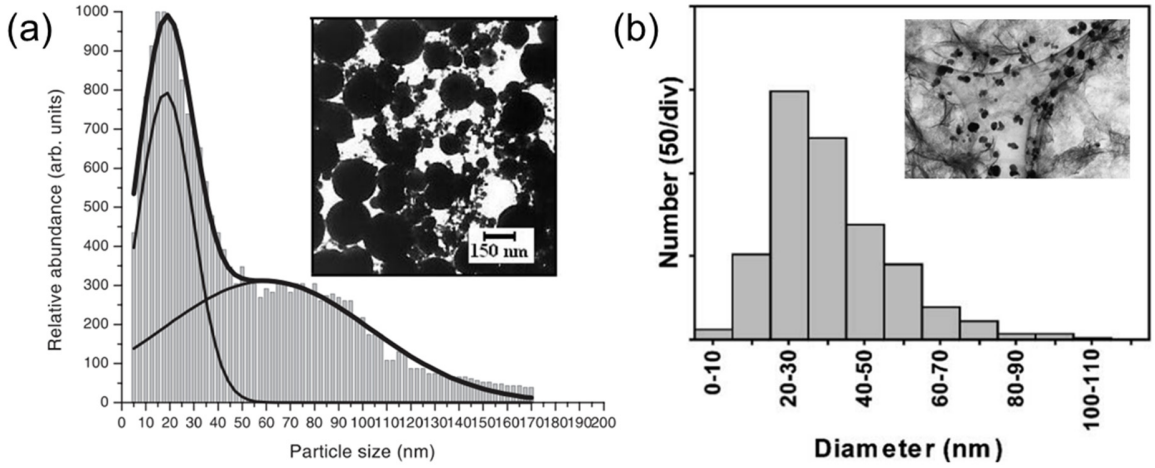


**Figure 2.23.** (a) Size distribution of gold nanoparticles prepared by femtosecond laser (800 nm, 120 fs, 1 kHz, 1 mJ/pulse) ablation of a gold target in water. The inset picture is the microscopic image of the gold nanoparticles.[147] Reprinted with permission from *Appl. Phys. A Mater. Sci. Process.* 2005, *80*(4), 753-758. Copyright 2005 Springer Nature. (b) Size distribution of silver nanoparticles prepared by femtosecond laser (800 nm, 120 fs, 10 Hz, 4 mJ/pulse) ablation of a silver plate in water. The inset picture is the microscopic image of the silver nanoparticles.[149] Reprinted with permission from *Appl. Surf. Sci.* 2003, *206*(1–4), 314-320. Copyright 2003 Elsevier B.V.

Moreover, Stratakis et al. reported the synthesis of aluminum nanoparticles by femtosecond laser ablation (800 nm, 200 fs, 1 kHz, 0.2 J/cm$^2$) of aluminum pellets in ethanol.[134] The average size of the produced Al nanoparticles was 20 nm.[134] It was found that the nanoparticles were mostly amorphous with some single crystals included and surrounded with an oxide cladding layer which prevented the Al nanoparticles from further oxidation.[134] Al nanoparticles were also reported to be prepared by laser ablation in other organic solvents including chloroform and carbon tetrachloride which can minimize the oxidation of the aluminum.[150,151]

For biomedical applications, nanoparticles need to be surface functionalized with ligands such as biocompatible polymers. On one hand, the surface functionalization can be conducted after ablation. For example, the laser-synthesized gold nanoparticles can be surface functionalized by mixing the nanoparticles with PEG in water to improve their colloidal stability,[152] just like the gold nanoparticles prepared by hydrothermal methods.[153] On the other hand, nanoparticles can be in-situ surface functionalized when they are produced by ablation in aqueous solutions containing these polymers. Tsuji et al. prepared silver nanoparticles surface functionalized with PVP by laser ablation of a silver plate in aqueous PVP solutions.[154] The silver nanoparticles prepared in PVP solutions were better dispersed than the nanoparticles prepared in pure water.[154] The average size of the silver nanoparticles decreased with the concentration of PVP until 6 mM and kept stable for the nanoparticles prepared in PVP solutions with higher concentrations (**Figure 2.24**).[154] The size reduction was probably caused by the interaction between PVP molecules and emitted materials from the ablated silver plate. The emitted materials, including atoms and clusters, were prevented from coalescence when they were attached with PVP molecules.[154] Similarly, when gold nanoparticles were prepared by laser ablation in aqueous cyclodextrin solutions, the size of the gold nanoparticles also decreased with increasing concentration of cyclodextrin.[155] Colloidally stable gold nanoparticles could also be prepared in aqueous solutions containing other surfactant polymers such as cetyl-trimethylammonium bromide and sodium dodecyl sulfate (SDS).[156,157]

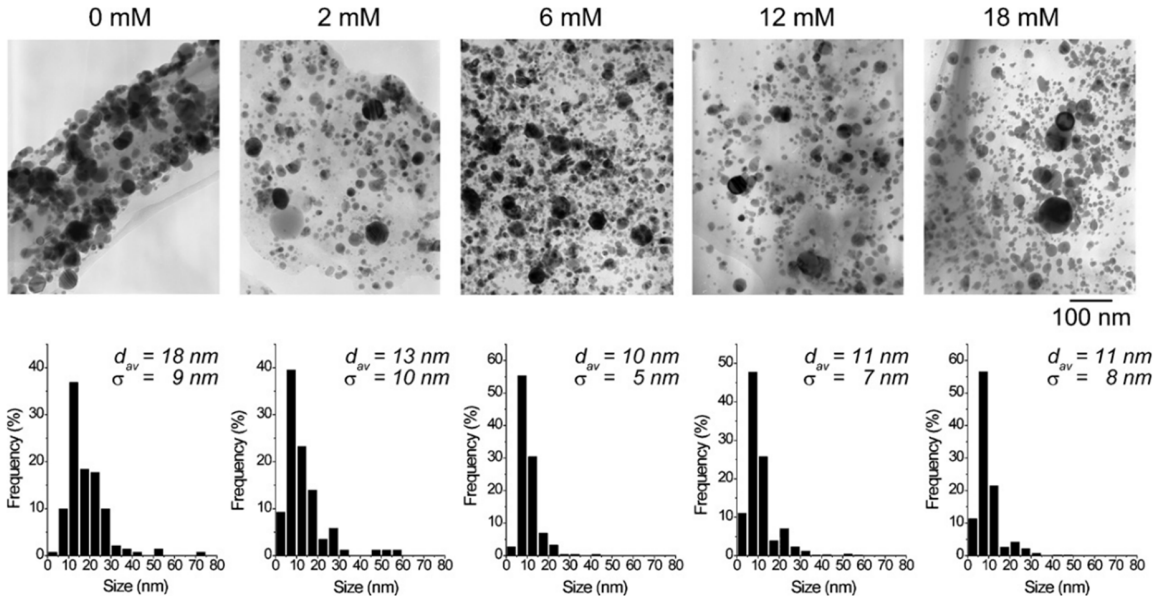


**Figure 2.24.** TEM images and size distributions of silver nanoparticles prepared by laser ablation of a silver plate in aqueous PVP solutions with different concentrations.[154] Reprinted with permission from *Appl. Surf. Sci.* 2008, *254*(16), 5224-5230. Copyright 2008 Elsevier B.V.

Besides pure metal nanoparticles, alloy nanoparticles can also be produced by femtosecond laser ablation of corresponding alloy targets. Stoichiometric Pt-Ir alloy nanoparticles were synthesized by femtosecond laser ablation of a $Pt_9Ir$ target in acetone (300 μJ/pulse) without using any stabilizing agents.[158] The formation of the stoichiometric alloy nanoparticles was attributed to close heat of evaporation of Pt (510 kJ/mol) and Ir (604 kJ/mol), which allows stoichiometric vaporization and uniform distribution of emitted clusters in plasma plume.[158] Similarly, stoichiometric Ni-Fe alloy nanoparticles were produced by femtosecond laser ablation of a $Ni_{48}Fe_{52}$ target in cyclopentanone.[159] In contrast, samarium-enriched alloy nanoparticles were formed when ablating a $Sm_2Co_{17}$ target.[159] This was attributed to the large gap between the heat of evaporation of Sm (164.8 kJ/mol) and Co (382.4 kJ/mol) such that Sm requires less heat to evaporate than Co, while the heat of evaporation of Ni

(374.8 kJ/mol) and Fe (340.2 kJ/mol) are close.[159] The compositions of a produced Ni-Fe alloy nanoparticle and a Sm-Co nanoparticle are shown in **Figure 2.25**.

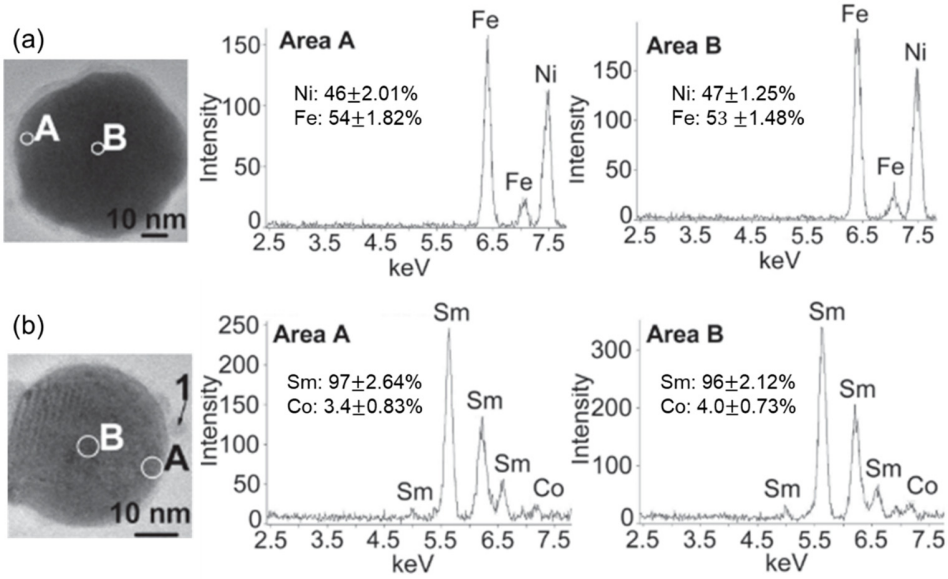


**Figure 2.25.** (a) TEM image of a Ni-Fe nanoparticle produced by femtosecond laser ablation of a $Ni_{48}Fe_{52}$ target in cyclopentanone, and corresponding EDX spectra from two different regions (A and B) of the nanoparticle. (b) TEM image of a Sm-Co nanoparticle produced by femtosecond laser ablation of a $Sm_2Co_{17}$ target in cyclopentanone, and corresponding EDX spectra from two different regions (A and B) of the nanoparticle.[159] Adapted with permission from *Langmuir* 2010, *26*(10), 6892-6897. Copyright 2010 American Chemical Society.

### 2.5.4 Synthesis of Oxide Nanomaterials by Femtosecond PLAL

Oxide nanoparticles can be produced by directly ablating corresponding targets in aqueous solvents. A mixture of $HfO_X$ nanoparticles and nanoribbons were produced by femtosecond laser ablation (800 nm, 50 fs, 1 kHz) of $HfO_2$ pellets in water (**Figure 2.26a**).[160] It was found that the average size of nanoparticles and the content of nanoribbons in the mixtures increased with laser energy.[160] Laser ablation with lower fluence (200-300 μJ/pulse) led to the formation monoclinic $HfO_2$, while higher fluence led to the formation of hexagonal $Hf_6O$, which is usually formed at high pressure.[160] α-$Bi_2O_3$ nanoparticles were also reported to be

produced by femtosecond laser ablation of a $Bi_2O_3$ target in ethanol.[135] Similarly, ZnO quantum dots can be produced by ablating a ZnO target in different solvents including water, ethanol and octadecanethiol.[161] Furthermore, Chelnokov et al. reported the production of Mg-doped ZnO nanoparticles by femtosecond laser ablation of targets made of Zn and Mg acetylacetonates in ethanol.[136] The targets were made by mixing Zn and Mg acetylacetonates with different Zn/Mg ratios followed by heating at 130 °C for 1 hr to evaporate water and 350 °C for 3 hrs to destroy organics, and then compressed to form plates and sintered at 700 °C for 2 days.[136] **Figure 2.26b** shows the TEM image of a Mg-doped ZnO nanoparticle where the bright parts are Mg-rich regions which were formed by the diffusion of Mg during cooling of the nanoparticle.[136] The photoluminescence spectra of the nanoparticles (**Figure 2.26c**) indicated that the bandgap of the nanoparticles can be tuned by changing the concentration of Mg.[136]

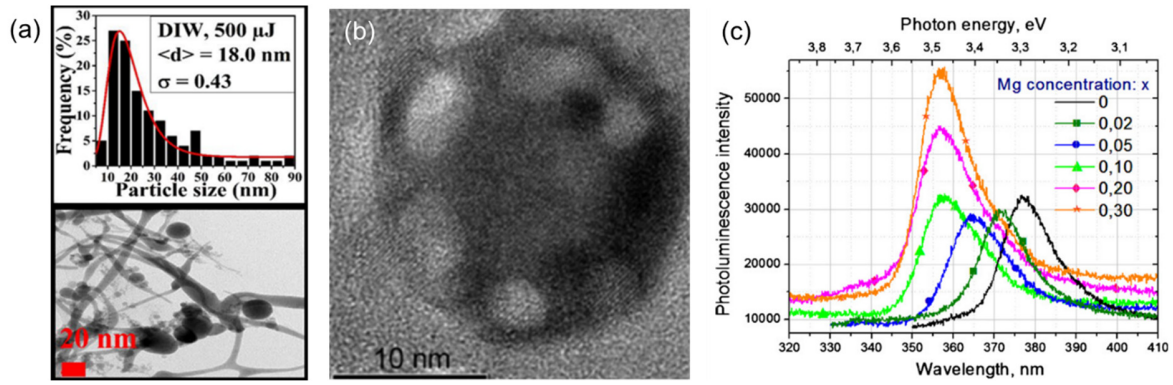


**Figure 2.26.** (a) Size distribution of HfOx nanoparticles (top) and the TEM image of HfOx nanoparticles and nanoribbons (Botton).[160] Adapted with permission from *Appl. Phys. A Mater. Sci. Process.* 2019, *125*(1), 74. Copyright 2019 Springer Nature. (b) TEM image of a Mg doped ZnO nanoparticle. The bright zones are Mg rich areas.[136] (c) Photoluminescence spectra of Mg-doped nanoparticles with different concentrations of Mg.[136] Adapted with permission from *Appl. Surf. Sci.* 2012, *258*(23), 9408-9411. Copyright 2012 Elsevier B.V.

Additionally, metallic oxide nanoparticles can also be produced by reactive ablation of corresponding metal targets in oxidizing solvents. Alnassar et al. reported the synthesis of

$TiO_2$ nanoparticles by femtosecond laser ablation of a Ti target immersed in water containing 0.1 mM SDS which can attach to the produced nanoparticles to control the size of the nanoparticles and improve their colloidal stability in water.[162] The chemical reaction can be described as below[162]:

$$Ti(nanoclusters) + 4H_2O \rightarrow Ti(OH)_4H_2 \quad (2.27)$$

$$Ti(OH)_4H_2 \rightarrow TiO_2 + 2H_2O \quad (2.28)$$

Similarly, iron oxide can also be produced by reactive ablation of an iron target in water.[163] The femtosecond laser ablation (527 nm, 250 fs, 10 Hz, 15 J/cm$^2$) of the iron target in water led to the formation of nanoparticles with mixed phases of FeO and $Fe_3O_4$.[163] In contrast, the ablation of an iron target in acetone resulted in the formation of nanoparticles with mixed phases of Fe and $Fe_2O_3$ and the nanoparticles were covered by a thick layer of graphite.[163] It was concluded that the formation of the graphite layer due to the femtosecond laser ablation of acetone prevented the nanoparticles from being further oxidized.[163]

Like the above-mentioned iron/iron oxide-graphite core-shell structure, PLAL can also be used to prepare metal-metal oxide core-shell nanostructures. Schinca et al. reported the synthesis of Ag-$Ag_2O$ core-shell nanoparticles by femtosecond laser ablation (800 nm, 120 fs, 1kHz) of a silver target in either water or ethanol.[164] It was found that the thickness of the $Ag_2O$ shell was an inverse function of laser fluence, and a possible explanation given by authors is that increased fluence increases plasma temperature and facilitates the reduction of $Ag_2O$.[164] Similarly, Ni-NiO core-shell nanoparticles were produced by femtosecond laser ablation of a nickel disk immersed in water.[165] Interestingly, NiO-Ni core-shell nanoparticles could also be observed. One explanation proposed by authors is that the oxidation of Ni by water released $H_2$ which further reduced NiO at the hot surface of the NiO nanoparticles before they cooled down.[165]

### 2.5.5 Synthesis of Chalcogenide Nanomaterials by Femtosecond PLAL

Like the preparation of oxide nanomaterials, sulfide nanomaterials can also be prepared by laser ablation of corresponding targets in solvents. Gong et al. reported the synthesis of CdS

nanoparticles by femtosecond laser ablation (800 nm, 120 fs, 1 kHz) of a CdS target in water.[166] It was found that the size of the nanoparticles increased and the population distributions broadened with increasing fluence.[166] Similarly, CdTe, CdSe, and ZnTe nanoparticles could also be prepared by femtosecond laser ablation (387 nm, 180 fs, 1 kHz) of corresponding bulk targets in methanol, water or acetone.[167,168]

Recently, much work has tried to prepare TMDC nanomaterials by PLAL due to increasing popularity of these nanomaterials. $MoS_2$ and $WS_2$ quantum dots can be produced by femtosecond laser ablation of corresponding powder particles or targets in N-methyl-2-pyrrolidone (NMP),[169,170] diethylamine[171] or water/ethanol (1:1) mixed solvent.[172] The quantum dots prepared in NMP and water/ethanol were slightly oxidized, probably due to reactive oxygen species dissociated from solvents under femtosecond laser irradiation, while the quantum dots produced in diethylamine were not.[169–172] **Figure 2.27a** shows the $MoS_2$ quantum dots with an average diameter of 1.8 nm prepared by femtosecond laser (800 nm, 150 fs, 1 kHz) ablation in diethylamine at a fluence of 200 J/cm$^2$ for 30 min. Meanwhile, it was found that the quantum dots produced in NMP and diethylamine were surface functionalized with C-O, C=O, and C-N radicals which worked as isolated emission centers and contributed to increased photoluminescence quantum yields of the quantum dots.[169–171]

Additionally, onion-structured $MoS_2$ nanoparticles comprised of an amorphous core and a layered shell (**Figure 2.27b**) were also observed in the products of femtosecond laser ablation of $MoS_2$ targets in water[173,174] and ethanol.[175] This nanostructure has also been reported in previous work using nanosecond laser ablation.[176–178] Compared to the onion-structured nanoparticles prepared by nanosecond laser ablation, the core of the nanoparticles prepared by femtosecond lasers is not completely amorphous, also contains crystalline regions (**Figure 2.27b**).[173–175] One formation model of this nanostructure given by Zuo and his co-authors is that the amorphous core is formed by agglomeration of ejected atoms, ions and clusters from the ablated target, while the shell is made of nanosheets exfoliated from the ablated target and the core-shell structure is formed when nanosheets wrap the amorphous nuclei.[173] However, no large nanosheets were observed in the femtosecond laser ablation, and

the laser might also ablate the exfoliated nanosheets. In contrast, the model proposed by Zhou and his co-workers is more reliable.[178] They proposed that the amorphous core is formed by rapid cooling and solidification of an ejected liquid droplet. During the cooling process, the inward temperature gradient induces the inward {002} oriented growth of nanosheets around the core, and the shell is formed by layer-by-layer growth of the nanosheets.[178]

Additionally, Zuo et al. reported the formation of $MoS_2$ elliptical nanosheets (**Figure 2.27c**) prepared by femtosecond laser ablation of $MoS_2$ crystal immersed in $FeCl_3$ (6.2 mM) aqueous solution.[119] The length distribution and width distribution of the elliptical nanoseets are shown in **Figure 2.27d and e**. The average length of the nanosheets is 95 nm and the average width of the nanosheets is 27 nm.[119] The formation of $FeS_2$, as indicated in SAED pattern of the nanosheets (**Figure 2.27f**), suggests that Fe ions were absorbed on the surface of active basal planes of $MoS_2$ nanosheets when they were exfoliated, which induced a phase change from 2H phase of bulk powder to 1T phase of nanosheets.[119] However, the authors didn't explain how the nanosheets grew to the oval shape.

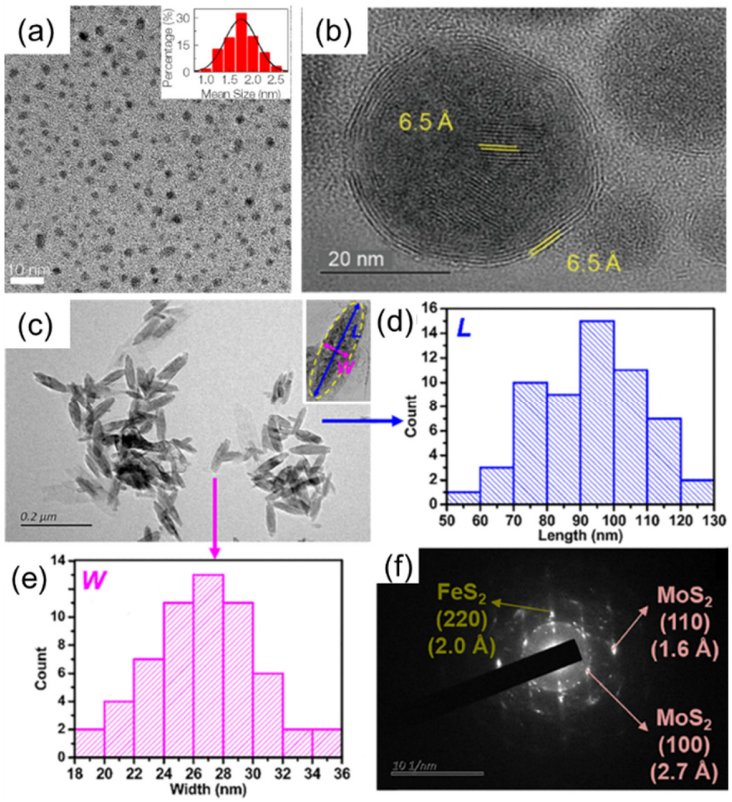


**Figure 2.27.** (a) TEM image of $MoS_2$ quantum dots prepared in diethylamine. The inset is the size distribution of the quantum dots.[171] Adapted with permission from *J. Lumin.* 2019, *214*, 116554. Copyright 2019 Elsevier B.V. (b) TEM image of onion-structured $MoS_2$ nanoparticles.[173] Adapted with permission from *Sci. China Technol. Sci.* 2023, *66*(3), 853-862. Copyright 2023 Science China Press. (c) TEM image of $MoS_2$ elliptical nanosheets. (d, e) Length and width distributions of the nanosheets. (f) SAED pattern of the nanosheet.[119] Adapted with permission from *J. Phys. Chem. C* 2021, *125*(15), 8304-8313. Copyright 2021 American Chemical Society.

### 2.5.6 Synthesis of Other Nanomaterials by Femtosecond PLAL

Femtosecond lasers can also be used to prepare carbon-based nanomaterials in liquid. Santagata et al. reported the synthesis of diamond-like-carbon (DLC) nanoparticles by femtosecond laser ablation (800 nm, 100 fs, 2.7 mJ/pulse) of a graphite plate in water.[179] It

was found that DLC was synthesized when the repetition rate was 10 and 100 Hz, while nanodiamond was formed when the repetition rate increased to 1 kHz.[179] It was hypothesized that the plasma expansion induced by a shockwave might create suitable physicochemical environment for diamond nucleation, and this environment can be self-sustained by a short delay of successive laser pulses when the laser repetition was 1 kHz.[179] Additionally, Novodchuk et al. prepared B/N co-doped reduced graphene oxide nanoflakes by femtosecond laser ablation of graphite oxide flakes and boron nitride (BN) quantum dots in water/ethanol (1:1) mixed solvent.[180] A possible explanation of the reduction of graphite oxide proposed by the authors is tunneling ionization and Coulomb explosion of ablated graphite oxide, which can remove C-O related radicals such as O-C=O, C-OH and C=O.[180]

Qiu's group prepared hydrophobic and hydrophilic silicon quantum dots by femtosecond laser ablation (800 nm, 120 fs, 1 kHz, 0.5 mJ/pulse) of a bulk silicon target in 1-hexene and acrylic acid/ethanol (1:1), respectively.[181,182] These quantum dots were all surface passivated by corresponding organic molecules and partially oxidized by $O_2$ and $H_2O$ dissolved in the solutions.[181,182] The hydrophobic Si quantum dots in 1-hexene had an average size of 2.4 nm and emitted stable and bright blue photoluminescence which was independent of the excitation wavelength.[182] The photoluminescence might originate from the radiative recombination of electron-hole pairs through the oxidized areas on the surface of the quantum dots.[182] In contrast, the photoluminescence wavelength of the hydrophilic Si quantum dots with an average size of 2.1 nm was dependent on the excitation wavelength, suggesting the photoluminescence originated from a quantum confinement effect.[181] Similarly, Zakharko et al. synthesized SiC quantum dots by femtosecond laser ablation of a polycrystalline SiC bulk target in water.[183] The SiC quantum dots were found to be surface passivated with hydroxyl and carboxyl groups and their photoluminescence originated from a quantum confinement effect.[183]

Additionally, femtosecond PLAL can be used to prepare nanowires. Shimotsuma et al. reported the synthesis of copper nanowires from femtosecond laser ablation (780 nm, 215 fs, 1 kHz) of copper flakes dispersed in ethanol or methanol.[184,185] The formation of nanowires

followed the nucleation and growth path. Cu nanoclusters/atoms created from laser ablation of Cu flakes were deposited on the surface of flakes first, which provided nucleation sites for the growth of nanorods. With increasing ablation time, the nanorods kept growing to nanowires at the cost of the flakes. When the flakes were consumed, they couldn't support the growth of nanowires any more, then the nanowires were converted to short nanorods and nanospheres with extended ablation, as shown in **Figure 2.28**.[185] Moreover, the Cu nanowires were found to be partially oxidized on the surface. The formation of an amorphous carbon layer prevented further oxidation.[185]

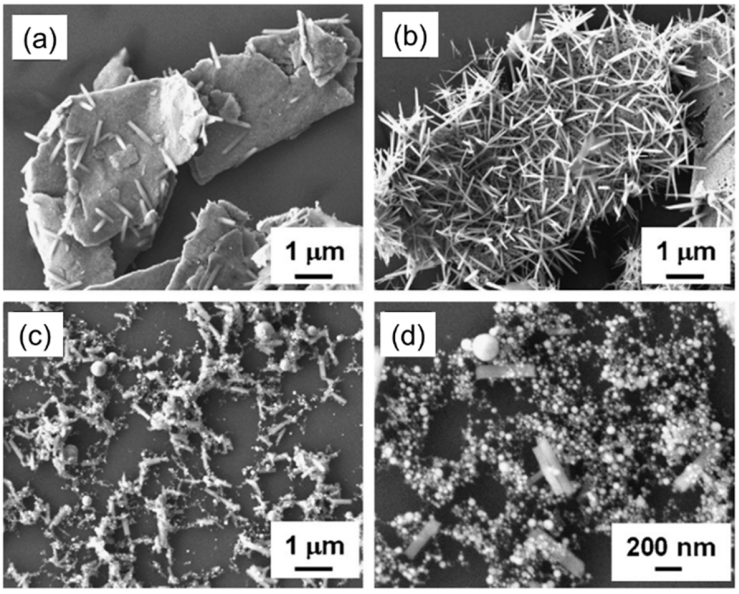


**Figure 2.28.** SEM images of copper nanomaterials prepared by femtosecond laser ablation for different times: (a) 1 min, (b) 5 min, (c) 20 min and (d) 40 min.[185] Reprinted with permission from *Appl. Surf. Sci.* 2008, *254*(16), 4992-4998. Copyright 2008 Elsevier B.V.

Fei et al. reported the formation of silver nanowires by femtosecond laser ablation (800 nm, 85 fs, 25 kHz) of a silver plate in aqueous solution containing sodium citrate (0.3 mM) and PVP (0.1 mM).[186] Sodium citrate was found to be selectively attached to the (111) facet of the prepared silver nanoparticles, which allows the silver particles to only grow within the (111) plane.[186] The formation of the silver nanowires was explained by

polarization-induced plasmon-plasmon interaction.[186] The high electric field of incident laser pulses induced free electrons in the nanoparticles or short nanorods to oscillate collectively with the electric field of the laser pulses. As the diameter of the focal point was around 5 μm, a uniform electric field was assumed to act on the nanoparticles or short nanorods at the focal point to allow free electrons in different nanoparticles/nanorods to oscillate coherently.[186] Then the nanoparticles/nanorods with the same polarization direction attracted each other and finally connected to form longer nanorods. Repeated connection between different nanorods resulted in the formation of nanowires.[186] Ibrahim et al. also reported the formation of BN, $MoS_2$, $WS_2$ and graphene nanorods by femtosecond laser ablation based on the same mechanism.[187]

From the above literature review, it can be seen that many Mo-based nanomaterials including $MoO_{3-x}$, molybdenum blue and $MoSe_2$ are promising PTAs thanks to their high absorption of NIR light. But they are usually prepared by either bottom-up or top-down methods which need high temperatures and/or long times. Therefore, it is necessary to develop a facile synthesis method for these nanomaterials. The PLAL technique can be used to synthesize various nanomaterials. It is an easy and quick technique and is regarded as a green "synthesis" method as it needs few precursors. The chemical reactions during laser ablation can facilitate the synthesis of nanomaterials with complex structures or stoichiometries besides those produced by simple ablation. Most previous research, however, focused on the ablation of bulk targets. The mechanisms of the ablation of powders are still far from clear. In this thesis, Mo-based nanomaterials with high PTCEs are produced by femtosecond laser ablation in liquids. The laser system to synthesize the nanomaterials and the customized setup to measure the PTCEs of the nanomaterials are introduced in Chapter 3.

# Chapter 3
# Methodology

## 3.1 Femtosecond Laser System

All the nanomaterials including $MoO_{3-X}$, molybdenum blue and $MoSe_2$ in this work were synthesized by femtosecond laser ablation in liquid. This section introduces the basic structure of the femtosecond laser system used in this work and the setup of PLAL.

### 3.1.1 Structure of Femtosecond Laser System

PLAL usually needs laser pulses with high energy, but for femtosecond PLAL it requires high peak power (pulse energy divided by pulse duration), so that when focused the peak intensity is high. The femtosecond laser system used in this work outputs laser pulses with a wavelength centered at 800 nm, pulse duration of 35 fs, repetition rate of 1 kHz and the maximum average power of 5 mJ/pulse, this gives a peak power of $1.4 \times 10^{11}$ mJ/pulse. The diameter of the output beam is 1 cm. To achieve a high peak power, femtosecond laser pulses with low energy from an optical oscillator need to be amplified through a Chirped Pulse Amplification (CPA) system by a pump laser.

The oscillator can produce femtosecond laser pulses with the specifications listed below.

**Table 3.1.** Optical Specifications of The Oscillator

| Wavelength | 800 nm |
|---|---|
| Pulse Duration | <12 fs |
| Repetition Rate | 75 MHz |
| Output Power | >300 mW |

The laser pulses with an average pulse energy of 4 nJ/pulse from the optical oscillator are guided into a CPA system (Spitfire Ace-35F) to obtain high energies while maintaining the

femtosecond pulse duration. In the CPA system, the laser pulses experience three steps: stretching, amplification and compression. **Figure 3.1** shows the structure of the CPA system. In brief, the laser pulses, also known as the seed laser pulses, are first stretched to the time scale of picoseconds by a stretcher (marked with the yellow dashed box) to avoid high peak powers that may damage the amplifying medium. The stretched pulses are then amplified through a Ti:sapphire medium with a pump laser (Empower Q-switched green laser, 527 nm, 1 kHz, 30 W) in an amplifying cavity (marked with the blue dashed box). After amplification, the laser pulses are compressed back to the time scale of femtoseconds by a compressor (marked with the black dashed box). Through the CPA system, the laser pulses have a pulse duration of 35 fs and the maximum energy of 5 mJ/pulse.

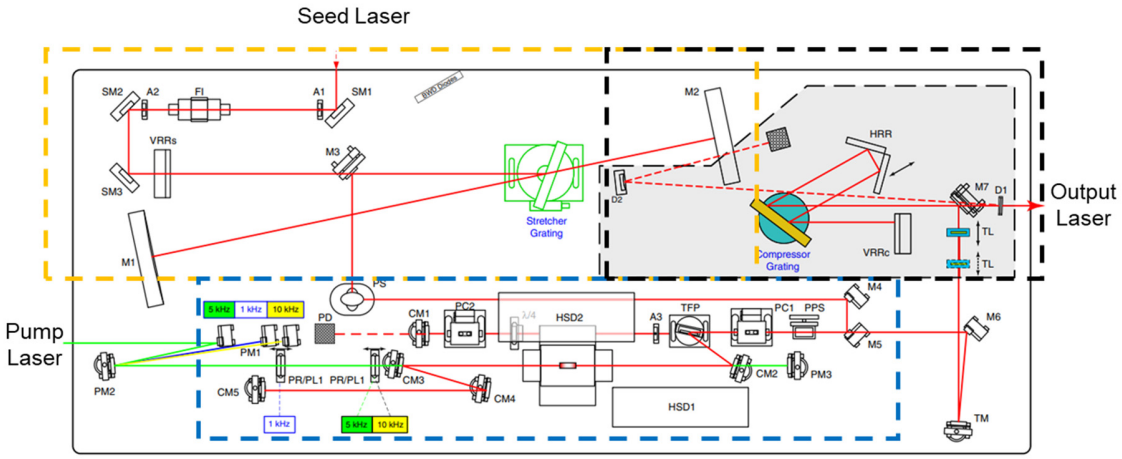


**Figure 3.1.** Spitfire Ace-35F layout.[188]

### 3.1.2 Setup of PLAL

The femtosecond laser beam coming out of the CPA system follows a beam path shown in **Figure 3.2** to a glass vial that contains liquid and dispersed powder particles for PLAL. The laser beam first passes through a half wave plate and a polarizing beam splitter, then is reflected downward by a dielectric mirror. After passing a plano-convex lens with the focal length of 5 cm, the laser beam is focused into the liquid. The focal point is precisely controlled at 1.5 cm under the liquid/air interface. A small magnetic stirring bar is always put

inside the vial to stir the powder particles to ensure uniform ablation. The power of the laser beam is controlled by rotating the half wave plate and measured by a power meter before each experiment.

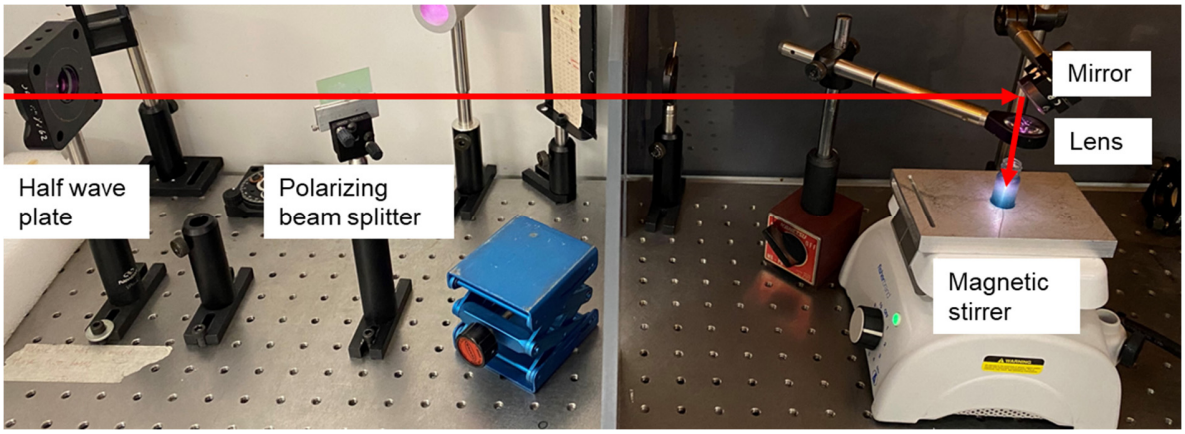


**Figure 3.2.** Image of the setup for PLAL.

## 3.2 Photothermal Conversion Efficiency (PTCE) Measurement

Photothermal conversion efficiency (PTCE) refers to the ratio of light energy converted to heat to the total light energy absorbed by nanomaterials. The total light energy absorbed by nanomaterials can be determined by the power of the incident laser and the absorbance of the nanomaterials measured by UV-vis-NIR absorption spectroscopy. The light energy converted to heat by the nanomaterials is usually measured by the heat dissipated to the surrounding environment including the solution and air.[189] In this work, the PTCEs of synthesized nanomaterials were measured by a custom-built setup and calculated based on a widely used method.[6,48,60,67,189–192]

### 3.2.1 PTCE Measurement Setup

As shown in **Figure 3.3**, the custom-built setup is primarily comprised of four parts: a NIR continuous-wave laser (BWF1-B&W Tek, 808 nm), a 3D-printed cuvette/laser holder, a laser power meter (Integra-Gentec-EO), and two thermocouples (Fisherbrand).

For PTCE measurement, 1 mL of solution containing nanomaterials was transferred to a quartz cuvette with a path length of 1 cm and illuminated by the 808 nm laser for 10 min, followed by cooling for another 10 min. The average power of the incident laser was measured by the laser power meter. The temperatures of the solvent and environment were measured every second using two thermocouple probes placed inside and outside the cuvette, respectively. By monitoring the temperature difference between the heated solution and environment, the dissipated heat can be calculated by equations introduced in Section 3.2.2.

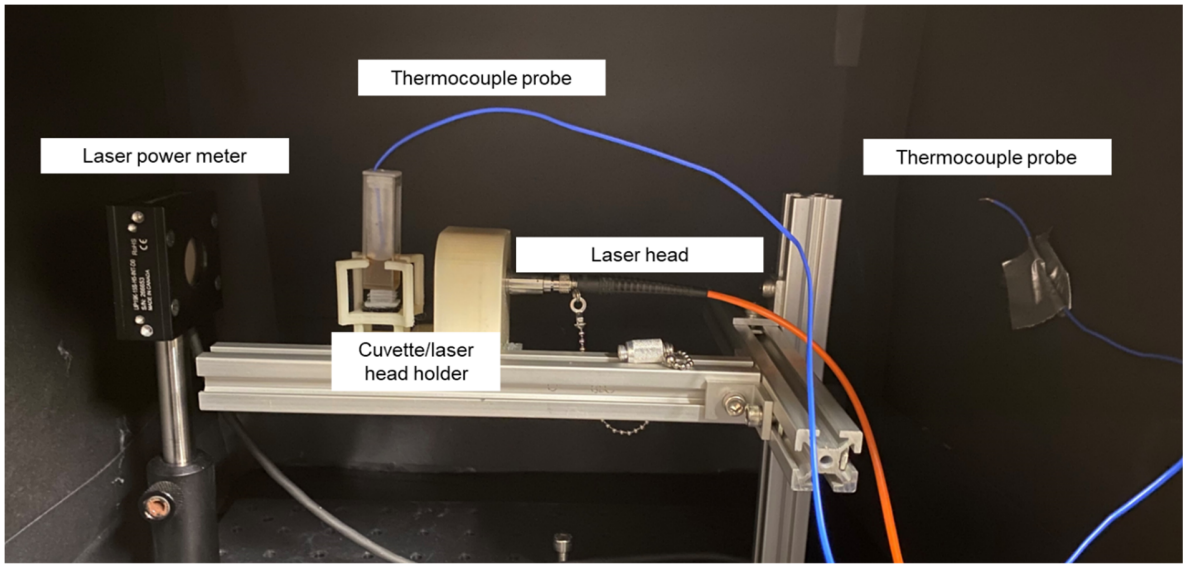


**Figure 3.3.** Image of PTCE measurement setup.

### 3.2.2 Calculation of PTCE

Solution that contains solvent and nanomaterial in a cuvette can be regarded as a system. When the system is illuminated by a laser beam, a continuum energy balance is reached and expressed by **Equation 3.1:**[189]

$$\sum_i m_i C_{p,i} \frac{dT}{dt} = Q_{NM} + Q_{dis} - Q_{ext} \quad (3.1)$$

where $m_i$ and $C_{p,i}$ represent the mass and heat capacity of each solvent component; $T$ represents the solution temperature; $Q_{NM}$ represents the power input of the nanomaterial;

$Q_{dis}$ represents the power input of the system without nanomaterials, which is much smaller than $Q_{NM}$, and $Q_{ext}$ represents the external heat transfer rate from the system surface by air.

According to Beer-Lambert Law,[189] the input energy to nanomaterials $Q_{NM}$ can be calculated by **Equation 3.2**:

$$Q_{NM} = I(1 - 10^{-A_\lambda})\eta \tag{3.2}$$

Where $I$ is the power of the incident laser beam; $A_\lambda$ is the absorbance of the nanomaterial at the wavelength (808 nm) of the incident laser measured by UV-vis-NIR spectroscopy; $\eta$ is the photothermal conversion efficiency (PTCE) of the nanomaterial.

The external heat transfer rate $Q_{ext}$ was found to be nearly proportional to the temperature difference between the system and the environment when the temperature difference was not high.[189] Then $Q_{ext}$ can be expressed by **Equation 3.3**:

$$Q_{ext} = hS(T - T_{amb}) \tag{3.3}$$

Where $h$ is the system heat transfer coefficient; $S$ is the surface area of the cuvette where heat exchange occurs; $T$ is the temperature of the system during laser illumination; $T_{amb}$ is the ambient temperature.

Here two parameters $\theta$ and $\tau_s$ are introduced. $\theta$ is a dimensionless driving force temperature, defined by **Equation 3.4**. $\tau_s$ is a sample system time constant, defined by **Equation 3.5**.[189]

$$\theta = \frac{T_{amb} - T(t)}{T_{amb} - T_{max}} \tag{3.4}$$

$$\tau_s = \frac{\sum_i m_i C_{p,i}}{hS} \tag{3.5}$$

**Equation 3.6** can be obtained when substituting **Equation 3.3, 3.4** and **3.5** into **3.1**.

$$\frac{d\theta}{dt} = \frac{1}{\tau_s}\left[\frac{Q_{NM} + Q_{dis}}{hS(T_{max} - T_{amb})} - \theta\right] \tag{3.6}$$

When the laser illumination stops, $Q_{NM} + Q_{dis} = 0$. Then **Equation 3.6** is reduced to:

$$\frac{d\theta}{dt} = -\frac{\theta}{\tau_s} \tag{3.7}$$

Considering that the system starts cooling when the laser stops, **Equation 3.7** can be solved by using the initial condition $\theta = 1$ when $t = 0$, and gives **Equation 3.8**:

$$t = -\tau_s ln\theta \tag{3.8}$$

Therefore, $\tau_s$ can be obtained by linearly fitting the plot of the time against the negative natural logarithm of $\theta$ during the cooing process after laser illumination. $\tau_s$ is the slope of the linear fitting line.

During laser illumination, $Q_{NM} + Q_{dis}$ is finite. The system temperature reaches the maximum when the external heat flux $Q_{ext}$ equals the input energy of the whole system $Q_{NM} + Q_{dis}$ (**Equation 3.9**).

$$Q_{NM} + Q_{dis} = hS(T_{max} - T_{amb}) \tag{3.9}$$

The PTCE of the nanomaterial can be solved by substituting **Equation 3.2** into **3.9**.

$$\eta = \frac{hS(T_{max} - T_{amb}) - Q_{dis}}{I(1 - 10^{-A_\lambda})} \tag{3.10}$$

$Q_{dis}$ can be measured independently with pure solvent only.

$$Q_{dis} = \frac{\sum m_{solvent} C_{solvent}}{\tau_{s,solvent}} (T_{max,solvent} - T_{amb,solvent}) \tag{3.11}$$

Where $\tau_{s,solvent}$ is obtained *via* the same way as $\tau_s$ but with solvent only.

Take the $MoSe_2$ nanoparticles synthesized by laser ablation at 2.5 W for 10 min in isopropyl alcohol (IPA) in Chapter 6 for example. $m_{IPA}$ = 1 mL * 0.786 g/mL=0.786 g, and $C_{IPA}$ = 2.68 J/g*K. $\Sigma m_i C_i$ is calculated to be 2.106 J/K for 1 mL of IPA. The temperature change of the sample is plotted against time with 10 min of laser on and 10 min of laser off, as shown in **Figure 3.4a**. The laser power $I$ is 0.46 W. The absorbance at 808 nm is 0.416. The highest temperature reached *via* laser illumination is 37.5 °C and the ambient temperature is 21.1 °C. $\tau_s$ is calculated by measuring the slope of the linear fitting line in

**Figure 3.4b**, which is 309.83 s. For illumination of the solvent alone with the NIR laser with the same power, the time constant ($\tau_{s,solvent}$) is 279.48 s and the temperature change is 0.4 °C. According to **Equation 3.11**, $Q_{dis}$ is 0.003 W. By substituting these values into **Equation 3.10**, the photothermal conversion efficiency of the sample is 38.3%.

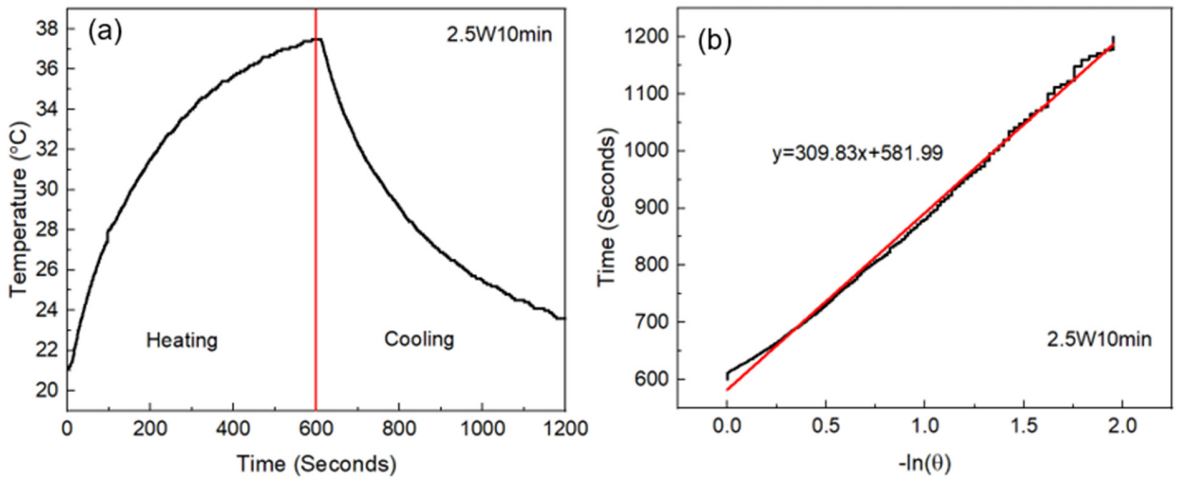


**Figure 3.4.** (a) Temperature change curve of $MoSe_2$ nanoparticles prepared by laser ablation at 2.5 W for 10 min in IPA. (b) Time constant calculated from cooling process in (a).[193]

It should be noted that this method to measure the PTCE may be not accurate, even though most work researching PTAs uses it.[6,48,60,67,189–192] The approximation of **Equation 3.3** only applies when the temperature increase of a tested sample is below 11 °C.[189] In most cases, however, the temperature of 1 mL of the tested sample increases well above 11 °C during the laser illumination. To solve this problem, Bednarkiewicz et al. recently reported a method to determine the PTCEs of nanomaterials by measuring the temperature increase of a small droplet, which can ensure the temperature increase is below 11 °C.[194] Additionally, they used a thermographic camera instead of thermocouples to obtain more accurate temperature readings. Both these changes allow a more precise and accurate measurement of the PTCEs of the nanomaterials.

# Chapter 4
# Synthesis of $MoO_{3-X}$ Nanosheets by Femtosecond Laser Ablation

## 4.1 Introduction

Section 2.1.2 has introduced that $MoO_{3-X}$ relies on localized surface plasmon resonance (LSPR) to absorb NIR light and transfer the light energy to heat to kill tumor cells. Several strategies have been developed to synthesize $MoO_{3-X}$ nanoparticles, which are generally classified into two groups. One is to use solvothermal or hydrothermal processes. The second approach is to reduce $MoO_3$ by hydrogen intercalation to create molybdenum bronze ($H_XMoO_3$). The degradation of $H_XMoO_3$ results in the formation of $MoO_{3-X}$. The details of traditional methods to produce $MoO_{3-X}$ are introduced in Section 2.2. Solvothermal processes usually require high temperatures and a long synthesis time for the reaction. Hydrogen intercalation by light illumination is much safer, however additional steps are required to exfoliate $MoO_3$ nanosheets first, and the hydrogen intercalation efficiency is highly dependent on the light intensity.[83,195]

Herein, an efficient one-pot process to synthesize substoichiometric molybdenum oxide nanosheets from $MoS_2$ by femtosecond laser ablation is introduced. $MoS_2$ bulk powder is suspended in an ethanol/water mixture, where the $MoS_2$ serves as the Mo precursor and is oxidized during laser ablation. Different laser ablation times and ethanol/water ratios are researched for their impact on the formation of $MoO_{3-X}$. The LSPR properties of the fabricated $MoO_{3-X}$ are evaluated by UV-vis spectroscopy and photothermal conversion measurements. By using this approach, oxidation and hydrogen intercalation occur simultaneously under femtosecond laser ablation, as the ethanol and water generate reactive oxygen and hydrogen species at the same time, such that the $MoO_{3-X}$ synthesis time is dramatically reduced and almost all the $MoS_2$ bulk powders are transformed to molybdenum oxide with minimal waste. Additionally, the whole process takes place at room temperature and no dangerous or toxic materials are involved.

## 4.2 Experimental Methods

### 4.2.1 Synthesis of $MoO_{3-X}$ Nanosheets

Ultrafine $MoS_2$ powders (Graphene Supermarket) were dispersed in different solvents including pure water, pure ethanol, and mixtures consisting of 30%, 70%, 75%, 80%, 85%, 90%, and 95% ethanol in water, 80% methanol in water, 80% IPA in water, 80% 1-propanol in water, and 80% acetone in water, followed by ultrasonication for 15 min to break agglomerates. All percentages are volume percentages. The concentration of $MoS_2$ was kept at 0.125 mg/mL and 4 mL of each suspension was transferred into a small vial for laser ablation.

A femtosecond laser beam following the beam path introduced in Section 3.1.2 was employed to irradiate the suspensions. The average power was fixed at 2 W by using a half-wave plate and a polarizing beam splitter. The suspension was stirred by a magnetic stirring bar at 300 rpm during laser ablation.

### 4.2.2 Characterization of Nanomaterials

The laser-synthesized nanomaterials were drop-casted on silicon wafers for characterization. A ZEISS Ultraplus scanning electron microscope (SEM) and Bruker Dimension Fastscan atomic force microscope (AFM) were used to observe the nanomaterials' morphology and measure the dimensions of the nanomaterials. Grazing incidence X-ray diffraction (GIXRD) with Cu Kα radiation was conducted using a PANalytical X'Pert Pro MRD diffractometer to identify the phases of the nanomaterials. A Renishaw micro-Raman spectrometer (laser wavelength of 632 nm) was used to analyze the bonding states of the nanomaterials. X-ray photoelectron spectra (XPS) of the nanomaterials were measured using a Thermo-VG Scientific ESCALab 250 microprobe. Monochromatic Al Kα excitation was used with the energy of 1486.6 eV. The absorbance spectra of the nanomaterials were measured using a Horiba QuantaMaster 8000 spectrometer. The lattice spacings of the nanomaterials were measured by a FEI Titan 80-300 LB high-resolution transmission electron microscope (HRTEM). Particle size of the $MoO_{3-X}$ was measured at

room temperature using a Malvern Zetasizer Ultra instrument (Malvern Panalytical, UK). The particle size distribution in 90% ethanol (in water) was obtained from the light scattered by particles which were illuminated with a laser beam (at a scattering angle of 173°). The measured sizes were reported using an intensity distribution. Each data point was automatically repeated in 5 replicates, and the average was reported.

The PTCEs of the fabricated nanomaterial suspensions were evaluated using an 808 nm continuous-wave laser with a power of 0.464 W. The details of measurement procedures and the calculation of PTCEs of the nanoparticles are described in Section 3.2. The thermal stability of the nanoparticles was evaluated by repeating laser illumination and cooling cycles 5 times.

## 4.3 Results and Discussion

### 4.3.1 Influence of Laser Ablation Time

SEM images of the original $MoS_2$ powder and the nanomaterials laser-synthesized at 2 W for 10 min, 30 min and 50 min in 80% ethanol are shown in **Figure 4.1**. The original $MoS_2$ bulk powder particles have an average size of around 1.5 μm, as shown in **Figure 4.1a**. The GIXRD pattern of the original $MoS_2$ is shown in **Figure 4.2a**, where the peaks of (002), (100), (101), (102), (103), (104), (105), (106), (110) and (112) planes of 2H-$MoS_2$ can be observed (PDF#37-1492). After 10 min of laser ablation, the SEM image shows all the bulk powder particles were dissociated into nanoparticles with an average size of 30 nm (**Figure 4.1b**). The GIXRD pattern (**Figure 4.2b**) shows peaks attributable to the silicon substrate and a sharp peak at 14.4° that is assigned to the (002) plane of $MoS_2$, indicating that the dissociated nanoparticles mainly consisted of $MoS_2$. After 30 min of laser ablation, the diameters grew to about 40-100 nm (**Figure 4.1c**). It is hard to observe $MoS_2$ peaks in the GIXRD pattern (**Figure 4.2c**). Instead, five small peaks corresponding to (601), (610), (302), (212) and (502) planes of $Mo_4O_{11}$ (PDF#05-0337) are observed. The small broad peaks are probably caused by the limited size and crystallinity of the nanosheets formed. The lattice spacing of the nanosheets is observed to be 0.35 nm by HRTEM (**Figure 4.1e**),

corresponding to the (601) plane of $Mo_4O_{11}$. After 50 min of laser ablation, the majority of the material was transformed to nanobelts and some nanosheets remained (**Figure 4.1d**). One sharp peak corresponding to (100) and two small peaks corresponding to (202) and ($\bar{3}$02) planes of $Mo_8O_{23}$ (PDF#65-6901) are observed in the GIXRD pattern (**Figure 4.2d**), together with several small peaks corresponding to (040), (021) and (111) planes of α-$MoO_3$ (PDF#05-0508). This implies the remaining nanosheets were probably $Mo_8O_{23}$ that had not been completely oxidized.

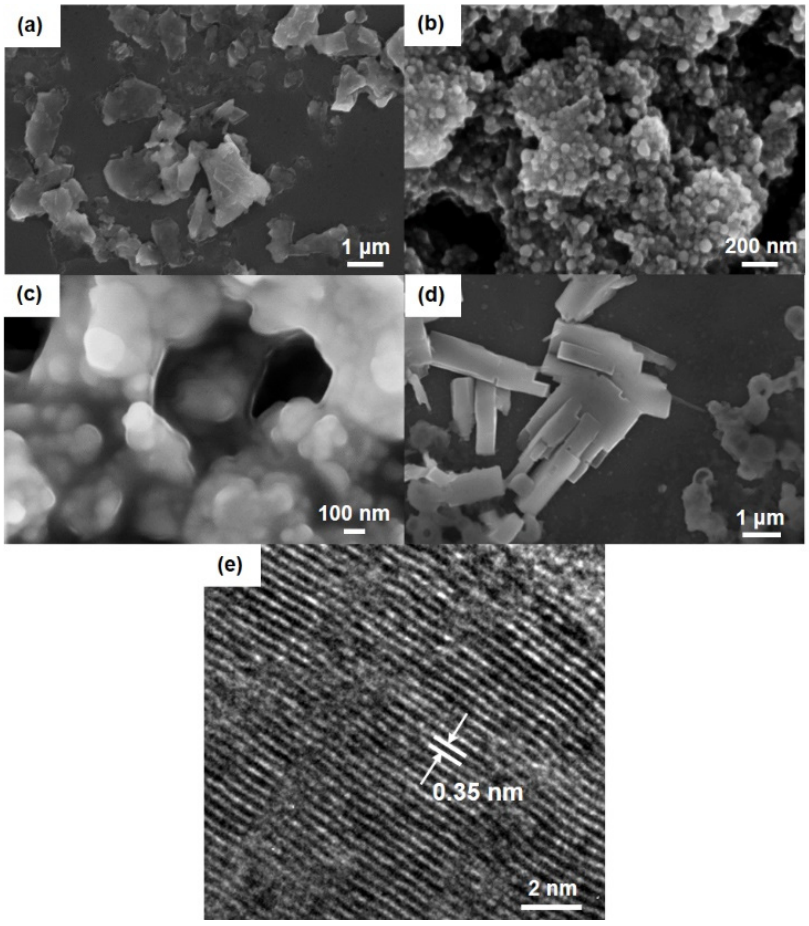


**Figure 4.1.** SEM images of (a) the original $MoS_2$ powder and samples after (b) 10 min, (c) 30 min and (d) 50 min of laser ablation in 80% ethanol. (e) HRTEM image of the sample after 30 min of laser ablation.[196] Reprinted with permission from Chem. Mater. 2021, 33, 12, 4510-4521. Copyright 2021 American Chemical Society.

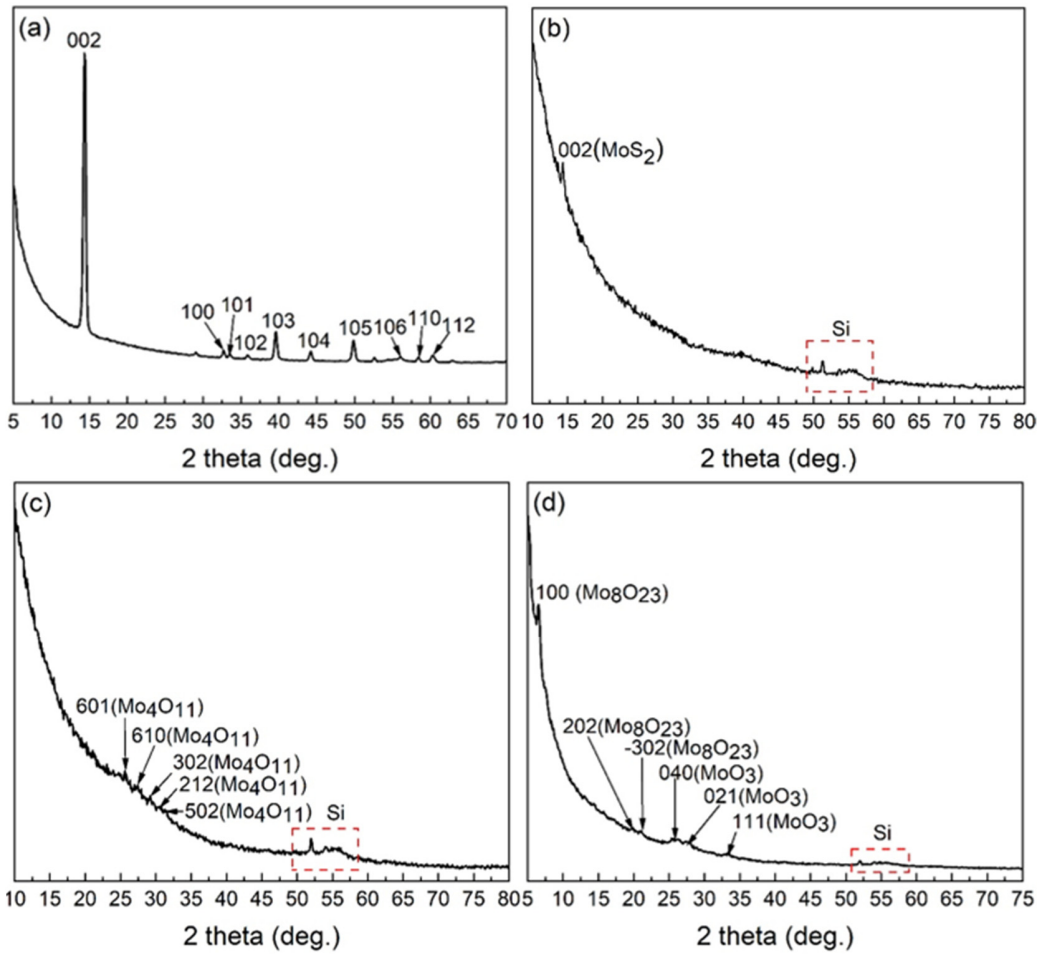


**Figure 4.2.** GIXRD patterns of (a) original $MoS_2$ powder and samples laser-ablated in 80% ethanol for (b) 10 min, (c) 30 min and (d) 50 min. All the labeled peaks in (a) are assigned to $MoS_2$.[196] Reprinted with permission from Chem. Mater. 2021, 33, 12, 4510-4521. Copyright 2021 American Chemical Society.

The AFM images after 30 min and 50 min of laser ablation are shown in **Figure 4.3**. After 30 min of laser ablation, the $Mo_4O_{11}$ nanosheets have a thickness of around 3.5 nm and diameter of around 50 nm. The $MoO_3$ nanobelts formed after 50 min of laser ablation have a thickness of 160 nm and width of 0.5 μm. The formation of the nanobelts is probably caused by the linear growth of the nanosheets under the high electric field of the intense laser.[187]

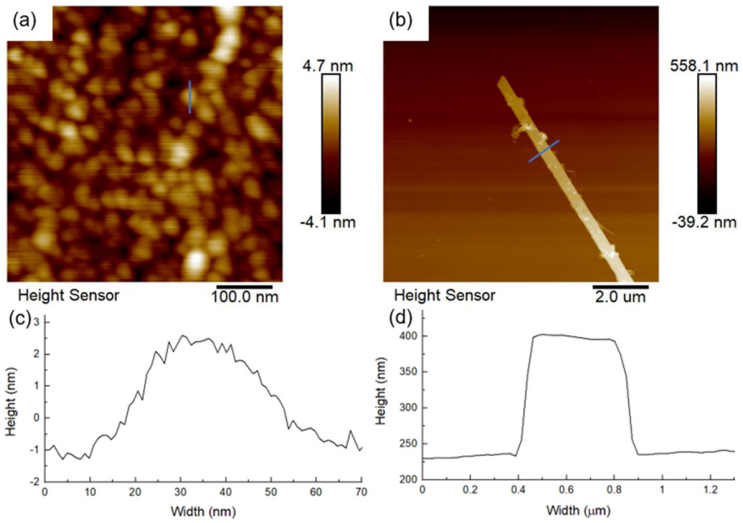


**Figure 4.3.** AFM images of samples laser-ablated in 80% ethanol for (a) 30 min and (b) 50 min. (c) and (d) are surface profiles of the blue lines in (a) and (b).[196] Reprinted with permission from Chem. Mater. 2021, 33, 12, 4510-4521. Copyright 2021 American Chemical Society.

The Raman spectra of laser-synthesized samples are presented in **Figure 4.4**. The $E_{2g}$ and $A_{1g}$ peaks of $MoS_2$ are observed in the original powder. After 10 min of laser ablation, the intensity of the $E_{2g}$ and $A_{1g}$ peaks of $MoS_2$ drops significantly and many new peaks appear. The peaks at 195 $cm^{-1}$, 222 $cm^{-1}$, 350 $cm^{-1}$, 489 $cm^{-1}$ and 725 $cm^{-1}$ belong to $MoO_{3-x}$.[83,197] The peaks at 195 $cm^{-1}$ and 222 $cm^{-1}$ are assigned to the doubly coordinated oxygen bending mode of $A_g$-δ($Mo_2$-O), the peak at 350 $cm^{-1}$ is assigned to the $A_g$-δ(Mo=O) bending mode, and the peaks at 489 $cm^{-1}$ and 725 $cm^{-1}$ are assigned to the triply coordinated oxygen stretching modes of $B_{1g}$-ν($Mo_3$-O) and $B_{3g}$-ν($Mo_3$-O), respectively.[83,198,199] The small peak at 122 $cm^{-1}$ is assigned to the lattice deformation mode, and the peaks at 565 $cm^{-1}$ and 826 $cm^{-1}$ are assigned to the $B_{1g}$-ν($Mo_3$-O) stretching mode of $MoO_2$ and the $B_{1g}$-ν($Mo_2$-O) stretching mode of $MoO_3$ with minor oxygen vacancies, respectively.[199] The peaks at 170 $cm^{-1}$, 273 $cm^{-1}$, 417 $cm^{-1}$, 441 $cm^{-1}$, 786 $cm^{-1}$ and 898 $cm^{-1}$ (highlighted with orange arrows in **Figure 4.4a**) were reported to belong to $H_XMoO_3$ ($x<0.4$).[83,85] This suggests that after the first 10 min of laser ablation, the bulk $MoS_2$ powder was dissociated into nanoparticles and their surfaces

were oxidized with some oxidized areas bonded with H atoms. After 30 min of laser ablation, all the peaks of $MoS_2$ and $H_XMoO_3$ disappear and the peaks belonging to $MoO_{3-X}$ and $MoO_2$ increase. This is consistent with the GIXRD pattern (**Figure 4.2c**). After 50 min of laser ablation, the intensity of the peaks at 195 $cm^{-1}$ and 222 $cm^{-1}$ representing the $Mo_2$-O bending mode of $MoO_{3-X}$ dramatically decreases and the peaks at 350 $cm^{-1}$, 489 $cm^{-1}$, 565 $cm^{-1}$ and 725 $cm^{-1}$ representing the Mo=O bending mode and the $Mo_3$-O stretching modes of $MoO_{3-X}$ and $MoO_2$ disappear. The new peaks at 236 $cm^{-1}$, 283 $cm^{-1}$, 333 $cm^{-1}$ and 373 $cm^{-1}$ are assigned to the $A_g$-δ($Mo_2$-O), $B_{2g}$-δ(Mo=O), $A_g$-δ($Mo_3$-O) and $A_g$-δ(Mo=O) bending modes of α-$MoO_3$, respectively.[83,199] The new peaks at 660 $cm^{-1}$ and 816 $cm^{-1}$ are assigned to the $B_{3g}$-ν($Mo_3$-O) and $B_{1g}$-ν($Mo_2$-O) stretching modes of α-$MoO_3$, respectively.[83,85,199] The peak at 990 $cm^{-1}$ is for the terminal oxygen ($Mo^{6+}$=O) stretching mode of α-$MoO_3$,[83,85] and the peak at 145 $cm^{-1}$ represents the lattice deformation mode.[83,198] The appearance of these new peaks of $MoO_3$ is in agreement with the GIXRD result (**Figure 4.2d**).

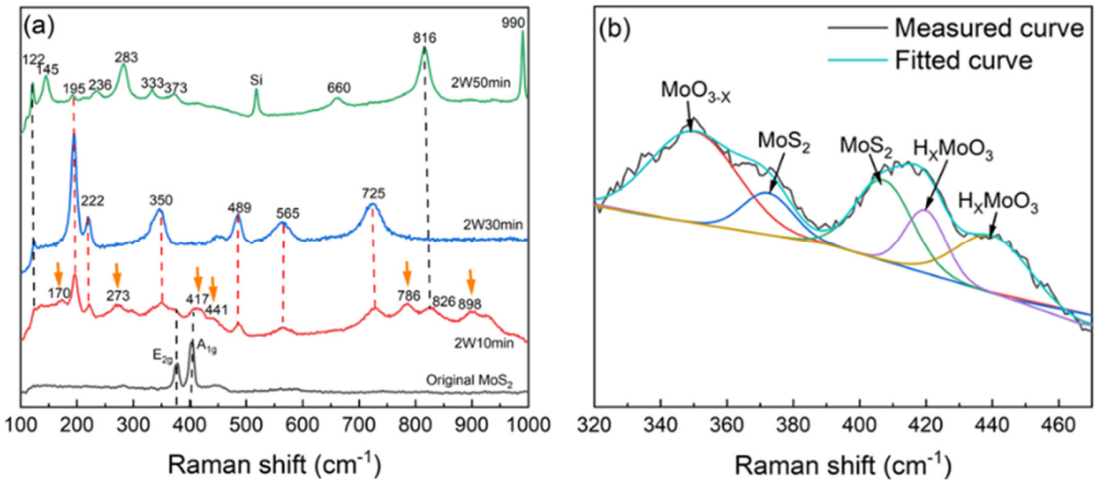


**Figure 4.4.** (a) Raman spectra of the original $MoS_2$ powder and samples laser-ablated in 80% ethanol with 2 W for 10 min, 30 min and 50 min. The peaks marked by orange arrows are assigned to $H_XMoO_3$, the peaks marked by red dashed lines are assigned to $MoO_{3-X}$. The deconvolution of the broad peaks in the 320 $cm^{-1}$ to 460 $cm^{-1}$ range of the 10-min laser-ablated sample is shown in (b).[196] Reprinted with permission from Chem. Mater. 2021, 33, 12, 4510-4521. Copyright 2021 American Chemical Society.

The Raman spectra together with the GIXRD patterns and SEM images suggest that the oxidation of $MoS_2$ in ethanol/water mixtures under femtosecond laser ablation followed three steps, as illustrated in **Figure 4.5a**. In step 1, the original $MoS_2$ bulk powder particles were broken into nanoparticles due to Coulomb explosion, photoexfoliation or plasma-based thermal ablation. In Coulomb explosion, the high electric field of the laser removes the electrons from the bulk particles, then the multiply ionized molecular constituents repel each other and finally break covalent bonds and explode into nanoparticles.[172] In photoexfoliation, the removal of electrons changes the interplanar van der Waals force and results in the exfoliation of layers.[200,201] At the same time, the femtosecond laser also created many reactive oxygen ions such as $O^+$ and $O^{2+}$ from either water[202] or ethanol.[139,203] The oxygen ions partially oxidized the dissociated $MoS_2$ nanoparticles. Additionally, the reactive hydrogen species dissociated from solvent molecules bonded to the oxidized $MoS_2$ to form Mo-$OH_2$ bonds. Kourosh's previous research suggests that reactive hydrogen prefers to interact with doubly coordinated oxygen, terminated oxygen and triply coordinated oxygen of $MoO_3$ in sequence and form -$OH_2$ groups ($H_XMoO_3$).[85] In step 2, oxidation of the nanoparticles continued and the -$OH_2$ groups were released from the lattice as $H_2O$, resulting in the formation of molybdenum oxide with oxygen vacancies ($MoO_{3-X}$). The nanoparticles were transformed to two dimensional nanosheets due to photoexfoliation and the crystal structure changed. The formation and disappearance of $H_XMoO_3$ is similar with Kourosh's research that used solar light to reduce $MoO_3$, where the $H_XMoO_3$ only formed at the beginning of solar illumination and decomposed into $Mo_4O_{11}$ and $MoO_2$ with longer illumination.[83] In step 3, the $MoO_{3-X}$ nanosheets were further oxidized and finally transformed to $MoO_3$ nanobelts. **Figure 4.5b** shows the color change of the samples with different laser ablation times. The color of the samples started from grey of the original $MoS_2$ bulk powder, gradually turned brown/dark green as the bulk powder was dissociated and gradually oxidized and reached blue after around 30 min of laser irradiation indicating the majority of $MoS_2$ was oxidized to the plasmonic $MoO_{3-X}$. Then the blue color gradually faded out with longer laser ablation as the plasmonic $MoO_{3-X}$ was further oxidized to $MoO_3$.

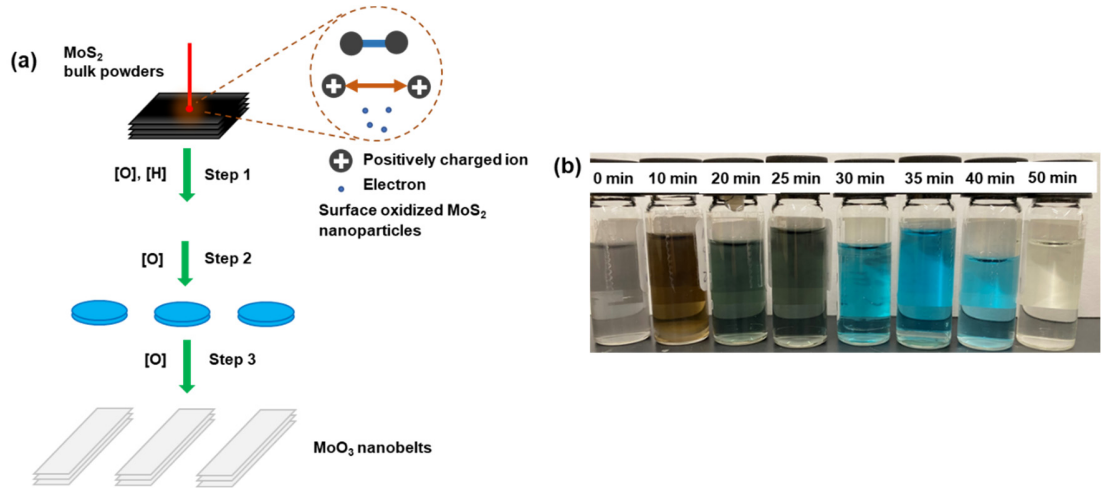


**Figure 4.5.** (a) Schematic illustration of the process of $MoS_2$ oxidation in ethanol/water under femtosecond laser ablation. (b) Color change of samples in 80% ethanol after laser ablation for different times at 2 W.[196] Reprinted with permission from Chem. Mater. 2021, 33, 12, 4510-4521. Copyright 2021 American Chemical Society.

The XPS spectra of the samples are displayed in **Figure 4.6**. In the original $MoS_2$ (**Figure 4.6a**), three peaks corresponding to S2s, $Mo3d_{5/2}$ and $Mo3d_{3/2}$ of $MoS_2$ are located at 227 eV, 229.8 eV and 233 eV, respectively. After 10 min of laser ablation (**Figure 4.6b**), four new peaks at 231.5 eV, 232.9 eV, 234.5 eV and 236 eV are discovered. The peaks at 231.5 eV and 234.5 eV are assigned to $Mo3d_{5/2}$ and $Mo3d_{3/2}$ of Mo (V), while the peaks at 232.9 eV and 236 eV are assigned to $Mo3d_{5/2}$ and $Mo3d_{3/2}$ of Mo (VI).[83] The appearance of Mo (V) and Mo (VI) peaks suggests that the original $MoS_2$ particles were partially oxidized and substoichiometric molybdenum oxide was formed. The peaks corresponding to S2s and $Mo3d_{5/2}$ of Mo (IV) are still distinguishable indicating the presence of $MoS_2$. This is consistent with the GIXRD pattern (**Figure 4.2b**) and the Raman spectrum (**Figure 4.4**). After 30 min of laser ablation (**Figure 4.6c**), the intensity of peaks belonging to $MoS_2$ significantly decreases and the Mo peaks corresponding to Mo (V) and Mo (VI) continue increasing suggesting that almost all the $MoS_2$ was oxidized. As the $Mo3d_{5/2}$ and $Mo3d_{3/2}$ peaks of Mo (V) are higher than that of Mo (VI), the nanosheets at this stage are dominated by the substoichiometric molybdenum oxide ($MoO_{3-X}$). This is consistent with the Raman

spectrum (**Figure 4.4a**) and the appearance of $Mo_4O_{11}$ peaks in the GIXRD pattern (**Figure 4.2c**). After 50 min of laser ablation (**Figure 4.6d**), the $MoS_2$ peaks disappear and only four Mo peaks of Mo (V) and Mo (VI) are observed. The Mo (VI) peaks are higher than the Mo (V) peaks, implying most $MoO_{3-X}$ nanosheets were oxidized to $MoO_3$. This change is consistent with the SEM, GIXRD, and Raman observations. The presence of Mo (V) peaks suggests that some substoichiometric molybdenum oxide remained and was mixed with $MoO_3$. This is supported by the $Mo_8O_{23}$ peaks in the GIXRD pattern (**Figure 4.2d**) and two small peaks at 195 $cm^{-1}$ and 222 $cm^{-1}$ assigned to $MoO_{3-X}$ in the Raman spectrum (**Figure 4.4a**).

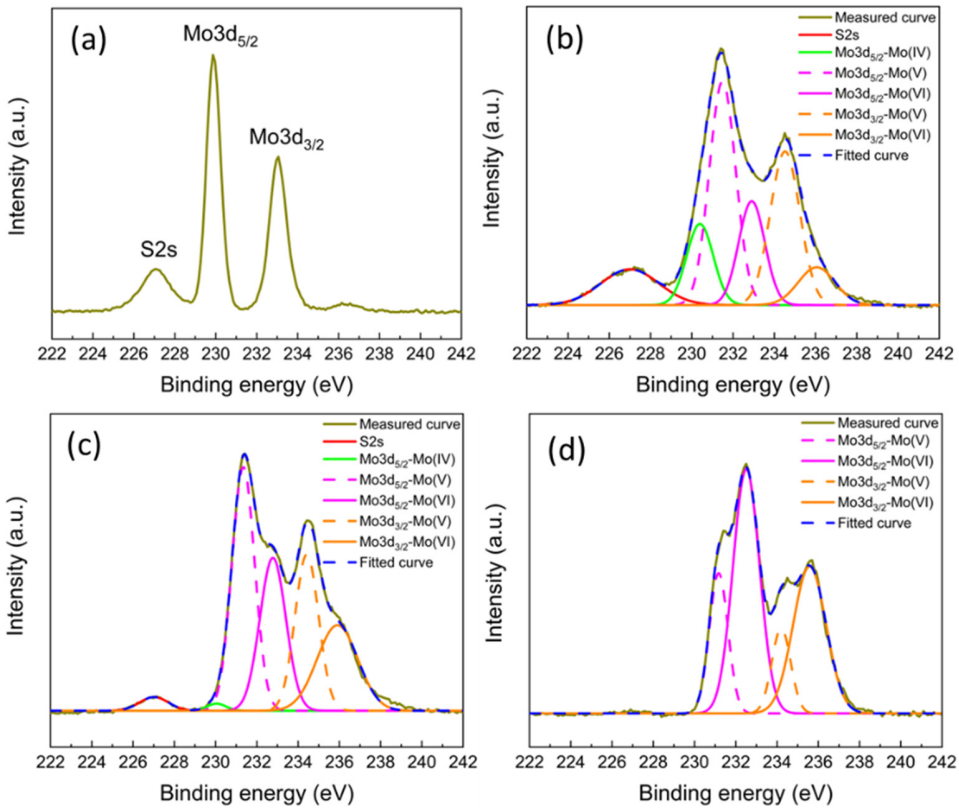


**Figure 4.6.** XPS spectra of Mo3d peaks of (a) the original $MoS_2$ and samples after laser ablation in 80% ethanol for (b) 10 min, (c) 30 min and (d) 50 min.[196] Reprinted with permission from Chem. Mater. 2021, 33, 12, 4510-4521. Copyright 2021 American Chemical Society.

**Figure 4.7a** displays the normalized absorbance spectra of the $MoO_X$ in 80% ethanol with different laser ablation times. It shows that there is no obvious LSPR peaks after the first 10 min of laser ablation, even though the Raman, GIXRD and XPS results imply the partial oxidation of $MoS_2$ and formation of substoichiometric molybdenum oxide. This suggests that the concentration of substoichiometric molybdenum oxide was low and $MoS_2$ and $H_XMoO_3$ were the dominant phases at this stage. Starting from 20 min of laser ablation, one LSPR peak at 675 nm emerges and continues increasing with the laser ablation time, suggesting an increasing concentration of oxygen vacancies and electrons. Starting from 30 min of laser ablation, another LSPR peak at around 750 nm emerges and increases with laser ablation time like the peak at 675 nm. The second peak is usually caused by the formation of two dimensional nanomaterials,[204] implying the shape of the nanoparticles changed from spherical to two dimensional nanosheets, consistent with the AFM image shown in **Figure 4.3**. After 40 min of laser ablation, the LSPR peaks slightly blueshift. This change was also observed in Kourosh's research[83] that used solar irradiation to reduce $MoO_3$ and Hu's report[82] which used the solvothermal method to oxidize $MoS_2$. The LSPR blueshift usually suggests a reduction in the nanoparticle size and a higher electron concentration caused by oxygen vacancies. After 50 min of laser ablation, the LSPR peaks vanish as the majority of the particles were transformed to $MoO_3$ nanobelts, as shown in the SEM (**Figure 4.1d**) and supported by the GIXRD pattern (**Figure 4.2d**) and Raman spectrum (**Figure 4.4a**). The Tauc plot of the sample after 50 min of laser ablation is presented in **Figure 4.7b**. The measured band gap is 2.85 eV, consistent with α-$MoO_3$.[205]

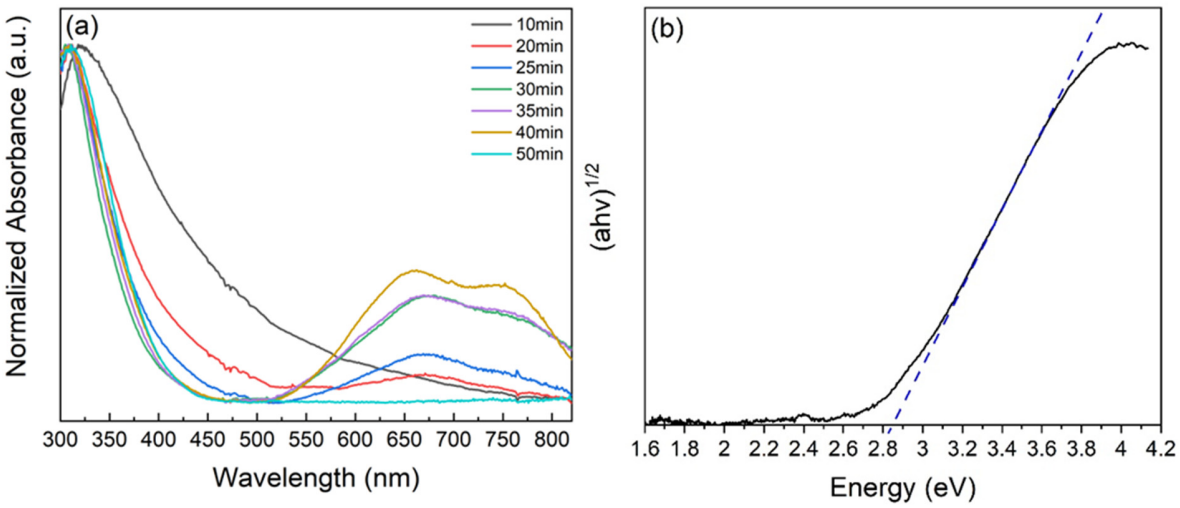


**Figure 4.7.** (a) Normalized absorbance of samples in 80% ethanol after different laser ablation times. (b) Tauc plot used to determine the indirect band gap of $MoO_3$ laser-synthesized in 80% ethanol for 50 min.[196] Reprinted with permission from Chem. Mater. 2021, 33, 12, 4510-4521. Copyright 2021 American Chemical Society.

### 4.3.2 Role of Water and Ethanol

Having established the progression from $MoS_2$ to $H_XMoO_3$, $MoO_{3-X}$, and $MoO_3$ during laser ablation, the role of water and ethanol in the oxidation process of $MoS_2$ under femtosecond laser ablation was also researched. Ethanol/water mixtures with ethanol concentrations ranging from 0% to 100% were used. **Figure 4.8a** displays the normalized absorbance spectra of the samples that were laser-synthesized in the different mixtures. All the samples were laser ablated for 30 min except the sample in 95% ethanol. For that sample, the laser ablation was stopped after 10 min when its color quickly changed from light blue to transparent (**Figure 4.8b**), suggesting the substoichiometric molybdenum oxide was oxidized to $MoO_3$. It is interesting to observe in **Figure 4.8a** that the LSPR peaks only appear when the ethanol concentration is 75% or greater. The peak intensity increases with the concentration of ethanol and reaches a maximum at 90% ethanol, then quickly drops at 95% and 100% ethanol. One exception is the sample in pure DI water whose LSPR peak redshifts to beyond 800 nm.

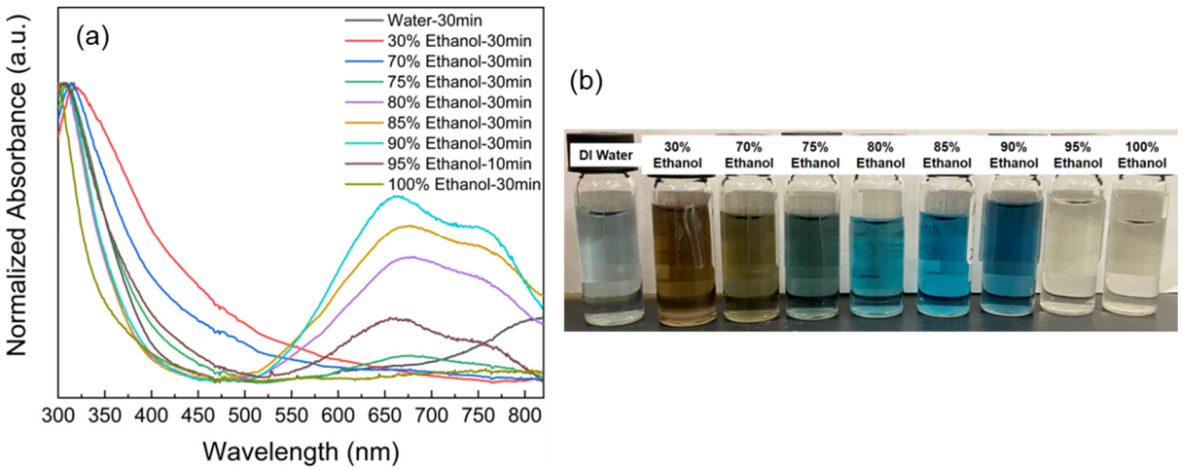


**Figure 4.8.** (a) Normalized absorbance of samples with various concentrations of ethanol after laser ablation for 30 min at 2 W except the sample in 95% ethanol which was only laser ablated for 10 min as the light blue color of the liquid faded for longer ablation. (b) Photos of samples with various concentrations of ethanol after laser ablation for 30 min at 2 W.[196] Reprinted with permission from Chem. Mater. 2021, 33, 12, 4510-4521. Copyright 2021 American Chemical Society.

A SEM image (**Figure 4.9a**) of the nanoparticles fabricated in pure water shows aggregated amorphous particles and some $MoO_3$ nanobelts. The GIXRD pattern (**Figure 4.9c**) of the nanoparticles fabricated in pure water suggests the aggregated amorphous nanoparticles are $Mo_{17}O_{47}$ while the nanobelts are II-$MoO_3$ (space group: P21/m), which is a layered metastable $MoO_3$ phase.[206] So the redshift of the LSPR may be caused by the disordered crystal structure of $Mo_{17}O_{47}$ nanoparticles, which increases the effective mass of the electrons.[42] For the sample laser-synthesized in 100% ethanol, many rod-shaped particles with a size around 2 μm and aspect ratio close to 2 can be observed and are mixed with smaller nanoparticles (**Figure 4.9b**). The GIXRD pattern (**Figure 4.9d**) reveals (100) and (202) peaks of $Mo_8O_{23}$(PDF#65-6901), which may be attributable to the nanoparticles mixed with nanorods in the SEM image. Additionally, peaks at 25.9°, 27.3° and 50.2° are observed and assigned to the $(\bar{2}04)$, (310) and (515) planes of $Mo_9O_{26}$ (PDF#05-0441), which is attributed to the nanorods in the SEM image.[207] Given the different LSPR behavior

of the molybdenum oxide fabricated from the solvents with different concentrations of ethanol, it can be concluded that water and ethanol play different roles in the formation of plasmonic $MoO_{3-X}$, although both can oxidize $MoS_2$ under femtosecond laser ablation. As only $MoO_{3-X}$ phases with $0.125<X<1$ have sufficient free electrons to show metallic characteristics,[205] it appears that the concentration of ethanol affects the amount of oxygen vacancies in the laser-synthesized $MoO_{3-X}$.

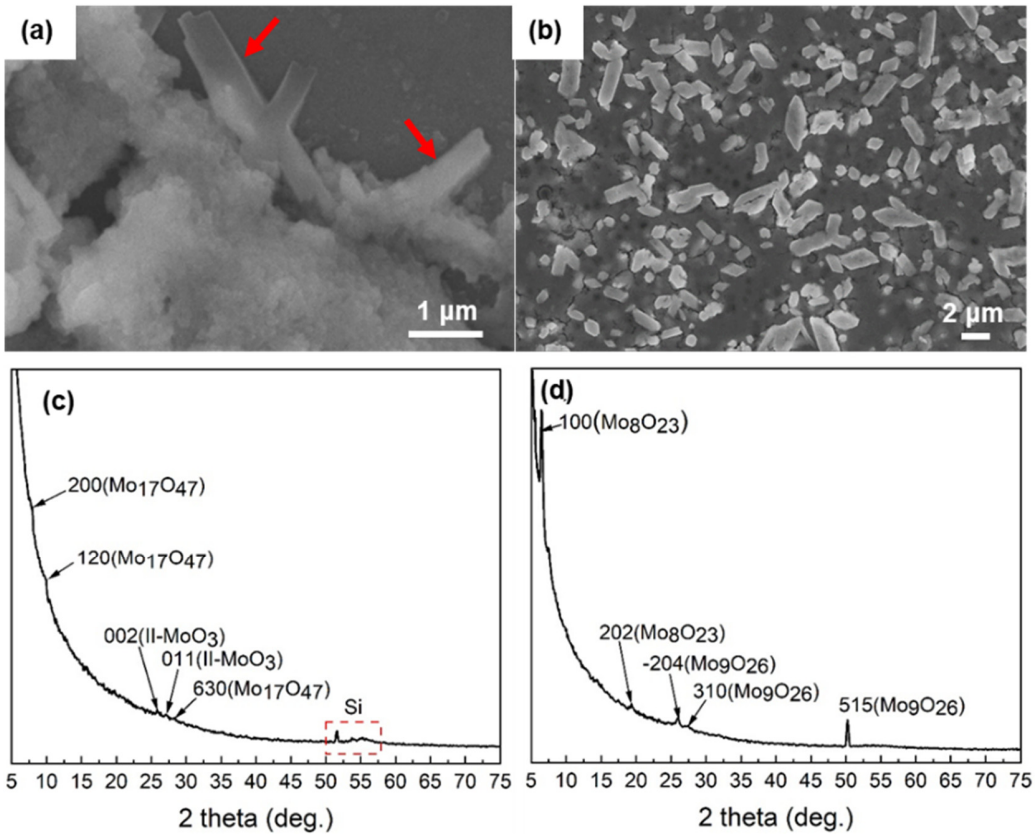


**Figure 4.9.** (a) SEM image and (c) GIXRD pattern of the sample laser-ablated in water for 30 min at 2 W. The nanobelts marked by red arrows are $MoO_3$ nanobelts. (b) SEM image and (d) GIXRD pattern of the sample laser-ablated in 100% ethanol for 30 min at 2 W.[196] Reprinted with permission from Chem. Mater. 2021, 33, 12, 4510-4521. Copyright 2021 American Chemical Society.

**Figure 4.10a** shows the Raman spectra of the samples laser-synthesized in the solvents with different concentrations of ethanol for 30 min (95% ethanol for 10 min). For the sample synthesized in water, the peaks at 123 $cm^{-1}$ and 145 $cm^{-1}$ are assigned to the lattice deformation mode and the peaks at 280 $cm^{-1}$, 816 $cm^{-1}$ and 991 $cm^{-1}$ are assigned to the $B_{2g}$-δ(Mo=O) bending mode, $B_{1g}$-ν($Mo_2$-O) stretching mode and terminal oxygen ($Mo^{6+}$=O) stretching mode of $MoO_3$, respectively.[83,197,199] The peaks at 195 $cm^{-1}$, 220 $cm^{-1}$, 341 $cm^{-1}$, 485 $cm^{-1}$ and 726 $cm^{-1}$ are assigned to the $A_g$-δ($Mo_2$-O), $A_g$-δ($Mo_3$-O), $B_{1g}$-ν($Mo_3$-O) and $B_{3g}$-ν($Mo_3$-O) vibrational modes of substoichiometric molybdenum oxide.[83,85,199] The peak at 564 $cm^{-1}$ is assigned to the $B_{1g}$-ν($Mo_3$-O) stretching mode of $MoO_2$[199] and no peaks of $H_XMoO_3$ are observed. The Raman spectrum is consistent with the GIXRD pattern (**Figure 4.9c**) and is also supported by the XPS spectrum of the sample synthsized in water (**Figure 4.10b**), in which Mo (IV), Mo (V) and Mo (VI) peaks are all observed. In contrast, the samples laser-synthesized in 30%, 70% and 95% ethanol only show Raman peaks assigned to substoichiometric molybdenum oxide (no $MoO_3$ peaks) and one small peak at 123 $cm^{-1}$ assigned to the lattice deformation mode, similar to the sample laser-synthesized in 80% ethanol for 30 min (**Figure 4.4a**). However, the samples in 30% and 70% ethanol don't show LSPR peaks in the normalized absorbance spectra (**Figure 4.8a**). Hence it appears that the quantity of water present in the 30% and 70% ethanol samples prevented the formation of a high concentration of oxygen vacancies, even if it was insufficient to oxidize the $MoO_{3-X}$ to $MoO_3$. A high concentration of oxygen vacancies (X>0.125) and electrons is required for LSPR. LSPR only takes place when the dielectric constant of the nanoparticles ($\varepsilon_{np}$) goes negative and reaches a maximum when $\varepsilon_{np} = -2\varepsilon_m$, where $\varepsilon_m$ is the dielectric constant of surrounding medium.[42] In the Raman spectrum of the sample laser-synthesized in 100% ethanol, the peaks at 290 $cm^{-1}$, 370 $cm^{-1}$ and 826 $cm^{-1}$ are assigned to the $B_{2g}$-δ(Mo=O) and $A_g$-δ(Mo=O) bending modes and the $B_{1g}$-ν($Mo_2$-O) stretching mode of $Mo_9O_{26}$.[207,208] The peak at 136 $cm^{-1}$ is assigned to the lattice deformation mode and the peaks at 195 $cm^{-1}$, 220 $cm^{-1}$, 350 $cm^{-1}$, 485 $cm^{-1}$ and 726 $cm^{-1}$ are again assigned to $MoO_{3-X}$ with higher metallic characteristics.[83,197,199] This is also supported by the XPS spectrum (**Figure 4.10c**) where

high Mo (V) peaks are observed. Notably, Raman peaks belonging to $H_XMoO_3$ are observed at 171 $cm^{-1}$, 267 $cm^{-1}$, 417 $cm^{-1}$, 438 $cm^{-1}$, 778 $cm^{-1}$ and 897 $cm^{-1}$.

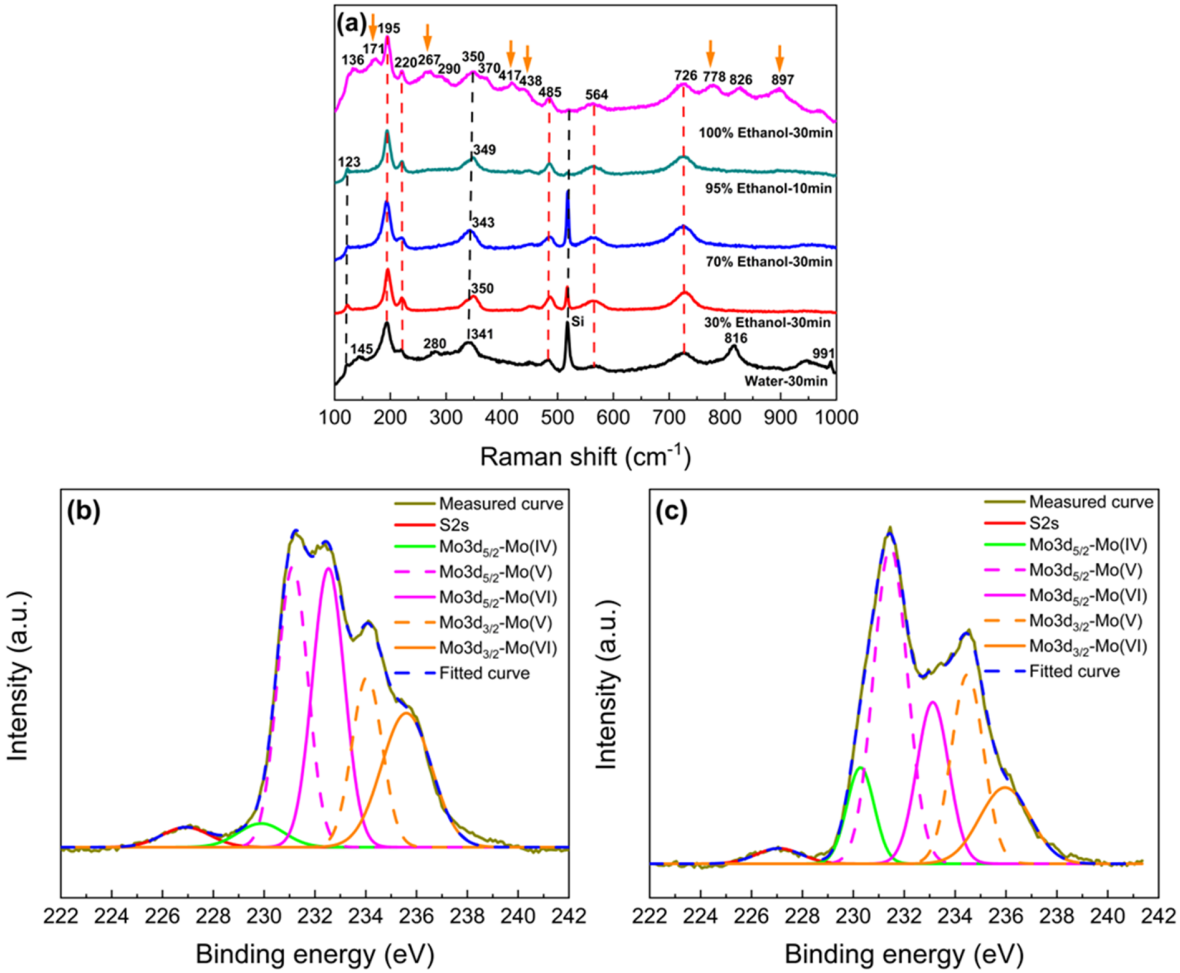


**Figure 4.10.** (a) Raman spectra of samples in pure water, and 30%, 70% and 100% ethanol after laser ablation for 30 min (95% ethanol for 10 min). The peaks marked by orange arrows are assigned to $H_XMoO_3$, the peaks marked by red dashed lines are assigned to $MoO_{3-X}$. XPS spectrum of Mo3d peaks of the sample laser-synthesized in (b) pure water and (c) 100% ethanol.[196] Reprinted with permission from Chem. Mater. 2021, 33, 12, 4510-4521. Copyright 2021 American Chemical Society.

This observation implies another role of water besides providing reactive oxygen ions to oxidize $MoS_2$, as discussed in Section 4.3.1. The water appears to facilitate the release of -$OH_2$ groups from $H_XMoO_3$, likely *via* hydrogen bonding. Compared with water, ethanol molecules have smaller polarities to form hydrogen bonds such that the molybdenum oxide suspended in 100% ethanol takes a longer time to release -$OH_2$ groups. After 30 min of laser ablation of the 100% ethanol sample, many -$OH_2$ groups remained such that fewer oxygen vacancies were formed and no LSPR is observed in **Figure 4.8a**. Hence this analysis suggests that the ethanol content must be >75% and the water content must be >5% (to release -$OH_2$ groups from $H_XMoO_3$) in order to obtain plasmonic $MoO_{3-X}$.

The previous discussion has shown that the plasmonic $MoO_{3-X}$ is formed by releasing -$OH_2$ groups from $H_XMoO_3$. Therefore, it is important to understand the formation of Mo-$OH_2$ bonds. Both water and ethanol can generate substantial amounts of $H^+$ under ultrafast laser irradiation.[139,202,203] However, laser ablation of $MoS_2$ for 10 min in water doesn't show any $H_XMoO_3$ Raman peaks, suggesting that $H^+$ is probably not the primary hydrogen source to create Mo-$OH_2$ bonds in this case. Previous studies have found that femtosecond laser ablation of ethanol will generate a trihydrogen cation ($H_3^+$), which is an initiator for a series of chemical reactions.[141,143,209] Jackson and co-workers concluded that $H_3^+$ is formed from ethanol through a primary pathway that involves a roaming $H_2$ molecule that abstracts a proton from the methyl carbon or hydroxyl oxygen.[143] The roaming $H_2$ molecule is dissociated from a doubly ionized ethanol molecule when the C-H bonds are elongated, and the H-C-H bond angle is narrowed. The hydrogen in the roaming $H_2$ molecule can come from the carbon next to the hydroxyl group or from the terminal methyl carbon by hydrogen migration.[143,209] Another low yield pathway to form $H_3^+$ is that all the three hydrogen atoms come from the terminal methyl group. Therefore, the hydrogen atoms in the Mo-$OH_2$ bonds may predominantly come from the creation of $H_3^+$ ions during femtosecond laser irradiation of the ethanol, consistent with the previous observation that an ethanol concentration >75% is necessary to create sufficient oxygen vacancies and generate LSPR (**Figure 4.8a**). The proposed process is illustrated in **Figure 4.11**. **Figure 4.11a** illustrates the generation of $H_3^+$

from ethanol and **Figure 4.11b** shows the formation of $H_XMoO_3$ from $MoS_2$ and subsequent water-mediated removal of $-OH_2$ groups to generate oxygen vacancies. The proposed process would explain why the sample in 95% ethanol produced plasmonic $MoO_{3-X}$ more quickly, as noted earlier. The high concentration of ethanol would facilitate faster formation of $H_3^+$ and $H_XMoO_3$ to generate oxygen vacancies.

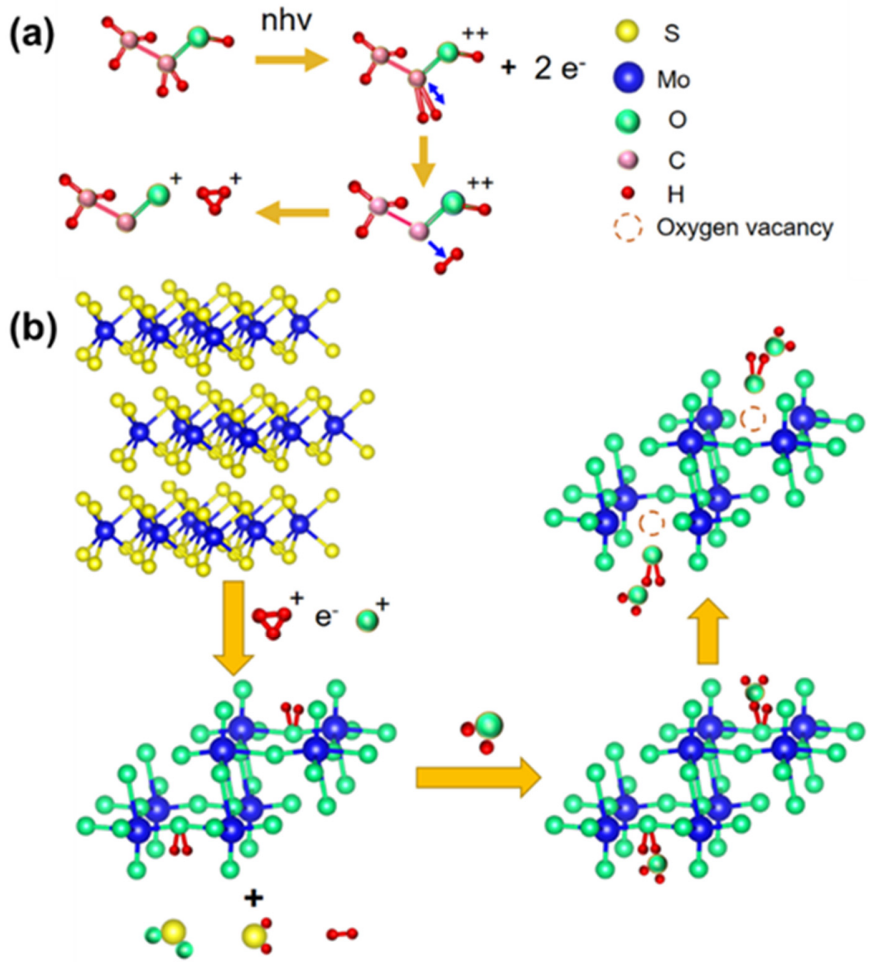


**Figure 4.11.** (a) Schematic illustration of one primary pathway to produce $H_3^+$ ions from ethanol. (b) Schematic illustration of the proposed $MoS_2$ oxidation process and how oxygen vacancies are created.[196] Reprinted with permission from Chem. Mater. 2021, 33, 12, 4510-4521. Copyright 2021 American Chemical Society.

To verify the proposed process, different organic solvents including methanol, 1-propanol, IPA and acetone were tested to obtain plasmonic $MoO_{3-X}$. Among these solvents, methanol was reported to have the highest yield of $H_3^+$, while acetone has the lowest yield as it only has one pathway to create $H_3^+$, due to its lack of a hydroxyl group.[139,142,143] The Raman spectra for the samples laser-synthesized in the different solvents for 10 min and 30 min are shown in **Figure 4.12a** and **4.12b**, respectively. It is seen that the 80% methanol, 80% IPA and 80% 1-propanol samples all show $H_XMoO_3$ peaks (identified with orange arrows in **Figure 4.12a**) after 10 min of laser ablation, whereas the sample in 80% acetone only shows $MoO_{3-X}$ and $MoO_2$ peaks at 196 $cm^{-1}$, 221 $cm^{-1}$, 349 $cm^{-1}$, 454 $cm^{-1}$, 487 $cm^{-1}$, 565 $cm^{-1}$ and 730 $cm^{-1}$.[83,199,208] The samples in water and 80% methanol also show four $MoO_3$ peaks at 282 $cm^{-1}$, 336 $cm^{-1}$, 817 $cm^{-1}$ and 991 $cm^{-1}$.[83,199,208] Additionally, the peak at 817 $cm^{-1}$ corresponding to the $B_{1g}$-ν($Mo_2$-O) stretching mode shifts to 825 $cm^{-1}$ and 839 $cm^{-1}$ for the 80% IPA and 80% 1-propanol samples, respectively. This may suggest a minor change of Mo-O-Mo bond length due to intercalation of hydrogen atoms. After 30 min of laser ablation, the $H_XMoO_3$ peaks disappear and only $MoO_{3-X}$ peaks are observed in the 80% methanol and 80% IPA samples. In the 80% 1-proponal sample, $MoO_3$ peaks at 661 $cm^{-1}$ and 817 $cm^{-1}$ show up together with $MoO_{3-X}$ peaks. The 80% acetone sample shows sharp $MoO_3$ peaks at 234 $cm^{-1}$, 277 $cm^{-1}$, 332 $cm^{-1}$, 373 $cm^{-1}$, 661 $cm^{-1}$, 817 $cm^{-1}$ and 990 $cm^{-1}$, and two small $MoO_{3-X}$ peaks at 193 $cm^{-1}$ and 208 $cm^{-1}$.[83,199] Another three peaks at 108 $cm^{-1}$, 120 $cm^{-1}$ and 145 $cm^{-1}$ are assigned to the lattice deformation mode.[198,199] Hence the Raman spectra suggest that methanol, IPA, and 1-propanol, like ethanol, could produce $H_3^+$ during femtosecond laser irradiation and facilitated the formation of $H_XMoO_3$ which is a critical intermediate product during the transformation of $MoS_2$ to plasmonic $MoO_{3-X}$. In contrast, no $H_XMoO_3$ was detected when acetone was used and the $MoS_2$ was almost completely oxidized to $MoO_3$ after 30 min of laser ablation.

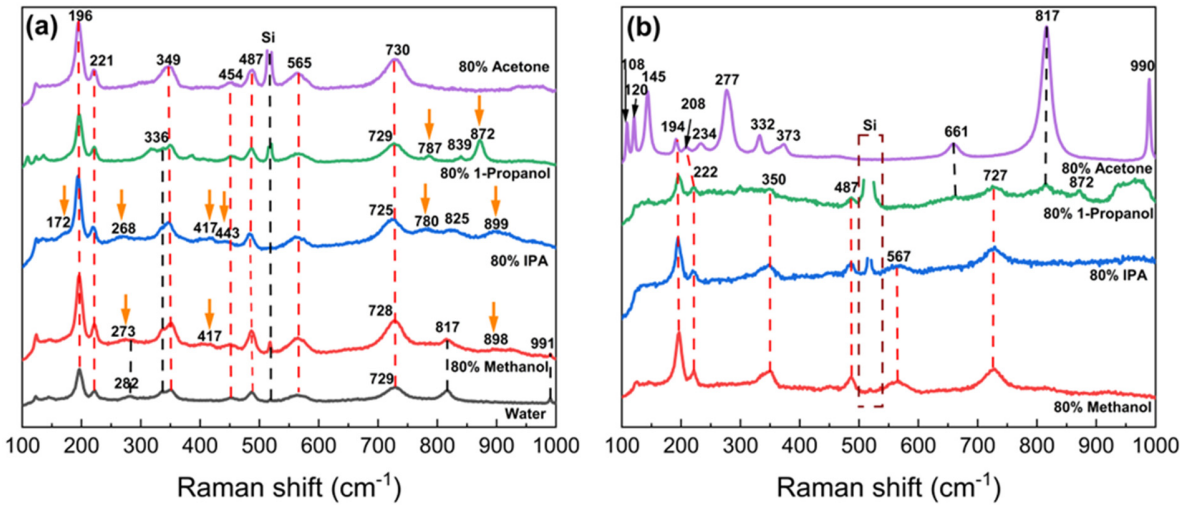


**Figure 4.12.** Raman spectra of (a) samples in water, 80% methanol, 80% IPA, 80% 1-proponal and 80% acetone after laser ablation for 10 min; and (b) the samples in 80% methanol, 80% IPA, 80% 1-proponal and 80% acetone after laser ablation for 30 min. The peaks marked by orange arrows are assigned to $H_XMoO_3$, the peaks marked by red dashed lines are assigned to $MoO_{3-X}$.[196] Reprinted with permission from Chem. Mater. 2021, 33, 12, 4510-4521. Copyright 2021 American Chemical Society.

**Figure 4.13** shows the normalized absorbance spectra for the samples laser-synthesized in the different solvents. The 80% acetone sample shows no LSPR peaks after 30 min of laser ablation, and its solution turns transparent, consistent with the formation of $MoO_3$. The 80% methanol, 80% IPA and 80% 1-propanol samples all show the LSPR peaks. One surprising observation is that the 80% methanol sample only shows one small, broad LSPR peak at around 665 nm after 30 min of laser ablation, however the intensity of its LSPR peaks does increase after 50 min of laser ablation. We expected it would form plasmonic $MoO_{3-X}$ more quickly as it was reported to have the highest $H_3^+$ yield. Considering that oxidation and hydrogen intercalation are competitive processes during laser ablation, the reactive $H_3^+$ ions may preferably react with $O^+$ and $O^{2+}$ ions in methanol and delay the oxidation process.

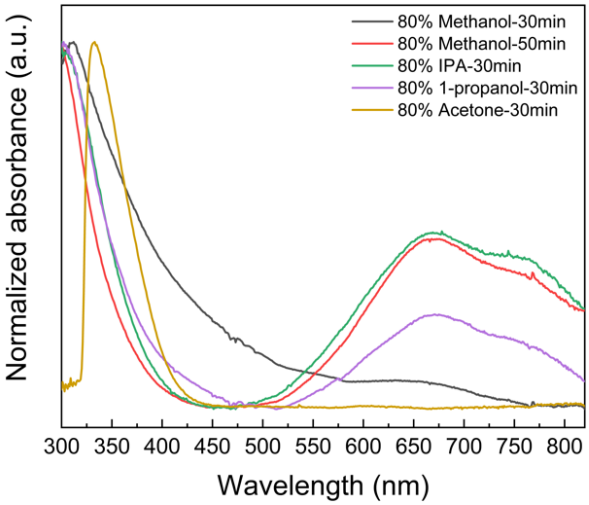


**Figure 4.13.** Normalized absorbance spectra of samples in 80% methanol, 80% IPA, 80% 1-propanol, 80% acetone after laser ablation for 30 min and the sample in 80% methanol after laser ablation for 50 min.[196] Reprinted with permission from Chem. Mater. 2021, 33, 12, 4510-4521. Copyright 2021 American Chemical Society.

### 4.3.3 Photothermal Conversion Performance of the Fabricated $MoO_{3-X}$.

Photothermal measurements at 808 nm were performed on the samples laser-synthesized in 80% ethanol for different ablation times and are plotted in **Figure 4.14a**. It is shown that the temperature only increases by 5 °C in 10 min for the original $MoS_2$ particles. The temperature change increases with the laser ablation time until reaching a maximum at 25-30 min where the temperature change is close to 16 °C. Then the temperature change drops for longer laser ablation times. After 50 min of laser ablation, the temperature change is only about 0.5 °C due to the formation of stoichiometric $MoO_3$. Photothermal measurements for the samples laser-synthesized in different concentrations of ethanol are shown in **Figure 4.14b**. The temperature change is low for the samples in pure water and pure ethanol, only 2.3 °C and 3.1 °C, respectively. The temperature change increases with the concentration of ethanol and reaches a maximum of 18.8 °C for 90% ethanol. This behavior is in agreement with the LSPR peak intensities shown in **Figure 4.8a**.

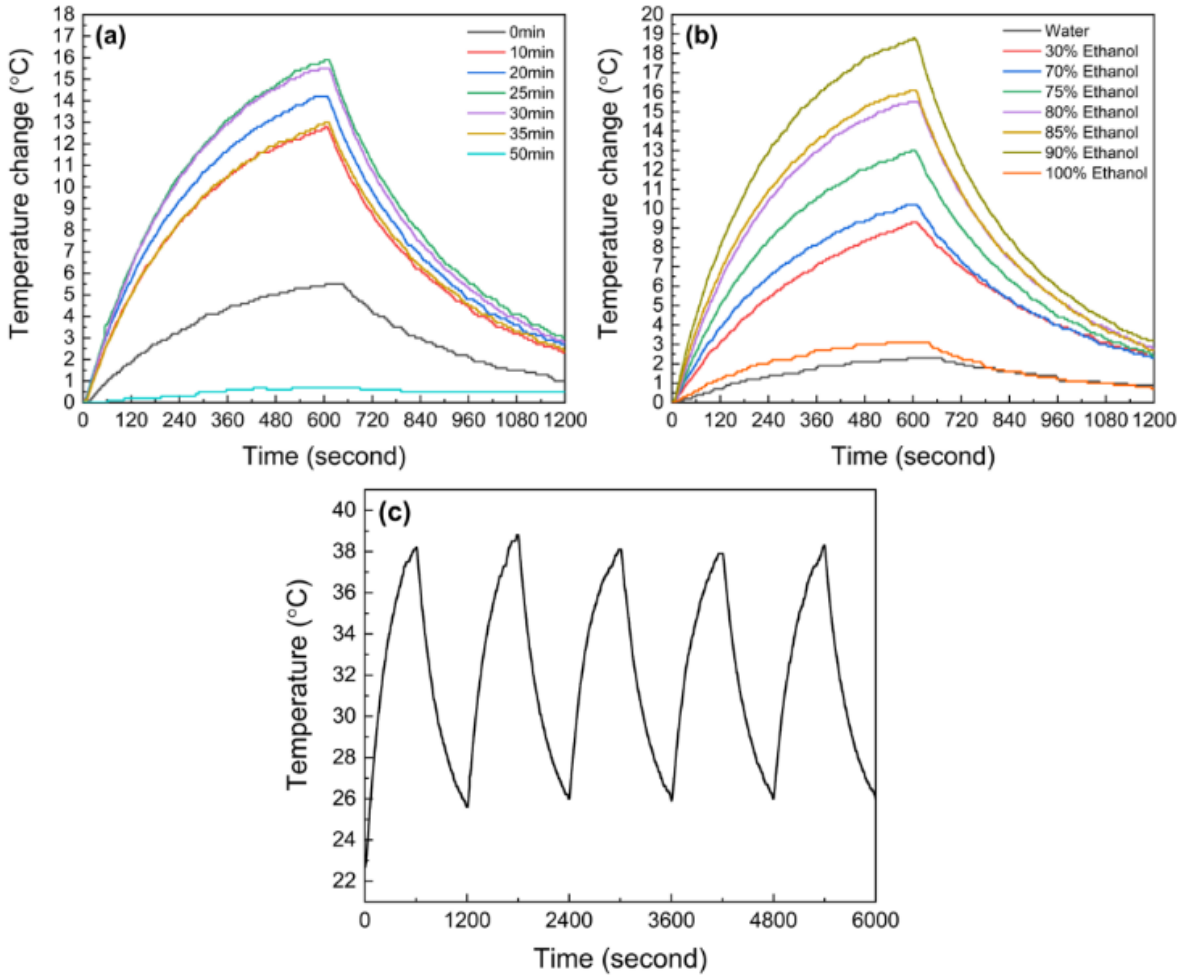


**Figure 4.14.** Temperature change curves under laser illumination (10 min on/10 min off). (a) Samples prepared by laser ablation for various times in 80% ethanol. (b) Samples prepared by laser ablation for 30 min in solvents with various ethanol concentrations in water. (c) 80% ethanol sample prepared by laser ablation for 30 min experiencing 5 illumination/cooling cycles. The concentration of molybdenum oxide in all the samples was 0.78 mM.[196] Reprinted with permission from Chem. Mater. 2021, 33, 12, 4510-4521. Copyright 2021 American Chemical Society.

The size distribution for the $MoO_{3-X}$ produced in 90% ethanol was measured by dynamic light scattering (DLS) and is presented in **Figure 4.15**. The average hydrodynamic size of the nanoparticles is 90.5 nm and the polydispersity index (PDI) is 0.152. Particle distributions

with a PDI of 0 - 0.1 are generally considered as monodisperse, while distributions with PDI between 0.1 and 0.4 are considered as polydisperse. A PDI of 0.152 suggests a small amount of polydispersity; however, the results also indicate the samples had good dispersibility and stability. Additionally, no sediment was observed at room temperature. Five illumination cycles of the sample prepared by laser ablation for 30 min in 80% ethanol are presented in **Figure 4.14c** and consistent heating and cooling behavior is observed over 100 min, indicating a good thermal stability. The PTCEs of the 80% ethanol and 90% ethanol samples are listed in **Table 4.1**. The highest PTCE is obtained in the 80% ethanol sample after 30 min of laser ablation, which is 33 ±2%. This lies in the range of 25% - 41% of some previous reports where $MoO_{3-X}$ was prepared by hydrothermal methods.[12,86,210,211]

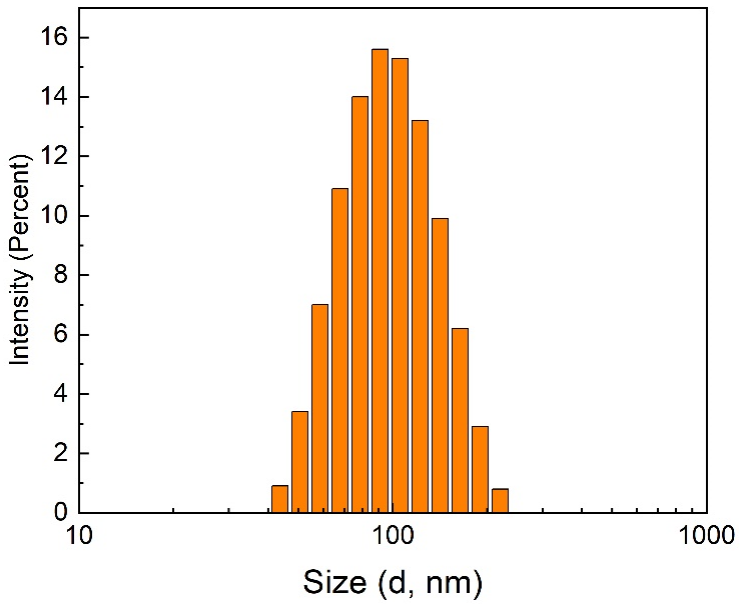


**Figure 4.15.** Size distribution of $MoO_{3-X}$ nanosheets laser-synthesized in 90% ethanol measured by DLS. The average hydrodynamic size is 90.5 nm and the polydispersity index is 0.152.[196] Reprinted with permission from Chem. Mater. 2021, 33, 12, 4510-4521. Copyright 2021 American Chemical Society.

**Table 4.1.** PTCEs of several $MoO_{3-X}$ samples synthesized in solvents of 80% and 90% ethanol with various laser ablation times.[196] Reprinted with permission from Chem. Mater. 2021, 33, 12, 4510-4521. Copyright 2021 American Chemical Society.

| Ethanol concentration | Laser ablation time | PTCE |
|---|---|---|
| 80% | 10 min | 29% |
| 80% | 20 min | 30% |
| 80% | 25 min | 31% |
| 80% | 30 min | 33% |
| 80% | 35 min | 31% |
| 90% | 30 min | 32% |

## 4.4 Conclusions

Plasmonic $MoO_{3-X}$ nanosheets were synthesized by oxidizing $MoS_2$ in ethanol/water under femtosecond laser ablation. Compared with conventional hydrothermal methods that need high temperatures or pressures, the femtosecond laser can break the chemical bonds at room temperature and the application of ethanol and water as oxidants makes this novel synthesis process environment friendly. It was found that the synthesis of plasmonic $MoO_{3-X}$ was highly dependent on the concentration of ethanol and the optimum concentration was between 80-90%. This was attributed to the formation of $H_3^+$ ions when the ethanol was irradiated under the femtosecond laser. $H_3^+$ may react with oxidized $MoS_2$ to form $-OH_2$ groups and the release of the $-OH_2$ groups can create oxygen vacancies in the molybdenum oxide structure. A sufficient quantity of water in the solvent (>5%) was found to be necessary to facilitate the release of the $-OH_2$ groups. Other alcohols that were reported to create high concentrations of $H_3^+$ under femtosecond laser irradiation were also verified to successfully synthesize plasmonic $MoO_{3-X}$. The photothermal conversion behavior of the synthesized plasmonic $MoO_{3-X}$ nanosheets at 808 nm was evaluated. The highest temperature increase (18.8 °C) was achieved by the $MoO_{3-X}$ synthesized in 90% ethanol and the highest PTCE

(33 ±2%) was obtained by the $MoO_{3-X}$ nanosheets synthesized in 80% ethanol due to a lower absorbance.

# Chapter 5
# Synthesis of Molybdenum Blue Nanorings by Femtosecond Laser Ablation

## 5.1 Introduction

Molybdenum blues (MBs) refer to blue molybdenum polyoxometalates (POMs), which have strong absorption of light with wavelengths of 600 - 1100 nm due to delocalized electrons and intervalence charge transfer caused by partial reduction of molybdenum, as described in Section 2.1.3. One special structure of molybdenum POMs is giant nanoclusters with more than 100 Mo atoms. These nanoclusters can further self-assemble into bigger super-structures.[49,98] Most giant molybdenum-POM nanoclusters have ring structures such as $Mo_{176}$,[212] $Mo_{154\text{-}x}$,[98,213–215] etc., while others have spherical structures such as $Mo_{102}$,[216] $Mo_{132}$,[217] etc., cage structures such as $Mo_{240}$[217] and $Mo_{248}$,[218] and lemon structures such as $Mo_{368}$.[219] It was reported that the color of molybdenum-POM nanoclusters depends on the $Mo^{V}/Mo^{VI}$ ratio. When the ratio is approximately 0.3 or lower, the molybdenum POMs (all the MB nanorings and $Mo_{102}$, $Mo_{248}$, etc.) are blue. When the ratio approaches 0.45, the color turns brown ($Mo_{132}$). When the ratio increases to 0.75, the color changes to red ($Mo_{240}$).[49]

MB nanorings are usually prepared by thermal reduction methods, as described in Section 2.3. However, these preparation methods require either heating or long-term aging, and sometimes introduce impurities from the chemicals used. In this work, a femtosecond laser is used to ablate $MoO_3$ in water/ethanol solvents to synthesize MB nanorings. The dissolution of $MoO_3$ in water during femtosecond laser ablation provides an acidic environment for the formation of MBs. Various concentrations of ethanol in water are tested, and it is found that as low as 1 vol.% of ethanol in water can lead to the formation of MBs under femtosecond laser ablation. The absorption band of the MBs can be tuned by changing the concentration of ethanol in the solvent. The darkest blue solution is achieved in 30 vol.% ethanol after 15 min of laser ablation. The photoluminescence spectra and photothermal conversion performance of the laser-synthesized MBs are also examined. Compared with

other synthesis methods, this novel method is highly efficient; almost all the $MoO_3$ is converted to MBs in 15 min. It is convenient to operate with no heating requirement. Moreover, as only water, ethanol and $MoO_3$ are used, this method can mitigate impurities from the starting materials.

## 5.2 Experimental Methods

### 5.2.1 Synthesis of Molybdenum Blue

$MoO_3$ powder (≥99.5%, Sigma-Aldrich) was dispersed in different solvents including pure deionized water, pure ethanol, 1 vol.%, 10 vol.%, 30 vol.%, 50 vol.%, 70 vol.% and 90 vol.% ethanol in water. The concentration of $MoO_3$ was kept at 3.5 mM. After 15 min of ultrasonication to break agglomerates, 4 mL of each sample was transferred into a small vial for laser ablation. The small vial was placed on a magnetic stirrer plate and irradiated by a focused femtosecond laser beam as described in Section 3.2.1. The average power of the incident laser was fixed as 2 W. The suspension was stirred at 300 rpm during laser irradiation.

### 5.2.2 Characterization of Nanomaterials

After laser ablation, the nanomaterials were drop-casted on silicon wafers for characterization. The bonding states of the nanomaterials were analyzed with a Renishaw micro-Raman spectrometer (laser wavelength of 632 nm) and a Bruker Tensor 27 FTIR spectrometer with attenuated total reflection (ATR) mode. The phases of the nanomaterials were identified by GIXRD using a PANalytical X'Pert Pro MRD diffractometer with Cu Kα radiation. The MB-nanoring morphologies were observed *via* the high-angle annular dark-field (HAADF) mode of a FEI Titan 80-300 LB transmission electron microscope (TEM/STEM). XPS spectra of the nanomaterials were obtained using a Thermo VG Scientific ESCALab 250 microprobe with Monochromatic Al Kα excitation (1486.6 eV). The thermogravimetric analysis (TGA) curves of the MB nanomaterials after freeze drying were recorded using a TA Instruments TGA Q500 with a ramp rate of 10 °C/min. The UV-vis absorbance spectra and the photoluminescence excitation and emission spectra of the

nanomaterials were measured using a Horiba QuantaMaster 8000 spectrometer. The X-ray absorption spectra of the nanomaterials were measured using the BioXAS beamline of the Canadian Light Source and the Fourier-transformed extended X-ray absorption fine structure (FT-EXAFS) of the nanomaterials was analyzed using Athena and Artemis software. The size of self-assembled MB vesicles was measured at room temperature by dynamic light scattering (DLS) using a Malvern Zetasizer Ultra instrument (Malvern Panalytical, UK). The vesicle size distribution was obtained from the light scattered by vesicles that were illuminated with a laser beam (at a scattering angle of 173°). The measured sizes were reported using an intensity distribution and the reported data was averaged over five replicates. The pH values of the solutions after laser ablation were measured using an Accumet Basic AB15 pH meter. The PTCEs of the MBs were evaluated with an 808 nm continuous-wave laser using a custom-built setup, as described in Section 3.2.1. The calculation of the PTCE of the MB samples is detailed in Section 3.2.2.

## 5.3 Results and Discussion

### 5.3.1 Structural Characterization

Characterization of MB is challenging, especially determination of the chemical formula. High-angle annular dark-field (HAADF) imaging has been demonstrated to be a useful method to directly observe the morphology of MBs.[97] Therefore, a scanning transmission electron microscope (STEM) with HAADF mode was applied to successfully capture the shape of the MB synthesized in the 30% ethanol solvent after 15 min of laser ablation. In **Figure 5.1a**, ring-structured MB can be observed with an outer diameter of 3.5 nm and an inner diameter of 1.7 nm, which is consistent with the size of {$Mo_{154}$}-based nanorings.[97] The {$Mo_{154}$} nanoring is made of fourteen {$Mo_8$} units (blue moieties in **Figure 5.1d**), fourteen {$Mo_2$} linkers (red moieties in **Figure 5.1d**) that link the {$Mo_8$} repeating units, and fourteen {$Mo_1$} (yellow moieties in **Figure 5.1d**) that are inside the ring. The defects of {$Mo_2$} or {$Mo_1$} contribute to the formation of {$Mo_{154-X}$}, including {$Mo_{150}$},[95,220] {$Mo_{142}$},[214] {$Mo_{138}$},[221] etc. The formation of {$Mo_{154-X}$} derivatives is sensitive to the pH

value of the solution. The pH values of the 1%-ethanol and 30%-ethanol samples after laser ablation were 3.06 and 2.68 respectively, higher than the pH value of 1.5 that is required to generate {$Mo_{154}$}, but located in the pH range of {$Mo_{142}$} (2.5-3.3),[92] suggesting the MBs prepared in the 1% and 30% ethanol samples were probably {$Mo_{142}$}. {$Mo_{142}$} is the derivative of {$Mo_{154}$} with six missing {$Mo_2$} moieties, as indicated in **Figure 5.1d**, and it has 28 reduced $Mo^{V}$ and 114 $Mo^{VI}$.

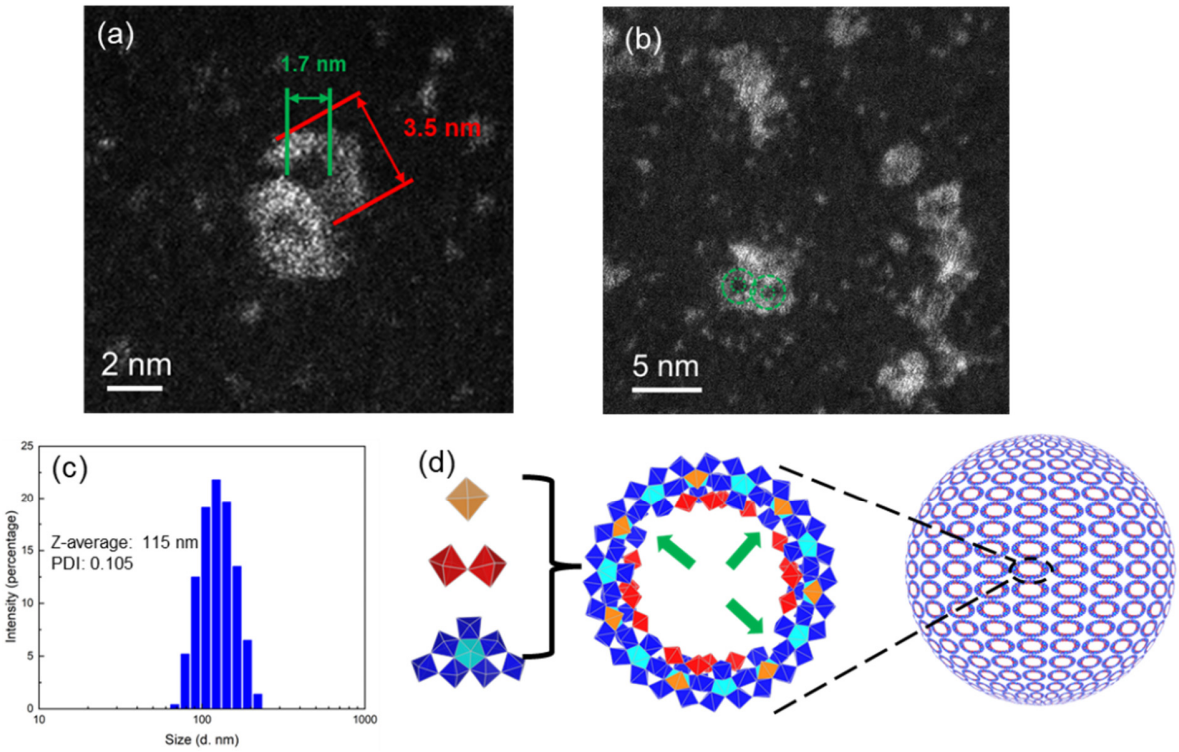


**Figure 5.1.** (a and b) STEM-HAADF images of {$Mo_{154-x}$} nanorings synthesized by laser ablation of $MoO_3$ in 30% ethanol for 15 min. (c) Size distribution of self-assembled vesicles in 30% ethanol measured by DLS. (d) Schematic illustration of the formation of {$Mo_{142}$} nanorings and self-assembled vesicles. The {$Mo_{154-x}$} nanoring is formed from {$Mo_1$} (yellow), {$Mo_2$} (red) and {$Mo_8$} (blue). The vesicle is self-assembled from {$Mo_{154-x}$} nanorings.[25]

The STEM-HAADF image (**Figure 5.1b**) also shows that the MB nanorings are prone to connect to each other to form larger superstructures. This is supported by DLS measurements, which detected self-assembled vesicles with an average size of 115 nm and polydispersity index of 0.105 (**Figure 5.1c**). This is consistent with {$Mo_{154}$} and its derivatives that were reported to self-assemble into big vesicles with sizes of around 100 nm.[52,98,222] The TGA curve (**Figure 5.2a**) shows a total weight loss of 18.21% when the MB sample was heated to 500 °C. The weight loss before 400°C is attributable to loss of water since {$Mo_{154}$} derivatives contain a lot of water in their structures,[94,213] while the abrupt weight loss at around 400°C is probably caused by decomposition of Mo-OH groups, which is usually observed in the dehydrogenation process of $H_XMoO_3$.[223] The FTIR spectrum of the sample irradiated in 30% ethanol (**Figure 5.2b**) also verifies the presence of water and hydroxyl groups. Two peaks at 1633 and 3446 $cm^{-1}$ belong to attached water, and two peaks at 1454 and 2928 $cm^{-1}$ are assigned to hydroxyl groups. Additionally, the peaks at 977, 756, and 619 $cm^{-1}$ are assigned to Mo-$O_t$ (terminal oxygen), Mo-$O_b$ (bridging oxygen) and $O_b$-Mo-$O_t$ vibrations of MB, respectively.[224]

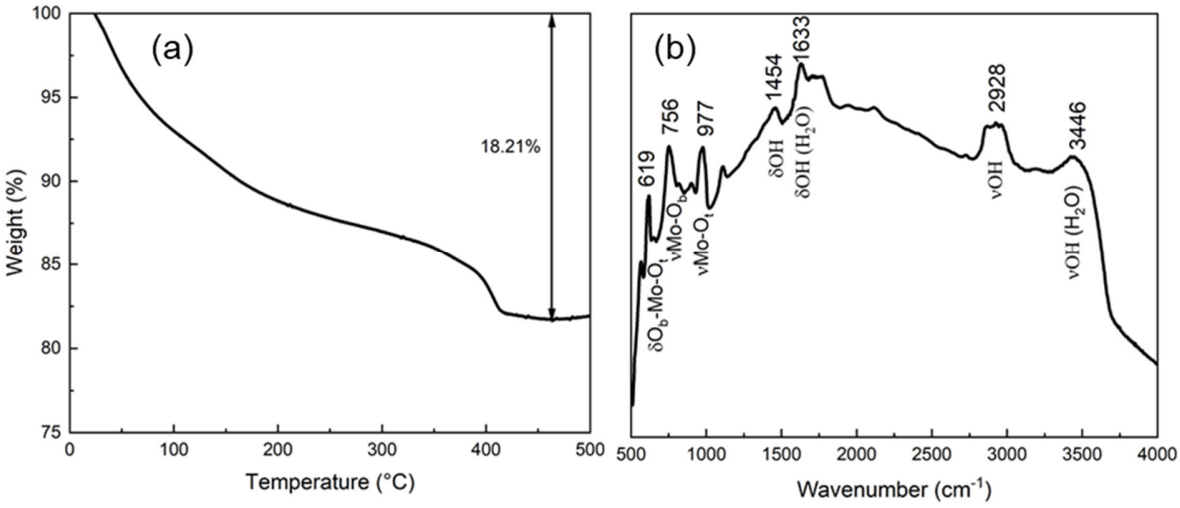


**Figure 5.2.** (a) TGA curve and (b) ATR-FTIR spectrum of the MB sample prepared in 30% ethanol after 15 min of laser irradiation.[25]

### 5.3.2 Role of Water and Ethanol

To examine the role of water and ethanol in the formation of MB, $MoO_3$ mixtures with different concentrations of ethanol were irradiated with the femtosecond laser for 15 min. As shown in **Figure 5.3a**, the samples prepared in pure water and pure ethanol were clear after 15 min of laser ablation, implying both ethanol and water are necessary for the preparation of MB. **Figure 5.3c** shows the XRD patterns of orginial $MoO_3$ and nanomaterials prepared in pure water and other aqeuous solvents containing different concentrations of ethanol. The original $MoO_3$ shows (001), $(10\bar{1})$, (002), (011), (102), $(10\bar{3})$, (013) and (020) $MoO_3$ peaks at 12.72°, 23.42°, 25.76°, 27.32°, 38.91°, 39.69°, 46.38° and 49.28°, respectively (PDF#:47-1320). It is interesting to notice that the XRD pattern reveals that the sample prepared in water is $MoO_3 \cdot H_2O$ with (010), (020), (011), (210), $(0\bar{1}1)$, (220), $(\bar{1}\bar{2}1)$ and (002) peaks of $MoO_3 \cdot H_2O$ at 12.72°, 25.54°, 26.98°, 28.10°, 29.88°, 31.34°, 33.90° and 50.73° respectively (PDF#: 26-1449), implying that molybdic acid was created when laser ablating $MoO_3$ in water, which provided the acidic environment necessary for the formation of MB. The XRD patterns of the other samples only show small, broad peaks between 20° and 35°, suggesting low crystallinity of the drop-casted samples. Though the sample prepared in 30% ethanol appeared darkest blue, it was found that as low as 1% ethanol could facilitate the formation of MB under femtosecond laser irradiation. Both the 1% and 10% ethanol samples show a primary absorption band at around 750-800 nm and a shoulder band at around 550-650 nm (**Figure 5.3b**), consistent with other $\{Mo_{154}\}$ cluster derivatives.[53,95,225] However, the absorption bands of the 30% ethanol sample merge to one centered at 690 nm. As MB's absorption of NIR light results from intervalence charge transfer of $Mo^{V}$-O-$Mo^{VI}$ entities,[97,226] the change in absorption is probably caused by a change of the $Mo^{V}/Mo^{VI}$ ratio in the MB resulting from the modification of $Mo^{V}$-O-$Mo^{VI}$ bonds, such as deficiencies of oxygen and breakage of the bonds.[97] The broad absorption band gradually drops with increasing concentrations of ethanol. When the concentration of ethanol is high (70% and 90%), the absorption band slightly shifts to 675 nm. This shift is probably caused by the

formation of $H_XMoO_3$ or $MoO_{3-X}$ at higher concentrations of ethanol. The work introduced in Chapter 4 also observed the absorption band at 675 nm in $MoO_{3-X}$ samples.[196]

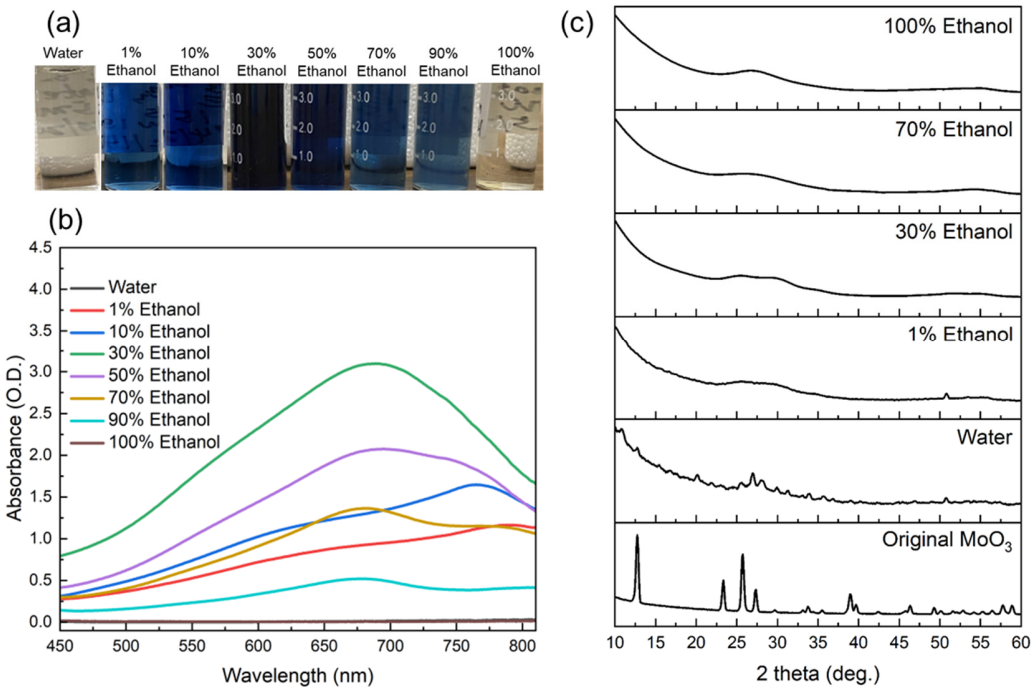


**Figure 5.3.** (a) Photos, (b) UV-vis absorbance spectra and (c) XRD patterns of samples prepared in solvents with various concentrations of ethanol after 15 min of laser ablation.[25]

The formation of $H_XMoO_3$ and $MoO_{3-X}$ in the samples with high concentrations of ethanol was confirmed by Raman analysis (**Figure 5.4**). Since the Raman spectra of $\{Mo_{154}\}$ derivatives are the same as the spectrum of $MoO_3$,[91,95,227] it is difficult to distinguish MB from $MoO_3$; the MB sample prepared in 1% ethanol has the same Raman spectrum as the $MoO_3 \cdot H_2O$ sample prepared in pure water, though the absorption spectra of two samples are different. However, Raman spectroscopy is still a powerful tool to identify $H_XMoO_3$ and $MoO_{3-X}$.[83,196,228] When the concentration of ethanol increases, the peaks assigned to $H_XMoO_3$ at 892, 778, 420, 437 and 170 $cm^{-1}$ appear while the peaks at 991 and 816 $cm^{-1}$ that belong to MB decrease.[83,95,196,227,229] Noticeably, when the concentration of ethanol is higher than 50%, the MB peaks at 991 and 816 $cm^{-1}$ disappear and the peaks assigned to $H_XMoO_3$ decrease,

whereas the peaks at 197, 222, 349, 484, 566 and 725 $cm^{-1}$ that are attributed to $MoO_{3-X}$ increase.[83,196] When the concentration of ethanol is 90%, the $MoO_{3-X}$ peaks become dominant in the Raman spectrum, consistent with the work introduced in Chapter 4 that 80-90% ethanol is optimum to prepare $MoO_{3-X}$ from $MoS_2$ *via* femtosecond laser ablation.[196] In the 100% ethanol sample, almost all the Raman peaks belong to $MoO_3$.

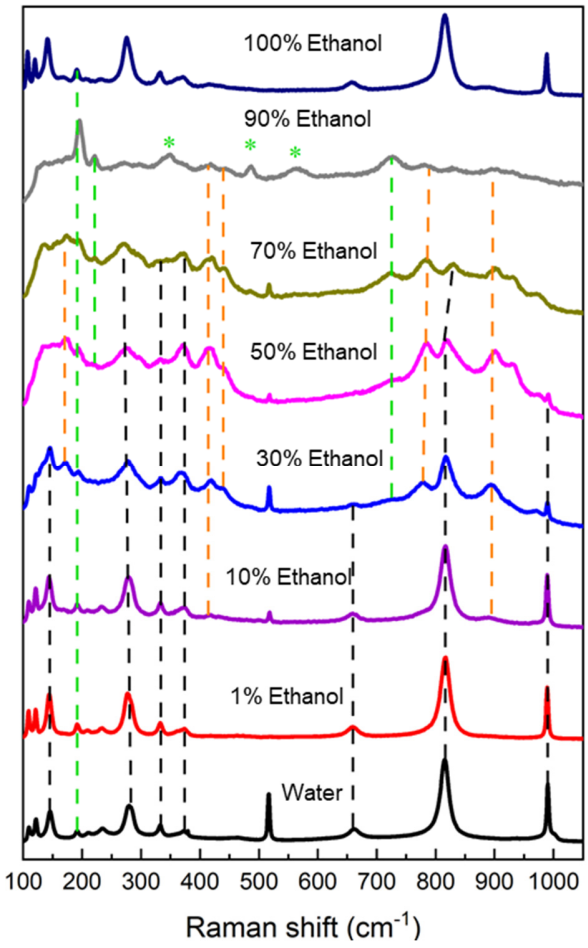


**Figure 5.4.** Raman spectra of samples prepared in solvents with various concentrations of ethanol after 15 min of laser ablation. The peaks marked by black dashed lines are assigned to either $MoO_3$ or MBs. The peaks marked by orange dashed lines are assigned to $H_XMoO_3$. The peaks marked by green dashed lines and green asterisks are assigned to $MoO_{3-X}$. The peak at around 520 $cm^{-1}$ is the silicon substrate peak for the drop-casted samples.[25]

The photoluminescence exitation and emission spectra of the MBs synthesized in 1% and 30% ethanol solvents were also investigated. As **Figure 5.5** shows, both MBs have the same excitation band at 315 nm and emission band at 375 nm, though their UV-vis absorbance spectra are slightly different. The photoexcitation bands in the UV spectral range usually originate from oxygen-to-metal (O→M) ligand-to-metal charge transfer (LMCT) for POMs, and the Stokes shift of the emission band could be attributed to triplet states of the LMCT.[230]

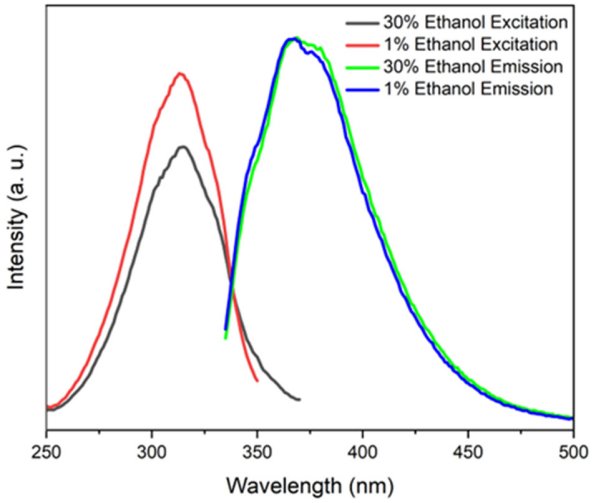


**Figure 5.5.** Photoluminescence excitation and emission spectra of MBs synthesized in 1% and 30% ethanol solvents after 15 min of laser ablation.[25]

As Raman spectroscopy cannot differentiate MB and $MoO_3$, X-ray absorption spectroscopy was used to analyze structural differences. Fitting of the original $MoO_3$ and the 70%-ethanol sample was conducted based on the α-$MoO_3$ model (**Figure 5.6a**). Fitting of the 1%-ethanol and 30%-ethanol samples was difficult because a model describing the exact positions of each atom was lacking. These fittings were conducted using {$Mo_{154-x}$}-based structures from Tomoji's work.[92] As some positions of Mo and O atoms are partially occupied, the model was modified based on their average positions. As {$Mo_8$} moieties are the major component of {$Mo_{154-x}$} nanorings, the EXAFS peaks are largely contributed by the pentagonal Mo structure in the {$Mo_8$} moiety (**Figure 5.6b)**. The fitted interatomic distances and coordination numbers of the samples are listed in **Table 5.1** and **5.2.**

The FT-EXAFS spectrum (**Figure 5.6c**) of the original $MoO_3$ has two principal Mo-O shells peaked at 1.23 and 1.63 Å and one Mo-Mo shell peaked at 3.18 Å. The FT-EXAFS spectra of the MB samples prepared in 1% and 30% ethanol are similar, which have two Mo-O shells peaked at 1.10 and 1.63 Å and one Mo-Mo shell peaked at 3.01 Å. Compared with the 1%-ethanol sample, the shorter and broader Mo-Mo shell in the 30%-ethanol sample might be affected by the breakage of $Mo^{V}$-O-$Mo^{VI}$ bonds, and the fitted coordination number of oxygen in the 30%-ethanol is also smaller than that of 1%-ethanol sample (**Table 5.2**). In the 70%-ethanol sample, the first Mo-O shell and Mo-Mo shell shift to 1.05 and 2.90 Å respectively, and the coordination number of the doubly bonded O (Mo-$O_2$) is 0.79 (**Table 5.1**), probably caused by the oxygen vacancies in $MoO_{3-X}$.

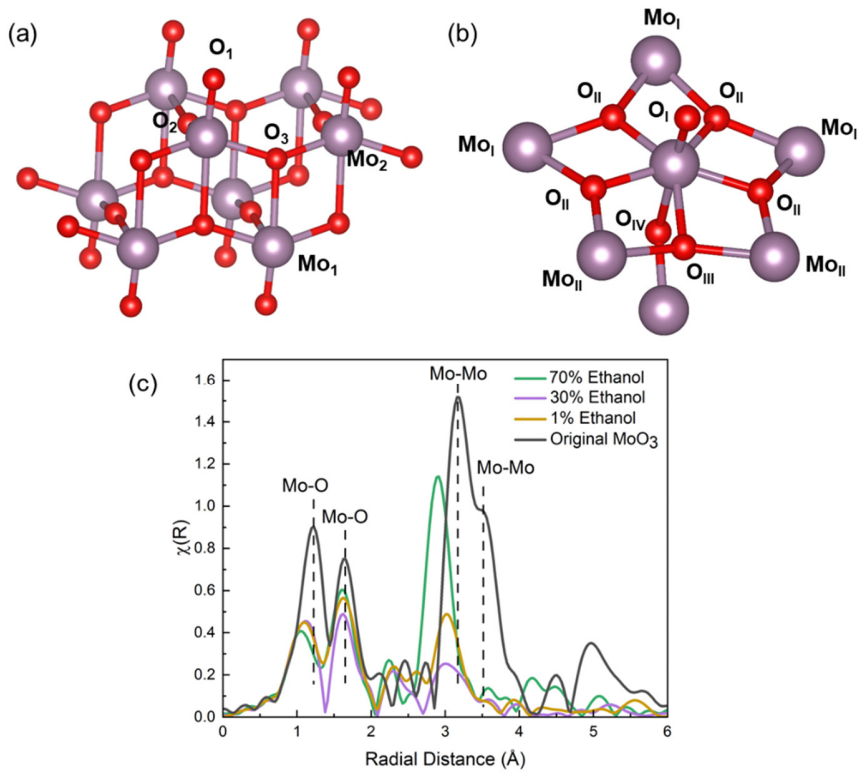


**Figure 5.6.** Schematic diagram of (a) α-$MoO_3$ and (b) pentagonal Mo structure in MB nanorings. (c) FT-EXAFS spectra of original $MoO_3$ powder and samples in 1%, 30% and 70% ethanol after 15 min of laser ablation.[25]

**Table 5.1.** Fitted coordination numbers and interatomic distances of FT-EXAFS spectra of the original $MoO_3$ and the 70%-ethanol sample.[25]

| | Original $MoO_3$ | | 70%-ethanol sample | |
|---|---|---|---|---|
| | Coordination number | Interatomic Distance (Å) | Coordination number | Interatomic Distance (Å) |
| Mo-$O_1$ | 1 | 1.67 | 1 | 1.64 |
| Mo-$O_2$ | 1 | 1.73 | 0.79 | 1.77 |
| Mo-$O_3$ | 2 | 1.98 | 2 | 1.94 |
| Mo-$O_2$ | 1 | 2.27 | 0.79 | 2.26 |
| Mo-$O_3$ | 1 | 2.34 | 1 | 2.39 |
| Mo-$Mo_1$ | 2 | 3.44 | 2 | 3.30 |
| Mo-$Mo_2$ | 2 | 3.75 | - | - |

**Table 5.2.** Fitted coordination numbers and interatomic distances of FT-EXAFS spectra of the 30%-ethanol and the 1%-ethanol samples.[25]

| | 30%-ethanol sample | | 1%-ethanol sample | |
|---|---|---|---|---|
| | Coordination number | Interatomic Distance (Å) | Coordination number | Interatomic Distance (Å) |
| Mo-$O_I$ | 1 | 1.67 | 1 | 1.67 |
| Mo-$O_{II}$ | 3.92 | 1.98 | 4 | 1.98 |
| Mo-$O_{III}$ | 1 | 2.27 | 1 | 2.30 |
| Mo-$O_{IV}$ | 1 | 2.34 | 1 | 2.34 |
| Mo-$Mo_I$ | 3 | 3.21 | 3 | 3.27 |
| Mo-$Mo_{II}$ | 2 | 3.39 | 2 | 3.39 |

**Figure 5.7** shows the XPS spectra of various samples synthesized in different water/ethanol mixtures. The XPS spectrum of the sample preprared in pure water (**Figure 5.7a**) only has $Mo^{VI}$ peaks, consistent with the XRD result of the formation of $MoO_3 \cdot H_2O$. While for all the ethanol-containing mixtures, both $Mo^{V}$ and $Mo^{VI}$ XPS peaks are observed (**Figure 5.7b-e**), even for the sample prepared in pure ethanol where two weak $Mo^{V}$ peaks can still be observed. Ethanol may work as an electron donor to reduce the valence of $Mo^{VI}$ in the formation of MBs, which was also reported in other work that used UV light to irradiate isopolyoxomolybdates in water/ethanol mixed solutions to generate MBs.[214] More research, however, is needed to clarify the ethanol-mediated reduction mechanism. The XPS spectrum of MB prepared in 1% ethanol with 15 min of laser ablation (**Figure 5.7b**) indicates a $Mo^{V}/Mo^{VI}$ ratio of 0.24, consistent with the $Mo^{V}/Mo^{VI}$ ratio of $\{Mo_{142}\}$,[96,214] but the ratio increases to 0.36 in the 30% ethanol sample (**Figure 5.7c**). These changes were also reported in Liu's work on thermal treatment of MB in helium gas.[97] Liu reported that even though the absorption bands and $Mo^{V}/Mo^{VI}$ ratio changed after thermal treatment, the MB ring structure stayed intact.[97] The breakage of $Mo^{V}$-O-$Mo^{VI}$ bonds in the 30% ethanol sample is likely caused by $H_3^+$, which is expected to dissociate from ethanol during femtosecond laser irradiation,[142,143] bond to Mo-O-Mo to form -$OH_2$ groups, and finally create oxygen deficiencies in the lattice with the release of -$OH_2$ groups, as described in Chapter 4 to explain the formation of $MoO_{3-X}$ *via* laser ablation of $MoS_2$ in ethanol/water mixtures.[196] This change is also supported by the XPS spectrum of the 70% ethanol sample (**Figure 5.7d**), which shows an increased $Mo^{V}/Mo^{VI}$ ratio due to the formation of $MoO_{3-X}$ and $H_XMoO_3$.

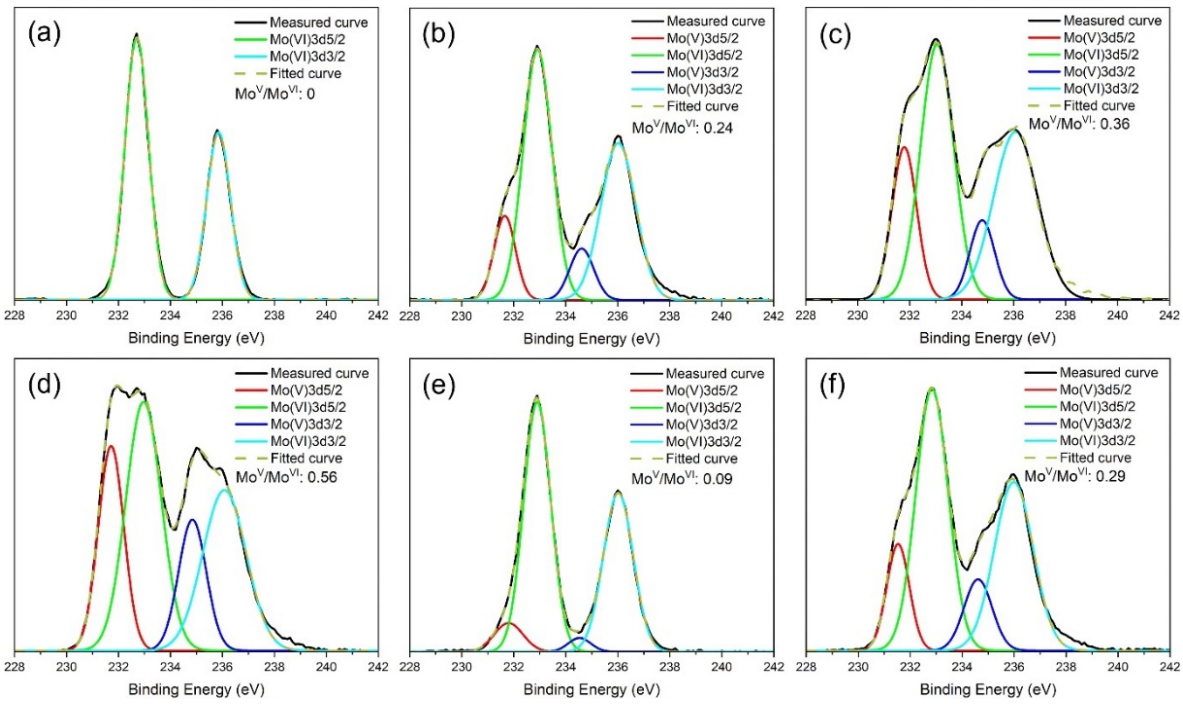


**Figure 5.7.** Mo3d XPS spectra of samples in (a) water, (b) 1% ethanol, (c) 30% ethanol, (d) 70% ethanol and (e)100% ethanol after 15 min of laser ablation and (f) the sample in 30% ethanol after 45 min of laser ablation.[25]

Based on the results presented thus far, it can be concluded that a high concentration of water is necessary to dissolve $MoO_3$ and form molybdic acid to provide an acidic environment for MB formation and that ethanol may work as an electron donor in the formation of MB under femtosecond laser irradiation. The concentration of ethanol in the irradiated solvent can change the $Mo^V/Mo^{VI}$ ratio of the MB and affect its absorption bands. When the concentration of ethanol is high, $H_XMoO_3$ and $MoO_{3-X}$ become the dominant products of the laser ablation.

### 5.3.3 Role of Laser Ablation Time

**Figure 5.8a** shows the absorbance spectra of 30%-ethanol samples (3.5 mM) prepared by laser ablation for various times. As shown in **Figure 5.8b**, the color of the solution turned blue after 3 min and became darker with increasing time until 15 min, then turned to dark

green after 45 min of laser ablation. The UV-vis spectrum of the dark green sample doesn't have absorption bands between 550 and 800 nm. The Raman spectra of these samples (**Figure 5.9**) reveal the disappearance of the MB peak at 990 $cm^{-1}$ and the shift of another MB peak from 815 $cm^{-1}$ to 823 $cm^{-1}$ after 30 min of laser ablation, implying the MB structure might be damaged by elongated laser irradiation. The $Mo^{V}/Mo^{VI}$ ratio calculated from the XPS spectrum of the sample laser-ablated for 45 min (**Figure 5.7f**) decreases to 0.29, suggesting that part of the $Mo^{V}$ was oxidized to $Mo^{VI}$. Interestingly, this dark green sample turned back to blue after storing at room temperature for 1 day, as shown in **Figure 5.8b**, and the MB peaks at 990 and 815 $cm^{-1}$ reappear in the Raman spectrum (**Figure 5.9**), suggesting reassembly of the MB structure. Noticeably, unlike the MB synthesized from laser ablation for 15 min, the UV-vis spectrum of the reassembled MB shows absorption bands at around 600 and 750 nm, consistent with MB synthesized by the conventional thermal reduction method and the MB synthesized from 1% ethanol in this work, suggesting that the reassembled MB had intact $Mo^{V}$-O-$Mo^{VI}$ entities.

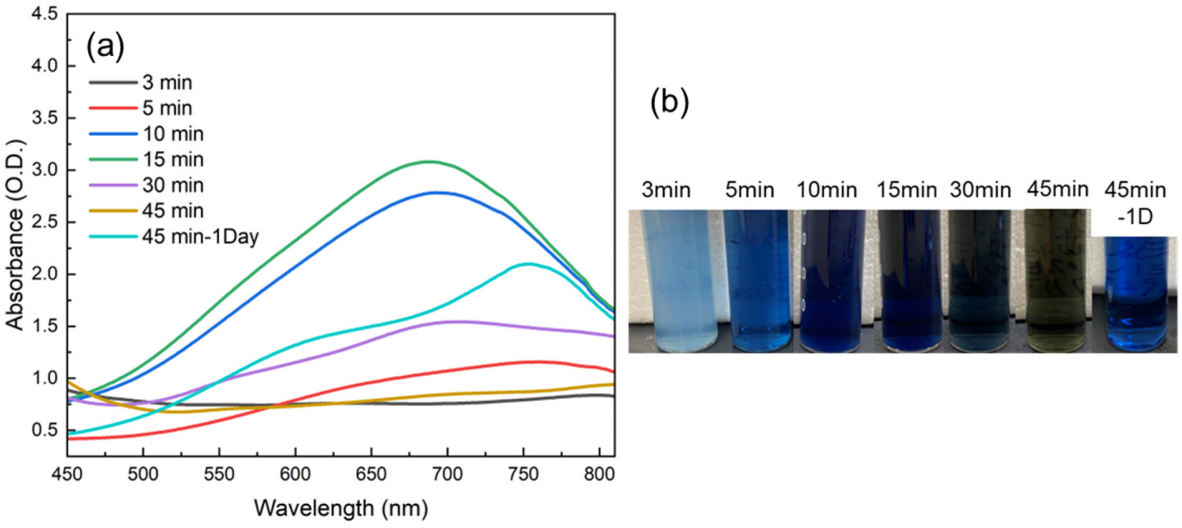


**Figure 5.8.** (a) UV-vis absorbance spectra and (b) photos of samples (3.5 mM) prepared in 30% ethanol with different laser ablation times.[25]

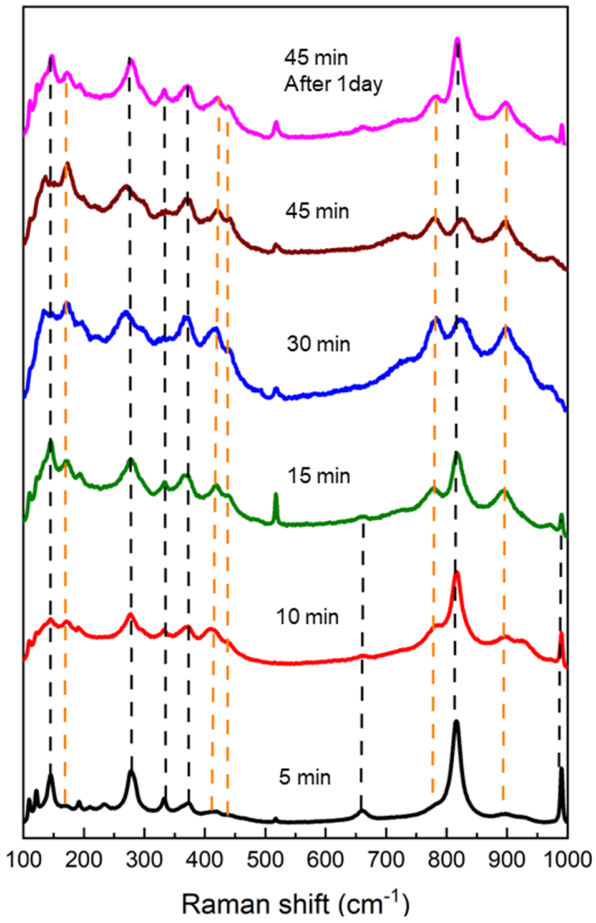


**Figure 5.9.** Raman spectra of samples (3.5 mM) prepared in 30% ethanol with different laser ablation times. The peaks marked by black dashed lines are assigned to either $MoO_3$ or MBs. The peaks marked by orange dashed lines are assigned to $H_XMoO_3$. The peak at around 520 $cm^{-1}$ is the silicon substrate peak for the drop-casted samples.[25]

To further explore the effect of the laser ablation time on the absorption bands of MBs, two samples with lower concentrations (2.8 mM and 2.1 mM) were examined. It was found that the laser ablation time needed to turn the solutions from blue to green decreased with decreasing concentration. Compared to the 3.5 mM sample that needed 45 min to turn green, it only took 35 min and 25 min for the 2.8 mM and 2.1 mM samples to turn green, respectively (**Figure 5.10**). The samples with higher concentrations absorbed more laser light

and diminished the intensity of the laser at the focal region, resulting in a longer time to damage the MB structure.

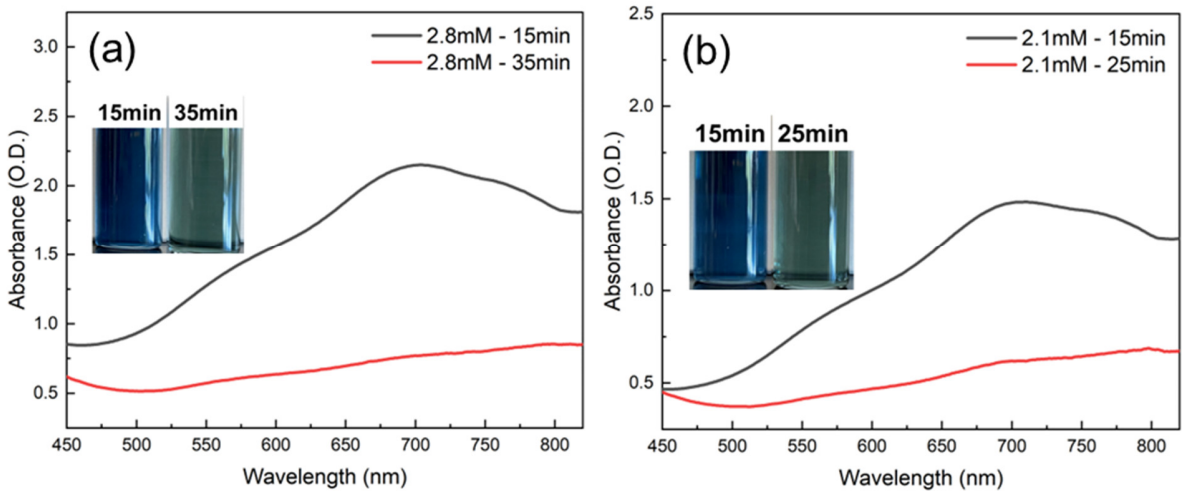


**Figure 5.10.** (a) UV-vis absorbance spectra of the 2.8 mM samples in 30% ethanol with ablation times of 15 min and 35 min. (b) UV-vis absorbance spectra of the 2.1 mM samples in 30% ethanol with ablation times of 15 min and 25 min. The inset images are photos of the samples with different ablation times.[25]

### 5.3.4 Photothermal Conversion Performance of MBs

The PTCE of the MBs prepared in 10% and 30% ethanol (15 min laser ablation) were examined for different solution concentrations. The maximum temperature increases of the 1% ethanol sample (**Figure 5.11a**) and the 30% ethanol sample (**Figure 5.11b**) after 10 min of NIR laser illumination were 20.5 and 22 °C, respectively, at a concentration of 3.5 mM. From **Figure 5.11a and b**, it was found that the temperature increases were not linearly related to the concentration of the MBs, especially when the solutions were lightly diluted such as the samples with concentrations of 3.5 mM and2.8 mM. In addition, it can be seen from the UV-vis absorbance spectra (**Figure 5.11c and d**) that the absorption bands of both samples redshift with decreasing concentration, implying the $Mo^{V}$-O-$Mo^{VI}$ entities of both MB samples might be slightly changed when they were diluted. However, they still

demonstrated good photostability regardless of the concentration, as shown from the repeated illumination and cooling processes (**Figure 5.12**).

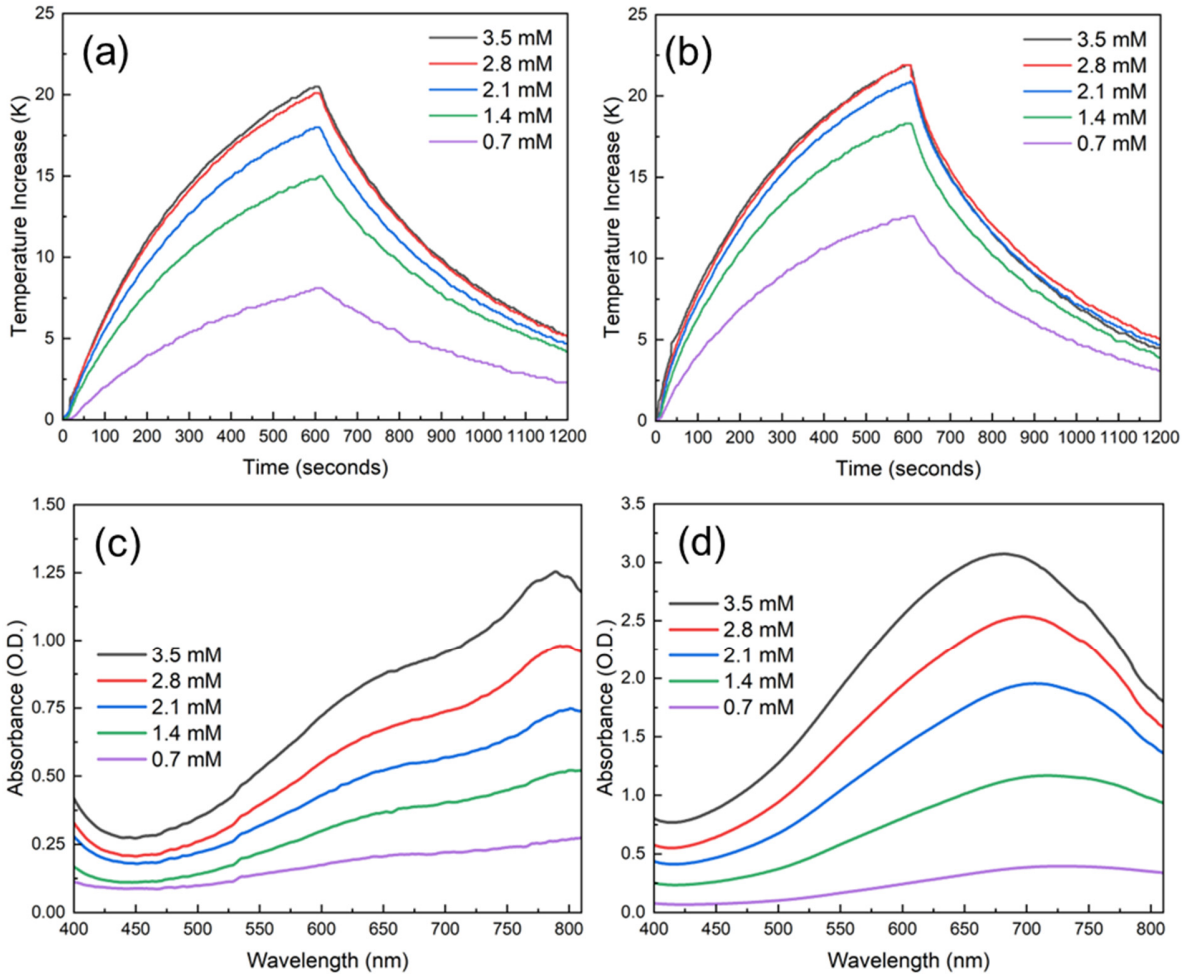


**Figure 5.11.** Temperature change curves of (a) the 1%-ethanol samples and (b) the 30%-ethanol samples with different concentrations under laser illumination (808 nm, 2.39 W $cm^{-2}$, 10 min on/10 min off). UV-vis absorbance spectra of the samples in (c) 1% ethanol and (d) 30% ethanol with different concentrations.[25]

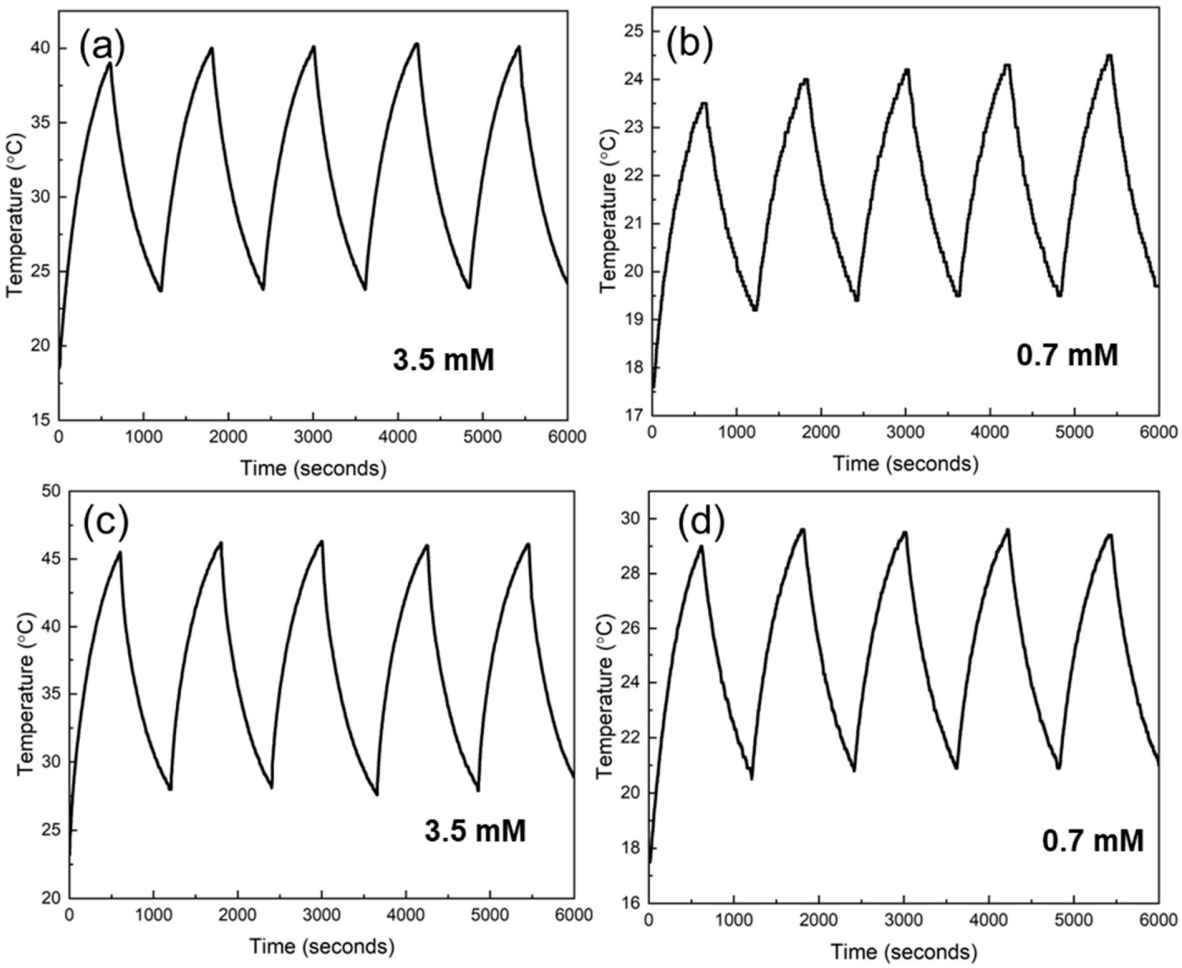


**Figure 5.12.** 5 cycles of illumination and cooling (10 min on/10 min off) for (a) the 1%-ethanol sample (3.5 mM), (b) the 1%-ethanol sample (0.7 mM), (c) the 30%-ethanol sample (3.5 mM) and (d) the 30%-ethanol sample (0.7 mM). Good photostability is observed.[25]

The PTCE of the MB samples with various concentrations are listed in **Table 5.3**. The highest PTCE observed is 45%, which was achieved from the 1%-ethanol sample with the concentration of 2.8 mM. The PTCEs of the MB prepared from 1% ethanol are consistent across the samples with different concentrations, with the exception of the heavily diluted 0.7 mM sample. The MB samples prepared from 30% ethanol also demonstrate consistent PTCEs regardless of concentration, and the highest PTCE is 42% for measurement at a concentration of 3.5 mM. The PTCEs of both the 1% and 30% ethanol samples are not only

higher than the laser-synthesized $MoO_{3-X}$ reported in Chapter 4,[196] but also many other inorganic PTAs such as carbon dots,[191] $MoS_2$,[10] black phosphorus,[72] graphene oxide,[231] etc.

**Table 5.3.** Photothermal conversion efficiencies of the 1% ethanol and 30% ethanol samples with different concentrations (15 min laser irradiation).[25]

| | 3.5 mM | 2.8 mM | 2.1 mM | 1.4 mM | 0.7 mM |
|---|---|---|---|---|---|
| 1% ethanol sample | 44.0% | 45.0% | 42.8% | 41.1% | 30.8% |
| 30% ethanol sample | 41.9% | 39.0% | 39.1% | 37.5% | 38.6% |

## 5.4 Conclusions

MB nanorings were synthesized by laser irradiation of $MoO_3$ in water/ethanol mixtures for 15 min. Given that only 15 min or less is needed to convert 4 mL of 3.5 mM $MoO_3$ into MBs, it is a very efficient method compared to other traditional synthesis methods. The dissolution of $MoO_3$ in water during femtosecond laser irradiation created molybdic acid and provided an acidic environment, which is favorable for the formation of MB. Concentrations of ethanol as low as 1% in water resulted in the formation of MB. Increasing the concentration of ethanol may increase the $Mo^V/Mo^{VI}$ ratio and change $Mo^V$-O-$Mo^{VI}$ entities in the MB to tune the absorption bands. The darkest blue color of MB was achieved when the ethanol concentration was 30%. The MB nanorings self-assembled into vesicles with an average size of 115 nm. High concentrations of ethanol (>70%) led to the formation of $H_XMoO_3$ and $MoO_{3-X}$ instead of MB. Prolonged laser irradiation was found to damage the MB; however, reassembly of the MB was observed after storage at room temperature for one day. The laser-synthesized MB displayed outstanding PTCE above 40%, making it promising for many applications requiring photothermal conversion, such as photothermal therapy, photothermal catalysis and photothermal water evaporation.

# Chapter 6

# Synthesis of $MoSe_2$ Spherical Nanoparticles by Femtosecond Laser Ablation

## 6.1 Introduction

Interest in transition metal dichalcogenide (TMDC) materials has been growing due to their graphene-like layered structures and their tunable electronic and optical properties. TMDC materials usually have multiple phases based on stacking order and metal atom coordination.[55] The stable 2H phase has a hexagonal symmetry while the metastable 1T phase has a tetragonal symmetry.[55] Among TMDC materials, $MoS_2$, $WS_2$, $MoSe_2$ and $WSe_2$ are among some of the most widely researched. They are semiconductors in the stable 2H phase and their band structures change from an indirect bandgap for bulk materials or multilayer nanosheets to a direct bandgap for monolayer nanosheets, whereas the metastable 1T phase demonstrates metallic electronic properties. The tunable band structures based on different numbers of layers and phases result in tunable electronic and optical properties such that TMDCs are broadly applied in semiconductor devices,[232–234] catalysts,[235–238] batteries,[239–242] solar cells,[243–245] etc.

In 2013, Chou and his co-workers first demonstrated the good photothermal conversion performance of chemically exfoliated $MoS_2$ nanosheets thanks to their high absorbance of NIR light.[56] Since then much research has been conducted to apply TMDC nanosheets and flower-like nanoparticles including $MoS_2$,[7–11] $WS_2$,[57–60] $MoSe_2$,[61–63], $WSe_2$[64–66] and $MoTe_2$[67] in PTT. Details of applications of TMDC nanomaterials as PTAs are introduced in Section 2.1.4. However, little attention has been paid to spherical TMDC nanoparticles. Compared to two dimensional discoidal nanoparticles, spherical nanoparticles have a longer circulation time in the bloodstream and are less likely to accumulate in lungs and spleens.[246,247] Since the discovery of onion-structured (or Fullerene-like) $MoS_2$ and $WS_2$ quasi-spherical nanoparticles in the early 1990's,[248,249] a few methods have been developed to synthesize onion-structured TMDC nanoparticles including solid-gas chemical

reaction,[248–250] chemical vapor deposition[251–253] and hydrothermal reaction.[111] However, all these methods need high temperatures or lengthy preparation times.

Much previous research reported the synthesis of TMDC nanomaterials by pulsed laser ablation of TMDC powders or bulk materials in liquid.[169,170,172,176–178,254] As of today, most of the laser-synthesized spherical TMDC nanoparticles were prepared by using nanosecond lasers, and all of these nanoparticles are onion structured.[176–178,254] In contrast, femtosecond lasers were generally used to synthesize TMDC quantum dots[169,170,172] as they have much higher peak intensities and electric fields in the laser pulses than nanosecond lasers. Hence, the formation of quantum dots is usually attributed to non-thermal ablation processes such as Coulomb explosion and photo-exfoliation.[170,172] A summary of previous work on the synthesis of TMDC nanomaterials by PLAL is listed in **Table A1 (Appendix A)**. Compared to nanosecond laser ablation, femtosecond laser ablation needs far less energy per pulse to synthesize nanoparticles. Recently, Tselikov reported the synthesis of onion-structured (OS) $MoS_2$ nanospheres by femtosecond laser ablation of $MoS_2$ bulk crystals in water, and discussed their potential as PTAs.[174] However, the fundamentals of femtosecond laser ablation of TMDC bulk materials, especially powders in liquid, are still far from clear. Additionally, compared to the formation of quantum dots in femtosecond laser ablation, little is known about the laser-induced formation of spherical TMDC nanoparticles. Moreover, the origin of the high PTCEs of some TMDC nanomaterials, which don't show distinct absorption bands in the NIR light region, is still lacking a convincing explanation.

Herein, a femtosecond laser is used to synthesize spherical 2H/1T hybrid-phase $MoSe_2$ nanoparticles by ablating $MoSe_2$ powder in IPA with different laser powers and ablation times. Two types of spherical $MoSe_2$ nanoparticles are observed regardless of the laser power and ablation time: nanoparticles with an onion-structured shell and an amorphous core and for the first time, polycrystalline nanoparticles. The nanoparticles are smaller overall (mean size: 10 - 40 nm) than nanoparticles prepared with nanosecond lasers in other work (mean size: around 60 nm).[176,178] The smaller size can ensure the PTAs are still favorable for cellular uptake after surface functionalization (e.g., attachment of biocompatible polymers),

as the optimum nanoparticle size for cellular uptake was found to be smaller than 50 nm.[255] The formation mechanisms of the spherical nanoparticles synthesized with different laser powers are studied in detail and these laser-synthesized nanoparticles show outstanding photothermal conversion performances. Notably, the PTCE of the nanoparticles increases with laser ablation time and power and PTCEs up to ~38% are observed, despite the absence of distinct absorption bands in the NIR region. Defects and structural disorder in the laser-synthesized nanoparticles are studied to elucidate this anomalously high PTCE. In doing so, femtosecond-laser defect engineering is demonstrated as a promising route for PTCE enhancement in PTAs and property modification in nanomaterials in general.

## 6.2 Experimental Methods

### 6.2.1 Synthesis of $MoSe_2$ Nanoparticles

$MoSe_2$ powder (99.9%, 325 mesh, Thermo Scientific) was added to IPA (99.9%, HPLC, Sigma-Aldrich) with a concentration of 0.28 mg/mL. After 20 min of bath sonication to break agglomerates, 4 mL of the suspension sample was transferred to a small vial for laser ablation. The details of laser ablation process is described in Section 3.1.2. The average power of the incident laser was controlled using a half-wave plate and a polarizing beam splitter. The suspension was stirred at 300 rpm during laser ablation. To research the influence of laser power on the properties of the nanoparticles, laser powers of 0.07 W, 0.15 W, 0.3 W, 0.6 W, 1.5 W and 2.5 W were applied to ablate $MoSe_2$ powder with a fixed ablation time of 10 min. To research the influence of ablation time on the properties of nanoparticles, $MoSe_2$ powder was ablated at 0.15 W for ablation times of 10 min, 20 min, 30 min, 45 min and 60 min. After ablation, the suspension was centrifuged at 2500 rpm for 10 min to remove remaining powder.

### 6.2.2 Characterization of Nanoparticles

A ZEISS Ultraplus SEM was used to observe the microstructures of the $MoSe_2$ powders before and after laser ablation. A Zeiss Libra 200MC HRTEM operating at 200 kV was used to observe the shapes and microstructures of the laser-synthesized $MoSe_2$ nanoparticles. A

PANalytical X'Pert Pro MRD diffractometer with Cu Kα radiation was used to measure the XRD patterns of the nanoparticles. A Renishaw micro-Raman spectrometer (laser wavelength of 632 nm) was used to observe the bonding state of the nanoparticles. XPS spectra of the nanoparticles were obtained using a Thermo VG Scientific ESCALab 250 microprobe with Monochromatic Al Kα excitation (1486.6 eV). The absorbance spectra of the nanoparticles were measured with a UV-vis-NIR spectrometer (Lambda 1050, PerkinElmer). The production yield of nanoparticles was calculated according to the Beer-Lambert law based on the absorbance spectra. The PTCEs of the nanoparticles were evaluated using a custom-built setup, as described in Section 3.2.1. For the PTCE measurements, the concentrations of all the samples were 0.2 mg/mL. The calculation of the PTCE of the samples is detailed in Section 3.2.2.

## 6.3 Results and Discussion

### 6.3.1 Crystal Structures of $MoSe_2$ Nanoparticles

**Figure 6.1a** shows filaments generated by femtosecond laser pulses with different powers of 0.07 W, 0.15 W, 0.3 W, 0.6 W, 1.5 W and 2.5 W in IPA. The theoretical peak intensities and fluences corresponding to the different powers are listed in **Table A2**. The filament length increases with the laser power and passes through the whole vial when the laser power is higher than 1.5 W. A discussion of femtosecond laser filamentation is presented in Section **A1 (Appendix A)**. **Figure 6.1b-e** show HRTEM images of nanoparticles produced by laser ablation of $MoSe_2$ powder in IPA with a power of 0.6 W and an ablation time of 10 min. HRTEM images of other spherical nanoparticles prepared with different powers and times are presented in **Figure A2 (Appendix A)**. Unlike many previous reports (**Table A1**) that synthesized quantum dots by using high-power femtosecond laser pulses to ablate TMDC powders in liquid for long time (> 30 min),[169,170,172] the short-time ablation with high power or long-time ablation with low power in this work produced spherical nanoparticles. **Figure 6.1b** shows an OS nanoparticle which contains a laminated shell like an onion and an amorphous core. This type of nanoparticle has been reported by several previous studies that

applied nanosecond lasers to ablate $MoS_2$ bulk materials.[176–178,256] The laminated shell is built of {002} planes. The interplanar distance is 0.694 nm, slightly larger than the interplanar distance (0.65 nm) of $MoSe_2$ powder measured by XRD, as shown in **Figure A3**. The slightly increased interplanar distance of the shell was also found in $MoS_2$ OS nanoparticles, owing to the strain-induced curvature of the layers.[177] Additionally, some nanocrystals showing {103} planes with an interplanar distance of 0.238 nm is observed in the amorphous core, which was also observed in femtosecond-laser-synthesized $MoS_2$ OS nanoparticles but not in nanosecond-laser-synthesized nanoparticles.[174] It should be noted that this small nanoparticle is actually polyhedral with a facet surface, which is consistent with laser-synthesized $MoS_2$ OS nanoparticles.[174,178] In **Figure 6.1c,** the shell surface becomes smooth for the larger OS nanoparticle when numerous {002} planes are connected. Another single-crystal nanoparticle with orientation of <103> is also observed. Besides the OS nanoparticles, polycrystalline (PC) nanoparticles are observed for the first time. **Figure 6.1d** shows the structure of a PC nanoparticle. The green dashed lines indicate grain boundaries. Several grains with <002> orientation can be clearly observed. The interplanar distance is 0.652 nm, consistent with the original $MoSe_2$ powder, suggesting the grains were fragmented from the original $MoSe_2$ powder. The area surrounded by a blue dashed line is amorphous. In **Figure 6.1e**, some linear defects marked with a red dashed box are observed, which may be caused by misalignment of lattices between different grains. Study of the HRTEM images of the nanoparticles found that the OS nanoparticles were most common among all the samples in the work regardless of the power and ablation time, even though the amount of PC nanoparticles increased with laser power.

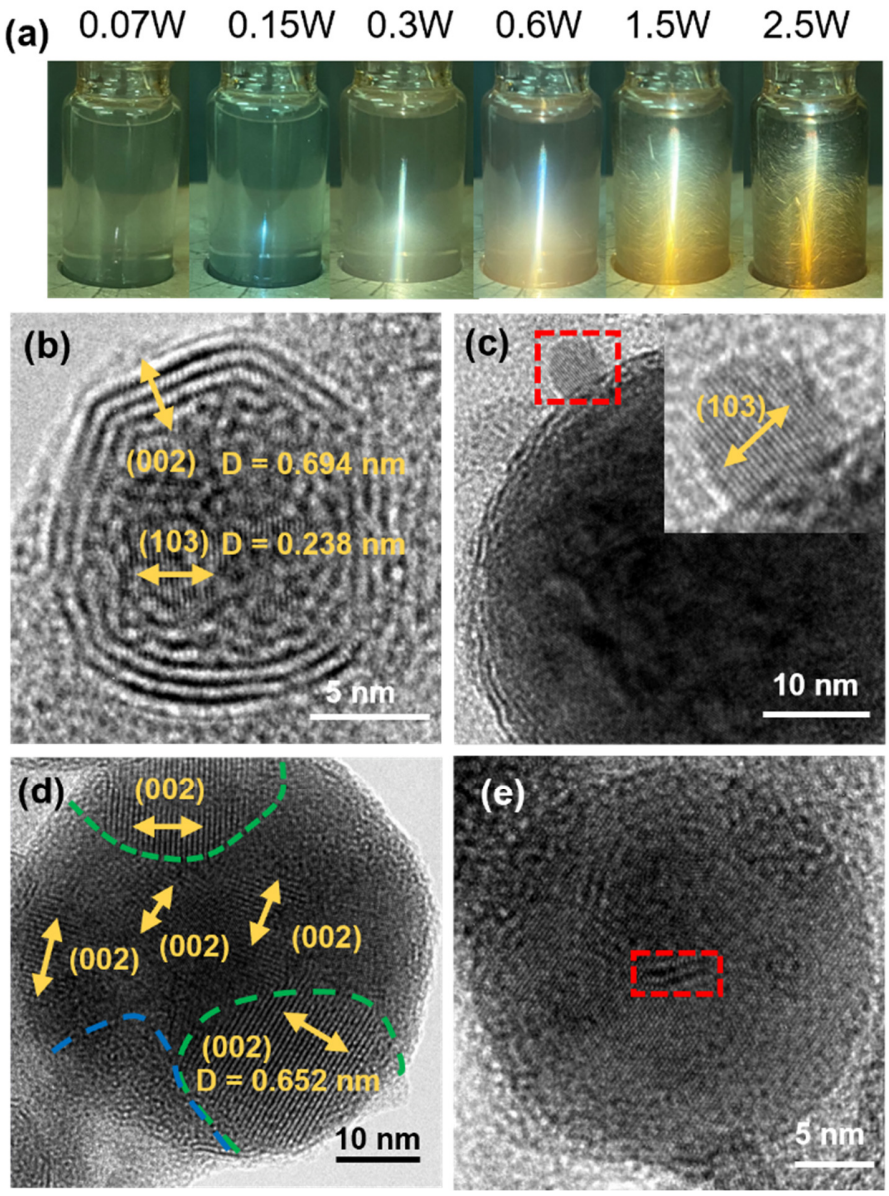


**Figure 6.1.** (a) Photos of femtosecond laser filamentation in $MoSe_2$-IPA suspensions with different powers. (b-e) HRTEM images of nanoparticles prepared from laser ablation at 0.6 W for 10 min. The inset image in (c) is the magnified image of the nanoparticle marked by the red dashed box. The green dashed lines in (d) indicate grain boundaries. The area surrounded by the blue dashed line in (d) is amorphous. The area marked with a red dashed box in (e) indicates defects.[193]

### 6.3.2 Influence of Laser Power

To research the influence of laser power on the properties of the synthesized nanoparticles, $MoSe_2$ powder was ablated with different powers for 10 min. The XPS spectrum of the original $MoSe_2$ powder (**Figure 6.2a**) shows two primary peaks assigned to $Mo3d_{5/2}$ (229 eV) and $Mo3d_{3/2}$ (232 eV) of the 2H phase.[109,110,237] In contrast, the XPS spectra of the laser-synthesized nanoparticles (**Figure 2b-g**) shows two additional peaks assigned to $Mo3d_{5/2}$ (~228 eV) and $Mo3d_{3/2}$ (~231 eV) of the 1T phase.[109,110,237] The mixture of 2H and 1T phases was also reported in some previous research on laser-ablated TMDC materials.[119,187] The 2H-to-1T phase transition of TMDC materials is usually attributed to electron doping.[257,258] Given the abundance of high-energy electrons that existed during the laser ablation process, it is not surprising to observe this transition here. Another two peaks at around 233 eV and 236 eV are assigned to Mo (VI),[196] indicating slight oxidation of the nanoparticles during laser ablation. The details of peak positions and contents are listed in **Table A3**. The amount of 1T phase increases with the laser power from 0% to 61% when the ablation time is 10 min. This is probably caused by the increased amount of photoexcited electrons that triggered the phase transition, as a result of the intense plasma created by the increased power. The Raman spectra (**Figure 6.2h**) also verify the formation of the 1T phase in the laser-synthesized nanoparticles. The height of the $A_{1g}$ peak of the 2H $MoSe_2$ phase (238 $cm^{-1}$) decreases with increasing power.[109,237] On the other hand, three peaks at 197 $cm^{-1}$ 223 $cm^{-1}$ and 353 $cm^{-1}$ assigned to the 1T phase appear in the nanoparticles.[109,237]

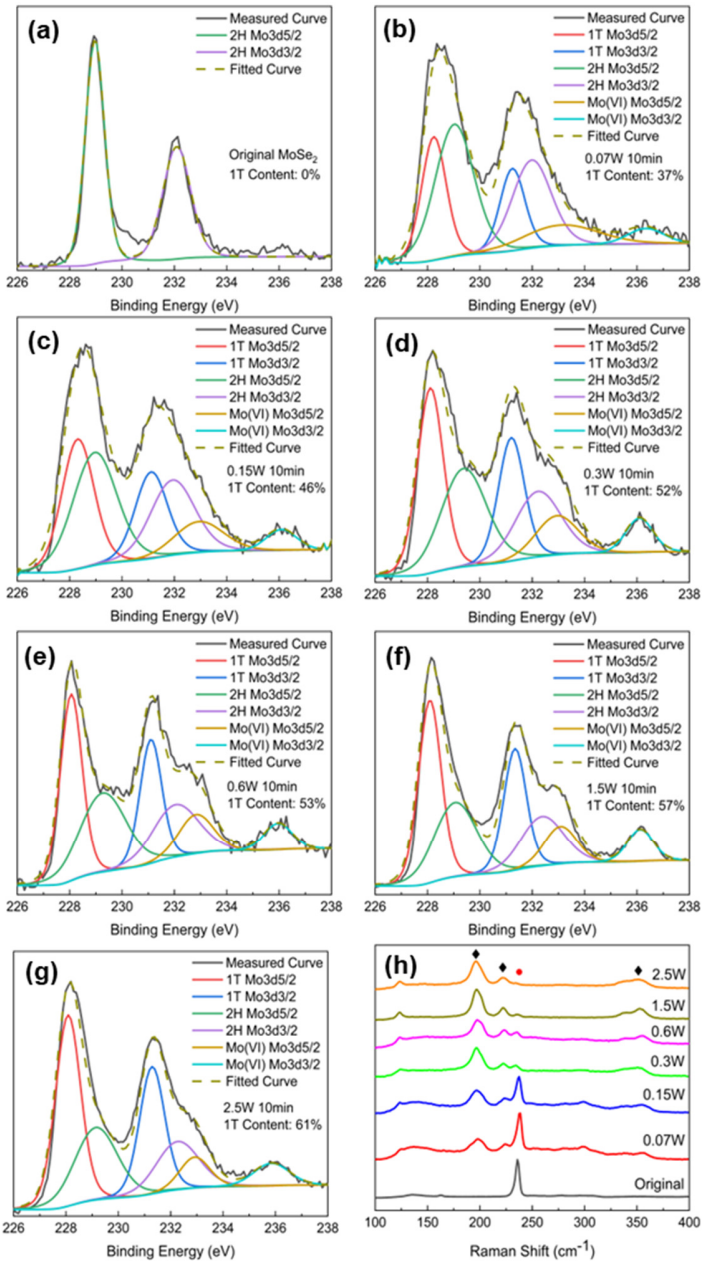


**Figure 6.2.** Mo3d XPS spectra of (a) original $MoSe_2$ powder and nanoparticles prepared by laser ablation at (b) 0.07 W, (c) 0.15 W, (d) 0.3 W, (e) 0.6 W, (f) 1.5 W and (g) 2.5 W for 10 min. (h) Raman spectra of original $MoSe_2$ powder and nanoparticles synthesized with different powers for 10 min. The peak labeled by a red dot is assigned to 2H phase, and the peaks labeled by black diamond symbols are assigned to 1T phase.[193]

The production yields of nanoparticles prepared with different laser powers with a fixed ablation time of 10 min are presented in **Figure 6.3a**. The production yield is defined as the ratio of the weight of the synthesized nanoparticles to the weight of the original powder. The weight of the nanoparticles was measured *via* light absorbance according to the Beer-Lambert law after centrifugation at 2,500 rpm for 10 min to remove powder residues. The production yield increases with the laser power and saturates after 1.5 W. This trend is consistent with the filament length as shown in **Figure 6.1a**, suggesting a larger laser ablation area contributed to a higher production yield. The highest yield achieved using 1.5 W and 2.5 W is 93%, such that the PLAL method is proven to be an efficient method to produce nanoparticles. In the PLAL setup, powder particles circulated around the laser beam which was located at the center of the vial, such that large particles might have a lower chance than the smaller ones to be ablated by the laser beam as they were more prone to circulate farther away from the center of the vial due to larger centrifugal force. The plateau after 1.5 W is probably caused by insufficient ablation of some large powder particles in the short time of 10 min.

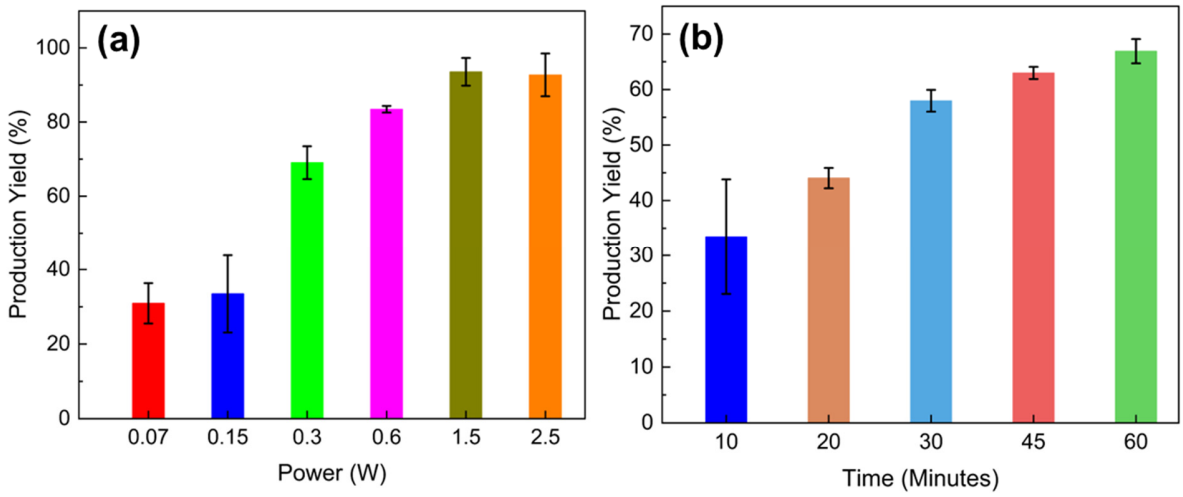


**Figure 6.3.** Production yields of (a) $MoSe_2$ nanoparticles synthesized by laser ablation at different powers for 10 min and (b) $MoSe_2$ nanoparticles synthesized by laser ablation at 0.15 W for different ablation times.[193]

The size distributions of the nanoparticles prepared with different laser powers for 10 min are shown in **Figure 6.4**. At least 300 nanoparticles were measured manually from TEM images to obtain the size distribution for each sample. Quantum dots with a size less than 3 nm were not counted as they are not the interest of this work. All the samples show a bimodal distribution after fitting with Gaussian functions. One population consisting of small nanoparticles shows a narrow size dispersion (Peak 1) and the other population consisting of larger nanoparticles shows a wide size dispersion (Peak 2). The mean size of the smaller nanoparticles decreases from 11.4 nm when the laser power is 0.07 W or 0.15 W to 9.5 nm when the laser power is 1.5 W, then drops slightly to 9.2 nm when the laser power increases to 2.5 W. The mean size of the large nanoparticles is found to decrease from 32.5 nm when the laser power is 0.07 W to 15.8 nm when the laser power increases to 2.5 W. Additionally, the fraction of small nanoparticles also increases with the laser power. The dependence of the nanoparticle size distribution on power is further discussed in Section 6.3.4.

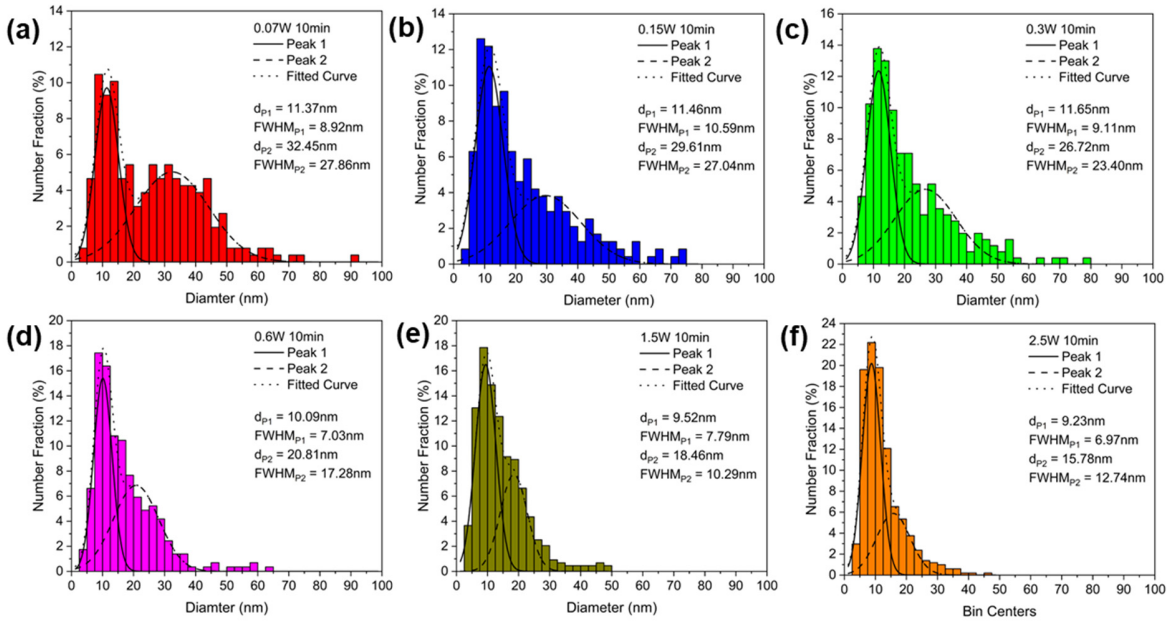


**Figure 6.4.** Size distributions of nanoparticles synthesized by laser ablation at (a) 0.07 W, (b) 0.15 W, (c) 0.3 W, (d) 0.6 W, (e) 1.5 W and (f) 2.5 W for 10 min.[193]

### 6.3.3 Influence of Laser Ablation Time

To research the influence of laser ablation time on the properties of the $MoSe_2$ nanoparticles, $MoSe_2$ powder was ablated with a relatively low power of 0.15 W (to avoid significant oxidation) for durations of 10 min, 20 min, 30 min, 45 min and 60 min. The production yield increases with the ablation time (**Figure 6.3b**), but the highest yield achieved is only 69% for the 60 min sample. The size distributions of nanoparticles synthesized at 0.15 W with different ablation times are presented in **Figure 6.5**. Again, each sample shows a bimodal distribution regardless of laser ablation time. The mean size of the smaller nanoparticles (peak 1) drops slightly from 11.5 nm when the ablation time is 10 min to 10.3 nm when the ablation time increases to 30 min, then quickly drops to around 7 nm when the ablation time increases to 45 or 60 min. The mean size of the larger nanoparticles (peak 2) gradually decreases from 29.6 nm when the ablation time is 10 min to 14.0 nm when the ablation time increases to 60 min.

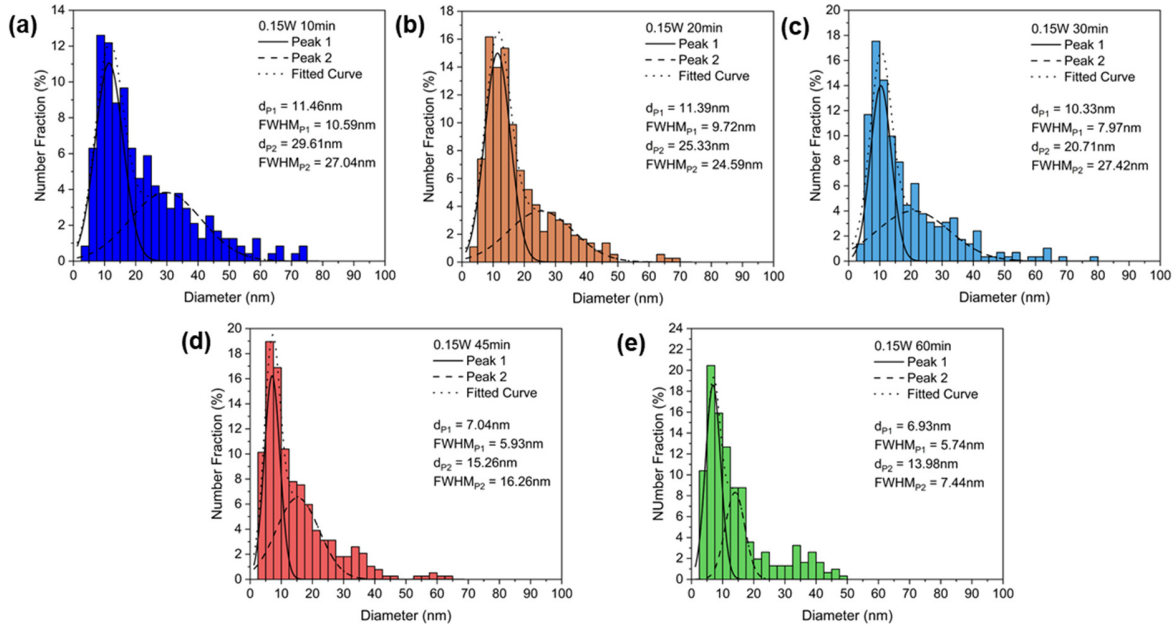


**Figure 6.5.** Size distributions of nanoparticles synthesized by laser ablation at 0.15 W for (a) 10 min, (b) 20 min, (c) 30 min, (d) 45 min and (e) 60 min.[193]

The XPS spectra of the nanoparticles prepared with different ablation times at 0.15 W are shown in **Figure 6.6a-e**. All the nanoparticles show two peaks assigned to the 1T phase in addition to two peaks assigned to the 2H phase. The amount of 1T phase in the nanoparticles increases from 46% after 10 min of laser ablation to 61% after 60 min of laser ablation. This is probably caused by the nanoparticles' repetitive passing through the plasma region such that more 2H phase nanoparticles were transformed to 1T phase due to electron doping. The peak positions and 1T-phase contents of the nanoparticles are listed in **Table A4**. The XPS result is also consistent with the Raman spectra (**Figure 6.6f**). The height of the peak representing the 2H phase (labeled with a red dot) decreases with increasing ablation time. At the same time the peaks belonging to the 1T phase (labeled with black diamonds) appear in all the laser-ablated nanoparticle samples.[109,237]

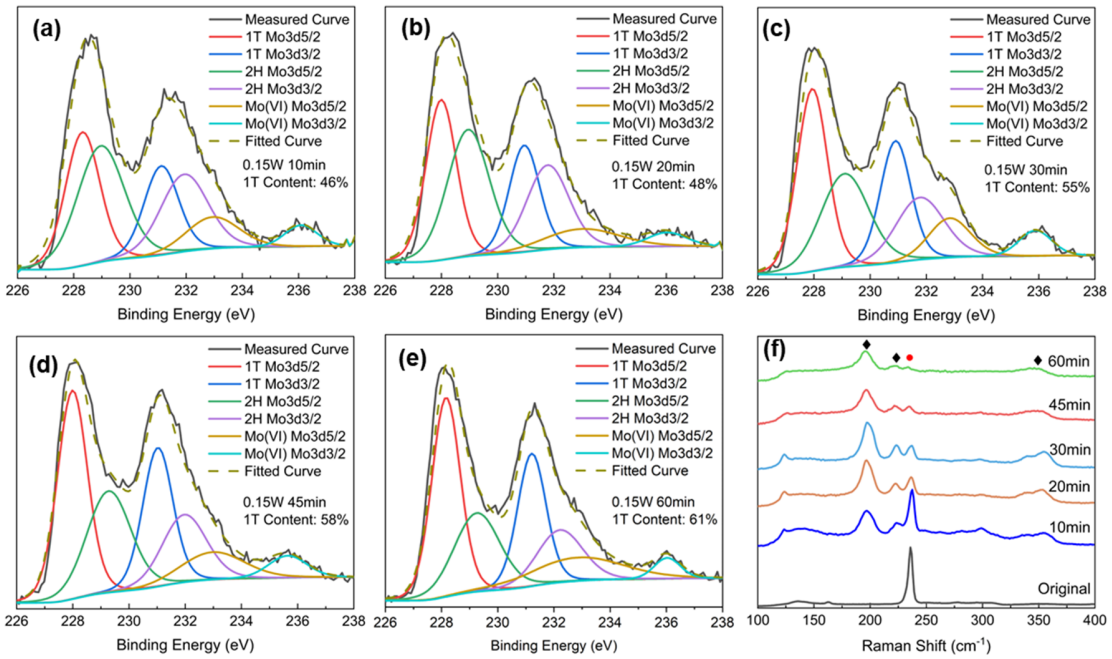


**Figure 6.6.** Mo3d XPS spectra of nanoparticles prepared by laser ablation at 0.15 W for (a) 10 min, (b) 20 min, (c) 30 min, (d) 45 min and (e) 60 min. (f) Raman spectra of original $MoSe_2$ powder and nanoparticles synthesized with different ablation times at 0.15 W. The peak labeled by a red dot is assigned to 2H phase, and the peaks labeled by black diamond symbols are assigned to 1T phase.[193]

### 6.3.4 Formation Mechanisms of Nanoparticles

As of today, most proposed formation mechanisms of spherical nanoparticles prepared by PLAL focused on OS nanoparticles synthesized by nanosecond laser ablation of bulk targets. One reliable explanation for the formation of OS nanoparticles is local melting of the ablated bulk target upon nanosecond laser irradiation and re-solidification of ejected melted liquid droplets.[178] However, the mechanisms for femtosecond laser ablation of TMDC powder in liquid to synthesize spherical nanoparticles have never been clearly elucidated.

The formation of spherical $MoSe_2$ nanoparticles can be divided into two steps: fragmentation from the ablated powder particles and formation of unique OS and PC structures. The fragmentation mechanism can be studied by examining the ablated powder particles. **Figure 6.7** show SEM images of $MoSe_2$ powder particles after laser ablation with different powers for 10 min. Laser ablation of powder particles stirred in a liquid is not always uniform as large particles circulating farther away from the laser beam might have a lower chance than smaller ones of being ablated by the laser beam. Therefore, it is possible to observe powder particles that experienced different amounts of laser ablation in one sample. **Figure 6.7a, c, e, g, i and k** are powder particles that experienced less ablation at different powers, while **Figure 6.7b, d, f, h, j and l** are powder particles that experienced more ablation at different powers but are obtained from the same samples. When the power is low, such as 0.07 W, 0.15 W and 0.3 W, most of the ablated powder only show nanoglobules (marked with red dashed circles) at edges of the powder and the surface of the powder is still flat if it was ablated less. If the powder experienced more ablation, it turns into a coral reef structure (**Figure 6.7b, d and f**), indicating significant melting of the powder. For the samples ablated with higher powers of 0.6 W, 1.5 W and 2.5 W, the surface of the ablated powder is not flat and many nanocraters (marked with yellow arrows) and surface bulges are observed. It should be noted that nanocraters can be observed in all the samples, but they are more prevalent in the samples ablated with higher powers. Some powder particles show a lot of cracks on their surface in addition to the increased number of nanocraters (**Figure 6.7h, j and l**), suggesting they were ablated with more pulses. The surface cracks are attributable to

thermal stress caused by repeated heating and cooling. These different features observed on the surfaces of powder particles ablated with different powers suggest that the nanoparticles produced by PLAL involved multiple fragmentation mechanisms, especially at different laser powers.

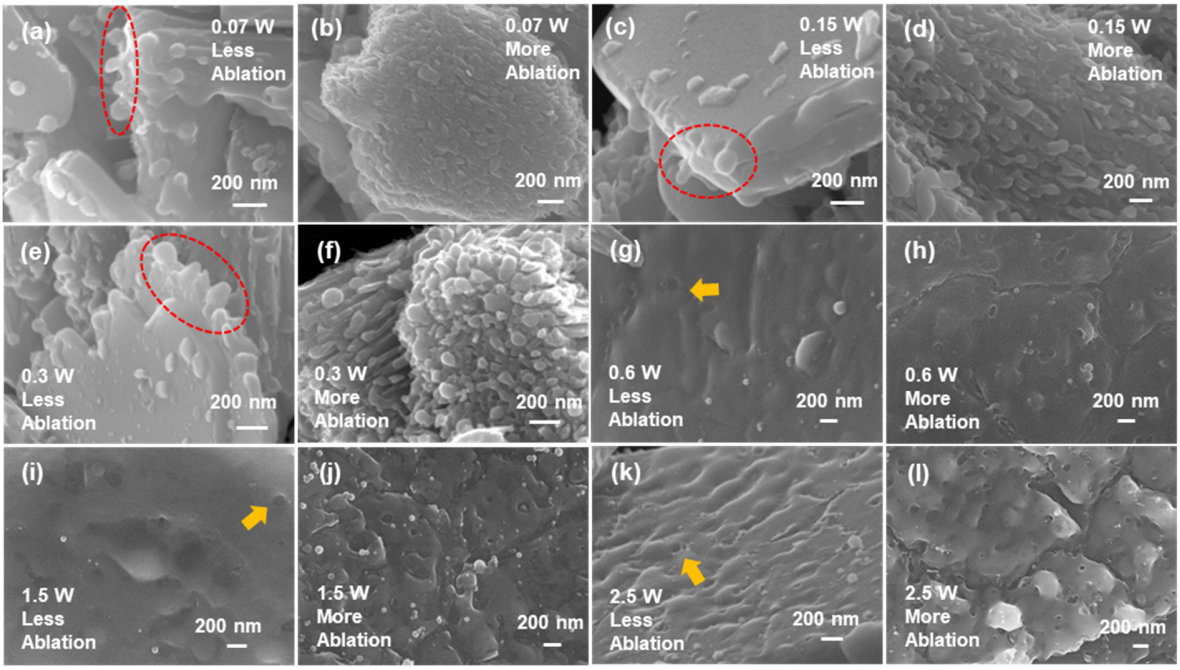


**Figure 6.7.** SEM images of $MoSe_2$ powder after laser ablation with different powers of (a and b) 0.07 W, (c and d) 0.15 W, (e and f) 0.3 W, (g and h) 0.6 W, (i and j) 1.5 W and (k and l) 2.5 W for 10 min. Nanoglobules (red dashed lines) and nanocraters (yellow arrows) are highlighted.[193]

The femtosecond laser-material interaction typically includes photo-induced ionization such as multiple photon absorption and ionization, tunneling ionization and avalanche ionization and Coulomb explosion.[259] Coulomb explosion of a small cluster takes place when the strong electric field of a laser pulse extricates multiple electrons from constituents of the cluster causing the constituents to be extremely ionized. The extremely ionized constituents experience Coulomb repulsion, which results in disintegration of the cluster.[196,259,260] Thanks to Coulomb explosion and photo-induced ionization, the ejected electrons have high

temperatures of tens of thousands of degrees Kelvin. The hot electrons will return back to clusters and thermalize lattices after 10-100 picoseconds through electron-phonon coupling such that the material is heated up and melted.[115,259] The thermal ablation is accompanied by different detachment processes, such as normal vaporization, spallation, and explosive boiling, which starts at a few picoseconds after the end of the laser pulse and can last up to several nanoseconds.[23,115,259,261] Different laser energies absorbed by the material result in different detachment processes. Normal thermodynamic equilibrium melting and vaporization occurs when the absorbed energy is low and the material is heated up relatively slowly, whereas explosive boiling is a primary detachment process when the absorbed energy is high and the material is quickly superheated up to its critical temperature.[23,115,261] In the case of explosive boiling, the detached material consists of both superheated liquid and vapor bubbles that nucleate in the liquid homogeneously.[115,262] Therefore, it is likely that the nanoglobules observed on the $MoSe_2$ powders ablated with relatively low powers (**Figure 6.7a-f**) correspond to solidification of melted material that followed an equilibrium thermal detachment process. When ablated powder left the hot plasma region and was quickly cooled down to the temperature of the surrounding liquid, the melted parts that were left on the powder were resolidified.[261] The amount of nanoglobules decreased in the samples ablated with high powers and instead more nanocraters appeared suggesting enhanced non-equilibrium explosive boiling. It should be noted that the nanocraters observed on the laser-ablated powder in this work are different than the craters observed on laser-ablated bulk materials, which usually have a diameter of several microns matching the size of the focused beam spot on the surface of the ablated bulk material.[263] The theoretical size of the laser beam at its focal point in this work was around 13.27 μm, as described in Section **A1 (Appendix A)**, while the actual beam size was expected to be larger when considering plasma scattering. Given the size of the original $MoSe_2$ powder particles was generally smaller than 10 μm, as shown in **Figure A4**, whole powder particles might be completely exposed to the focused laser beam during the laser ablation and heated up by the laser-induced plasma, such that the nanocraters were likely caused by non-equilibrium explosive boiling as a result of superheating of the powder. The ablation process of the $MoSe_2$ powder

can be illustrated as shown in **Figure 6.8a**. Crystalline nanoclusters and atomic ions were formed by fragmentation of the powder due to Coulomb explosion after extreme ionization. The hot electrons returned to the powder and heated it up. When the power was low, the powder was heated up to a relatively low temperature due to the relatively weak plasma, such that the fragmentation of the ablated powder followed thermodynamic equilibrium melting and vaporization. The melting started from the edge of the powder. This was attributed to lattice disorder at the edge where there were more holes to combine with hot electrons. When the laser power was high, the whole powder particle was heated up to an ultrahigh temperature above the boiling temperature such that superheated droplets that included vapor bubbles were ejected, leaving nanocraters on the surface.

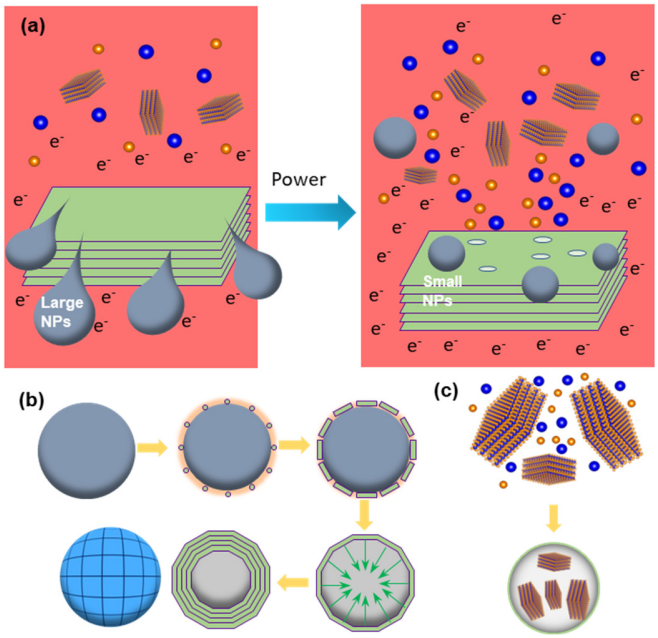


**Figure 6.8.** (a) Schematic illustration of femtosecond laser ablation of a $MoSe_2$ powder at a low (left) and high (right) power. The red background denotes a laser beam; the grey balls denote detached liquid droplets; the laminated particles denote fragmented crystalline nanoclusters; the blue and orange dots denote Mo atoms and Se atoms respectively. (b) Schematic diagram showing the formation mechanism of onion-structured nanoparticles. (c) Schematic diagram showing the formation mechanism of polycrystalline nanoparticles.[193]

The influence of laser power on the nanoparticle fragmentation mechanisms is also supported by the nanoparticle size distributions in **Figure 6.4**. Unlike nanoparticles prepared by nanosecond laser ablation, which show wide monomodal size distributions with mean sizes of around 60 nm,[176,178] all nanoparticle samples synthesized by femtosecond laser ablation in this work have bimodal size distributions, regardless of the laser ablation power and time. Most large nanoparticles (peak 2) were probably detached from the ablated powder *via* equilibrium thermal melting like nanosecond laser ablation as their size has a wide dispersion with a large mean size of around 30 nm. The small nanoparticles (peak 1) may be caused by additional ablation of already-produced large nanoparticles or fragmentation from the original powder particles *via* a different route. Further examination of the size distributions of the small nanoparticles suggests that most small nanoparticles were detached from the ablated powder *via* explosive boiling. For samples ablated at the same power of 0.15 W but with different times, the mean size of small nanoparticles and large nanoparticles dropped by 39.5% (from 11.5 nm to 6.9 nm) and 52.8% (from 29.6 nm to 14.0 nm), respectively when the ablation time increased from 10 min to 60 min. In contrast, for ablation with a fixed time of 10 min but at different powers, the mean size of the small nanoparticles kept relatively stable with only a 18.8% drop (from 11.4 nm to 9.2 nm) when the laser power increased from 0.07 W to 2.5 W, whereas the mean size of the larger nanoparticles dropped by 51.4% (from 32.5 nm to 15.8 nm). The different sensitivity of the mean size of the small nanoparticles to the ablation power and time suggests that most of these small nanoparticles were not caused by further fragmentation of already-produced large nanoparticles. If that was the case, when the laser power increased, their mean size should decrease as quickly as the already-produced large nanoparticles. Instead, the small nanoparticles were more likely to be fragmented directly from the ablated powder *via* explosive boiling. Supercritical liquid droplets ejected from nanocraters by explosive boiling contain vapor bubbles, such that they will experience secondary fragmentation when the vapor bubbles are quickly expanded. As a result, the liquid droplets detached from the ablated powder *via* explosive boiling are expected to be smaller than those detached *via* thermal melting. The increased proportion of small nanoparticles produced at higher laser powers (**Figure 6.4**) is also consistent with the

increased amount of nanocraters observed in **Figure 6.7**. Accordingly, the decrease of the mean size of large nanoparticles with increasing laser power is probably caused by a shift of the primary nanoparticle fragmentation mechanism from thermal melting to explosive boiling.

The size decrease of both the small and large nanoparticles with increasing ablation time (**Figure 6.5**) suggests that the already-produced nanoparticles were further ablated and fragmented, especially when the ablation time was longer than 30 min. In the first 30 min, the mean sizes of both the small and large nanoparticles decreased more slowly compared to the next 30 min. This is probably because further ablation of the already-produced nanoparticles was partially offset by the creation of new nanoparticles in the first 30 min (the production yield was less than 60% when the ablation time was shorter than 30 min, **Figure 6.3b**). When the ablation time was longer than 30 min, the production yield didn't increase much, likely because the larger powder particles that circulated farther away from the laser beam had less chance to be ablated, while most of the smaller powder particles that circulated closer to the laser beam had probably been ablated in the first 30 min. As a result, the longer ablation times fragmented the nanoparticles more than the original powder, such that the mean sizes of both small nanoparticles and large nanoparticles decreased. Some outlier nanoparticles with sizes between 30 to 40 nm in the 45-min and 60-min samples (**Figure 6.5d and e**) are probably due to the coalescence of smaller nanoparticles and new large nanoparticles detached from the ablated powder.

The formation of OS nanoparticles was well illustrated by Zhou.[178] The surfaces of detached liquid droplets quickly cooled down when they left the plasma region. The supercooled surface of a liquid droplet provided sites for nucleation (**Figure 6.8b**). The surface nuclei preferred to grow laterally along the {002} plane due to the special layered structure of $MoSe_2$ and only the nuclei with {002} planes parallel to the surface-tangent plane of the droplet could grow along the surface until they met neighboring planes to form the first layer of the shell.[178] The next layer of the shell grew inward along the <002> direction thanks to the cooling driving force along the radial direction of the droplet to its hot

core.[178] That's how the shell was formed layer-by-layer. The number of layers in the shell increased until the core of the droplet dropped below the melting temperature such that the atoms left at the core formed an amorphous phase. It should be noted that compared with OS nanoparticles prepared by nanosecond lasers, the amorphous cores of OS nanoparticles prepared by femtosecond lasers sometimes were mixed with nanocrystals, as seen in **Figure 6.1b**. It might be attributed to the mixing of liquid droplets and crystalline nanoclusters before the OS shells were formed. This is more obvious in the $MoS_2$ OS nanoparticles prepared by femtosecond laser ablation of a $MoS_2$ bulk crystal in Tselikov's work.[174] The formation of the unique PC nanoparticles, on the other hand, is similar to the formation of noble metal nanoparticles.[148,264] The crystalline nanoclusters fragmented from the ablated powder joined other fragmented atoms or ions and coalesced to form PC nanoparticles, as described in **Figure 6.8c**. This is supported by the polycrystalline structure observed in **Figure 6.1d**. It should be emphasized that these PC nanoparticles were not observed in previous work using nanosecond laser ablation because nanosecond laser ablation does not produce the required crystalline nanoclusters *via* Coulomb explosion.

### 6.3.5 Photothermal Conversion Efficiencies of $MoSe_2$ Nanoparticles

The PTCEs of the $MoSe_2$ nanoparticles were evaluated with a customized setup which illuminates the nanoparticles in IPA with a continuous-wave laser (808 nm) for 10 min followed by cooling for another 10 min. **Figure 6.9a** shows the temperature-change curve of samples prepared with different powers at a fixed ablation time of 10 min. The maximum temperature change of the samples after 10 min of continuous-wave laser illumination increases with the laser ablation power from 7.1 °C at 0.07 W to 16.4 °C at 1.5 W but doesn't improve any more when the laser ablation power increases to 2.5 W. This is consistent with the PTCE trend of the samples (**Figure 6.9c**). The PTCE of samples increases from 24.4% for the 0.07 W sample to 37.8% for the 1.5 W sample, then slightly increases to 38.2% for the 2.5 W sample. **Figure 6.9b** shows the temperature change of samples prepared with different ablation times at a fixed power of 0.15 W. The maximum temperature change increases from 10.3 °C when the ablation time is 10 min to 15.9 °C when the ablation time is

60 min. The temperature increase slows down when the ablation time is longer than 30 min. Correspondingly, the PTCE increases from 29.6% for the 10 min sample to 37.1% for the 60 min sample (**Figure 6.9d**).

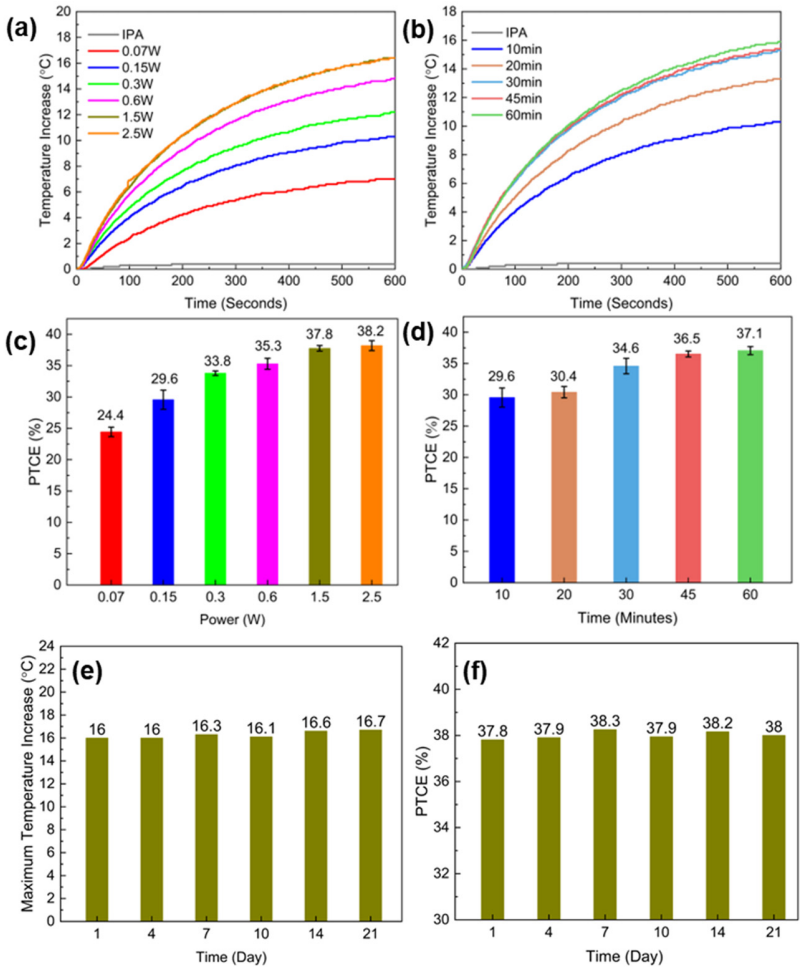


**Figure 6.9.** (a) Temperature-change curves and (c) PTCEs of nanoparticles prepared by laser ablation with different powers for 10 min. (b) Temperature-change curves and (d) PTCEs of nanoparticles prepared by laser ablation with different ablation times at 0.15 W. Stability of (e) the maximum temperature increase and (f) PTCE of the nanoparticles prepared by laser ablation at 1.5 W for 10 min as a function of time when stored at room temperature. The nanoparticles were illuminated by an NIR continuous-wave laser (808 nm, 0.46 W) for 10 min. The concentration of all the samples in IPA was 0.2 mg/mL.[193]

**Figure 6.9e and f** shows the maximum temperature increase and PTCE of the sample prepared by laser ablation at 1.5 W for 10 min as a function of time when it was stored at room temperature. The sample showed good stability over 3 weeks with a maximum temperature increase of around 16.3 °C and PTCE of around 38.0%. The temperature-change curves and absorbance spectra of the same sample measured on different days are presented in **Figure A5**. Even though the highest PTCE reported in this work is lower than that of $MoSe_2$ quantum dots and nanosheets reported by other work,[61,62] it is still higher than many other TMDC PTAs such as $MoS_2$ nanosheets (24.4%,[7] 27.6%[10]), $WS_2$ nanosheets (32.8%,[59] 35%[60]) and $MoTe_2$ nanosheets (33.8%),[67] and is comparable to $wSe_2$ nanosheets (35.1%,[64] 38.3%[65]).

The normalized UV-vis-NIR absorption spectra of the nanoparticles prepared with different times and powers are shown in **Figure 6.10**. Similar to other 2H/1T hybrid-phase TMDC materials,[56,265,266] most of the laser synthesized $MoSe_2$ nanoparticles don't show excitonic absorption bands except the one prepared with the low power of 0.07 W that shows two weak bands at 707 nm and 810 nm corresponding to the excitonic transitions of 2H $MoSe_2$.[61] This is also the sample with the lowest amount of 1T phase.

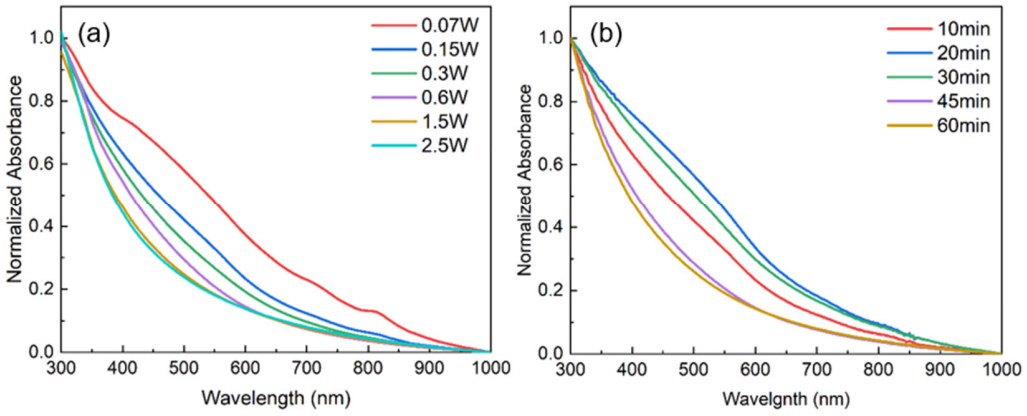


**Figure 6.10.** Normalized UV-vis-NIR absorbance spectra of nanoparticles prepared by laser ablation (a) with different powers for 10 min or (b) with different ablation times at 0.15 W.[193]

A search of published literature was unable to provide a clear explanation about how TMDC materials without distinct absorption bands in the NIR region can still demonstrate high PTCEs. To explore the origin of the high PTCEs achieved with the $MoSe_2$ nanoparticles, the bandgaps of the nanoparticles were measured by Tauc plots (**Figure A6**). **Figure 6.11a and b** present the bandgaps of the nanoparticles prepared by laser ablation with different laser powers for 10 min and with different ablation times at 0.15 W, respectively. It was surprising to find that the bandgap of the nanoparticles increased with the laser power in **Figure 6.11a**, given the amount of 1T phase also increased with the laser power (**Figure 6.2**). This contradicts previous reports that the bandgap of $MoSe_2$ drops with increasing amount of 1T phase.[109,110] The PTCE was also found to generally increase with the bandgap of nanoparticles (**Figure 6.11c**), which was unexpected.

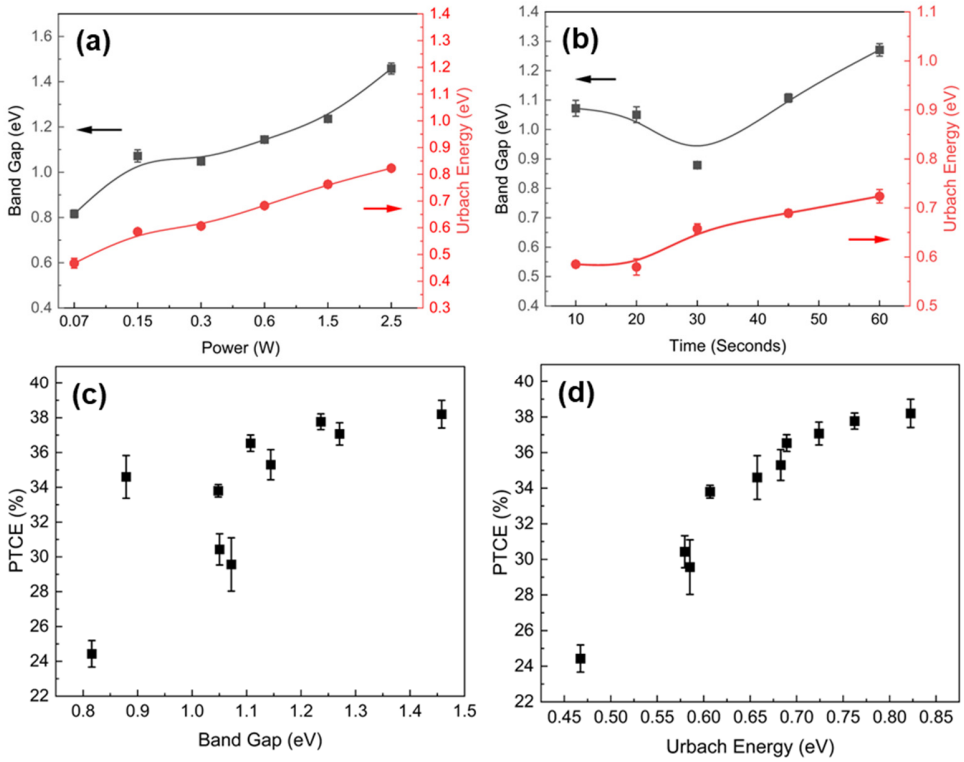


**Figure 6.11.** Bandgaps and Urbach energies of nanoparticles prepared by laser ablation with (a) different powers for 10 min and (b) different times at 0.15 W. Plots of PTCEs with respect to (c) the bandgaps and (d) the Urbach energies of all the samples.[193]

As the nanoparticles in all the samples showed bimodal size distributions (**Figure 6.4 and 6.5**), the increase in bandgap might be caused by nanoparticles smaller than 10 nm that increased the effective bandgap due to quantum confinement effects. This was verified by an additional experiment that measured the bandgaps of four groups of nanoparticles with different sizes. The different groups of nanoparticles were collected by centrifugation of the 1.5 W sample at 3 different speeds. The details are presented in Section **A2 (Appendix A)**. Additionally, the bandgap of the nanoparticles prepared with different ablation times at a fixed power of 0.15 W was found to slightly dip when the ablation time was 30 min, then increased with the ablation time (**Figure 6h**). The final increase of the bandgap is also attributable to the creation of small nanoparticles with sizes less than 10 nm after extended ablation, whereas the dip in the measured bandgap at 30 min is likely caused by the increased amount of 1T phase compared with the other two samples prepared with shorter ablation times (**Figure 4**). Therefore, the sudden increase in PTCE for the 30-min sample (**Figure 6d**) is probably caused by the lowered bandgap.

As the nanoparticles prepared by laser ablation contained amorphous regions and defects, the Urbach energies of all the samples were calculated from the UV-vis-NIR spectra (**Figure A2**). For perfect crystalline semiconductors, the minimum energy for an electron to be excited from the valence band to the conduction band upon the absorption of a photon is the bandgap energy (path "1" in **Figure 6.12**). For defective semiconductors, however, the absorption of a photon also takes place when the photon energy is less than the bandgap energy (path "2" and "3" in **Figure 6.12)**. This is due to the presence of tails in the density of electronic states for both the valence band and the conduction band due to the presence of defects.[267,268] The tail in the density of electronic states extending into the forbidden bandgap is called the Urbach tail.[267] The absorption of photons ($\alpha$) in the Urbach tail region is governed by **Equation 6.1**[267]:

$$\alpha(h\upsilon) = \alpha_0 \exp\left(\frac{h\upsilon}{E_u}\right) \tag{6.1}$$

Where $\alpha_0$ is a constant, $hv$ is the photon energy and $E_u$ is the Urbach energy. The linearization of **Equation 6.2** results in:

$$ln(\alpha) = \ln(\alpha_0) + \frac{hv}{E_u} \quad (6.2)$$

By plotting $ln(\alpha)$ versus $hv$, the Urbach energy is the inverted slope of the linear fitting line. A high Urbach energy usually indicates an increase in structural disorder and contribution of defects in localized states in the forbidden bandgap.[269] The Urbach energy of the $MoSe_2$ nanoparticles was found to increase with either laser power (**Figure 6.11a**) or laser ablation time (**Figure 6.11b**), implying an increase in defects and structural disorder in the nanoparticles. The PTCE of nanoparticles was also found to increase with the Urbach energy for all the samples (**Figure 6.11d**), suggesting another possible reason for the increased PTCE. The localized electronic states in the forbidden bandgap caused by defects and structural disorder lower the energy barrier for NIR light absorption even though the bandgap is increased and would be expected to facilitate non-radiative recombination of photo-excited carriers, producing more heat from absorbed light.

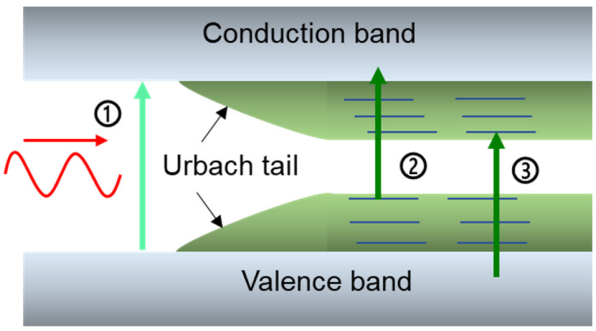


**Figure 6.12.** Schematic illustration showing electron transitions in a semiconductor with localized tail states in the forbidden bandgap.[193]

## 6.4 Conclusions

$MoSe_2$ 2H/1T hybrid phase nanoparticles were synthesized by femtosecond laser ablation of $MoSe_2$ powder with different laser powers and ablation times and their formation mechanisms were examined. The $MoSe_2$ powder ablated by the femtosecond laser

experienced laser-induced ionization, Coulomb explosion, and was finally heated up by laser-induced hot electrons. It was found that the material detachment process follows different approaches depending on laser power. When the laser power was low, the primary process to detach material from the powder was thermodynamic equilibrium melting like nanosecond laser ablation, whereas it turned to non-equilibrium explosive boiling to eject liquid droplets when the laser power was high. The nanoparticles produced by femtosecond laser ablation had smaller size than those produced by nanosecond laser ablation. Two types of spherical nanoparticles were formed corresponding to different formation mechanisms. The onion-structured nanoparticles were formed by nucleation on the surfaces of melted droplets followed by inward growth of {002} planes of $MoSe_2$ along the radial direction of the droplets layer-by-layer. The polycrystalline nanoparticles were formed by the coalescence of fragmented crystalline nanoclusters, which were only observed in femtosecond laser ablation. The 2H-to-1T phase transition was likely caused by electrons in the laser-induced plasma. The PTCE of the nanoparticles was found to increase with either laser power or ablation time. The highest PTCE was 38.2%, achieved with the nanoparticles produced with the laser power of 2.5 W. Further examination of the bandgaps and the Urbach energies of the nanoparticles revealed that the high PTCE of the nanoparticles was primarily attributed to the enhanced sub-bandgap light absorption and enhanced non-radiative recombination, as the tails of localized states for both the valence band and the conduction band are extended into the forbidden bandgap due to the defects and structural disorder in the laser-synthesized nanoparticles. As far as we know, this is the first study of the formation mechanisms of TMDC spherical nanoparticles produced by femtosecond laser ablation of powder and the first time the origin of the high PTCE of TMDC nanomaterials without distinct absorption bands in the NIR light region has been explored. It indicates that laser-induced defect engineering may be a new way to tune the properties of nanomaterials for photothermal therapy.

# Chapter 7

# Synthesis of PEGylated $MoSe_2$ Nanoparticles and Quantum Dots by Femtosecond Laser Ablation

## 7.1 Introduction

Section 2.1.4 has shown that TMDC nanomaterials are not only good PTAs but also good drug carriers for synergistic therapy. However, TMDC nanomaterials need to be surface functionalized with biocompatible polymers to improve their physiological stability and biocompatibility. One way to attach biopolymers is van der Waals force. For example, soybean phospholipid, polyethylene glycol (PEG), polyvinylpyrrolidone, polyethylene imine (PEI) and F-127 were attached to TMDC nanomaterials *via* van der Waals force.[11,58,270–272] Another way to conjugate TMDC nanomaterials with biopolymers is through chemical bonds. TMDC nanomaterials can attach biopolymers terminated with lipoic acid groups, such as LA-PEG, and LA-PEI by forming metal-sulfur bonds.[8,10,273,274] All these methods needs hours or even days of stirring of nanomaterials and biopolymers together. Therefore, there exists a need to shorten the surface functionalization time.

PLAL was proven to be an efficient, simple and green method to prepare TMDC nanomaterials including quantum dots or spherical nanoparticles,[169,172,176,177,275] as shown in Section 2.5.5. The nanomaterials are usually stable in the ablated liquid thanks to surface attached radicals such as hydroxyl groups when laser ablated in water, ethanol, and ethylene glycol.[172,275] The hydroxyl group formed on the nanomaterials results in a negatively charged surface that prevents aggregation and sedimentation.[275] Additionally, nanomaterials prepared by PLAL in oxygen containing solvents, especially water, are easily oxidized.[169–172,196] Sometimes the formation of oxide coatings or carbon coatings outside nanomaterials can protect the nanomaterials from further oxidation. It was reported that the formation of *in-situ* surface aluminum oxide coatings outside aluminum nanoparticles during femtosecond laser ablation of aluminum pellets in ethanol can prevent further oxidation of the nanoparticles.[134] Similarly, the formation of graphite coatings outside iron nanoparticles during femtosecond

laser ablation of an iron target in acetone can also prevent further oxidation.[163] However, there have been no reports about preventing oxidation of TMDC nanomaterials during pulsed laser ablation in oxygen containing solvents.

In this work, PEGylated $MoSe_2$ nanomaterials including quantum dots and spherical nanoparticles are prepared by femtosecond laser ablation of $MoSe_2$ powder in aqueous PEG solutions. High-power and long-time laser ablation result in the formation of $MoSe_2$ quantum dots. The oxidation of the quantum dots is suppressed with increasing concentration of PEG in the solutions. In contrast, laser ablation in water or a solution with a low concentration of PEG (0.0625 mg/mL) results in oxidation of the $MoSe_2$ powder into $MoO_3$ nanoparticles. Short-time ablation results in the formation of spherical nanoparticles. PEG molecules can be attached to the nanoparticles *via* van der Waals forces or chemical bonds. High-power laser ablation results in more PEG attached to the nanoparticles *via* Mo-O chemical bonds, which prevents the nanoparticles from further oxidation. Both the PEGylated $MoSe_2$ quantum dots and the spherical nanoparticles have high PTCEs. But the PTCEs of the $MoSe_2$ quantum dots are overall higher than those of the $MoSe_2$ spherical nanoparticles.

## 7.2 Experimental Methods

### 7.2.1 Synthesis of PEGylated $MoSe_2$

PEG (4000 MW, Sigma-Aldrich) was added into deionized water to prepare PEG solutions with different concentrations of 0.0625 mg/mL, 0.125 mg/mL, 0.25 mg/mL, 0.5 mg/mL and 1 mg/mL. After complete dissolution of the PEG in water, $MoSe_2$ powder (99.9%, 325 mesh, Thermo Scientific) with a concentration of 0.28 mg/mL was added into each solution. After 20 min of bath sonication to break agglomerates, 4 mL of the suspension sample was transferred to a small vial for laser ablation. The details of the laser ablation process are described in Section 3.1.2. The average power of the incident laser was tuned to be 0.15 W, 0.3 W, 0.6 W and 1.5 W using a half-wave plate and a polarizing beam splitter. The suspension was stirred at 300 rpm during laser ablation. After laser ablation, the solutions were dialyzed against deionized water for 3 days to remove extra PEG.

### 7.2.2 Characterization of Nanomaterials

A Zeiss Libra 200MC HRTEM operating at 200 kV was used to observe the shapes and microstructures of the laser-synthesized nanoparticles. The bonding states of the nanoparticles were analyzed with a Renishaw micro-Raman spectrometer (laser wavelength of 532 nm). XPS spectra of the nanoparticles were obtained using a Thermo VG Scientific ESCALab 250 microprobe with Monochromatic Al Kα excitation (1486.6 eV). The surface attached PEG on the nanoparticles was analyzed using a Bruker Tensor 27 FTIR spectrometer with attenuated total reflection (ATR) mode. The thermogravimetric analysis (TGA) curves of pure PEG and the PEGylated $MoSe_2$ quantum dots after freeze drying were recorded using a TA Instruments TGA Q500 with a ramp rate of 10 °C/min. The absorbance spectra of the nanoparticles were measured with an UV-vis-NIR spectrometer (Lambda 1050, PerkinElmer). The PTCEs of the nanoparticles were evaluated using a custom-built setup as described in Section 3.2.1. For the PTCE measurements, the concentration of $MoSe_2$ in all the samples was 1.1mM. The calculation of the PTCEs of the samples is detailed in Section 3.2.2.

## 7.3 Results and Discussion

### 7.3.1 Influence of Concentration of PEG

**Figure 7.1** shows the TEM images of nanomaterials prepared by femtosecond laser ablation in water with different concentrations of PEG for 30 min at 1.5 W. When the concentration of PEG is higher than 0.125 mg/mL, as shown in **Figure 7.1a-d**, quantum dots with lattice spacing of 2.89 Å corresponding to (100) planes of $MoSe_2$ are observed. This is consistent with previous research that long-time ablation with high-power laser pulses leads to the formation of quantum dots which are fragmented from ablated materials *via* Coulomb explosion or explosive boiling.[169–171] Instead of quantum dots, larger spherical nanoparticles are observed in **Figure 7.1e and f**. **Figure 7.1e** shows a nanoparticle prepared in 0.0625 mg/mL PEG solution; it has a lattice spacing of 3.21 Å corresponding to (011) planes of $MoO_3$,. **Figure 7.1f** shows a nanoparticle prepared in pure water; it has a lattice spacing of

3.52 Å corresponding to (002) planes of $MoO_3$. This suggests that the $MoSe_2$ was oxidized into $MoO_3$ when laser ablated in water or the solution with a low concentration of PEG.

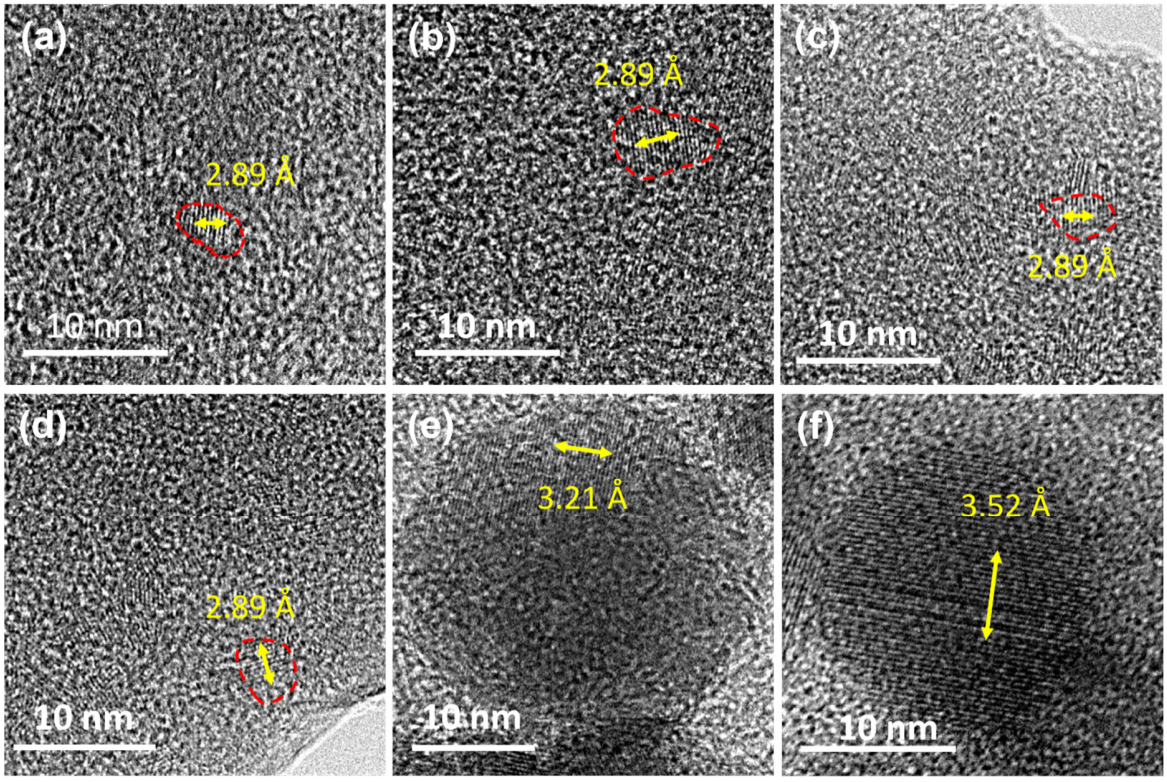


**Figure 7.1.** TEM images of nanomaterials prepared by femtosecond laser ablation of $MoSe_2$ powder in PEG solutions with different concentrations of (a) 1 mg/mL, (b) 0.5 mg/mL, (c) 0.25 mg/mL, (d) 0.125 mg/mL, (e) 0.0625 mg/mL and pure water.

**Figure 7.2a** shows the TGA curve of PEG and PEGylated $MoSe_2$ prepared in the 0.5 mg/mL PEG solution using laser ablation for 30 min with 1.5 W laser pulses. The weight of pure PEG drops by 91.42% when the temperature increases from 25 °C to 400 °C due to decomposition. The weight of the PEGylated $MoSe_2$ quantum dots drops by 37.18% in the same temperature range, which is attributed to decomposition of the PEG. This suggests that PEG molecules were successfully attached to the $MoSe_2$ quantum dots during laser ablation. The FTIR spectra of the original $MoSe_2$, PEG and PEGylated $MoSe_2$ quantum dots are shown in **Figure 7.2b**. The original $MoSe_2$ powder has no active FTIR peaks. PEG has a

major peak at 1108 $cm^{-1}$ assigned to C-O stretching vibration, peaks at 1233 $cm^{-1}$ and 1343 $cm^{-1}$ assigned to C-H symmetric and asymmetric bending vibrations, and a peak at 2873 $cm^{-1}$ assigned to C-H stretching vibration.[276] The $MoSe_2$ quantum dots prepared in PEG solutions with concentrations ranging from 0.25 mg/mL to 1 mg/mL all show PEG peaks, suggesting the surface attachment of PEG. The sample prepared in 0.125 mg/mL PEG solution doesn't show PEG peaks, probably because the amount of the attached PEG was too low to be detected. The size distributions of the quantum dots are presented in **Figure 7.3**. The mean size of quantum dots is around 3.8 nm when the concentration of PEG ranges from 0.125 mg/mL to 0.5 mg/mL, and drops slightly to 3.4 nm when the concentration of PEG increases to 1 mg/mL. The drop in size might be caused by an increased amount of PEG attached to the quantum dots, which blocked further aggregation of fragmented ions, atoms or nanoclusters.

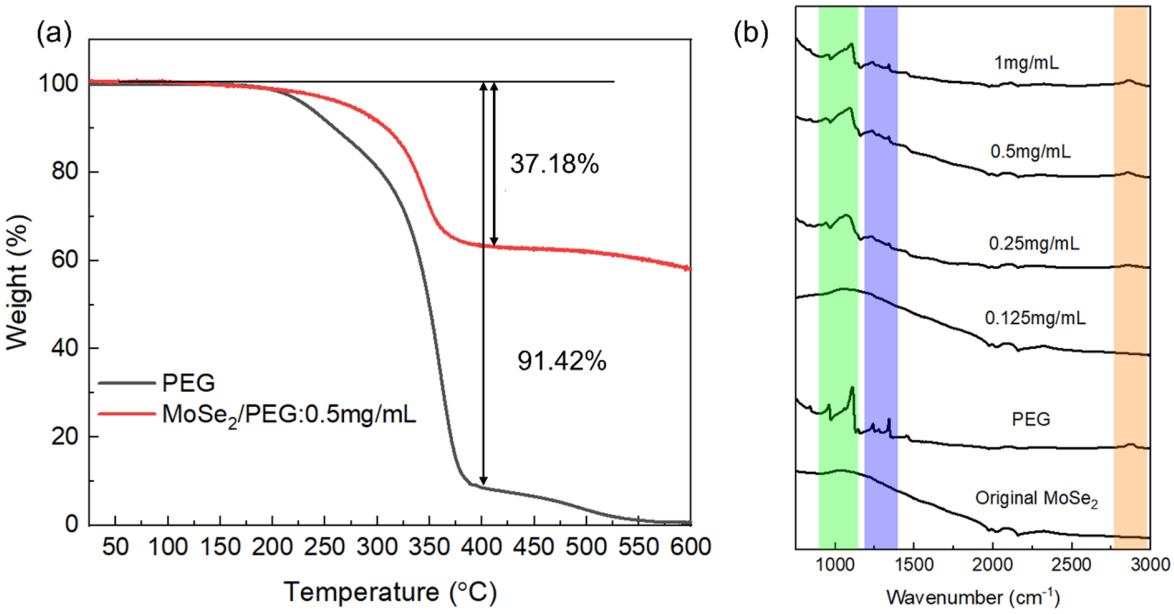


**Figure 7.2.** (a) TGA curves of PEG powder and PEGylated $MoSe_2$ quantum dots prepared in the 0.5 mg/mL PEG solution. (b) ATR-FTIR spectra of original $MoSe_2$ powder, PEG and quantum dots prepared in PEG solutions with different concentrations.

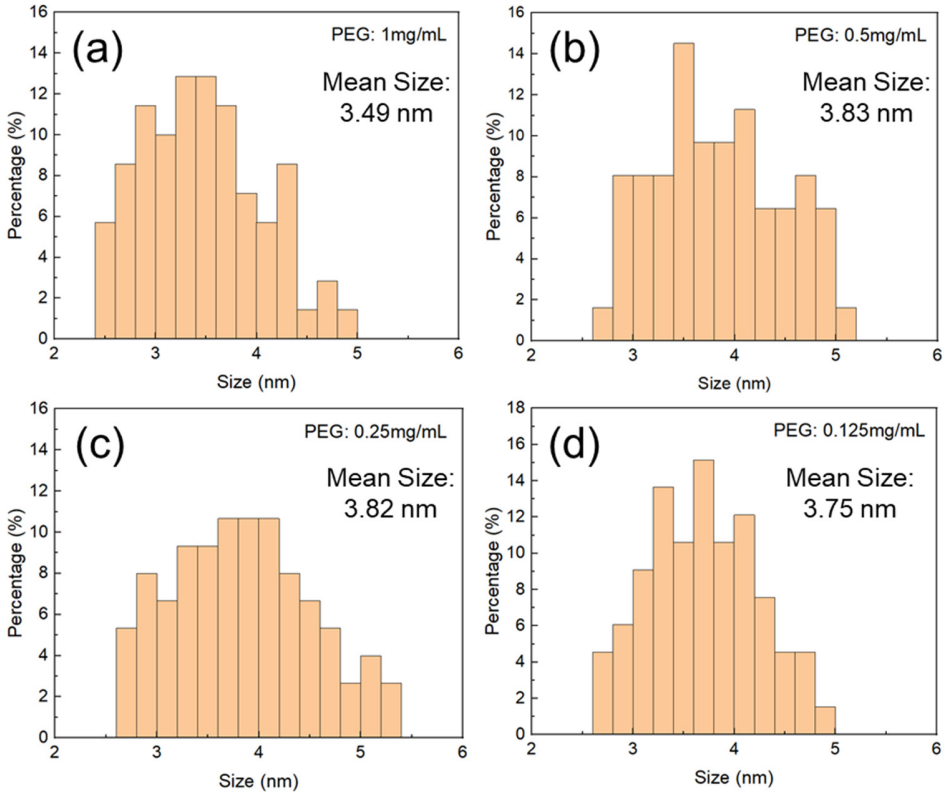


**Figure 7.3.** Size distributions of $MoSe_2$ quantum dots prepared in PEG solutions with different concentrations of (a) 1 mg/mL, (b) 0.5 mg/mL, (c) 0.25 mg/mL and (d) 0.125 mg/mL.

**Figure 7.4** shows the Mo3d XPS spectra of the original $MoSe_2$ powder and the quantum dots prepared in PEG solutions with different concentrations. The original $MoSe_2$ powder (**Figure 7.4a**) shows two peaks at 228.9 eV and 232.1 eV assigned to $Mo3d_{5/2}$ and $Mo3d_{3/2}$ of $MoSe_2$. The sample prepared in pure water (**Figure 7.4b**) shows two peaks at 232.9 eV and 235.9 eV assigned to $Mo3d_{5/2}$ and $Mo3d_{3/2}$ of Mo(VI)-O bonds, suggesting that the sample was oxidized to $MoO_3$. Besides the $MoSe_2$ and $MoO_3$ peaks, the sample prepared in the 0.0625 mg/mL PEG solution (**Figure 7.4c**) has two other small peaks at 230.3 eV and 232.7 eV, which are assigned to $Mo3d_{5/2}$ and $Mo3d_{3/2}$ of Mo(IV)-O bonds.[277,278] The high $MoO_3$ peaks for the sample prepared in the 0.0625 mg/mL PEG solution imply the sample was also significantly oxidized during laser ablation, which is consistent with the TEM image

(**Figure 7.1e**). When the concentration of PEG is 0.125 mg/mL or higher, high $MoSe_2$ peaks and reduced Mo(VI)-O peaks are observed (**Figure 7.4d-g**), implying that oxidation was suppressed in the $MoSe_2$ quantum dots. As shown in **Table 7.1**, the contribution of the Mo(VI)-O bond in the $MoSe_2$ quantum dots decreases with increasing concentration of PEG. On the other hand, the Mo(IV)-O content is similar in all samples prepared with PEG and in fact decreases slightly in the 0.5 mg/mL PEG sample. The decrease might be attributed to the suppressed oxidation as the Mo(VI)-O content also decreases. However, the Mo(IV)-O content increases slightly in the 1 mg/mL PEG sample, while the Mo(VI)-O content continues decreasing. This might be caused by increased surface attachment of PEG to the quantum dots *via* Mo(IV)-O bonds, suggesting that the Mo(IV)-O bond is not only caused by partial oxidation but also surface attachment of PEG *via* chemical bonds. Laser ablation can ionize and fragment PEG at the same time when fragmentating $MoSe_2$ powder such that the ionized PEG can bond with the fragmented $MoSe_2$ through chemical bonds. **Figure 7.5** shows the C1s XPS spectra of the original $MoSe_2$ powder and nanomaterials prepared in pure water and PEG solutions with different concentrations. All the samples show a peak at 285 eV assigned to C-C bonds and a peak at 286.6 eV assigned to C-O bonds.[279] The height of the C-O peak in $MoSe_2$ quantum dots was found to grow with increasing concentration of PEG, implying more PEG molecules were attached to the quantum dots during laser ablation.[279]

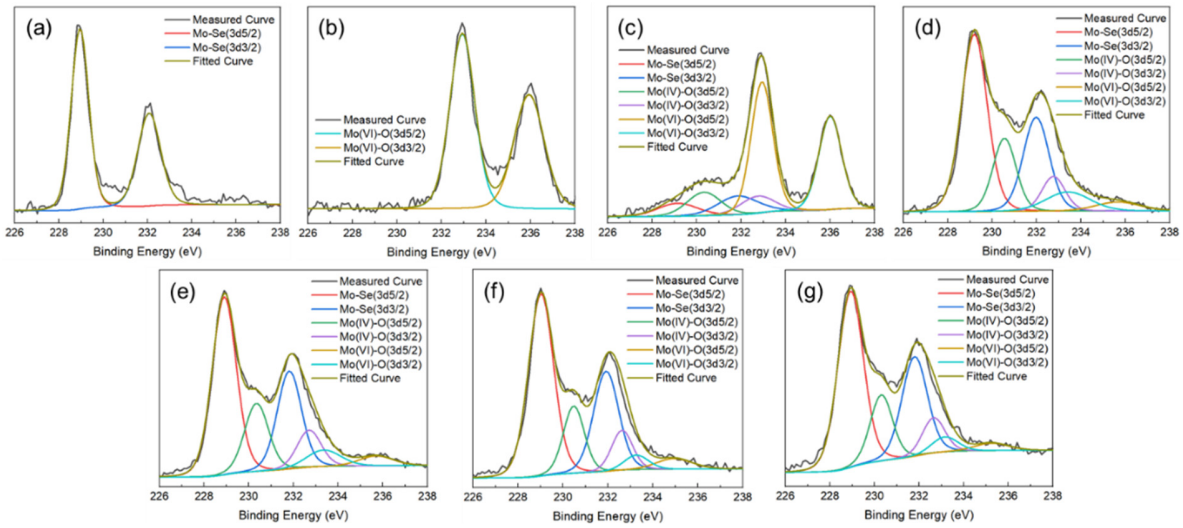


**Figure 7.4.** Mo3d XPS spectra of (a) original $MoSe_2$ powder and nanomaterials prepared in (b) pure water and PEG solutions with concentrations of (c) 0.0625 mg/mL, (d) 0.125 mg/mL, (e) 0.25 mg/mL, (f) 0.5 mg/mL and (g) 1 mg/mL.

**Table 7.1.** Proportions of Mo-Se, Mo(IV)-O and Mo(VI)-O bonds in the nanomaterials prepared in PEG solutions with different concentrations.

| | 0 mg/mL | 0.0625 mg/mL | 0.125 mg/mL | 0.25 mg/mL | 0.5 mg/mL | 1 mg/mL |
|---|---|---|---|---|---|---|
| Mo-Se | 0 | 17% | 66% | 66% | 71% | 71% |
| Mo(IV)-O | 0 | 18% | 24% | 25% | 22% | 24% |
| Mo(VI)-O | 100% | 65% | 10% | 9% | 7% | 5% |

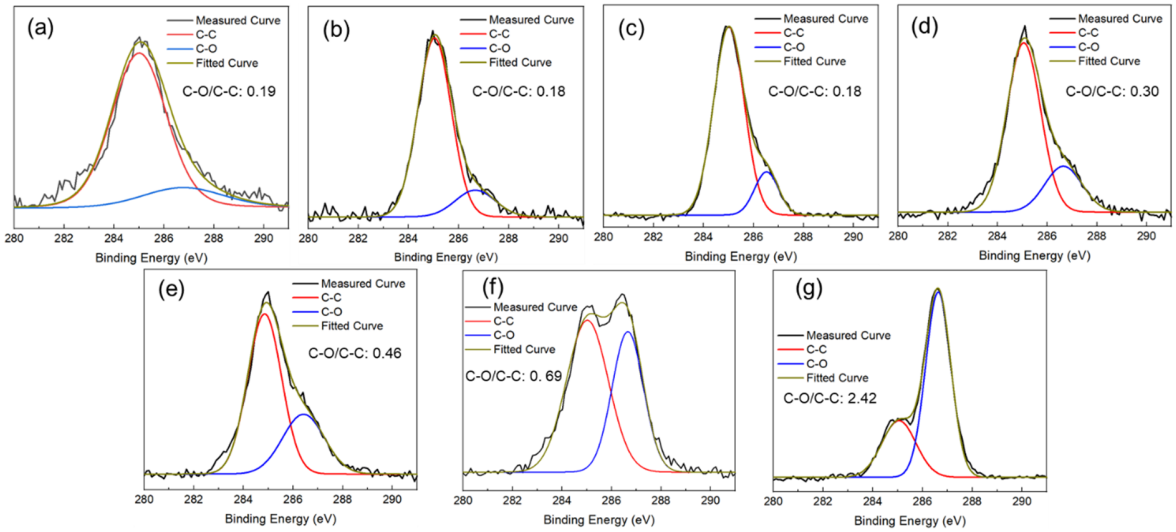


**Figure 7.5.** C1s XPS spectra of (a) original $MoSe_2$ powder and nanomaterials prepared in (b) pure water and PEG solutions with concentrations of (c) 0.0625 mg/mL, (d) 0.125 mg/mL, (e) 0.25 mg/mL, (f) 0.5 mg/mL and (g) 1 mg/mL.

**Figure 7.6** shows the Raman spectra of the original $MoSe_2$ power and nanomaterials prepared in pure water and PEG solutions with different concentrations. The original $MoSe_2$ powder has a peak at 241 $cm^{-1}$ assigned to the $A_{1g}$ vibration mode. This peak disappears in the nanoparticles prepared in pure water and the 0.0625 mg/mL PEG solution. Instead, another two peaks located at 796 $cm^{-1}$ and 962 $cm^{-1}$, which are assigned to Mo-O stretching modes of molybdenum oxide, appear.[280,281] This is consistent with the TEM images (**Figure 7.1e and f**) and the XPS spectra (**Figure 7.4 b and c**). The nanomaterials prepared in the PEG solutions with concentrations greater or equal to 0.125 mg/mL have a primary peak at 255 $cm^{-1}$ (blue dashed line in **Figure 7.6a**) in addition to the $A_{1g}$ peak of $MoSe_2$ (red dashed line in **Figure 7.6a**). The peak at 255 $cm^{-1}$ is probably attributable to blueshift of the $A_{1g}$ peak of oxygen-doped $MoSe_2$ ($MoSe_{2-x}O_x$), which might be formed by partial oxidation and the attachment of PEG to the quantum dots *via* Mo-O bonds during laser ablation. Blueshift of the $A_{1g}$ peak was previously reported in oxygen-doped $MoS_2$.[282,283]

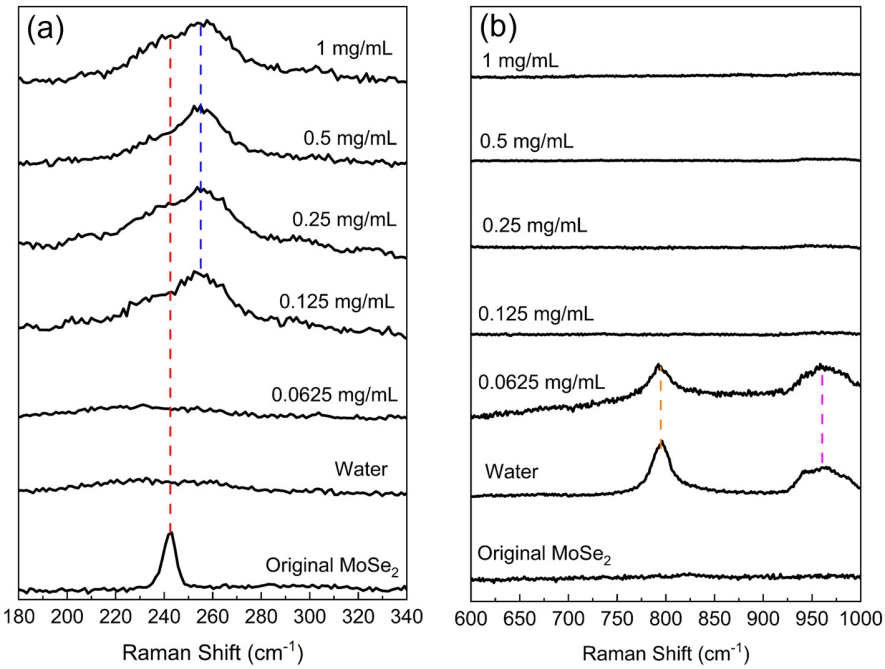


**Figure 7.6.** Raman spectra ranging (a) from 180 to 340 $cm^{-1}$ and (b) from 600 to 1000 $cm^{-1}$ of original $MoSe_2$ powder and nanomaterials prepared in pure water and PEG solutions with different concentrations of PEG.

Therefore, it can be concluded that the addition of a large amount of PEG (no less than 0.125 mg/mL) in water during laser ablation of $MoSe_2$ powder can protect the formed quantum dots from oxidation due to the surface attachment of PEG to the quantum dots *via* Mo-O chemical bonds, which isolated the quantum dots from reactive oxygen species created during the laser ablation. However, a small amount of PEG cannot protect the $MoSe_2$ from oxidation, probably due to insufficient coverage of the formed nanoparticles.

### 7.3.2 Influence of Laser Power

The last section has shown that PEG can be attached to $MoSe_2$ nanomaterials via Mo-O chemical bonds during laser ablation with high power (1.5W) for a long time (30 min). This section examines if different laser powers can affect the attachment of PEG to $MoSe_2$ nanomaterials. Four different laser powers of 0.15 W, 0.3 W, 0.6 W and 1.5 W were selected

to ablate $MoSe_2$ powder dispersed in a 0.5 mg/mL aqueous PEG solution for 10 min. **Figure 7.7a, c, e and g** show that spherical nanoparticles are produced by laser ablation with the powers of 0.15 W, 0.3 W, 0.6 W and 1.5 W, respectively. This is consistent with the results in Chapter 6 that spherical nanoparticles, rather than quantum dots, are produced using short ablation times.

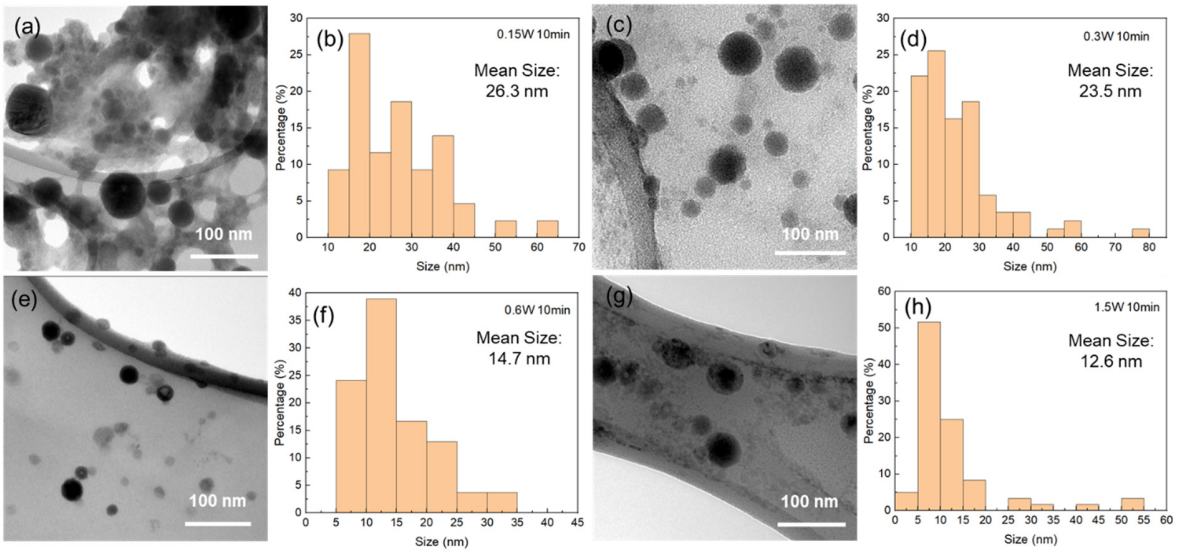


**Figure 7.7.** TEM images of nanoparticles prepared by laser ablation in the 0.5 mg/mL PEG solution with different powers of (a) 0.15 W, (c) 0.3 W, (e) 0.6 W and (g) 1.5 W for 10 min. Size distributions of nanoparticles prepared by laser ablation in the 0.5 mg/mL PEG solution with different powers of (b) 0.15 W, (d) 0.3 W, (f) 0.6 W and (h) 1.5 W for 10 min.

The size distributions of the nanoparticles prepared with the different laser powers are presented in **Figure 7.7b, d, f and h**. The nanoparticles prepared with 0.15 W and 0.3 W laser pulses have mean sizes of 26.3 nm and 23.5 nm, respectively, while the nanoparticles prepared with 0.6 W and 1.5 W laser pulses have smaller mean sizes of 14.7 nm and 12.6 nm, respectively. As detailed in Chapter 6,[193] the large spherical nanoparticles formed by low-power laser ablation are primarily formed by thermodynamic equilibrium melting and evaporation of the ablated particles, while the smaller nanoparticles formed in high-power laser ablation are primarily formed by explosive boiling of the ablated particles.

The Mo3d and C1s XPS spectra of the nanoparticles prepared with different laser powers are presented in **Figure 7.8**. All the nanoparticles have peaks assigned to Mo-Se, Mo(IV)-O, Mo(VI)-O, C-C and C-O bonds. The proportions of Mo-Se, Mo(IV)-O and Mo(VI)-O bonds are listed in **Table 7.2**. It can be seen that the nanoparticles prepared with 0.15 W laser pulses have the highest content of Mo-Se bond and the lowest content of Mo(IV)-O bond. In addition, it also has the highest C-O/C-C ratio (**Figure 7.8e**). As the C-O bond is primarily contributed by surface attached PEG and the Mo(IV)-O bond is contributed by oxygen doping that results from partial oxidation and surface attachment of PEG *via* Mo-O chemical bonds, it is reasonable to attribute the lower content of Mo(IV)-O bond and higher C-O/C-C ratio to the surface attachment of PEG *via* van der Waals force. When the laser power increases to 0.3 W, the proportion of Mo(IV)-O and Mo(VI)-O bonds increases, suggesting increased oxidation caused by increased reactive oxygen species as a result of increased laser power. Even though the surface attachment of PEG to the nanoparticles is still high (high C-O/C-C ratio), the oxidation increases probably because most PEG molecules were attached to the nanoparticles *via* van der Waals force, which could not effectively suppress oxidation. When the laser power increases above 0.6 W, the Mo(IV)-O bond signal increases whereas the Mo(VI)-O bond signal decreases. This might be caused by increased surface attachment of PEG to the nanoparticles *via* Mo-O chemical bonds which prevented further oxidation of the nanoparticles. Meanwhile, it is interesting to find that the C-O/C-C ratio decreases with increasing laser power. This might be caused by fragmentation of PEG chains under high-power ablation, such that the PEG molecules attached to the nanoparticles became shorter but could still protect the nanoparticles from further oxidation, as long as they were attached to the nanoparticles *via* chemical bonds. Additionally, it is also interesting to find that the proportion of Mo-O bonds, especially the Mo(IV)-O bond, is larger in nanoparticles prepared with shorter ablation time (1.5 W, 10 min, 0.5 mg/mL PEG) than in quantum dots prepared with longer ablation time (1.5 W, 30 min, 0.5 mg/mL PEG) by comparing **Table 7.1 and 7.2**. This might be caused by the ablation of the surface attached PEG in the long-time ablation process, as the C-O/C-C ratio also drops in the quantum dots prepared by laser ablation for 30 min.

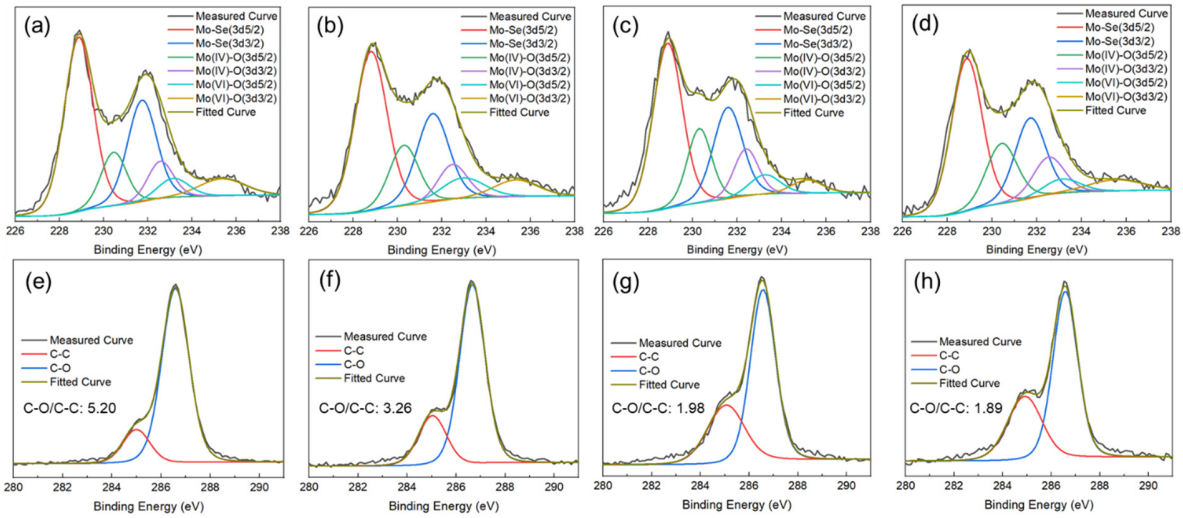


**Figure 7.8.** Mo3d XPS spectra of the nanoparticles prepared by laser ablation in the 0.5 mg/mL PEG solution with different powers of (a) 0.15 W, (b) 0.3 W, (c) 0.6 W and (d) 1.5 W for 10 min. C1s XPS spectra of the nanoparticles prepared by laser ablation with different powers of (e) 0.15 W, (f) 0.3 W, (g) 0.6 W and (h) 1.5 W for 10 min.

**Table 7.2.** Proportions of Mo-Se, Mo(IV)-O and Mo(VI)-O bonds in the nanoparticles prepared in the 0.5 mg/mL PEG solution by laser ablation with different powers for 10 min.

| | 0.15 W | 0.3 W | 0.6 W | 1.5 W |
|---|---|---|---|---|
| Mo-Se | 69% | 64% | 65% | 63% |
| Mo(IV)-O | 20% | 23% | 26% | 27% |
| Mo(VI)-O | 11% | 13% | 9% | 10% |

The Raman spectra of the nanoparticles prepared by laser ablation with different powers are shown in **Figure 7.9**. The nanoparticles prepared with 0.15 W laser pulses show the $A_{1g}$ peak at 241 $cm^{-1}$. This peak gradually decreases with increasing laser power, while the peak at 255 $cm^{-1}$ assigned to the $A_{1g}$ vibration mode of oxygen-doped $MoSe_2$ increases. This

agrees with the change in the proportion of Mo(IV)-O bonds, as shown in **Table 7.2**, implying more PEG were attached to the nanoparticles *via* Mo-O chemical bonds with increasing laser power.

Therefore, it can be concluded that $MoSe_2$ nanoparticles prepared by laser ablation in PEG solutions can attach PEG *via* either van der Waals force or Mo-O chemical bonds. Increased laser power led to more PEG attached to the nanoparticles *via* Mo-O chemical bonds, which led to the suppression of further oxidation of the nanoparticles.

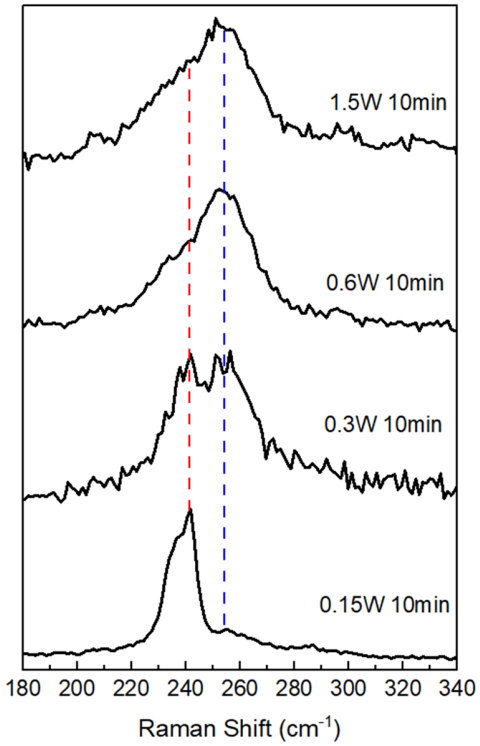


**Figure 7.9.** Raman spectra of the nanoparticles prepared by laser ablation in the 0.5 mg/mL PEG solution with different powers for 10 min.

### 7.3.3 Photothermal Conversion Efficiencies of the PEGylated Nanoparticles.

PTCEs of the PEGylated $MoSe_2$ nanoparticles were measured to evaluate the influence of surface attachment of PEG on their PTCEs. The concentration of $MoSe_2$ in all the measured samples was 0.11 mM. The sample prepared by laser ablation for 10 min in the 0.5 mg/mL

PEG solution with a low laser power of 0.15 W was not measured because it had a large amount of sediment caused by the unablated bulk powder particles. The temperature changes of the samples prepared in PEG solutions with different concentrations and different laser powers after being illuminated by an 808 nm laser beam (2.39 W/cm$^2$) for 10 min followed by cooling for another 10 min are presented in **Figure 7.10 a and b** respectively.

It is found in **Figure 7.10a** that the temperature of water and PEG solution (0.5 mg/mL) only increases by 0.7 °C and 0.5 °C respectively after laser illumination for 10 min, suggesting that PEG had no contribution to the heat generation upon NIR light illumination. The temperature changes of the samples prepared in pure water and the 0.0625 mg/mL PEG solution are also tiny with only 0.9 °C and 0.7 °C, respectively, since most nanoparticles inside these solutions have been oxidized into $MoO_3$ which cannot contribute to heat generation upon NIR laser illumination.[196] The temperature of the samples prepared in PEG solutions with concentrations of 0.125 mg/mL, 0.25 mg/mL, 0.5 mg/mL and 1 mg/mL increases by 7.5 °C, 9.3 °C, 14 °C and 14.9 °C, respectively. The higher temperature changes of the samples prepared in the 0.5 mg/mL and 1 mg/mL PEG solutions, in contrast to the other two samples, are probably attributable to higher NIR light absorption as shown in **Figure 7.10c.** This is consistent with the bandgap measurements (**Table 7.3**); the nanoparticles prepared in the 0.5 mg/mL and 1 mg/mL PEG solutions have lower bandgaps of around 1.1 eV while the nanoparticles prepared in the 0.125 mg/mL and 0.25 mg/mL PEG solutions have bandgaps of around 1.38 eV. The bandgaps of the samples were measured using Tauc plots, which are presented in **Appendix B (Figure B1)**. Considering that the sizes of the quantum dots prepared by laser ablation for 30 min at 1.5 W are close to each other (**Figure 7.3**), the higher bandgaps of the quantum dots prepared in the PEG solutions with low concentrations might be caused by more significant oxidation, as shown in **Table 7.1**. The PTCEs of the quantum dots prepared in the PEG solutions with low concentrations are around 42.5%, while the PTCEs of the quantum dots prepared in the PEG solutions with high concentrations are around 44%, as shown in **Table 7.3**. This is consistent with the PTCE of $MoSe_2$ quantum dots prepared by probe sonication (46.5%),[272] and higher than many other

TMDC nanomaterials such as $MoS_2$ (24.4%,[7] 27.6%[10]), $WS_2$ (32.8%,[59] 35%[60]), $MoTe_2$ (33.8%),[67] and $WSe_2$ (35.1%,[64] 38.3%[65]).

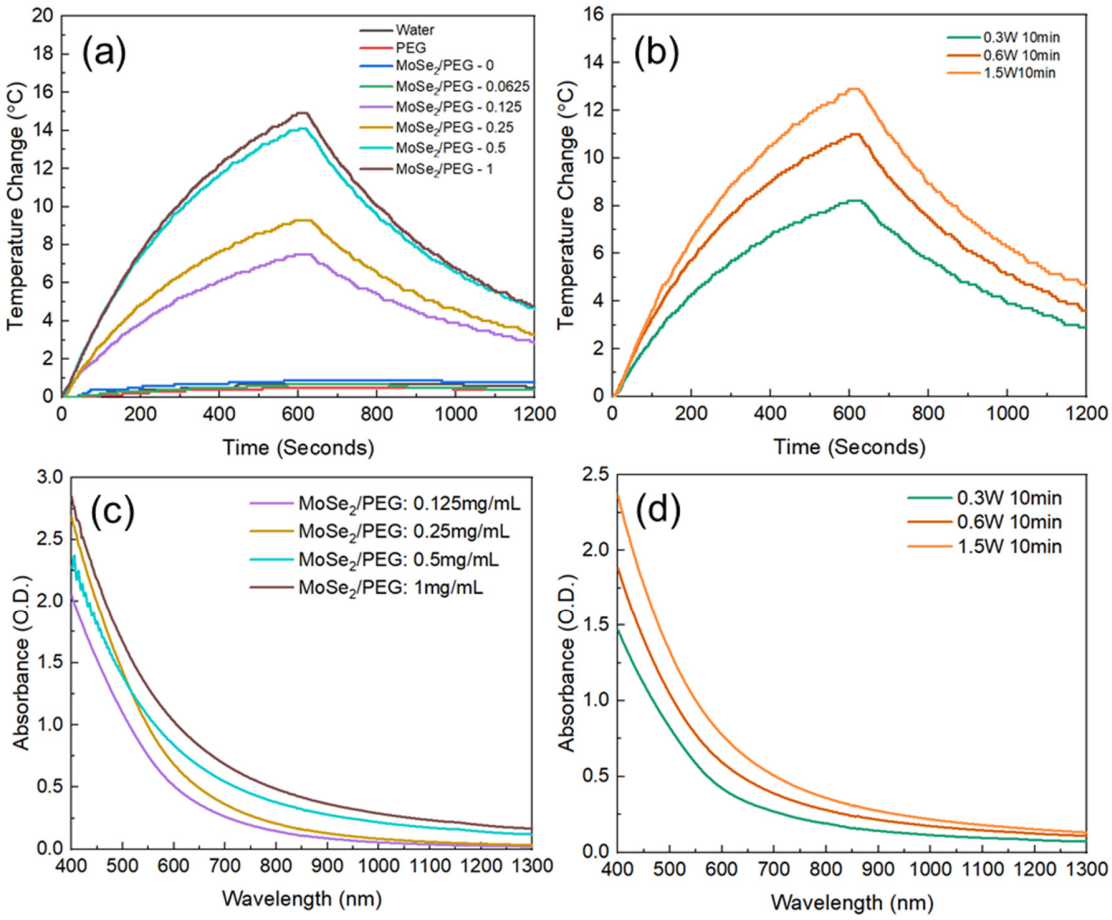


**Figure 7.10.** Temperature change curves of (a) water, PEG solution (0.5 mg/mL) and samples prepared by laser ablation (1.5 W, 30 min) in water and PEG solutions with different concentrations, and (b) samples prepared by laser ablation for 10 min with different laser powers in the 0.5 mg/mL PEG solution after being illuminated by an 808 nm laser beam for 10 min followed by cooling for another 10 min. UV-vis-NIR absorbance spectra of (c) the quantum dots prepared by laser ablation (1.5 W, 30 min) in PEG solutions with different concentrations and (d) the nanoparticles prepared by laser ablation with different laser powers in the 0.5 mg/mL PEG solution.

**Table 7.3.** Summary of bandgaps, Urbach energy, optical absorbance of 808 nm light, maximum temperature increase upon laser illumination and PTCEs of PEGylated $MoSe_2$ nanomaterials.

| Sample | Bandgap | Urbach Energy | Absorbance @808nm | Temperature Increase | PTCE |
|---|---|---|---|---|---|
| Quantum dots prepared in PEG solutions with different concentrations (1.5W 30min) | | | | | |
| PEG:0.125mg/mL | 1.39eV | 0.336eV | 0.140 | 7.5°C | 42.3% |
| PEG:0.25mg/mL | 1.38eV | 0.353eV | 0.200 | 9.3°C | 42.8% |
| PEG:0.5mg/mL | 1.08eV | 0.564eV | 0.368 | 14°C | 44.2% |
| PEG:1mg/mL | 1.10eV | 0.612eV | 0.473 | 14.9°C | 43.8% |
| Spherical nanoparticles prepared in 0.5 mg/mL PEG solutions with different laser powers | | | | | |
| 0.3 W 10min | 1.29eV | 0.620eV | 0.186 | 8.2°C | 36.9% |
| 0.6 W 10min | 1.25eV | 0.641eV | 0.273 | 10.2°C | 38.2% |
| 1.5 W 10min | 1.25eV | 0.663eV | 0.360 | 12.9°C | 40.9% |

As shown in **Figure 7.10b**, the temperature of the samples prepared in the 0.5 mg/mL PEG solution with different laser powers of 0.3 W, 0.6 W and 1.5 W increases by 8.2°C, 10.2°C and 12.9°C, respectively. Similar to the $MoSe_2$ quantum dots, the increased temperature change of the samples prepared with higher laser ablation powers could be attributable to the higher absorbance of NIR light (**Figure 7.10d**). The PTCEs of the samples are listed in **Table 7.3**. The PTCE increases with laser ablation power with the highest value of 40.9% obtained in the sample prepared with the laser power of 1.5 W. It is interesting to find in **Table 7.3** that the bandgaps of the nanoparticles prepared with 0.6 W and 1.5 W laser pulses are both 1.25 eV, slightly smaller than that of the nanoparticles prepared with 0.3 W laser pulses (1.29 eV). The higher bandgap of the nanoparticles prepared with 0.3 W laser pulses

might be caused by more oxidation, as shown in **Table 7.2**. As the bandgaps are close to each other, the increased PTCE and absorbance of NIR light could be attributable to enhanced sub-bandgap absorption of photons and nonradiative recombination of the excited carriers because of extended tails of density of electronic states in the forbidden gap (Urbach tails), as discussed in Chapter 6. The Urbach energies of the nanoparticles were calculated by the method introduced in Section 6.3.5. The plots to determine the Urbach energies of the nanoparticles are presented in **Figure B2**. A higher Urbach energy suggests higher sub-bandgap absorption. As shown in **Table 7.3**, the Urbach energy of the spherical nanoparticles also increases with the laser ablation power, consistent with the previous research in Chapter 6 that higher laser ablation power introduces more defects into the nanoparticles, which increase the sub-bandgap absorption and facilitate the non-radiative recombination of excited carriers.[193]

It is also interesting to note that the PTCEs of the $MoSe_2$ quantum dots prepared by laser ablation for 30 min with 1.5 W laser pulses are overall larger than those of the $MoSe_2$ spherical nanoparticles prepared by laser ablation for 10 min. Quantum dots are usually considered to have lower electron relaxation rates after excitation, as the lattice vibrations cannot couple widely separated electronic states.[284] However, much research has also found that many colloidal quantum dots with surface passivation or attachment of ligands have much faster carrier relaxation in the timescale of picoseconds or even sub-picosecond like bulk materials thanks to non-diabatic decay channels.[285–290] Meanwhile, quantum dots have larger absorption cross-sections and can generate multiple excitons after single photon absorption.[289] The transformation of multiple excitons to single excitons can also generate heat.[289] Therefore, the higher PTCEs of the $MoSe_2$ quantum dots might be attributed to larger absorption cross-sections, multiple electron decay channels and multiple exciton generation.

## 7.4 Conclusions

A one-pot synthesis method was developed to prepare PEGylated $MoSe_2$ nanoparticles by femtosecond laser ablation of $MoSe_2$ powder particles in aqueous PEG solutions. $MoSe_2$ quantum dots were synthesized by laser ablation in PEG solutions with 1.5 W laser pulses for

30 min. However, $MoSe_2$ powder could be oxidized and transformed into $MoO_3$ when the PEG concentration was low, like laser ablation in pure water. When the PEG concentration was higher than 0.125 mg/mL, the oxidation was suppressed. Analysis of the XPS spectra of the synthesized nanoparticles revealed not only a peak for Mo(VI)-O bonds attributed to the formation of $MoO_3$ but also a peak for Mo(IV)-O bonds, which might be caused by partial oxidation or the surface attachment of PEG molecules *via* Mo-O chemical bonds. Increasing the concentration of PEG in solutions during laser ablation led to a reduced proportion of Mo(VI)-O bonds, suggesting surface attachment of PEG to $MoSe_2$ quantum dots can effectively protect them from oxidation during the laser ablation process. Short-time laser ablation of the $MoSe_2$ powder generated spherical nanoparticles. Even though PEG could also be attached to the nanoparticles *via* van der Waals forces, laser ablation with higher power led to more PEG molecules attached to the nanoparticles *via* chemical bonds. It was found that surface attachment of PEG to the nanoparticles *via* van der Waals force could not protect the nanoparticles from oxidation into $MoO_3$ as effectively as the surface attachment *via* chemical bonds. It might be the formation of Mo(IV)-O bonds during surface attachment of PEG that prevents further oxidation. Both the PEGylated $MoSe_2$ quantum dots and spherical nanoparticles demonstrated high PTCEs. However, the PTCEs of the quantum dots were found to be higher than those of the larger spherical nanoparticles. This might be caused by a larger absorption cross-section, multiple electron decay channels and multiple exciton generation.

# Chapter 8

## Conclusions and Future Work

### 8.1 Conclusions

This work developed techniques to prepare molybdenum-based nanomaterials with high photothermal conversion efficiencies (PTCEs) by femtosecond laser ablation in various liquids. Pulsed laser ablation in liquid (PLAL) has been widely researched in past decades as an alternative to conventional synthesis methods to prepare single-element nanomaterials such as noble metals and basic oxide nanomaterials like aluminum oxide and iron oxide. It is fast to prepare nanoparticles, easy to set up and usually regarded as a "green chemistry" method as few contaminants are introduced from precursors. This work broadened the application of this technique to prepare more nanomaterials for photothermal cancer therapy.

The PLAL technique was applied to prepare more complex molybdenum oxide nanomaterials including substoichiometric molybdenum oxide ($MoO_{3-X}$) nanosheets (Chapter 4) and molybdenum blue (MB) nanorings (Chapter 5). $MoO_{3-X}$ nanosheets were synthesized by femtosecond laser ablation of $MoS_2$ powder particles in ethanol/water mixtures. $MoS_2$ was oxidized during the laser ablation. 80 vol.%-90 vol.% is the optimum concentration of ethanol to produce $MoO_{3-X}$. It is attributed to the generation of $H^{3+}$ during the femtosecond laser ablation of ethanol, which is expected to combine with the oxidized $MoS_2$ to form $-OH_2$ radicals. By releasing the $-OH_2$ radicals with the assistance of water molecules, oxygen vacancies are created to form $MoO_{3-X}$. This mechanism can also be used to tune the structure of molybdenum blue (MB) prepared by femtosecond laser ablation of $MoO_3$ powder in water/ethanol mixtures. Femtosecond laser ablation of $MoO_3$ powder in the solvents dissolved $MoO_3$ and created molybdic acid, providing an acidic environment for the formation of MB. The MBs produced by the femtosecond laser ablation were nanorings. It was found that as low as 1% of ethanol in the solvent could produce MB. The MB became darker with higher concentrations of ethanol until 30%, which is attributed to the increased reduction of Mo(VI) to Mo(V) as a result of oxygen vacancies. Further increasing the

concentration of ethanol in the solvent continued increasing the reduction of Mo(VI); however, the synthesized nanomaterials changed from MB to $MoO_{3-X}$. The highest PTCE of the $MoO_{3-X}$ nanosheets and MB nanorings was 33% and 45%, respectively.

Chapter 6 researched the formation mechanisms of spherical $MoSe_2$ nanoparticles using $MoSe_2$ powder particles in isopropyl alcohol. Spherical nanoparticles are usually observed in short-time laser ablation or long-time laser ablation with low powers. It was found that spherical nanoparticles were fragmented from ablated powder particles *via* thermodynamic equilibrium melting and evaporation when the laser power was low, and explosive boiling when the laser power was high. Therefore, in the short-time laser ablation, the nanoparticles produced with high laser powers were smaller than those produced with low powers as the superheated liquid droplets in explosive boiling contained vapor bubbles and experienced further fragmentation caused by expansion of these bubbles. Two kinds of spherical nanoparticles including polycrystalline nanoparticles and onion-structured nanoparticles were observed. The polycrystalline nanoparticles were formed by the combination of nanocrystals ejected by the ablated powder particles, while the onion-structured nanoparticles were formed by nucleation on the surfaces of melted droplets followed by inward growth of {002} planes of $MoSe_2$ along the radial direction of the droplets layer-by-layer. The highest PTCE of the $MoSe_2$ nanoparticles was measured to be 38% thanks to enhanced sub-bandgap light absorption and non-radiation recombination. To improve the biocompatibility and stability of the produced $MoSe_2$ nanoparticles in aqueous solutions, Chapter 7 developed a one-pot method to prepare PEGylated $MoSe_2$ spherical nanoparticles by femtosecond laser ablation of $MoSe_2$ powder particles and PEG together in water. It was found that PEG can be attached to the produced nanoparticles *via* Mo-O chemical bonds and that the surface attachment of the PEG *via* Mo-O bonds can suppress further oxidation of the nanoparticles. Additionally, laser ablation for a longer time (30 min) produced PEGylated $MoSe_2$ quantum dots showing a PTCE of 44%, which was larger than that observed for the larger spherical nanoparticles. This can be attributed to a larger absorption cross-section, multiple electron decay channels and multiple exciton generation in the quantum dots.

The high PTCEs of the Mo-based nanomaterials prepared in this thesis indicate they are potential candidates for photothermal cancer therapy. The $MoO_{3-X}$ nanosheets can also be used as a photosensitizer for photodynamic therapy, which produces reactive oxygen species upon laser illumination to kill cancer cells. Therefore, the $MoO_{3-X}$ nanosheets have the potential to be used for synergistic cancer therapy combining both photothermal therapy and photodynamic therapy, which is expected to increase the efficacy of cancer treatment. When loading anti-cancer drugs on the nanosheets, chemotherapy is also engaged into the synergistic therapy.

## 8.2 Contributions

The PTCEs of the Mo-based nanomaterials prepared in this thesis were found to be consistent with the same nanomaterials prepared by conventional wet-chemistry methods, and overall higher than many other popular PTA nanomaterials such as gold nanoparticles, carbon dots, graphene nanosheets, black phosphorus, $MoS_2$ and $WS_2$. Given the simpler and quicker preparation of nanomaterials, the PLAL technique is a novel and promising method. Additionally, Chapter 4 and 5 report the synthesis of $MoO_{3-X}$ nanosheets and MB nanorings, which were prepared by reactive ablation in liquid where chemical reactions were involved. This demonstrates that the PLAL technique can be used to prepare more novel nanomaterials with complex shapes and stoichiometries than simple ablation. Moreover, Chapter 6 reports detailed research about the formation mechanisms of spherical $MoSe_2$ nanoparticles prepared by femtosecond laser ablation of powder in liquid for the first time. It provides insight into the approaches to research the ablation of powders in liquid (examination of the ablated powders) and the formation mechanisms of other TMDC nanoparticles including both the onion-structured nanoparticles and polycrystalline nanoparticles. Chapter 7 reports the in-situ PEGylation of $MoSe_2$ quantum dots and nanoparticles. The one-pot synthesis method saves time for surface functionalization. It was also found that the type of bonding between PEG molecules and the $MoSe_2$ nanomaterials is dependent on laser power. Only the Mo(VI)-O chemical bonds between the PEG molecules and the $MoSe_2$ nanomaterials, formed preferably at high laser powers, can effectively suppress the oxidation of the nanomaterials.

## 8.3 Future Work

First, the PTCE measurement method can be improved. The equation to calculate PTCE introduced in Chapter 3 is only valid when the temperature increase of tested samples is lower than 11 °C, where the heat transfer approach between the tested sample and the environment is limited to heat conduction. The current measurement setup, which contains 1 mL of liquid in a cuvette, can easily increase the tested sample to a higher temperature. Therefore, it is more suitable to measure the PTCE of the tested sample by focusing a laser beam on a small droplet hanging on a pipette tip, and a thermographic camera can be used to monitor the temperature change. In this way, the temperature increase can be well-controlled to below 11 °C due to the small amount of PTAs in the sample. Additionally, the incident laser beam directly reacts with the tested sample without passing through cuvette walls such that all the generated heat is caused by the PTAs and solvents. Moreover, the temperature measured by a thermographic camera will be more accurate, especially in the area around the laser-focused point.

Second, the merit of evaluating the photothermal conversion performance of PTAs can be revised. The PTCE measured in this thesis is the intrinsic efficiency. The clinic application of photothermal therapy requires not only high intrinsic PTCE but also high absorption of NIR light. Therefore, the extrinsic PTCE which equals the intrinsic PTCE multiplied by the absorbance of the PTAs is more appropriate to evaluate the photothermal conversion performance of the PTAs.

Third, the toxicity and the effectiveness of the photothermal therapy of the laser-synthesized nanomaterials should also be evaluated *via* cytotoxicity, *in-vitro*, and *in-vivo* tests. When laser ablating powders in organic solvents or aqueous solvents containing organic molecules like PEG, complex chemical reactions might be involved to form new chemical compounds thanks to the extreme plasma environment during the laser ablation. The newly formed compounds mixed in the synthesized nanomaterials may be toxic to human cells. Therefore, it is necessary to do cytotoxicity tests to prove that the laser-synthesized nanomaterials are non-toxic. After that, the photothermal conversion

performance of the laser-synthesized nanomaterials should be further evaluated in cell-culture media via *in-vitro* and *in-vivo* tests.

Fourth, light-matter interactions during the PLAL process can be further researched with in-situ characterization methods. In this thesis, light-matter interactions during the laser ablation were researched by examining the final products. It will be more helpful to directly analyze the ablation process when equipped with in-situ characterization techniques such as optical emission spectroscopy, dynamic light scattering and Shadowgraphy.

Finally,, more efforts can be devoted to synthesizing nanomaterials other than quantum dots and spherical nanoparticles such as nanorods and nanobelts. These non-spherical nanomaterials were occasionally observed during the laser ablation, but their formation mechanisms are still unknown. In addition, these nanomaterials are always mixed with spherical nanomaterials or quantum dots. Therefore, more efforts are needed to explore their formation mechanisms and purify the nanomaterials with different shapes.

## References


(1) Urruticoechea, A.; Alemany, R.; Balart, J.; Villanueva, A.; Vinals, F.; Capella, G. Recent Advances in Cancer Therapy: An Overview. *Curr. Pharm. Des.* **2010**, *16* (1), 3–10.

(2) Chen, J.; Fan, T.; Xie, Z.; Zeng, Q.; Xue, P.; Zheng, T.; Chen, Y.; Luo, X.; Zhang, H. Advances in Nanomaterials for Photodynamic Therapy Applications: Status and Challenges. *Biomaterials* **2020**, *237*, 119827.

(3) Fernandes, N.; Rodrigues, C. F.; Moreira, A. F.; Correia, I. J. Overview of the Application of Inorganic Nanomaterials in Cancer Photothermal Therapy. *Biomater. Sci.* **2020**, *8* (11), 2990–3020.

(4) Li, Z.; Huang, H.; Tang, S.; Li, Y.; Yu, X. F.; Wang, H.; Li, P.; Sun, Z.; Zhang, H.; Liu, C.; Chu, P. K. Small Gold Nanorods Laden Macrophages for Enhanced Tumor Coverage in Photothermal Therapy. *Biomaterials* **2016**, *74*, 144–154.

(5) Huang, S.; Peng, S.; Wang, Q.; Hu, Q.; Zhang, R.; Liu, L.; Liu, Q.; Lin, J.; Zhou, Q. Gold Nanorods Conjugated with Biocompatible Zwitterionic Polypeptide for Combined Chemo-Photothermal Therapy of Cervical Cancer. *Colloids Surfaces B Biointerfaces* **2021**, *207*, 112014.

(6) Ma, K.; Li, Y.; Wang, Z.; Chen, Y.; Zhang, X.; Chen, C.; Yu, H.; Huang, J.; Yang, Z.; Wang, X.; Wang, Z. Core-Shell Gold Nanorod@Layered Double Hydroxide Nanomaterial with Highly Efficient Photothermal Conversion and Its Application in Antibacterial and Tumor Therapy. *ACS Appl. Mater. Interfaces* **2019**, *11* (33), 29630–29640.

(7) Yin, W.; Yan, L.; Yu, J.; Tian, G.; Zhou, L.; Zheng, X.; Zhang, X.; Yong, Y.; Li, J.; Gu, Z.; Zhao, Y. High-Throughput Synthesis of Single-Layer MoS 2 Nanosheets as a Near-Infrared Photothermal-Triggered Drug Delivery for Effective Cancer Therapy. *ACS Nano* **2014**, *8* (7), 6922–6933.

(8) Liu, T.; Wang, C.; Gu, X.; Gong, H.; Cheng, L.; Shi, X.; Feng, L.; Sun, B.; Liu, Z. Drug Delivery with PEGylated $MoS_2$ Nano-Sheets for Combined Photothermal and Chemotherapy of Cancer. *Adv. Mater.* **2014**, *26* (21), 3433–3440.

(9) Chen, L.; Feng, Y.; Zhou, X.; Zhang, Q.; Nie, W.; Wang, W.; Zhang, Y.; He, C. One-Pot Synthesis of $MoS_2$ Nanoflakes with Desirable Degradability for Photothermal Cancer Therapy. *ACS Appl. Mater. Interfaces* **2017**, *9* (20), 17347–17358.

(10) Feng, W.; Chen, L.; Qin, M.; Zhou, X.; Zhang, Q.; Miao, Y.; Qiu, K.; Zhang, Y.; He, C. Flower-like PEGylated $MoS_2$ Nanoflakes for near-Infrared Photothermal Cancer Therapy. *Sci. Rep.* **2015**, *5* (1), 17422.

(11) Wang, S.; Li, K.; Chen, Y.; Chen, H.; Ma, M.; Feng, J.; Zhao, Q.; Shi, J. Biocompatible PEGylated $MoS_2$ Nanosheets: Controllable Bottom-up Synthesis and Highly Efficient Photothermal Regression of Tumor. *Biomaterials* **2015**, *39*, 206–217.

(12) Ding, D.; Guo, W.; Guo, C.; Sun, J.; Zheng, N.; Wang, F.; Yan, M.; Liu, S. $MoO_{3-X}$ Quantum Dots for Photoacoustic Imaging Guided Photothermal/Photodynamic Cancer Treatment. *Nanoscale* **2017**, *9* (5), 2020–2029.

(13) Bao, T.; Yin, W.; Zheng, X.; Zhang, X.; Yu, J.; Dong, X.; Yong, Y.; Gao, F.; Yan, L.; Gu, Z.; et al. One-Pot Synthesis of PEGylated Plasmonic $MoO_{3-X}$ Hollow Nanospheres for Photoacoustic Imaging Guided Chemo-Photothermal Combinational Therapy of Cancer. *Biomaterials* **2016**, *76*, 11–24.

(14) Lin, H.; Wang, X.; Yu, L.; Chen, Y.; Shi, J. Two-Dimensional Ultrathin MXene Ceramic Nanosheets for Photothermal Conversion. *Nano Lett.* **2016**, *17* (1), 384–391.

(15) Dai, C.; Chen, Y.; Jing, X.; Xiang, L.; Yang, D.; Lin, H.; Liu, Z.; Han, X.; Wu, R. Two-Dimensional Tantalum Carbide (MXenes) Composite Nanosheets for Multiple Imaging-Guided Photothermal Tumor Ablation. *ACS Nano* **2017**, *11* (12), 12696–12712.

(16) Yang, K.; Zhang, S.; Zhang, G.; Sun, X.; Lee, S.-T.; Liu, Z. Graphene in Mice:

Ultrahigh In Vivo Tumor Uptake and Efficient Photothermal Therapy. *Nano Lett.* **2010**, *10* (9), 3318–3323.

(17) Robinson, J. T.; Tabakman, S. M.; Liang, Y.; Wang, H.; Sanchez Casalongue, H.; Vinh, D.; Dai, H. Ultrasmall Reduced Graphene Oxide with High Near-Infrared Absorbance for Photothermal Therapy. *J. Am. Chem. Soc.* **2011**, *133* (17), 6825–6831.

(18) Li, L.; Rashidi, L. H.; Yao, M.; Ma, L.; Chen, L.; Zhang, J.; Zhang, Y.; Chen, W. CuS Nanoagents for Photodynamic and Photothermal Therapies: Phenomena and Possible Mechanisms. *Photodiagnosis Photodyn. Ther.* **2017**, *19*, 5–14.

(19) Chen, W.; Ouyang, J.; Liu, H.; Chen, M.; Zeng, K.; Sheng, J.; Liu, Z.; Han, Y.; Wang, L.; Li, J.; Liu, D.; Liu, Y.; Guo, S. Black Phosphorus Nanosheet-Based Drug Delivery System for Synergistic Photodynamic/Photothermal/Chemotherapy of Cancer. *Adv. Mater.* **2017**, *29* (5), 1603864.

(20) Wang, S.; Weng, J.; Fu, X.; Lin, J.; Fan, W.; Lu, N.; Qu, J.; Chen, S.; Wang, T.; Huang, P. Black Phosphorus Nanosheets for Mild Hyperthermia-Enhanced Chemotherapy and Chemo-Photothermal Combination Therapy. *Nanotheranostics* **2017**, *1* (2), 208–216.

(21) Yogesh, G. K.; Shukla, S.; Sastikumar, D.; Koinkar, P. Progress in Pulsed Laser Ablation in Liquid (PLAL) Technique for the Synthesis of Carbon Nanomaterials: A Review. *Appl. Phys. A: Mater. Sci. Process.* **2021**, *127*, 810

(22) Amans, D.; Cai, W.; Barcikowski, S. Status and Demand of Research to Bring Laser Generation of Nanoparticles in Liquids to Maturity. *Appl. Surf. Sci.* **2019**, *488*, 445–454.

(23) Tan, D.; Zhou, S.; Qiu, J.; Khusro, N. Preparation of Functional Nanomaterials with Femtosecond Laser Ablation in Solution. *J. Photochem. Photobiol. C Photochem. Rev.* **2013**, *17*, 50–68.

(24) Beik, J.; Abed, Z.; Ghoreishi, F. S.; Hosseini-Nami, S.; Mehrzadi, S.; Shakeri-Zadeh,

A.; Kamrava, S. K. Nanotechnology in Hyperthermia Cancer Therapy: From Fundamental Principles to Advanced Applications. *J. Control. Release* **2016**, *235*, 205–221.

(25) Ye, F.; Ayub, A.; Chang, D.; Chernikov, R.; Chen, Q.; Karimi, R.; Wettig, S.; Sanderson, J.; Musselman, K. P. Molybdenum Blues with Tunable Light Absorption Synthesized by Femtosecond Laser Irradiation of Molybdenum Trioxide in Water/Ethanol Mixtures. *Adv. Opt. Mater.* **2022**, *10* (23), 2201304.

(26) Wang, B.; He, X.; Zhang, Z.; Zhao, Y.; Feng, W. Metabolism of Nanomaterials in Vivo : Blood Circulation and Organ Clearance. *Acc. Chem. Res.* **2013**, *46* (3), 761–769.

(27) Jaque, D.; Martínez Maestro, L.; Del Rosal, B.; Haro-Gonzalez, P.; Benayas, A.; Plaza, J. L.; Martín Rodríguez, E.; García Solé, J. Nanoparticles for Photothermal Therapies. *Nanoscale* **2014**, *6* (16), 9494–9530.

(28) Kelly, K. L.; Coronado, E.; Zhao, L. L.; Schatz, G. C. The Optical Properties of Metal Nanoparticles: The Influence of Size, Shape, and Dielectric Environment. *J. Phys. Chem. B* **2003**, *107* (3), 668–677.

(29) Papavassiliou, G. C. Optical Properties of Small Inorganic and Organic Metal Particles. *Prog. Solid St. Chem.* **1979**, *12*, 185–271.

(30) Petryayeva, E.; Krull, U. J. Localized Surface Plasmon Resonance: Nanostructures, Bioassays and Biosensing - A Review. *Anal. Chim. Acta* **2011**, *706* (1), 8–24.

(31) Mie, G. Beiträge Zur Optik Trüber Medien, Speziell Kolloidaler Metallösungen. *Ann. Phys.* **1908**, *330* (3), 377–445.

(32) Link, S.; El-Sayed, M. A. Size and Temperature Dependence of the Plasmon Absorption of Colloidal Gold Nanoparticles. *J. Phys. Chem. B* **1999**, *103* (21), 4212–4217.

(33) Link, S.; El-Sayed, M. A. Shape and Size Dependence of Radiative, Non-Radiative

and Photothermal Properties of Gold Nanocrystals. *Int. Rev. Phys. Chem.* **2000**, *19* (3), 409–453.

(34) Huang, X.; Neretina, S.; El-Sayed, M. A. Gold Nanorods: From Synthesis and Properties to Biological and Biomedical Applications. *Adv. Mater.* **2009**, *21* (48), 4880–4910.

(35) Loo, C.; Lin, A.; Hirsch, L.; Lee, M.-H.; Barton, J.; Halas, N.; West, J.; Drezek, R. Nanoshell-Enabled Photonics-Based Imaging and Therapy of Cancer. *Technol. Cancer Res. Treat.* **2004**, *3* (1), 33–40.

(36) Chen, J.; Wiley, B.; Li, Z.-Y.; Campbell, D.; Saeki, F.; Cang, H.; Au, L.; Lee, J.; Li, X.; Xia, Y. Gold Nanocages: Engineering Their Structure for Biomedical Applications. *Adv. Mater.* **2005**, *17* (18), 2255–2261.

(37) Yuan, H.; Khoury, C. G.; Wilson, C. M.; Grant, G. A.; Bennett, A. J.; Vo-Dinh, T. In Vivo Particle Tracking and Photothermal Ablation Using Plasmon-Resonant Gold Nanostars. *Nanomedicine Nanotechnology, Biol. Med.* **2012**, *8* (8), 1355–1363.

(38) Wang, Y.; Yang, Y.; Yang, L.; Lin, Y.; Tian, Y.; Ni, Q.; Wang, S.; Ju, H.; Guo, J.; Lu, G. Gold Nanostar@Polyaniline Theranostic Agent with High Photothermal Conversion Efficiency for Photoacoustic Imaging-Guided Anticancer Phototherapy at a Low Dosage. *ACS Appl. Mater. Interfaces* **2022**, *14* (25), 28570–28580.

(39) Sun, Y.; Xia, Y. Mechanistic Study on the Replacement Reaction between Silver Nanostructures and Chloroauric Acid in Aqueous Medium. *J. Am. Chem. Soc.* **2004**, *126* (12), 3892–3901.

(40) Boca, S. C.; Potara, M.; Gabudean, A.-M.; Juhem, A.; Baldeck, P. L.; Astilean, S. Chitosan-Coated Triangular Silver Nanoparticles as a Novel Class of Biocompatible, Highly Effective Photothermal Transducers for in Vitro Cancer Cell Therapy. *Cancer Lett.* **2011**, *311* (2), 131–140.

(41) Dreaden, E. C.; Mwakwari, S. C.; Sodji, Q. H.; Oyelere, A. K.; El-Sayed, M. A.

Tamoxifen-Poly(Ethylene Glycol)-Thiol Gold Nanoparticle Conjugates: Enhanced Potency and Selective Delivery for Breast Cancer Treatment. *Bioconjug. Chem.* **2009**, *20* (12), 2247–2253.

(42) Manthiram, K.; Alivisatos, A. P. Tunable Localized Surface Plasmon Resonances in Tungsten Oxide Nanocrystals. *J. Am. Chem. Soc.* **2012**, *134* (9), 3995–3998.

(43) Salje, E.; Güttler, B. Anderson Transition and Intermediate Polaron Formation in $WO_{3-X}$ Transport Properties and Optical Absorption. *Philos. Mag. B* **1984**, *50* (5), 607–620.

(44) Wu, F.; Zhang, Q.; Sun, B.; Chu, X.; Zhang, M.; She, Z.; Li, Z.; Zhou, N.; Wang, J.; Li, A. $MoO_{3-X}$ Nanosheets-Based Platform for Single NIR Laser Induced Efficient PDT/PTT of Cancer. *J. Control. Release* **2021**, *338*, 46–55.

(45) Song, G.; Hao, J.; Liang, C.; Liu, T.; Gao, M.; Cheng, L.; Hu, J.; Liu, Z. Degradable Molybdenum Oxide Nanosheets with Rapid Clearance and Efficient Tumor Homing Capabilities as a Therapeutic Nanoplatform. *Angew. Chemie - Int. Ed.* **2016**, *55* (6), 2122–2126.

(46) Chen, Z.; Wang, Q.; Wang, H.; Zhang, L.; Song, G.; Song, L.; Hu, J.; Wang, H.; Liu, J.; Zhu, M.; Zhao, D. Ultrathin PEGylated $W_{18}O_{49}$ Nanowires as a New 980 nm-Laser-Driven Photothermal Agent for Efficient Ablation of Cancer Cells In Vivo. *Adv. Mater.* **2013**, *25* (14), 2095–2100.

(47) Li, B.; Zhang, Y.; Zou, R.; Wang, Q.; Zhang, B.; An, L.; Yin, F.; Hua, Y.; Hu, J. Self-Assembled $WO_{3-X}$ Hierarchical Nanostructures for Photothermal Therapy with a 915 nm Laser Rather than the Common 980 nm Laser. *Dalt. Trans.* **2014**, *43* (16), 6244.

(48) Sun, L.; Li, Z.; Su, R.; Wang, Y.; Li, Z.; Du, B.; Sun, Y.; Guan, P.; Besenbacher, F.; Yu, M. Phase-Transition Induced Conversion into a Photothermal Material: Quasi-Metallic $WO_{2.9}$ Nanorods for Solar Water Evaporation and Anticancer Photothermal Therapy. *Angew. Chemie Int. Ed.* **2018**, *57* (33), 10666–10671.

(49) Long, D.-L.; Cronin, L. Advances in Gigantic Polyoxomolybdate Chemistry. In *Advances in Inorganic Chemistry*; 2021; pp 227–267.

(50) Gumerova, N. I.; Rompel, A. Synthesis, Structures and Applications of Electron-Rich Polyoxometalates. *Nat. Rev. Chem.* **2018**, *2* (2), 0112.

(51) Kong, X.; Wan, G.; Li, B.; Wu, L. Recent Advances of Polyoxometalates in Multi-Functional Imaging and Photothermal Therapy. *J. Mater. Chem. B* **2020**, *8* (36), 8189–8206.

(52) Zhang, C.; Bu, W.; Ni, D.; Zuo, C.; Cheng, C.; Li, Q.; Zhang, L.; Wang, Z.; Shi, J. A Polyoxometalate Cluster Paradigm with Self-Adaptive Electronic Structure for Acidity/Reducibility-Specific Photothermal Conversion. *J. Am. Chem. Soc.* **2016**, *138* (26), 8156–8164.

(53) Zhang, S.; Chen, H.; Zhang, G.; Kong, X.; Yin, S.; Li, B.; Wu, L. An Ultra-Small Thermosensitive Nanocomposite with a $Mo_{154}$ -Core as a Comprehensive Platform for NIR-Triggered Photothermal-Chemotherapy. *J. Mater. Chem. B* **2018**, *6* (2), 241–248.

(54) Zhang, S.; Peng, B.; Xue, P.; Kong, X.; Tang, Y.; Wu, L.; Lin, S. Polyoxometalate-Antioxidant Peptide Assembly Materials with NIR-Triggered Photothermal Behaviour and Enhanced Antibacterial Activity. *Soft Matter* **2019**, *15* (27), 5375–5379.

(55) Wang, Q. H.; Kalantar-Zadeh, K.; Kis, A.; Coleman, J. N.; Strano, M. S. Electronics and Optoelectronics of Two-Dimensional Transition Metal Dichalcogenides. *Nat. Nanotechnol.* **2012**, *7* (11), 699–712.

(56) Chou, S. S.; Kaehr, B.; Kim, J.; Foley, B. M.; De, M.; Hopkins, P. E.; Huang, J.; Brinker, C. J.; Dravid, V. P. Chemically Exfoliated $MoS_2$ as Near-Infrared Photothermal Agents. *Angew. Chemie Int. Ed.* **2013**, *52* (15), 4160–4164.

(57) Cheng, L.; Liu, J.; Gu, X.; Gong, H.; Shi, X.; Liu, T.; Wang, C.; Wang, X.; Liu, G.; Xing, H.; Bu, W.; Sun, B.; Liu, Z. PEGylated $WS_2$ Nanosheets as a Multifunctional Theranostic Agent for in Vivo Dual-Modal CT/Photoacoustic Imaging Guided

Photothermal Therapy. *Adv. Mater.* **2014**, *26* (12), 1886–1893.

(58) Zhang, C.; Yong, Y.; Song, L.; Dong, X.; Zhang, X.; Liu, X.; Gu, Z.; Zhao, Y.; Hu, Z. Multifunctional $WS_2$ @Poly(Ethylene Imine) Nanoplatforms for Imaging Guided Gene-Photothermal Synergistic Therapy of Cancer. *Adv. Healthc. Mater.* **2016**, *5* (21), 2776–2787.

(59) Yong, Y.; Zhou, L.; Gu, Z.; Yan, L.; Tian, G.; Zheng, X.; Liu, X.; Zhang, X.; Shi, J.; Cong, W.; Yin, W.; Zhao, Y. $WS_2$ Nanosheet as a New Photosensitizer Carrier for Combined Photodynamic and Photothermal Therapy of Cancer Cells. *Nanoscale* **2014**, *6* (17), 10394–10403.

(60) Cui, X.-Z.; Zhou, Z.-G.; Yang, Y.; Wei, J.; Wang, J.; Wang, M.-W.; Yang, H.; Zhang, Y.-J.; Yang, S.-P. PEGylated $WS_2$ Nanosheets for X-Ray Computed Tomography Imaging and Photothermal Therapy. *Chinese Chem. Lett.* **2015**, *26* (6), 749–754.

(61) Yuwen, L.; Zhou, J.; Zhang, Y.; Zhang, Q.; Shan, J.; Luo, Z.; Weng, L.; Teng, Z.; Wang, L. Aqueous Phase Preparation of Ultrasmall $MoSe_2$ Nanodots for Efficient Photothermal Therapy of Cancer Cells. *Nanoscale* **2016**, *8* (5), 2720–2726.

(62) Lei, Z.; Zhu, W.; Xu, S.; Ding, J.; Wan, J.; Wu, P. Hydrophilic $MoSe_2$ Nanosheets as Effective Photothermal Therapy Agents and Their Application in Smart Devices. *ACS Appl. Mater. Interfaces* **2016**, *8* (32), 20900–20908.

(63) Zhong, C.; Zhao, X.; Wang, L.; Li, Y.; Zhao, Y. Facile Synthesis of Biocompatible $MoSe_2$ Nanoparticles for Efficient Targeted Photothermal Therapy of Human Lung Cancer. *RSC Adv.* **2017**, *7* (12), 7382–7391.

(64) Jia, X.; Bai, J.; Ma, Z.; Jiang, X. BSA-Exfoliated $WSe_2$ Nanosheets as a Photoregulated Carrier for Synergistic Photodynamic/Photothermal Therapy. *J. Mater. Chem. B* **2017**, *5* (2), 269–278.

(65) Adetunji Moses, O.; Khan, M. I.; Fang, Q.; Qin, L.; Rehman, Z. U.; Zhang, Y.; Deng Feng, C.; Ma, Y.; Tang, X.; Wu, C.; et al. PVP Intercalated Metallic $WSe_2$ as NIR

Photothermal Agents for Efficient Tumor Ablation. *Nanotechnology* **2019**, *30* (6), 065102.

(66) Huang, Y.; Zhao, Y.; Liu, Y.; Ye, R.; Chen, L.; Bai, G.; Xu, S. Erbium-Doped Tungsten Selenide Nanosheets with near-Infrared II Emission and Photothermal Conversion. *Chem. Eng. J.* **2021**, *411*, 128610.

(67) Ma, N.; Zhang, M.-K.; Wang, X.-S.; Zhang, L.; Feng, J.; Zhang, X.-Z. NIR Light-Triggered Degradable $MoTe_2$ Nanosheets for Combined Photothermal and Chemotherapy of Cancer. *Adv. Funct. Mater.* **2018**, *28* (31), 1801139.

(68) Hao, J.; Song, G.; Liu, T.; Yi, X.; Yang, K.; Cheng, L.; Liu, Z. In Vivo Long-Term Biodistribution, Excretion, and Toxicology of PEGylated Transition-Metal Dichalcogenides $MS_2$ (M = Mo, W, Ti) Nanosheets. *Adv. Sci.* **2017**, *4* (1), 1600160.

(69) Kim, J.; Kim, F.; Huang, J. Seeing Graphene-Based Sheets. *Mater. Today* **2010**, *13* (3), 28–38.

(70) Naguib, M.; Gogotsi, Y. Synthesis of Two-Dimensional Materials by Selective Extraction. *Acc. Chem. Res.* **2015**, *48* (1), 128–135.

(71) Lin, H.; Gao, S.; Dai, C.; Chen, Y.; Shi, J. A Two-Dimensional Biodegradable Niobium Carbide (MXene) for Photothermal Tumor Eradication in NIR-I and NIR-II Biowindows. *J. Am. Chem. Soc.* **2017**, *139* (45), 16235–16247.

(72) Sun, Z.; Xie, H.; Tang, S.; Yu, X.; Guo, Z.; Shao, J.; Zhang, H.; Huang, H.; Wang, H.; Chu, P. K. Ultrasmall Black Phosphorus Quantum Dots: Synthesis and Use as Photothermal Agents. *Angew. Chemie Int. Ed.* **2015**, *54* (39), 11526–11530.

(73) Shao, J.; Xie, H.; Huang, H.; Li, Z.; Sun, Z.; Xu, Y.; Xiao, Q.; Yu, X.-F.; Zhao, Y.; Zhang, H.; Wang, H.; Chu, P. K. Biodegradable Black Phosphorus-Based Nanospheres for in Vivo Photothermal Cancer Therapy. *Nat. Commun.* **2016**, *7* (1), 12967.

(74) Yang, G.; Liu, Z.; Li, Y.; Hou, Y.; Fei, X.; Su, C.; Wang, S.; Zhuang, Z.; Guo, Z.

Facile Synthesis of Black Phosphorus–Au Nanocomposites for Enhanced Photothermal Cancer Therapy and Surface-Enhanced Raman Scattering Analysis. *Biomater. Sci.* **2017**, *5* (10), 2048–2055.

(75) Wang, L.; Ma, X.; Cai, K.; Li, X. Morphological Effect of Copper Sulfide Nanoparticles on Their near Infrared Laser Activated Photothermal and Photodynamic Performance. *Mater. Res. Express* **2019**, *6* (10), 105406.

(76) Mutalik, C.; Okoro, G.; Krisnawati, D. I.; Jazidie, A.; Rahmawati, E. Q.; Rahayu, D.; Hsu, W.-T.; Kuo, T.-R. Copper Sulfide with Morphology-Dependent Photodynamic and Photothermal Antibacterial Activities. *J. Colloid Interface Sci.* **2022**, *607*, 1825–1835.

(77) Wang, S.; Riedinger, A.; Li, H.; Fu, C.; Liu, H.; Li, L.; Liu, T.; Tan, L.; Barthel, M. J.; Pugliese, G.; Donato, F. D.; D'Abbusco, M. S.; Meng, X.; Manna, L.; Meng, H.; Pellegrino, T. Plasmonic Copper Sulfide Nanocrystals Exhibiting Near-Infrared Photothermal and Photodynamic Therapeutic Effects. *ACS Nano* **2015**, *9* (2), 1788–1800.

(78) Hessel, C. M.; Pattani, V. P.; Rasch, M.; Panthani, M. G.; Koo, B.; Tunnell, J. W.; Korgel, B. A. Copper Selenide Nanocrystals for Photothermal Therapy. *Nano Lett.* **2011**, *11* (6), 2560–2566.

(79) Wang, X.; Miao, Z.; Ma, Y.; Chen, H.; Qian, H.; Zha, Z. One-Pot Solution Synthesis of Shape-Controlled Copper Selenide Nanostructures and Their Potential Applications in Photocatalysis and Photothermal Therapy. *Nanoscale* **2017**, *9* (38), 14512–14519.

(80) Huang, Q.; Hu, S.; Zhuang, J.; Wang, X. $MoO_{3-X}$ -Based Hybrids with Tunable Localized Surface Plasmon Resonances: Chemical Oxidation Driving Transformation from Ultrathin Nanosheets to Nanotubes. *Chem. - A Eur. J.* **2012**, *18* (48), 15283–15287.

(81) Xiao, S. J.; Zhao, X. J.; Hu, P. P.; Chu, Z. J.; Huang, C. Z.; Zhang, L. Highly Photoluminescent Molybdenum Oxide Quantum Dots: One-Pot Synthesis and

Application in 2,4,6-Trinitrotoluene Determination. *ACS Appl. Mater. Interfaces* **2016**, *8* (12), 8184–8191.

(82) Zhan, Y.; Liu, Y.; Zu, H.; Guo, Y.; Wu, S.; Yang, H.; Liu, Z.; Lei, B.; Zhuang, J.; Zhang, X.; Huang, D.; Hu, C. Phase-Controlled Synthesis of Molybdenum Oxide Nanoparticles for Surface Enhanced Raman Scattering and Photothermal Therapy. *Nanoscale* **2018**, *10* (13), 5997–6004.

(83) Alsaif, M. M. Y. A.; Latham, K.; Field, M. R.; Yao, D. D.; Medehkar, N. V.; Beane, G. A.; Kaner, R. B.; Russo, S. P.; Ou, J. Z.; Kalantar-zadeh, K. Tunable Plasmon Resonances in Two-Dimensional Molybdenum Oxide Nanoflakes. *Adv. Mater.* **2014**, *26* (23), 3931–3937.

(84) Guo, C.; Yan, P.; Zhu, C.; Wei, C.; Liu, W.; Wu, W.; Wang, X.; Zheng, L.; Wang, J.; Du, Y.; Chen, J.; Xu, Q. Amorphous $MoO_{3-X}$ Nanosheets Prepared by the Reduction of Crystalline $MoO_3$ by Mo Metal for LSPR and Photothermal Conversion. *Chem. Commun.* **2019**, *55* (83), 12527–12530.

(85) Ou, J. Z.; Campbell, J. L.; Yao, D.; Wlodarski, W.; Kalantar-zadeh, K. In Situ Raman Spectroscopy of $H_2$ Gas Interaction with Layered $MoO_3$. *J. Phys. Chem. C* **2011**, *115* (21), 10757–10763.

(86) Zu, H.; Guo, Y.; Yang, H.; Huang, D.; Liu, Z.; Liu, Y.; Hu, C. Rapid Room-Temperature Preparation of $MoO_{3-X}$ Quantum Dots by Ultraviolet Irradiation for Photothermal Treatment and Glucose Detection. *New J. Chem.* **2018**, *42* (23), 18533–18540.

(87) Yamase, T. Photochemical Studies of Alkylammonium Molybdates. Part 9. Structure of Dimagnetic Blue Species Involved in the Photoredox Reaction of $[Mo_7O_{24}]^{6-}$. *J. Chem. Soc. Dalt. Trans.* **1991**, 3055–3063.

(88) Yamase, T. Photo- and Electrochromism of Polyoxometalates and Related Materials. *Chem. Rev.* **1998**, *98* (1), 307–326.

(89) Müller, A.; Serain, C. Soluble Molybdenum Blues“Des Pudels Kern.” *Acc. Chem. Res.* **2000**, *33* (1), 2–10.

(90) Kortz, U.; Pope, M. T. Polyoxometalate-Diphosphate Complexes. 2. Structure of 18-Molybdopyrophosphate, $[(P_2O_7)Mo_{18}O_{54}]^{4-}$, Which Encloses a Linear, Eclipsed Conformation of the Pyrophosphate Anion, and Preliminary Characterization of Its One- and Two-Electron Heteropoly Blues. *Inorg. Chem.* **1994**, *33* (25), 5643–5646.

(91) Xuan, W.; Surman, A. J.; Miras, H. N.; Long, D.-L.; Cronin, L. Controlling the Ring Curvature, Solution Assembly, and Reactivity of Gigantic Molybdenum Blue Wheels. *J. Am. Chem. Soc.* **2014**, *136* (40), 14114–14120.

(92) Shishido, S.; Ozeki, T. The PH Dependent Nuclearity Variation of $\{Mo_{154-x}\}$-Type Polyoxomolybdates and Tectonic Effect on Their Aggregations. *J. Am. Chem. Soc.* **2008**, *130* (32), 10588–10595.

(93) Nakamura, I.; Miras, H. N.; Fujiwara, A.; Fujibayashi, M.; Song, Y.-F.; Cronin, L.; Tsunashima, R. Investigating the Formation of “Molybdenum Blues” with Gel Electrophoresis and Mass Spectrometry. *J. Am. Chem. Soc.* **2015**, *137* (20), 6524–6530.

(94) Müller, A.; Krickemeyer, E.; Meyer, J.; Bögge, H.; Peters, F.; Plass, W.; Diemann, E.; Dillinger, S.; Nonnenbruch, F.; Randerath, M.; et al. $[Mo_{154}(NO)_{14}O_{420}(OH)_{28}(H_2O)_{70}]^{(25\pm5)-}$: A Water-Soluble Big Wheel with More than 700 Atoms and a Relative Molecular Mass of About 24000. *Angew. Chemie Int. Ed. English* **1995**, *34* (19), 2122–2124.

(95) Miras, H. N.; Richmond, C. J.; Long, D.-L.; Cronin, L. Solution-Phase Monitoring of the Structural Evolution of a Molybdenum Blue Nanoring. *J. Am. Chem. Soc.* **2012**, *134* (8), 3816–3824.

(96) Müller, A.; Beugholt, C.; Koop, M.; Das, S. K.; Schmidtmann, M.; Bögge, H. Facile and Optimized Syntheses and Structures of Crystalline Molybdenum Blue Compounds Including One with an Interesting High Degree of Defects:

$Na_{26}[Mo_{142}O_{432}(H_2O)_{58}H_{14}]\cdot ca.300H_2O$ and $Na_{16}[(MoO_3)_{176}(H_2O)_{63}(CH_3OH)_{17}H_{16}]\cdot ca.600H_2O\cdot ca.6CH_3OH$. *Zeitschrift für Anorg. und Allg. Chemie* **1999**, *625* (12), 1960–1962.

(97) Liu, X.; Conte, M.; Weng, W.; He, Q.; Jenkins, R. L.; Watanabe, M.; Morgan, D. J.; Knight, D. W.; Murphy, D. M.; Whiston, K.; Kiely, C. J.; Hutchings, G. J. Molybdenum Blue Nano-Rings: An Effective Catalyst for the Partial Oxidation of Cyclohexane. *Catal. Sci. Technol.* **2015**, *5* (1), 217–227.

(98) Liu, T.; Diemann, E.; Li, H.; Dress, A. W. M.; Müller, A. Self-Assembly in Aqueous Solution of Wheel-Shaped Mo154 Oxide Clusters into Vesicles. *Nature* **2003**, *426* (6962), 59–62.

(99) Bellus, M. Z.; Ceballos, F.; Chiu, H. Y.; Zhao, H. Tightly Bound Trions in Transition Metal Dichalcogenide Heterostructures. *ACS Nano* **2015**, *9* (6), 6459–6464.

(100) Novoselov, K. S.; Geim, A. K.; Morozov, S. V.; Jiang, D.; Zhang, Y.; Dubonos, S. V.; Grigorieva, I. V.; Firsov, A. A. Electric Field in Atomically Thin Carbon Films. *Science.* **2004**, *306* (5696), 666–669.

(101) Coleman, J. N.; Lotya, M.; O'Neill, A.; Bergin, S. D.; King, P. J.; Khan, U.; Young, K.; Gaucher, A.; De, S.; Smith, R. J.; Shvets, I. V.; Arora, S. K.; Stanton, G.; Kim, H.-Y.; Lee, K.; Kim, G. T.; DuesbergG. S.; Hallam, T.; Boland, J. J.; Wang, J. J.; Donegan, J. F.; Grunlan, J. C.; Moriarty, G.; Shmeliov, A.; Nicholls, R. J.; Perkins, J. M.; Grieveson, E. M.; Theuwissen, K.; McComb, D. W.; Nellist, P. D.; Nicolosi, V. Two-Dimensional Nanosheets Produced by Liquid Exfoliation of Layered Materials. *Science.* **2011**, *331* (6017), 568–571.

(102) Loo, A. H.; Bonanni, A.; Sofer, Z.; Pumera, M. Exfoliated Transition Metal Dichalcogenides ($MoS_2$, $MoSe_2$, $WS_2$, $WSe_2$): An Electrochemical Impedance Spectroscopic Investigation. *Electrochem. commun.* **2015**, *50*, 39–42.

(103) Eda, G.; Yamaguchi, H.; Voiry, D.; Fujita, T.; Chen, M.; Chhowalla, M. Photoluminescence from Chemically Exfoliated $MoS_2$. *Nano Lett.* **2011**, *11* (12),

5111–5116.

(104) Zhang, Q.; Mei, L.; Cao, X.; Tang, Y.; Zeng, Z. Intercalation and Exfoliation Chemistries of Transition Metal Dichalcogenides. *J. Mater. Chem. A* **2020**, *8* (31), 15417–15444.

(105) Gao, P.; Wang, L.; Zhang, Y.; Huang, Y.; Liu, K. Atomic-Scale Probing of the Dynamics of Sodium Transport and Intercalation-Induced Phase Transformations in $MoS_2$. *ACS Nano* **2015**, *9* (11), 11296–11301.

(106) Fan, S.; Zou, X.; Du, H.; Gan, L.; Xu, C.; Lv, W.; He, Y.-B.; Yang, Q.-H.; Kang, F.; Li, J. Theoretical Investigation of the Intercalation Chemistry of Lithium/Sodium Ions in Transition Metal Dichalcogenides. *J. Phys. Chem. C* **2017**, *121* (25), 13599–13605.

(107) Zheng, J.; Zhang, H.; Dong, S.; Liu, Y.; Tai Nai, C.; Suk Shin, H.; Young Jeong, H.; Liu, B.; Ping Loh, K. High Yield Exfoliation of Two-Dimensional Chalcogenides Using Sodium Naphthalenide. *Nat. Commun.* **2014**, *5*, 2995.

(108) Chen, X.; Fan, R. Low-Temperature Hydrothermal Synthesis of Transition Metal Dichalcogenides. *Chem. Mater.* **2001**, *13*, 802–805.

(109) Li, N.; Wu, J.; Lu, Y.; Zhao, Z.; Zhang, H.; Li, X.; Zheng, Y.-Z.; Tao, X. Stable Multiphasic 1T/2H $MoSe_2$ Nanosheets Integrated with 1D Sulfide Semiconductor for Drastically Enhanced Visible-Light Photocatalytic Hydrogen Evolution. *Appl. Catal. B Environ.* **2018**, *238*, 27–37.

(110) Wu, J.; Liu, Y.; Yao, Y.; Shao, Y.; Wu, X. Graphene-like 2H/1T-$MoSe_2$ with Superior Full Spectrum Absorption: Morphology and Phase Engineering. *J. Alloys Compd.* **2021**, *877*, 160317.

(111) Bi, E.; Chen, H.; Yang, X.; Ye, F.; Yin, M.; Han, L. Fullerene-Structured $MoSe_2$ Hollow Spheres Anchored on Highly Nitrogen-Doped Graphene as a Conductive Catalyst for Photovoltaic Applications. *Sci. Rep.* **2015**, *5*, 13214.

(112) Yang, G. W. Laser Ablation in Liquids: Applications in the Synthesis of Nanocrystals.

*Prog. Mater. Sci.* **2007**, *52* (4), 648–698.

(113) Tan, D.; Lin, G.; Liu, Y.; Teng, Y.; Zhuang, Y.; Zhu, B.; Zhao, Q.; Qiu, J. Synthesis of Nanocrystalline Cubic Zirconia Using Femtosecond Laser Ablation. *J. Nanoparticle Res.* **2011**, *13* (3), 1183–1190.

(114) Rethfeld, B.; Sokolowski-Tinten, K.; von der Linde, D.; Anisimov, S. I. Timescales in the Response of Materials to Femtosecond Laser Excitation. *Appl. Phys. A* **2004**, *79* (4–6), 767–769.

(115) Amendola, V.; Meneghetti, M. What Controls the Composition and the Structure of Nanomaterials Generated by Laser Ablation in Liquid Solution? *Phys. Chem. Chem. Phys.* **2013**, *15* (9), 3027–3046.

(116) Posthumus, J. H. The Dynamics of Small Molecules in Intense Laser Fields. *Reports Prog. Phys.* **2004**, *67* (5), 623–665.

(117) Leveugle, E.; Ivanov, D. S.; Zhigilei, L. V. Photomechanical Spallation of Molecular and Metal Targets: Molecular Dynamics Study. *Appl. Phys. A* **2004**, *79* (7), 1643–1655.

(118) Lorazo, P.; Lewis, L. J.; Meunier, M. Thermodynamic Pathways to Melting, Ablation, and Solidification in Absorbing Solids under Pulsed Laser Irradiation. *Phys. Rev. B - Condens. Matter Mater. Phys.* **2006**, *73* (13), 1–22.

(119) Zuo, P.; Jiang, L.; Li, X.; Tian, M.; Ma, L.; Xu, C.; Yuan, Y.; Li, X.; Chen, X.; Liang, M. Phase-Reversed $MoS_2$ Nanosheets Prepared through Femtosecond Laser Exfoliation and Chemical Doping. *J. Phys. Chem. C* **2021**, *125* (15), 8304–8313.

(120) Last, I.; Jortner, J. Dynamics of the Coulomb Explosion of Large Clusters in a Strong Laser Field. *Phys. Rev. A* **2000**, *62* (1), 013201.

(121) Stoian, R.; Ashkenasi, D.; Rosenfeld, A.; Campbell, E. E. B. Coulomb Explosion in Ultrashort Pulsed Laser Ablation of $Al_2O_3$. *Phys. Rev. B* **2000**, *62* (19), 13167–13173.

(122) Ferrari, A. C.; Robertson, J. Interpretation of Raman Spectra of Disordered and

Amorphous Carbon. *Phys. Rev. B* **2000**, *61* (20), 14095–14107.

(123) Gordel, M.; Olesiak-Banska, J.; Matczyszyn, K.; Nogues, C.; Buckle, M.; Samoc, M. Post-Synthesis Reshaping of Gold Nanorods Using a Femtosecond Laser. *Phys. Chem. Chem. Phys.* **2014**, *16*, 71–78.

(124) Pyatenko, A.; Wang, H.; Koshizaki, N.; Tsuji, T. Mechanism of Pulse Laser Interaction with Colloidal Nanoparticles. *Laser Photonics Rev.* **2013**, *7* (4), 596–604.

(125) Werner, D.; Furube, A.; Okamoto, T.; Hashimoto, S. Femtosecond Laser-Induced Size Reduction of Aqueous Gold Nanoparticles: In Situ and Pump-Probe Spectroscopy Investigations Revealing Coulomb Explosion. *J. Phys. Chem. C* **2011**, *115* (17), 8503–8512.

(126) Maximova, K.; Aristov, A.; Sentis, M.; Kabashin, A. V. Size-Controllable Synthesis of Bare Gold Nanoparticles by Femtosecond Laser Fragmentation in Water. *Nanotechnology* **2015**, *26* (6), 065601.

(127) Plech, A.; Kotaidis, V.; Lorenc, M.; Boneberg, J. Femtosecond Laser Near-Field Ablation from Gold Nanoparticles. *Nat. Phys.* **2006**, *2*, 44–47.

(128) Liu, W.; Kosareva, O.; Golubtsov, I. S.; Iwasaki, A.; Becker, A.; Kandidov, V. P.; Chin, S. L. Femtosecond Laser Pulse Filamentation versus Optical Breakdown in $H_2O$. *Appl. Phys. B Lasers Opt.* **2003**, *76* (3), 215–229.

(129) Frias Batista, L. M.; Nag, A.; Meader, V. K.; Tibbetts, K. M. Generation of Nanomaterials by Reactive Laser-Synthesis in Liquid. *Sci. China Physics, Mech. Astron.* **2022**, *65* (7), 274202.

(130) Couairon, A.; Mysyrowicz, A. Femtosecond Filamentation in Transparent Media. *Phys. Rep.* **2007**, *441* (2–4), 47–189.

(131) Nikogosyan, D. N.; Oraevsky, A. A.; Rupasov, V. I. Two-Photon Ionization and Dissociation of Liquid Water by Powerful Laser UV Radiation. *Chem. Phys.* **1983**, *77* (1), 131–143.

(132) Pommeret, S.; Gobert, F.; Mostafavi, M.; Lampre, I.; Mialocq, J. C. Femtochemistry of the Hydrated Electron at Decimolar Concentration. *J. Phys. Chem. A* **2001**, *105* (51), 11400–11406.

(133) BAXENDALE, J. H.; WARDMAN, P. Direct Observation of Solvation of the Electron in Liquid Alcohols by Pulse Radiolysis. *Nature* **1971**, *230* (5294), 449–450.

(134) Stratakis, E.; Barberoglou, M.; Fotakis, C.; Viau, G.; Garcia, C.; Shafeev, G. A. Generation of Al Nanoparticles via Ablation of Bulk Al in Liquids with Short Laser Pulses. *Opt. Express* **2009**, *17* (15), 12650.

(135) Lin, G.; Tan, D.; Luo, F.; Chen, D.; Zhao, Q.; Qiu, J.; Xu, Z. Fabrication and Photocatalytic Property of α-$Bi_2O_3$ Nanoparticles by Femtosecond Laser Ablation in Liquid. *J. Alloys Compd.* **2010**, *507* (2), 43–46.

(136) Chelnokov, E.; Rivoal, M.; Colignon, Y.; Gachet, D.; Bekere, L.; Thibaudau, F.; Giorgio, S.; Khodorkovsky, V.; Marine, W. Band Gap Tuning of ZnO Nanoparticles via Mg Doping by Femtosecond Laser Ablation in Liquid Environment. *Appl. Surf. Sci.* **2012**, *258* (23), 9408–9411.

(137) Chen, J.; Ma, R.; Ren, H.; Li, X.; Yang, H.; Gong, Q. Femtosecond Laser-Induced Dissociative Ionization and Coulomb Explosion of Ethanol. *Int. J. Mass Spectrom.* **2005**, *241*, 25–29.

(138) Yazawa, H.; Shioyama, T.; Suda, Y.; Kannari, F.; Itakura, R.; Yamanouchi, K. Dissociative Ionization of Ethanol by 400 nm Femtosecond Laser Pulses. *J. Chem. Phys.* **2006**, *125* (18), 184311.

(139) Hoshina, K.; Tsuge, M. Formation of $H_3O^+$ from Ethanol Clusters Induced by Intense Femtosecond Laser Fields. *Chem. Phys. Lett.* **2010**, *489* (4–6), 154–158.

(140) Shirota, T.; Mano, N.; Tsuge, M.; Hoshina, K. Formation of $H_3O^+$ from Alcohols and Ethers Induced by Intense Laser Fields. *Rapid Commun. Mass Spectrom.* **2010**, *24* (5), 679–686.

(141) Hoshina, K.; Furukawa, Y.; Okino, T.; Yamanouchi, K. Efficient Ejection of $H_3^+$ from Hydrocarbon Molecules Induced by Ultrashort Intense Laser Fields. *J. Chem. Phys.* **2008**, *129* (10), 104302.

(142) Ekanayake, N.; Nairat, M.; Kaderiya, B.; Feizollah, P.; Jochim, B.; Severt, T.; Berry, B.; Pandiri, K. R.; Carnes, K. D.; Pathak, S.; Rolles, D.; Rudenko, A.; Ben-Itzhak, I.; Mancuso, C. A.; Fales, B. S.; Jackson, J. E.; Levine, B. G.; Dantus, M. Mechanisms and Time-Resolved Dynamics for Trihydrogen Cation ($H_3^+$) Formation from Organic Molecules in Strong Laser Fields. *Sci. Rep.* **2017**, *7*, 4703.

(143) Ekanayake, N.; Severt, T.; Nairat, M.; Weingartz, N. P.; Farris, B. M.; Kaderiya, B.; Feizollah, P.; Jochim, B.; Ziaee, F.; Borne, K.; Kanaka, R. P.; Carnes, K. D.; Rolles, D.; Rudenko, A.; Levine, B. G.; Jackson, J. E.; Ben-Itzhak, I.; Dantus, M. $H_2$ Roaming Chemistry and the Formation of $H_3^+$ from Organic Molecules in Strong Laser Fields. *Nat. Commun.* **2018**, *9* (1), 5186.

(144) Bowers, M. T.; Chesnavich, W. J.; Huntress, W. T. Deactivation of Internally Excited $H_3^+$ Ions: Comparison of Experimental Product Distributions of Reactions of $H_3^+$ Ions with $CH_3NH_2$, $CH_3OH$ and $CH_3SH$ with Predictions of Quasiequilibrium Theory Calculations. *Int. J. Mass Spectrom. Ion Phys.* **1973**, *12* (4), 357–382.

(145) Simic, M.; Neta, P.; Hayon, E. Pulse Radiolysis Study of Alcohols in Aqueous Solution. *J. Phys. Chem.* **1969**, *73* (11), 3794–3800.

(146) Sobhan, M. A.; Ams, M.; Withford, M. J.; Goldys, E. M. Ultrafast Laser Ablative Generation of Gold Nanoparticles: The Influence of Pulse Energy, Repetition Frequency and Spot Size. *J. Nanoparticle Res.* **2010**, *12* (8), 2831–2842.

(147) Sylvestre, J. P.; Kabashin, A. V.; Sacher, E.; Meunier, M. Femtosecond Laser Ablation of Gold in Water: Influence of the Laser-Produced Plasma on the Nanoparticle Size Distribution. *Appl. Phys. A Mater. Sci. Process.* **2005**, *80* (4), 753–758.

(148) Kabashin, A. V.; Meunier, M. Synthesis of Colloidal Nanoparticles during

Femtosecond Laser Ablation of Gold in Water. *J. Appl. Phys.* **2003**, *94* (12), 7941–7943.

(149) Tsuji, T.; Kakita, T.; Tsuji, M. Preparation of Nano-Size Particles of Silver with Femtosecond Laser Ablation in Water. *Appl. Surf. Sci.* **2003**, *206* (1–4), 314–320.

(150) Hamad, S.; Podagatlapalli, G. K.; Sreedhar, S.; Tewari, S. P.; Venugopal Rao, S. Femtosecond and Picosecond Ablation of Aluminum for Synthesis of Nanoparticles and Nanostructures and Their Optical Characterization. *Synth. Photonics Nanoscale Mater. IX* **2012**, *8245*, 82450L.

(151) Podagatlapalli, G. K.; Hamad, S.; Sreedhar, S.; Tewari, S. P.; Venugopal Rao, S. Fabrication and Characterization of Aluminum Nanostructures and Nanoparticles Obtained Using Femtosecond Ablation Technique. *Chem. Phys. Lett.* **2012**, *530*, 93–97.

(152) Qian, W.; Murakami, M.; Ichikawa, Y.; Che, Y. Highly Efficient and Controllable PEGylation of Gold Nanoparticles Prepared by Femtosecond Laser Ablation in Water. *J. Phys. Chem. C* **2011**, *115* (47), 23293–23298.

(153) Riley, R. S.; Day, E. S. Gold Nanoparticle-mediated Photothermal Therapy: Applications and Opportunities for Multimodal Cancer Treatment. *WIREs Nanomedicine and Nanobiotechnology* **2017**, *9* (4). e1449

(154) Tsuji, T.; Thang, D.-H.; Okazaki, Y.; Nakanishi, M.; Tsuboi, Y.; Tsuji, M. Preparation of Silver Nanoparticles by Laser Ablation in Polyvinylpyrrolidone Solutions. *Appl. Surf. Sci.* **2008**, *254* (16), 5224–5230.

(155) Kabashin, A. V.; Meunier, M.; Kingston, C.; Luong, J. H. T. Fabrication and Characterization of Gold Nanoparticles by Femtosecond Laser Ablation in an Aqueous Solution of Cyclodextrins. *J. Phys. Chem. B* **2003**, *107* (19), 4527–4531.

(156) Sobhan, M. A.; Withford, M. J.; Goldys, E. M. Enhanced Stability of Gold Colloids Produced by Femtosecond Laser Synthesis in Aqueous Solution of CTAB. *Langmuir*

**2010**, *26* (5), 3156–3159.

(157) Akman, E.; Aktas, O. C.; Genc Oztoprak, B.; Gunes, M.; Kacar, E.; Gundogdu, O.; Demir, A. Fragmentation of the Gold Nanoparticles Using Femtosecond Ti:Sapphire Laser and Their Structural Evolution. *Opt. Laser Technol.* **2013**, *49*, 156–160.

(158) Jakobi, J.; Menéndez-Manjón, A.; Chakravadhanula, V. S. K.; Kienle, L.; Wagener, P.; Barcikowski, S. Stoichiometry of Alloy Nanoparticles from Laser Ablation of PtIr in Acetone and Their Electrophoretic Deposition on PtIr Electrodes. *Nanotechnology* **2011**, *22* (14), 145601

(159) Jakobi, J.; Petersen, S.; Menéndez-Manjón, A.; Wagener, P.; Barcikowski, S. Magnetic Alloy Nanoparticles from Laser Ablation in Cyclopentanone and Their Embedding into a Photoresist. *Langmuir* **2010**, *26* (10), 6892–6897.

(160) Dhanunjaya, M.; Byram, C.; Vendamani, V. S.; Rao, S. V.; Pathak, A. P.; Rao, S. V. S. N. Hafnium Oxide Nanoparticles Fabricated by Femtosecond Laser Ablation in Water. *Appl. Phys. A* **2019**, *125* (1), 74.

(161) Said, A.; Sajti, L.; Giorgio, S.; Marine, W. Synthesis of Nanohybrid Materials by Femtosecond Laser Ablation in Liquid Medium. *J. Phys. Conf. Ser.* **2007**, *59* (1), 259–265.

(162) Alnassar, S. I.; Akman, E.; Oztoprak, B. G.; Kacar, E.; Gundogdu, O.; Khaleel, A.; Demir, A. Study of the Fragmentation Phenomena of $TiO_2$ Nanoparticles Produced by Femtosecond Laser Ablation in Aqueous Media. *Opt. Laser Technol.* **2013**, *51*, 17–23.

(163) De Bonis, A.; Lovaglio, T.; Galasso, A.; Santagata, A.; Teghil, R. Iron and Iron Oxide Nanoparticles Obtained by Ultra-Short Laser Ablation in Liquid. *Appl. Surf. Sci.* **2015**, *353*, 433–438.

(164) Schinca, D. C.; Scaffardi, L. B.; Videla, F. A.; Torchia, G. A.; Moreno, P.; Roso, L. Silver-Silver Oxide Core-Shell Nanoparticles by Femtosecond Laser Ablation: Core and Shell Sizing by Extinction Spectroscopy. *J. Phys. D. Appl. Phys.* **2009**, *42* (21),

215102.

(165) Muñetón Arboleda, D.; Santillán, J. M. J.; Mendoza Herrera, L. J.; Van Raap, M. B. F.; Mendoza Zélis, P.; Muraca, D.; Schinca, D. C.; Scaffardi, L. B. Synthesis of Ni Nanoparticles by Femtosecond Laser Ablation in Liquids: Structure and Sizing. *J. Phys. Chem. C* **2015**, *119* (23), 13184–13193.

(166) Gong, W.; Zheng, Z.; Zheng, J.; Hu, X.; Gao, W. Water Soluble CdS Nanoparticles with Controllable Size Prepared via Femtosecond Laser Ablation. *J. Appl. Phys.* **2007**, *102* (6), 064304.

(167) Semaltianos, N. G.; Logothetidis, S.; Perrie, W.; Romani, S.; Potter, R. J.; Sharp, M.; Dearden, G.; Watkins, K. G. CdTe Nanoparticles Synthesized by Laser Ablation. *Appl. Phys. Lett.* **2009**, *95* (3), 033302.

(168) Semaltianos, N. G.; Logothetidis, S.; Perrie, W.; Romani, S.; Potter, R. J.; Sharp, M.; French, P.; Dearden, G.; Watkins, K. G. II-VI Semiconductor Nanoparticles Synthesized by Laser Ablation. *Appl. Phys. A Mater. Sci. Process.* **2009**, *94* (3), 641–647.

(169) Xu, Y.; Yan, L.; Li, X.; Xu, H. Fabrication of Transition Metal Dichalcogenides Quantum Dots Based on Femtosecond Laser Ablation. *Sci. Rep.* **2019**, *9*, 2931.

(170) Li, B.; Jiang, L.; Li, X.; Ran, P.; Zuo, P.; Wang, A.; Qu, L.; Zhao, Y.; Cheng, Z.; Lu, Y. Preparation of Monolayer $MoS_2$ Quantum Dots Using Temporally Shaped Femtosecond Laser Ablation of Bulk MoS2 Targets in Water. *Sci. Rep.* **2017**, *7*, 11182.

(171) Nguyen, V.; Dong, Q.; Yan, L.; Zhao, N.; Le, P. H. Facile Synthesis of Photoluminescent $MoS_2$ and $WS_2$ Quantum Dots with Strong Surface-State Emission. *J. Lumin.* **2019**, *214*, 116554.

(172) Ibrahim, K. H.; Irannejad, M.; Wales, B.; Sanderson, J.; Yavuz, M.; Musselman, K. P. Simultaneous Fabrication and Functionalization of Nanoparticles of 2D Materials with

Hybrid Optical Properties. *Adv. Opt. Mater.* **2018**, *6* (11), 1701365.

(173) Zuo, P.; Jiang, L.; Li, X.; Tian, M. Y.; Yuan, Y. J.; Han, W. N.; Ma, L.; Hu, L. F.; He, Z. C.; Li, F. $MoS_2$ Core-Shell Nanoparticles Prepared through Liquid-Phase Ablation and Light Exfoliation of Femtosecond Laser for Chemical Sensing. *Sci. China Technol. Sci.* **2023**, *66* (3), 853–862.

(174) Tselikov, G. I.; Ermolaev, G. A.; Popov, A. A.; Tikhonowski, G. V.; Panova, D. A.; Taradin, A. S.; Vyshnevyy, A. A.; Syuy, A. V.; Klimentov, S. M.; Novikov, S. M.; et al. Transition Metal Dichalcogenide Nanospheres for High-Refractive-Index Nanophotonics and Biomedical Theranostics. *Proc. Natl. Acad. Sci.* **2022**, *119* (39), e2208830119.

(175) Chernikov, A. S.; Tselikov, G. I.; Gubin, M. Y.; Shesterikov, A. V.; Khorkov, K. S.; Syuy, A. V.; Ermolaev, G. A.; Kazantsev, I. S.; Romanov, R. I.; Markeev, A. M.; Popov, A. A.; Tikhonowski, G. V.; Kapitanova, O. O.; Kochuev, D. A.; Leksin, A. Y.; Tselikov, D. I.; Arsenin, A. V.; Kabashin, A. V.; Volkov, V. S.; Prokhorov, A. V. Tunable Optical Properties of Transition Metal Dichalcogenide Nanoparticles Synthesized by Femtosecond Laser Ablation and Fragmentation. *J. Mater. Chem. C* **2023**, 3493–3503.

(176) Wu, H.; Yang, R.; Song, B.; Han, Q.; Li, J.; Zhang, Y.; Fang, Y.; Tenne, R.; Wang, C. Biocompatible Inorganic Fullerene-Like Molybdenum Disulfide Nanoparticles Produced by Pulsed Laser Ablation in Water. *ACS Nano* **2011**, *5* (2), 1276–1281.

(177) Wu, X.; Tian, X.; Chen, T.; Zeng, A.; Yang, G. Inorganic Fullerene-like Molybdenum Selenide with Good Biocompatibility Synthesized by Laser Ablation in Liquids. *Nanotechnology* **2018**, *29* (29), 295604.

(178) Zhou, L.; Zhang, H.; Bao, H.; Liu, G.; Li, Y.; Cai, W. Onion-Structured Spherical $MoS_2$ Nanoparticles Induced by Laser Ablation in Water and Liquid Droplets' Radial Solidification/Oriented Growth Mechanism. *J. Phys. Chem. C* **2017**, *121* (41), 23233–23239.

(179) Santagata, A.; De Bonis, A.; De Giacomo, A.; Dell'Aglio, M.; Laurita, A.; Senesi, G. S.; Gaudiuso, R.; Orlando, S.; Teghil, R.; Parisi, G. P. Carbon-Based Nanostructures Obtained in Water by Ultrashort Laser Pulses. *J. Phys. Chem. C* **2011**, *115* (12), 5160–5164.

(180) Novodchuk, I.; Irannejad, M.; Wales, B.; Ibrahim, K.; Sanderson, J.; Bajcsy, M.; Yavuz, M. Controlled Volume Production of Simultaneously B/N Co-Doped Reduced Graphene Oxide Nanoflakes Using Femtosecond Laser Ablation. *Mater. Res. Bull.* **2019**, *111*, 80–86.

(181) Tan, D.; Xu, B.; Chen, P.; Dai, Y.; Zhou, S.; Ma, G.; Qiu, J. One-Pot Synthesis of Luminescent Hydrophilic Silicon Nanocrystals. *RSC Adv.* **2012**, *2* (22), 8254–8257.

(182) Tan, D.; Ma, Z.; Xu, B.; Dai, Y.; Ma, G.; He, M.; Jin, Z.; Qiu, J. Surface Passivated Silicon Nanocrystals with Stable Luminescence Synthesized by Femtosecond Laser Ablation in Solution. *Phys. Chem. Chem. Phys.* **2011**, *13* (45), 20255–20261.

(183) Zakharko, Y.; Rioux, D.; Patskovsky, S.; Lysenko, V.; Marty, O.; Bluet, J.-M.; Meunier, M. Direct Synthesis of Luminescent SiC Quantum Dots in Water by Laser Ablation. *Phys. status solidi - Rapid Res. Lett.* **2011**, *5* (8), 292–294.

(184) Shimotsuma, Y.; Yuasa, T.; Homma, H.; Sakakura, M.; Nakao, A.; Miura, K.; Hirao, K.; Kawasaki, M.; Qiu, J.; Kazansky, P. G. Photoconversion of Copper Flakes to Nanowires with Ultrashort Pulse Laser Irradiation. *Chem. Mater.* **2007**, *19* (6), 1206–1208.

(185) Chang, G.; Shimotsuma, Y.; Sakakura, M.; Yuasa, T.; Homma, H.; Oyama, M.; Miura, K.; Qiu, J.; Kazansky, P. G.; Hirao, K. Photo-Conversion and Evolution of One-Dimensional Cu Nanoparticles under Femtosecond Laser Irradiation. *Appl. Surf. Sci.* **2008**, *254* (16), 4992–4998.

(186) Fei, B.; Rui, W.; Huai-Xin, Y.; Xin-Zheng, Z.; Jian-Qi, L.; Hong-Xing, X.; Jing-Jun, X.; Ji-Min, Z. Laser-Driven Silver Nanowire Formation: Effect of Femtosecond Laser Pulse Polarization. *Chinese Phys. Lett.* **2010**, *27* (8), 088101.

(187) Ibrahim, K.; Novodchuk, I.; Mistry, K.; Singh, M.; Ling, C.; Sanderson, J.; Bajcsy, M.; Yavuz, M.; Musselman, K. P. Laser-Directed Assembly of Nanorods of 2D Materials. *Small* **2019**, *15* (46), 1904415.

(188) Singh, M. D. Few-Cycle Laser Pulse Generation and Characterization for Coulomb Explosion Imaging of Molecules, M.Sc. Thesis, University of Waterloo, Waterloo, Canada, 2019.

(189) Roper, D. K.; Ahn, W.; Hoepfner, M. Microscale Heat Transfer Transduced by Surface Plasmon Resonant Gold Nanoparticles. *J. Phys. Chem. C* **2007**, *111* (9), 3636–3641.

(190) Liu, G.; Zou, J.; Tang, Q.; Yang, X.; Zhang, Y.; Zhang, Q.; Huang, W.; Chen, P.; Shao, J.; Dong, X. Surface Modified $Ti_3C_2$ MXene Nanosheets for Tumor Targeting Photothermal/Photodynamic/Chemo Synergistic Therapy. *ACS Appl. Mater. Interfaces* **2017**, *9* (46), 40077–40086.

(191) Geng, B.; Yang, D.; Pan, D.; Wang, L.; Zheng, F.; Shen, W.; Zhang, C.; Li, X. NIR-Responsive Carbon Dots for Efficient Photothermal Cancer Therapy at Low Power Densities. *Carbon N. Y.* **2018**, *134*, 153–162.

(192) Lin, H.; Wang, Y.; Gao, S.; Chen, Y.; Shi, J. Theranostic 2D Tantalum Carbide (MXene). *Adv. Mater.* **2018**, *30* (4), 1703284.

(193) Ye, F.; Ayub, A.; Karimi, R.; Wettig, S.; Sanderson, J.; Musselman, K. P. Defect-Rich $MoSe_2$ 2H/1T Hybrid Nanoparticles Prepared from Femtosecond Laser Ablation in Liquid and Their Enhanced Photothermal Conversion Efficiencies. *Adv. Mater.* **2023,** 202301129.

(194) Paściak, A.; Marin, R.; Abiven, L.; Pilch-Wróbel, A.; Misiak, M.; Xu, W.; Prorok, K.; Bezkrovnyi, O.; Marciniak, Ł.; Chanéac, C.; Gazeau, F.; Bazzi, R.; Roux, S.; Viana, B.; Lehto, V.-P.; Jaque, D.; Bednarkiewicz, A. Quantitative Comparison of the Light-to-Heat Conversion Efficiency in Nanomaterials Suitable for Photothermal Therapy. *ACS Appl. Mater. Interfaces* **2022**, *14* (29), 33555–33566.

(195) Liu, W.; Xu, Q.; Cui, W.; Zhu, C.; Qi, Y. $CO_2$ -Assisted Fabrication of Two-Dimensional Amorphous Molybdenum Oxide Nanosheets for Enhanced Plasmon Resonances. *Angew. Chemie Int. Ed.* **2017**, *56* (6), 1600–1604.

(196) Ye, F.; Chang, D.; Ayub, A.; Ibrahim, K.; Shahin, A.; Karimi, R.; Wettig, S.; Sanderson, J.; Musselman, K. P. Synthesis of Two-Dimensional Plasmonic Molybdenum Oxide Nanomaterials by Femtosecond Laser Irradiation. *Chem. Mater.* **2021**, *33* (12), 4510–4521.

(197) Dieterle, M.; Mestl, G. Raman Spectroscopy of Molybdenum Oxides Part II. Resonance Raman Spectroscopic Characterization of the Molybdenum Oxides $Mo_4O_{11}$ and $MoO_2$. *Phys. Chem. Chem. Phys.* **2002**, *4* (5), 822–826.

(198) Mestl, G.; Ruiz, P.; Delmon, B.; Knozinger, H. Oxygen-Exchange Properties of $MoO_3$: An in Situ Raman Spectroscopy Study. *J. Phys. Chem.* **1994**, *98* (44), 11269–11275.

(199) Camacho-López, M. A.; Escobar-Alarcón, L.; Picquart, M.; Arroyo, R.; Córdoba, G.; Haro-Poniatowski, E. Micro-Raman Study of the m-$MoO_2$ to α-$MoO_3$ Transformation Induced by Cw-Laser Irradiation. *Opt. Mater. (Amst).* **2011**, *33* (3), 480–484.

(200) Cao, X.; Ding, C.; Zhang, C.; Gu, W.; Yan, Y.; Shi, X.; Xian, Y. Transition Metal Dichalcogenide Quantum Dots: Synthesis, Photoluminescence and Biological Applications. *J. Mater. Chem. B* **2018**, *6* (48), 8011–8036.

(201) Miyamoto, Y.; Zhang, H.; Tománek, D. Photoexfoliation of Graphene from Graphite: An Ab Initio Study. *Phys. Rev. Lett.* **2010**, *104* (20), 208302.

(202) Sanderson, J. H.; El-Zein, A.; Bryan, W. A.; Newell, W. R.; Langley, A. J.; Taday, P. F. Geometry Modifications and Alignment of $H_2O$ in an Intense Femtosecond Laser Pulse. *Phys. Rev. A* **1999**, *59* (4), 2567–2570.

(203) Itakura, R.; Yamanouchi, K.; Tanabe, T.; Okamoto, T.; Kannari, F. Dissociative Ionization of Ethanol in Chirped Intense Laser Fields. *J. Chem. Phys.* **2003**, *119* (8),

4179–4186.

(204) Alsaif, M. M. Y. A.; Field, M. R.; Daeneke, T.; Chrimes, A. F.; Zhang, W.; Carey, B. J.; Berean, K. J.; Walia, S.; van Embden, J.; Zhang, B.; et al. Exfoliation Solvent Dependent Plasmon Resonances in Two- Dimensional. *ACS Appl. Mater. Interfaces* **2016**, *8* (5), 3482–3493.

(205) Alsaif, M. M. Y. A.; Chrimes, A. F.; Daeneke, T.; Balendhran, S.; Bellisario, D. O.; Son, Y.; Field, M. R.; Zhang, W.; Nili, H.; Nguyen, E. P.; et al. High-Performance Field Effect Transistors Using Electronic Inks of 2D Molybdenum Oxide Nanoflakes. *Adv. Funct. Mater.* **2016**, *26* (1), 91–100.

(206) Yun, J.; Jang, W.; Lee, T.; Lee, Y.; Soon, A. Aligning the Band Structures of Polymorphic Molybdenum Oxides and Organic Emitters in Light-Emitting Diodes. *Phys. Rev. Appl.* **2017**, *7* (2), 024025.

(207) Saravanakumar, B.; Shobana, R.; Ravi, G.; Ganesh, V.; Yuvakkumar, R. Preparation and Electrochemical Characterization of $Mo_9O_{26}$ Nanopowders for Supercapacitors Applications. *Nano-Structures & Nano-Objects* **2019**, *19*, 100340.

(208) Dieterle, M.; Weinberg, G.; Mestl, G. Raman Spectroscopy of Molybdenum Oxides Part I. Structural Characterization of Oxygen Defects in $MoO_{3-X}$ by DR UV/VIS, Raman Spectroscopy and X-Ray Diffraction. *Phys. Chem. Chem. Phys.* **2002**, *4* (5), 812–821.

(209) Wang, E.; Shan, X.; Chen, L.; Pfeifer, T.; Chen, X.; Ren, X.; Dorn, A. Ultrafast Proton Transfer Dynamics on the Repulsive Potential of the Ethanol Dication: Roaming-Mediated Isomerization versus Coulomb Explosion. *J. Phys. Chem. A* **2020**, *124* (14), 2785–2791.

(210) Dou, K.; Zhu, W.; Zou, Y.; Gu, Y.; Li, J.; Zhang, S.; Liu, Z.; Zeng, H. Metallic Oxide Nanocrystals with Near-Infrared Plasmon Resonance for Efficient, Stable and Biocompatible Photothermal Cancer Therapy. *J. Mater. Chem. B* **2017**, *5* (35), 7393–7402.

(211) Li, Y.; Miao, Z.; Shang, Z.; Cai, Y.; Cheng, J.; Xu, X. A Visible- and NIR-Light Responsive Photothermal Therapy Agent by Chirality-Dependent $MoO_{3-X}$ Nanoparticles. *Adv. Funct. Mater.* **2020**, *30* (4), 1906311.

(212) Müller, A.; Krickemeyer, E.; Bögge, H.; Schmidtmann, M.; Beugholt, C.; Kögerler, P.; Lu, C. Formation of a Ring-Shaped Reduced "Metal Oxide" with the Simple Composition $[(MoO_3)_{176}(H_2O)_{80}H_{32}]$. *Angew. Chemie Int. Ed.* **1998**, *37* (9), 1220–1223.

(213) Müller, A.; Meyer, J.; Krickemeyer, E.; Diemann, E. Molybdenum Blue: A 200 Year Old Mystery Unveiled. *Angew. Chemie Int. Ed. English* **1996**, *35* (11), 1206–1208.

(214) Yamase, T.; Prokop, P. V. Photochemical Formation of Tire-Shaped Molybdenum Blues: Topology of a Defect Anion, $[Mo_{142}O_{432}H_{28}(H_2O)_{58}]^{12-}$. *Angew. Chemie Int. Ed.* **2002**, *41* (3), 466–469.

(215) Müller, A.; Maiti, R.; Schmidtmann, M.; Bögge, H.; Das, S. K.; Zhang, W. Mimicking Oxide Surfaces: Different Types of Defects and Ligand Coordination at Well Defined Positions of a Molybdenum Oxide Based Nanocluster. *Chem. Commun.* **2001**, 2126–2127.

(216) Müller, A.; Shah, S. Q. N.; Bögge, H.; Schmidtmann, M.; Kögerler, P.; Hauptfleisch, B.; Leiding, S.; Wittler, K. Thirty Electrons "Trapped" in a Spherical Matrix: A Molybdenum Oxide-Based Nanostructured Keplerate Reduced by 36 Electrons. *Angew. Chemie Int. Ed.* **2000**, *39* (9), 1614–1616.

(217) Lin, J.; Li, N.; Yang, S.; Jia, M.; Liu, J.; Li, X.-M.; An, L.; Tian, Q.; Dong, L.-Z.; Lan, Y.-Q. Self-Assembly of Giant Mo 240 Hollow Opening Dodecahedra. *J. Am. Chem. Soc.* **2020**, *142* (32), 13982–13988. https://doi.org/10.1021/jacs.0c06582.

(218) Müller, A.; Shah, S. Q. N.; Bögge, H.; Schmidtmann, M. Molecular Growth from a $Mo_{176}$ to a $Mo_{248}$ Cluster. *Nature* **1999**, *397* (6714), 48–50.

(219) Müller, A.; Beckmann, E.; Bögge, H.; Schmidtmann, M.; Dress, A. Inorganic

Chemistry Goes Protein Size: A $Mo_{368}$ Nano-Hedgehog Initiating Nanochemistry by Symmetry Breaking. *Angew. Chemie Int. Ed.* **2002**, *41* (7), 1162–1167.

(220) Miras, H. N.; Cooper, G. J. T.; Long, D.-L.; Bögge, H.; Müller, A.; Streb, C.; Cronin, L. Unveiling the Transient Template in the Self-Assembly of a Molecular Oxide Nanowheel. *Science.* **2010**, *327* (5961), 72–74.

(221) Grzhegorzhevskii, K. V.; Ostroushko, A. A. Supramolecular Structural Design in a System Based on Nanocluster $Mo_{138}$ and a Cationic Surfactant: The Influence of Components Ratio and PH of the Solution. *Colloids Surfaces A Physicochem. Eng. Asp.* **2015**, *480*, 130–137.

(222) Akutagawa, T.; Jin, R.; Tunashima, R.; Noro, S.-I.; Cronin, L.; Nakamura, T. Nanoscale Assemblies of Gigantic Molecular $\{Mo_{154}\}$-Rings: $(Dimethyldioctadecylammonium)_{20}[Mo_{154}O_{462}H_8(H_2O)_{70}]$. *Langmuir* **2008**, *24*, 231–238.

(223) Sotani, N.; Kawamoto, Y.; Inui, M. Dehydrogenation Process in Orthorhombic Hydrogen Molybdenum Bronze under Vacuum Heating. *Mater. Res. Bull.* **1983**, *18* (7), 797–802.

(224) Buckley, R. I.; Clark, R. J. H. Structural and Electronics Properties of Some Polymolybdates Reducible to Molybdenum Blues. *Coord. Chem. Rev.* **1985**, *65*, 167–218.

(225) Clemente-León, M.; Ito, T.; Yashiro, H.; Yamase, T.; Coronado, E. Langmuir−Blodgett Films of a Mo-Blue Nanoring $[Mo_{142}O_{429}H_{10}(H_2O)_{49}(CH_3CO_2)_5(CH_3CH_2CO_2)]^{30-}$ (Mo142) by the Semiamphiphilic Method. *Langmuir* **2007**, *23* (7), 4042–4047.

(226) Bugayev, A. .; Nikitin, S. Optical Bleaching of the IVCT-Absorption Bands of the Molybdenum Blues. *Opt. Commun.* **2000**, *180* (1–3), 69–71.

(227) Koyun, O.; Gorduk, S.; Arvas, M. B.; Sahin, Y. Direct, One-Step Synthesis of

Molybdenum Blue Using an Electrochemical Method, and Characterization Studies. *Synth. Met.* **2017**, *233*, 111–118.

(228) Etman, A. S.; Abdelhamid, H. N.; Yuan, Y.; Wang, L.; Zou, X.; Sun, J. Facile Water-Based Strategy for Synthesizing $MoO_{3-X}$ Nanosheets: Efficient Visible Light Photocatalysts for Dye Degradation. *ACS Omega* **2018**, *3* (2), 2193–2201.

(229) Dickens, P. G.; Birtill, J. J. Elastic and Inelastic Neutron Studies of Hydrogen Molybdenum Bronzes. *J. Solid State Chem.* **1979**, *28*, 185–193.

(230) Yamase, T.; Sugeta, M. Charge-Transfer Photoluminescence of Polyoxo-Tungstates and -Molybdates. *J. Chem. Soc. Dalt. Trans.* **1993**, 759–765.

(231) Meng, D.; Yang, S.; Guo, L.; Li, G.; Ge, J.; Huang, Y.; Bielawski, C. W.; Geng, J. The Enhanced Photothermal Effect of Graphene/Conjugated Polymer Composites: Photoinduced Energy Transfer and Applications in Photocontrolled Switches. *Chem. Commun.* **2014**, *50* (92), 14345–14348.

(232) He, Q.; Zeng, Z.; Yin, Z.; Li, H.; Wu, S.; Huang, X.; Zhang, H. Fabrication of Flexible MoS 2 Thin-Film Transistor Arrays for Practical Gas-Sensing Applications. *Small* **2012**, *8* (19), 2994–2999.

(233) Lee, K.; Gatensby, R.; McEvoy, N.; Hallam, T.; Duesberg, G. S. High-Performance Sensors Based on Molybdenum Disulfide Thin Films. *Adv. Mater.* **2013**, *25* (46), 6699–6702.

(234) Nourbakhsh, A.; Zubair, A.; Sajjad, R. N.; Tavakkoli K. G., A.; Chen, W.; Fang, S.; Ling, X.; Kong, J.; Dresselhaus, M. S.; Kaxiras, E.; Berggren, K. K.; Antoniadis, D.; Palacios, T. $MoS_2$ Field-Effect Transistor with Sub-10 nm Channel Length. *Nano Lett.* **2016**, *16* (12), 7798–7806.

(235) Yue, X.; Yang, J.; Li, W.; Jing, Y.; Dong, L.; Zhang, Y.; Li, X. Electron Irradiation Induces the Conversion from 2H-$WSe_2$ to 1T-$WSe_2$ and Promotes the Performance of Electrocatalytic Hydrogen Evolution. *ACS Sustain. Chem. Eng.* **2022**, *10* (7), 2420–

2428.

(236) Abbasi, P.; Asadi, M.; Liu, C.; Sharifi-Asl, S.; Sayahpour, B.; Behranginia, A.; Zapol, P.; Shahbazian-Yassar, R.; Curtiss, L. A.; Salehi-Khojin, A. Tailoring the Edge Structure of Molybdenum Disulfide toward Electrocatalytic Reduction of Carbon Dioxide. *ACS Nano* **2017**, *11* (1), 453–460.

(237) Yin, Y.; Zhang, Y.; Gao, T.; Yao, T.; Zhang, X.; Han, J.; Wang, X.; Zhang, Z.; Xu, P.; Zhang, P.; et al. Synergistic Phase and Disorder Engineering in 1T-$MoSe_2$ Nanosheets for Enhanced Hydrogen-Evolution Reaction. *Adv. Mater.* **2017**, *29* (28), 1700311.

(238) Xie, J.; Zhang, H.; Li, S.; Wang, R.; Sun, X.; Zhou, M.; Zhou, J.; Lou, X. W. D.; Xie, Y. Defect-Rich $MoS_2$ Ultrathin Nanosheets with Additional Active Edge Sites for Enhanced Electrocatalytic Hydrogen Evolution. *Adv. Mater.* **2013**, *25* (40), 5807–5813.

(239) Bang, G. S.; Nam, K. W.; Kim, J. Y.; Shin, J.; Choi, J. W.; Choi, S.-Y. Effective Liquid-Phase Exfoliation and Sodium Ion Battery Application of $MoS_2$ Nanosheets. *ACS Appl. Mater. Interfaces* **2014**, *6* (10), 7084–7089.

(240) David, L.; Bhandavat, R.; Singh, G. $MoS_2$/Graphene Composite Paper for Sodium-Ion Battery Electrodes. *ACS Nano* **2014**, *8* (2), 1759–1770.

(241) Wang, Y.-Z.; Shan, X.-Y.; Wang, D.-W.; Sun, Z.-H.; Cheng, H.-M.; Li, F. A Rechargeable Quasi-Symmetrical $MoS_2$ Battery. *Joule* **2018**, *2* (7), 1278–1286.

(242) Hu, Z.; Wang, L.; Zhang, K.; Wang, J.; Cheng, F.; Tao, Z.; Chen, J. $MoS_2$ Nanoflowers with Expanded Interlayers as High-Performance Anodes for Sodium-Ion Batteries. *Angew. Chemie Int. Ed.* **2014**, *53* (47), 12794–12798.

(243) Huang, P.; Wang, Z.; Liu, Y.; Zhang, K.; Yuan, L.; Zhou, Y.; Song, B.; Li, Y. Water-Soluble 2D Transition Metal Dichalcogenides as the Hole-Transport Layer for Highly Efficient and Stable p–i–n Perovskite Solar Cells. *ACS Appl. Mater. Interfaces* **2017**, *9* (30), 25323–25331.

(244) Tsai, M.-L.; Su, S.; Chang, J.; Tsai, D.; Chen, C.-H.; Wu, C.; Li, L.; Chen, L.; He, J. Monolayer $MoS_2$ Heterojunction Solar Cells. *ACS Nano* **2014**, *8* (8), 8317–8322.

(245) Singh, E.; Kim, K. S.; Yeom, G. Y.; Nalwa, H. S. Atomically Thin-Layered Molybdenum Disulfide ($MoS_2$) for Bulk-Heterojunction Solar Cells. *ACS Appl. Mater. Interfaces* **2017**, *9* (4), 3223–3245.

(246) Black, K. C. L.; Wang, Y.; Luehmann, H. P.; Cai, X.; Xing, W.; Pang, B.; Zhao, Y.; Cutler, C. S.; Wang, L. V.; Liu, Y.; Xia, Y. Radioactive $^{198}$Au-Doped Nanostructures with Different Shapes for *In Vivo* Analyses of Their Biodistribution, Tumor Uptake, and Intratumoral Distribution. *ACS Nano* **2014**, *8* (5), 4385–4394.

(247) Decuzzi, P.; Godin, B.; Tanaka, T.; Lee, S.-Y.; Chiappini, C.; Liu, X.; Ferrari, M. Size and Shape Effects in the Biodistribution of Intravascularly Injected Particles. *J. Control. Release* **2010**, *141* (3), 320–327.

(248) Tenne, R.; Margulis, L.; Genut, M.; Hodes, G. Polyhedral and Cylindrical Structures of Tungsten Disulphide. *Nature* **1992**, *360* (6403), 444–446.

(249) Margulis, L.; Salitra, G.; Tenne, R.; Talianker, M. Nested Fullerene-like Structures. *Nature* **1993**, *365* (6442), 113–114.

(250) Rosentsveig, R.; Margolin, A.; Gorodnev, A.; Popovitz-Biro, R.; Feldman, Y.; Rapoport, L.; Novema, Y.; Naveh, G.; Tenne, R. Synthesis of Fullerene-like $MoS_2$ Nanoparticles and Their Tribological Behavior. *J. Mater. Chem.* **2009**, *19* (25), 4368.

(251) Li, X.-L.; Ge, J.-P.; Li, Y.-D. Atmospheric Pressure Chemical Vapor Deposition: An Alternative Route to Large-Scale $MoS_2$ and $WS_2$ Inorganic Fullerene-like Nanostructures and Nanoflowers. *Chem. - A Eur. J.* **2004**, *10* (23), 6163–6171.

(252) Etzkorn, J.; Therese, H. A.; Rocker, F.; Zink, N.; Kolb, U.; Tremel, W. Metal-Organic Chemical Vapor Depostion Synthesis of Hollow Inorganic-Fullerene-Type $MoS_2$ and $MoSe_2$ Nanoparticles. *Adv. Mater.* **2005**, *17* (19), 2372–2375.

(253) Vollath, D.; Szabó, D. V. Nanoparticles from Compounds with Layered Structures.

*Acta Mater.* **2000**, *48* (4), 953–967.

(254) Oztas, T.; Sen, H. S.; Durgun, E.; Ortaç, B. Synthesis of Colloidal 2D/3D $MoS_2$ Nanostructures by Pulsed Laser Ablation in an Organic Liquid Environment. *J. Phys. Chem. C* **2014**, *118* (51), 30120–30126.

(255) Lu, F.; Wu, S.-H.; Hung, Y.; Mou, C.-Y. Size Effect on Cell Uptake in Well-Suspended, Uniform Mesoporous Silica Nanoparticles. *Small* **2009**, *5* (12), 1408–1413.

(256) Compagnini, G.; Sinatra, M. G.; Messina, G. C.; Patanè, G.; Scalese, S.; Puglisi, O. Monitoring the Formation of Inorganic Fullerene-like $MoS_2$ Nanostructures by Laser Ablation in Liquid Environments. *Appl. Surf. Sci.* **2012**, *258* (15), 5672–5676.

(257) Lin, Y. C.; Dumcenco, D. O.; Huang, Y. S.; Suenaga, K. Atomic Mechanism of the Semiconducting-to-Metallic Phase Transition in Single-Layered $MoS_2$. *Nat. Nanotechnol.* **2014**, *9* (5), 391–396.

(258) Kang, Y.; Najmaei, S.; Liu, Z.; Bao, Y.; Wang, Y.; Zhu, X.; Halas, N. J.; Nordlander, P.; Ajayan, P. M.; Lou, J.; Fang, J. Plasmonic Hot Electron Induced Structural Phase Transition in a $MoS_2$ Monolayer. *Adv. Mater.* **2014**, *26* (37), 6467–6471.

(259) Nath, A. K. Laser Drilling of Metallic and Nonmetallic Substrates. In *Comprehensive Materials Processing*; Elsevier, Vol. 9, 2014; pp 115–175.

(260) Sharma, P.; Vatsa, R. K. Nanoclusters Under Extreme Ionization Conditions. In *Materials Under Extreme Conditions*; Elsevier, 2017; pp 575–613.

(261) Vorobyev, A. Y.; Guo, C. Direct Femtosecond Laser Surface Nano/Microstructuring and Its Applications. *Laser Photon. Rev.* **2013**, *7* (3), 385–407.

(262) Miotello, A.; Kelly, R. Laser-Induced Phase Explosion: New Physical Problems When a Condensed Phase Approaches the Thermodynamic Critical Temperature. *Appl. Phys. A Mater. Sci. Process.* **1999**, *69* (7), S67–S73.

(263) Hayat, A.; Bashir, S.; Strickland, D.; Shahid Rafique, M.; Wales, B.; Al-Tuairqi, S.;

Sanderson, J. H. The Role of Laser Fluence and Ambient Environments on Femtosecond Laser Induced Breakdown Spectroscopy and on Surface Morphology of Mg and Zr. *J. Appl. Phys.* **2019**, *125* (8), 083302.

(264) Amendola, V.; Meneghetti, M. Laser Ablation Synthesis in Solution and Size Manipulation of Noble Metal Nanoparticles. *Phys. Chem. Chem. Phys.* **2009**, *11* (20), 3805.

(265) Fan, X.; Xu, P.; Zhou, D.; Sun, Y.; Li, Y. C.; Nguyen, M. A. T.; Terrones, M.; Mallouk, T. E. Fast and Efficient Preparation of Exfoliated 2H $MoS_2$ Nanosheets by Sonication-Assisted Lithium Intercalation and Infrared Laser-Induced 1T to 2H Phase Reversion. *Nano Lett.* **2015**, *15* (9), 5956–5960.

(266) Setayeshgar, S.; Karimipour, M.; Molaei, M.; Moghadam, M. R.; Khazraei, S. Synthesis of Scalable 1T/2H–$MoSe_2$ Nanosheets with a New Source of Se in Basic Media and Study of Their HER Activity. *Int. J. Hydrogen Energy* **2020**, *45* (11), 6090–6101.

(267) . N. S.; . K. P.; . S. I.; . S. D.; . A. K. T. Optical Band-Gap and Associated Urbach Energy Tails in Defected AlN Thin Films Grown by Ion Beam Sputter Deposition: Effect of Assisted Ion Energy. *Adv. Mater. Proc.* **2017**, *2* (5), 342–346.

(268) Shimakawa, K.; Singh, J.; O'Leary, S. K. Optical Properties of Disordered Condensed Matter. In *Optical Properties of Materials and Their Applications*; Wiley, 2019; pp 67–81.

(269) Norouzzadeh, P.; Mabhouti, K.; Golzan, M. M.; Naderali, R. Investigation of Structural, Morphological and Optical Characteristics of Mn Substituted Al-Doped ZnO NPs: A Urbach Energy and Kramers-Kronig Study. *Optik (Stuttg).* **2020**, *204*, 164227.

(270) Yuwen, L.; Zhou, J.; Zhang, Y.; Zhang, Q.; Shan, J.; Luo, Z.; Weng, L.; Teng, Z.; Wang, L. Aqueous Phase Preparation of Ultrasmall $MoSe_2$ Nanodots for Efficient Photothermal Therapy of Cancer Cells. *Nanoscale* **2016**, *8* (5), 2720–2726.

(271) Wu, C.; Wang, S.; Zhao, J.; Liu, Y.; Zheng, Y.; Luo, Y.; Ye, C.; Huang, M.; Chen, H. Biodegradable Fe(III)@$WS_2$ -PVP Nanocapsules for Redox Reaction and TME-Enhanced Nanocatalytic, Photothermal, and Chemotherapy. *Adv. Funct. Mater.* **2019**, *29* (26), 1901722.

(272) Wang, S.; Li, X.; Gong, Y.; Zhou, X.; Jin, H.; Yan, H.; Liu, J. Facile Synthesis of Soybean Phospholipid-Encapsulated $MoS_2$ Nanosheets for Efficient in Vitro and in Vivo Photothermal Regression of Breast Tumor. *Int. J. Nanomedicine* **2016**, *11*, 1819.

(273) Kim, J.; Kim, H.; Kim, W. J. Single-Layered $MoS_2$-PEI-PEG Nanocomposite-Mediated Gene Delivery Controlled by Photo and Redox Stimuli. *Small* **2016**, *12* (9), 1184–1192.

(274) Yong, Y.; Cheng, X.; Bao, T.; Zu, M.; Yan, L.; Yin, W.; Ge, C.; Wang, D.; Gu, Z.; Zhao, Y. Tungsten Sulfide Quantum Dots as Multifunctional Nanotheranostics for *In Vivo* Dual-Modal Image-Guided Photothermal/Radiotherapy Synergistic Therapy. *ACS Nano* **2015**, *9* (12), 12451–12463.

(275) Moniri, S.; Hantehzadeh, M. R. Colloidal Synthesis of $MoS_2$ NPs by Nanosecond Laser Ablation of a Bulk MoS2 Target in Ethylene Glycol Solution. *Opt. Quantum Electron.* **2021**, *53* (5), 215.

(276) Chieng, B.; Ibrahim, N.; Yunus, W.; Hussein, M. Poly(Lactic Acid)/Poly(Ethylene Glycol) Polymer Nanocomposites: Effects of Graphene Nanoplatelets. *Polymers (Basel).* **2013**, *6*, 93–104.

(277) Zhao, X.; Sui, J.; Li, F.; Fang, H.; Wang, H.; Li, J.; Cai, W.; Cao, G. Lamellar $MoSe_2$ Nanosheets Embedded with $MoO_2$ Nanoparticles: Novel Hybrid Nanostructures Promoted Excellent Performances for Lithium Ion Batteries. *Nanoscale* **2016**, *8* (41), 17902–17910.

(278) Zhang, J.; Wu, M.; Liu, T.; Kang, W.; Xu, J. Hierarchical Nanotubes Constructed from Interlayer-Expanded $MoSe_2$ Nanosheets as a Highly Durable Electrode for Sodium Storage. *J. Mater. Chem. A* **2017**, *5* (47), 24859–24866.

(279) Bhatt, S.; Pulpytel, J.; Mirshahi, M.; Arefi-Khonsari, F. Catalyst-Free Plasma-Assisted Copolymerization of Poly(ε-Caprolactone)-Poly(Ethylene Glycol) for Biomedical Applications. *ACS Macro Lett.* **2012**, *1* (6), 764–767.

(280) Dobrea, I. D.; Ciocan, C. E.; Dumitriu, E.; Popa, M. I.; Petit, E.; Hulea, V. Raman Spectroscopy — Useful Tool for Studying the Catalysts Derived from Mo and V-Oxyanion-Intercalated Layered Double Hydroxides. *Appl. Clay Sci.* **2015**, *104*, 205–210.

(281) Kumari, L.; Ma, Y.-R.; Tsai, C.-C.; Lin, Y.-W.; Wu, S. Y.; Cheng, K.-W.; Liou, Y. X-Ray Diffraction and Raman Scattering Studies on Large-Area Array and Nanobranched Structure of 1D $MoO_2$ Nanorods. *Nanotechnology* **2007**, *18* (11), 115717.

(282) Tang, J.; Wei, Z.; Wang, Q.; Wang, Y.; Han, B.; Li, X.; Huang, B.; Liao, M.; Liu, J.; Li, N.; Zhao, Y.; Shen, C.; Guo, Y.; Bai, X.; Guo, P.; Yang, W.; Chen, L.; Wu, K.; Yang, R.; Shi, D.; Zhang, G. In Situ Oxygen Doping of Monolayer $MoS_2$ for Novel Electronics. *Small* **2020**, *16* (42), 2004276.

(283) Wei, Z.; Tang, J.; Li, X.; Chi, Z.; Wang, Y.; Wang, Q.; Han, B.; Li, N.; Huang, B.; Li, J.;Yu, H.; Yuan, J.; Chen, H.; Sun, J.; Chen, L.; Wu, K.; Gao, P.; He, C.; Yang, W.; Shi, D.; Yang, R.; Zhang, G. Wafer-Scale Oxygen-Doped $MoS_2$ Monolayer. *Small Methods* **2021**, *5* (6), 2100091.

(284) Pandey, A.; Guyot-Sionnest, P. Slow Electron Cooling in Colloidal Quantum Dots. *Science* **2008**, *322* (5903), 929–932.

(285) Schaller, R. D.; Klimov, V. I. High Efficiency Carrier Multiplication in PbSe Nanocrystals: Implications for Solar Energy Conversion. *Phys. Rev. Lett.* **2004**, *92* (18), 186601.

(286) Kilina, S. V.; Kilin, D. S.; Prezhdo, O. V. Breaking the Phonon Bottleneck in PbSe and CdSe Quantum Dots: Time-Domain Density Functional Theory of Charge Carrier Relaxation. *ACS Nano* **2009**, *3* (1), 93–99.

(287) Cooney, R. R.; Sewall, S. L.; Anderson, K. E. H.; Dias, E. A.; Kambhampati, P. Breaking the Phonon Bottleneck for Holes in Semiconductor Quantum Dots. *Phys. Rev. Lett.* **2007**, *98* (17), 177403.

(288) Schaller, R. D.; Pietryga, J. M.; Goupalov, S. V.; Petruska, M. A.; Ivanov, S. A.; Klimov, V. I. Breaking the Phonon Bottleneck in Semiconductor Nanocrystals via Multiphonon Emission Induced by Intrinsic Nonadiabatic Interactions. *Phys. Rev. Lett.* **2005**, *95* (19), 196401.

(289) Hyeon-Deuk, K.; Prezhdo, O. V. Photoexcited Electron and Hole Dynamics in Semiconductor Quantum Dots: Phonon-Induced Relaxation, Dephasing, Multiple Exciton Generation and Recombination. *J. Phys. Condens. Matter* **2012**, *24* (36), 363201.

(290) Knowles, K. E.; McArthur, E. A.; Weiss, E. A. A Multi-Timescale Map of Radiative and Nonradiative Decay Pathways for Excitons in CdSe Quantum Dots. *ACS Nano* **2011**, *5* (3), 2026–2035.

(291) An, S. J.; Park, D. Y.; Lee, C.; Bang, S.; Nguyen, D. A.; Kim, S. H.; Kim, H. Y.; Jeong, H. J.; Jeong, M. S. Facile Preparation of Molybdenum Disulfide Quantum Dots Using a Femtosecond Laser. *Appl. Surf. Sci.* **2020**, *511*, 145507.

(292) Sunitha, A. P.; Hajara, P.; Shaji, M.; Jayaraj, M. K.; Saji, K. J. Luminescent $MoS_2$ Quantum Dots with Reverse Saturable Absorption Prepared by Pulsed Laser Ablation. *J. Lumin.* **2018**, *203*, 313–321.

(293) Pradhan, G.; Dey, P. P.; Khare, A.; Sharma, A. K. Synthesis and Size Modulation of $MoS_2$ Quantum Dots by Pulsed Laser Ablation in Liquid for Viable Hydrogen Generation. *J. Appl. Phys.* **2021**, *129* (2), 025112.

(294) Balati, A.; Bazilio, A.; Shahriar, A.; Nash, K.; Shipley, H. J. Simultaneous Formation of Ultra-Thin $MoSe_2$ Nanosheets, Inorganic Fullerene-Like $MoSe_2$ and $MoO_3$ Quantum Dots Using Fast and Ecofriendly Pulsed Laser Ablation in Liquid Followed by Microwave Treatment. *Mater. Sci. Semicond. Process.* **2019**, *99*, 68–77.

(295) Boyd, R. W. Nonlinear Optics; Academic Press, **2003**.

(296) Roy, S.; Neupane, G. P.; Dhakal, K. P.; Lee, J.; Yun, S. J.; Han, G. H.; Kim, J. Observation of Charge Transfer in Heterostructures Composed of $MoSe_2$ Quantum Dots and a Monolayer of $MoS_2$ or $WSe_2$. *J. Phys. Chem. C* **2017**, *121* (3), 1997–2004.

(297) Yin, Y.; Zhang, Y.; Gao, T.; Yao, T.; Zhang, X.; Han, J.; Wang, X.; Zhang, Z.; Xu, P.; Zhang, P.; et al. Synergistic Phase and Disorder Engineering in 1T-$MoSe_2$ Nanosheets for Enhanced Hydrogen Evolution Reaction. *Adv. Mater.* **2017**, *29* (28), 1700311.

# Appendix A

## Supporting Information for Chapter 6

**Table A1.** A summary of previous work about the synthesis of TMDC nanomaterials by pulsed laser ablation in liquid.

| Material | Ablated Target | Solvent | Laser Condition | Power | Energy per Pulse | Fluence | Time | Ref. |
|---|---|---|---|---|---|---|---|---|
| $MoS_2$ QDs | $MoS_2$ bulk target | Water | 800 nm, 50 fs, 1 kHz | 3.5 mW | 3.5 μJ | 0.77 J/cm$^2$ | 2 hrs | [170] |
| $MoS_2$ QDs, $WS_2$ QDs | $MoS_2$ powder, $WS_2$ powder | N-methyl-2-pyrrolidone | 800 nm, 80 fs, 1 kHz | 400 mW | 400 μJ | - | 30 min | [169] |
| $MoS_2$ QDs, $WS_2$ QDs | $MoS_2$ powder, $WS_2$ powder | Ethanol: Water = 1:1 | 800 nm, 35 fs, 1 kHz | 2 W | 2 mJ | - | 70 min | [172] |
| $MoS_2$ QDs, $WS_2$ QDs | $MoS_2$ powder, $WS_2$ powder | Diethylamine | 800 nm, 150 fs, 1 kHz | - | - | 200 J/cm$^2$ | 30 min | [171] |
| $MoS_2$ QDs | Exfoliated $MoS_2$ nanosheet | Water | 800 nm, 80 fs, 1 kHz | 2 W | 2 mJ | - | 30 min | [291] |
| $MoS_2$ QDs | $MoS_2$ bulk target | Water | 355 nm, 6 ns, 10 Hz<br>532 nm, 7 ns, 10 Hz | 1 mW | 0.1 mJ | 1.5 J/cm$^2$ | 40 min | [292] |
| $MoS_2$ QDs | $MoS_2$ bulk target | Water | 532 nm, 8 ns, 10 Hz | 50 - 400 mW | 5 - 40 mJ | 0.16 – 1.27 J/cm$^2$ | 5 - 20 min | [293] |
| $MoS_2$ nanosheets | $MoS_2$ bulk target | $FeCl_3$ aqueous solution | 800 nm, 35 fs, 1 kHz | 0.25 - 0.4 W | 0.25 - 0.4 mJ | - | 1 hr | [119] |
| $MoSe_2$ fullerene nanoparticles | $MoSe_2$ powder | Water | 1064 nm, 3.6 ns, 20 Hz | 4.8 W | 240 mJ | - | 30 min | [294] |
| $MoS_2$ fullerene nanoparticles | $MoS_2$ bulk target | Water | 1064 nm, 10 ns, 10 Hz | 0.5 W | 50 mJ | 1.59 J/cm$^2$ | 1 hr | [178] |
| $MoS_2$ fullerene nanoparticles | $MoS_2$ bulk target | Water | 532 nm, 10 ns, 10 Hz | 3 W | 300 mJ | - | 3 min | [177] |

| | | | | | | | | |
|---|---|---|---|---|---|---|---|---|
| $MoS_2$ fullerene nanoparticles | $MoS_2$ bulk target | Water | 532 nm, 6-9 ns, 5 Hz | 0.2 - 0.25 W | 40 - 50 mJ | - | 20 min | [176] |
| $MoS_2$ fullerene nanoparticles | $MoS_2$ powder | Methanol | 527 nm, 100 ns, 1 kHz | 16 W | 16 mJ | - | 15 min | [254] |
| $MoS_2$ fullerene nanoparticles, $WS_2$ fullerene nanoparticles | $MoS_2$ bulk target, $WS_2$ bulk target | Water | 1030 nm, 270 fs, 10 kHz | 1 W | 0.1 mJ | - | 30 min | [174] |

## A1: Discussion of Femtosecond Laser Filamentation

Femtosecond laser filamentation can be observed when a continuous dielectric medium is weakly ionized by propagating femtosecond laser pulses at a typical peak intensity of greater than $10^{13}$ W/cm.[130] A filament is composed of repeated self-focusing and defocusing processes, as illustrated in **Figure A1**.

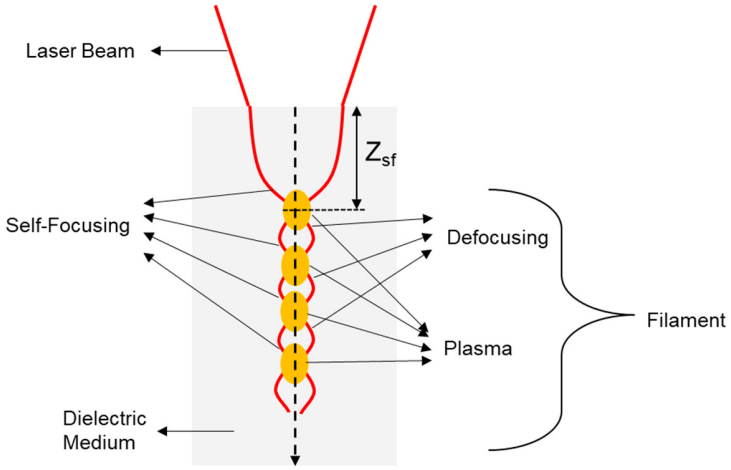


**Figure A1.** Schematic illustration of femtosecond laser filamentation in a dielectric medium.

Self-focusing is an intensity dependent nonlinear optical effect. When a femtosecond laser beam passes through a dielectric medium, the refractive index of the medium at the center of the beam is larger than that at the edge due to the nonuniform spatial intensity distribution of

the Gaussian laser beam where the laser intensity at the center is larger than that at the edge. The refractive index ($n$) of light in a medium can be calculated by **Equation A1** when considering the nonlinear effect.[295]

$$n = n_0 + n_2 I \qquad (A1)$$

Where $n_0$ is the linear refractive index, $\boldsymbol{I}$ is the intensity of the laser, $\boldsymbol{n_2}$ is the nonlinear index that can be calculated by **Equation A2**.[295]

$$n_2 = \frac{3}{4n_0^2 \epsilon_0 c} \chi^{(3)} \qquad (A2)$$

$\epsilon_0$ is the permittivity of vacuum, c is the speed of light, $\chi^{(3)}$ is the third order susceptibility. The difference of refractive indexes makes the medium act as a positive lens, resulting in the beam focusing within the medium by itself. Self-focusing overcomes diffraction of the beam and leads to collapse when the laser power is higher than a critical threshold ($P_{cr}$) which can be calculated by **Equation A3**.[130]

$$P_{cr} = \frac{3.72\lambda_0^2}{8\pi n_0 n_2} \qquad (A3)$$

Where $\lambda_0$ is the wavelength of the laser in vacuum.

On the other hand, the focused beam ionizes the medium and generates plasma leading to the defocusing of the beam.[130] The repeated cycles of self-focusing and defocusing create a filament. Accompanied with the repeated cycles, the energy of the beam is attenuated by other activities such as multiple photon absorption and plasma absorption which limit the propagation of the filament.[130] This is how the filament vanishes when the laser power is relatively low, as shown in Figure 1(a). The distance between the air/liquid interface to the start point of the filament can be represented by the distance ($Z_{sf}$) between the entrance face of light into a medium and the first self-focusing position, which can be evaluated by **Equation A4**.[295]

$$Z_{sf} = \frac{0.5k\omega^2}{(\frac{P}{P_{cr}} - 1)^{1/2} + \frac{2Z_{min}}{k\omega_0^2}} \quad (A4)$$

Where $P$ is the power of the laser, $k = n_0\omega/c$, $\omega$ and $\omega_0$ are the beam waists at the entrance face and the self-focusing position respectively. $Z_{min}$ is the distance between the entrance face and the self-focusing position without considering the nonlinear effect. From Equation S4, it can be found that $Z_{sf}$ decreases with increasing power ($P$) of the laser. That explains the observation that the starting point of the filament gets close to the air/liquid interface with increasing power in Figure 1(a).

The beam spot size at the focal point can be estimated by **Equation A5**[263]:

$$2\,\omega_f = \frac{4\lambda f M^2}{\pi\omega_0} \quad (A5)$$

Where $\omega_f$ is the beam radius at the focal point, $\lambda$ is the wavelength of the laser (800 nm), $f$ is the focal length of a focusing lens (5 cm), the beam quality factor ($M^2$) is estimated as 1.3 for our laser.[263] $\omega_0$ is the laser beam radius before focusing (0.5 cm). The beam spot size at the focal point in this work was calculated to be around 13.24 μm. It should be noted that the actual focal spot size is larger than the theoretical one when taking plasma defocusing into account.

The laser peak intensities and fluences corresponding to various laser powers based on the theoretical focal spot size are listed in **Table A2**.

**Table A2.** Laser fluences and peak intensities at theroretical self-focal spot corresponding to various average powers.

| Average Power | Energy per Pulse | Fluence | Peak Intensity |
|---|---|---|---|
| 0.07 W | 0.07 mJ | 50.84 J/cm$^2$ | $1.45 \times 10^{15}\ W/cm^2$ |
| 0.15 W | 0.15 mJ | 108.95 J/cm$^2$ | $3.11 \times 10^{15}\ W/cm^2$ |
| 0.3 W | 0.30 mJ | 217.90 J/cm$^2$ | $6.22 \times 10^{15}\ W/cm^2$ |
| 0.6 W | 0.60 mJ | 435.80 J/cm$^2$ | $12.44 \times 10^{15}\ W/cm^2$ |
| 1.5 W | 1.50 mJ | 1,089.50 J/cm$^2$ | $31.13 \times 10^{15}\ W/cm^2$ |
| 2.5 W | 2.50 mJ | 1,815.83 J/cm$^2$ | $51.88 \times 10^{15}\ W/cm^2$ |

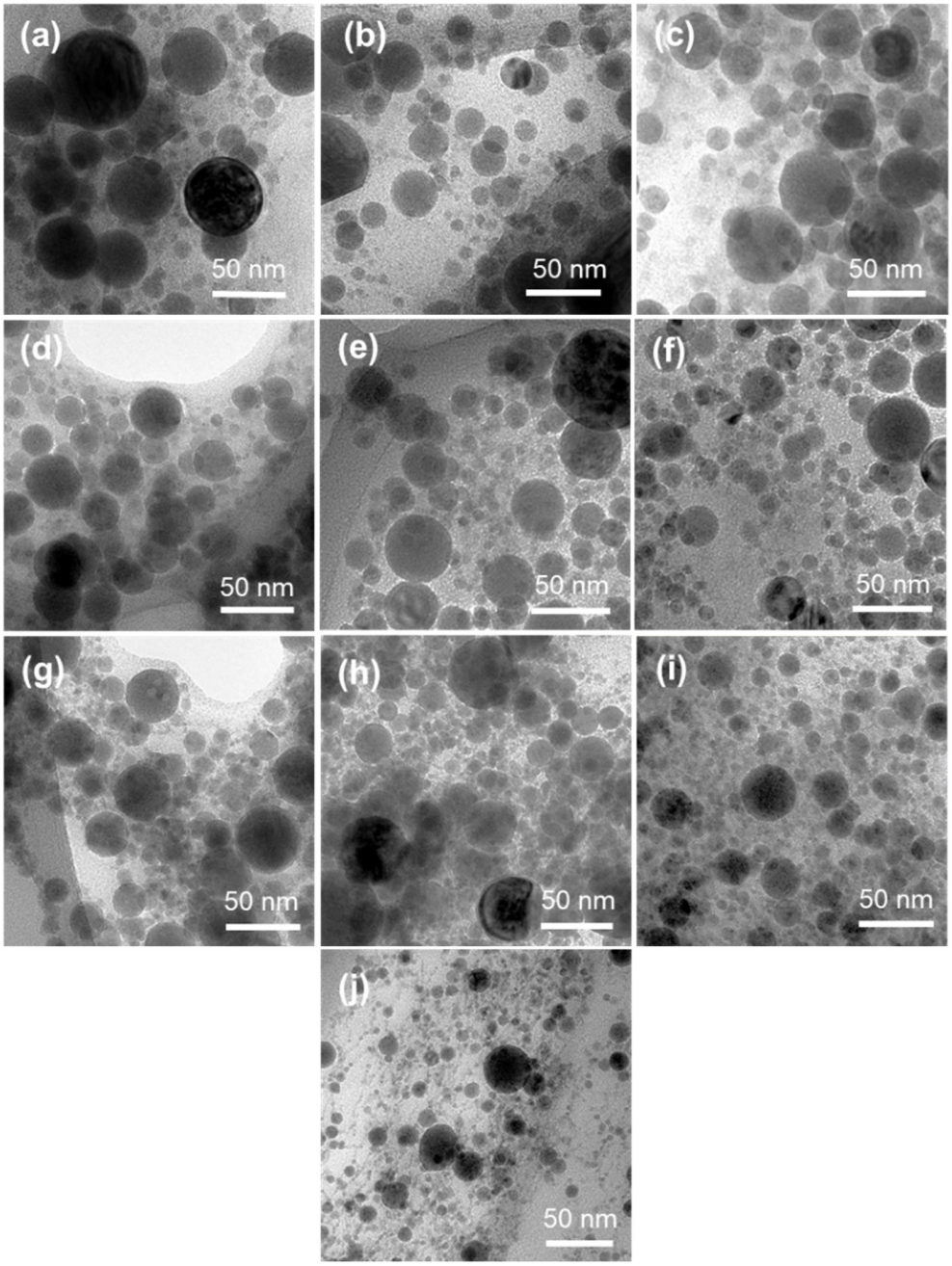


**Figure A2.** HRTEM images of nanoparticles prepared by laser ablation at (a) 0.07 W for 10 min, (b) 0.15 W for 10 min, (c) 0.3 W for 10 min, (d) 0.6 W for 10 min, (e) 1.5 W for 10 min, (f) 2.5 W for 10 min, (g) 0.15W for 20 min, (h) 0.15 W for 30 min, (i) 0.15 W for 45 min and (j) 0.15 W for 60min.

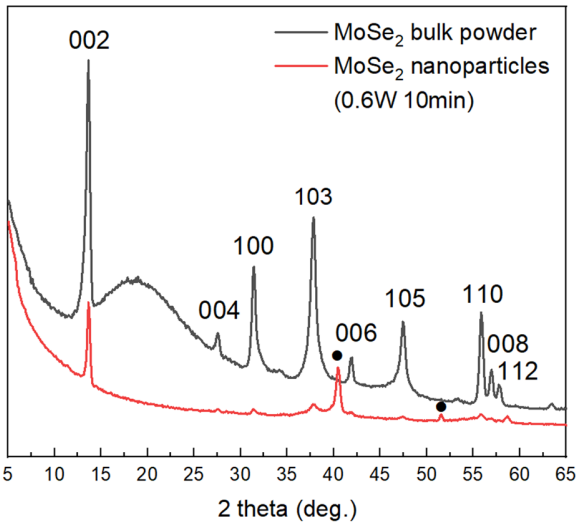


**Figure A3.** XRD patterns of original $MoSe_2$ powder and $MoSe_2$ nanoparticles prepared by laser ablation at 0.6 W for 10 min. Both samples show $MoSe_2$ peaks (PDF#: 29-0914), Another two peaks at 40.5° and 51.6° in the $MoSe_2$ nanoparticles sample might be assigned to $(10\bar{3})$ and (021) of $MoO_3$ (PDF#: 47-1320).

**Table A3.** Peak positions and proportions of 1T phase and oxide in nanoparticles prepared by laser ablation with different powers for 10 min.

| | Original | 0.07W | 0.15W | 0.3W | 0.6W | 1.5W | 2.5W |
|---|---|---|---|---|---|---|---|
| Mo3d5/2(1T) | - | 228.3eV | 228.3eV | 228.1eV | 228.1eV | 228.1eV | 228.1eV |
| Mo3d5/2(2H) | 229eV | 229eV | 229eV | 229.3eV | 229.3eV | 229.1eV | 229.1eV |
| Mo3d3/2(1T) | - | 231.2eV | 231.1eV | 231.2eV | 231.1eV | 231.3eV | 231.3eV |
| Mo3d3/2(2H) | 232eV | 232eV | 232eV | 232.2eV | 232.1eV | 232.3eV | 232.2eV |
| Mo3d5/2(MoVI) | - | 233eV | 232.9eV | 232.9eV | 232.8eV | 233.1eV | 232.9eV |
| Mo3d3/2(MoVI) | - | 236.3eV | 236.1eV | 236.1eV | 236eV | 236.1eV | 235.8eV |
| Amount of 1T phase | 0% | 37% | 46% | 52% | 53% | 57% | 61% |
| Amount of Oxide | 0% | 14% | 12% | 14% | 14% | 14% | 12% |

**Table A4.** Peak positions and proportions of 1T phase and oxide in nanoparticles prepared by laser ablation with different ablation times at 0.15 W.

| | 10min | 20min | 30min | 45min | 60min |
|---|---|---|---|---|---|
| Mo3d5/2(1T) | 228.3eV | 228eV | 228eV | 228eV | 228.1eV |
| Mo3d5/2(2H) | 231.1eV | 231eV | 231eV | 231eV | 231.2eV |
| Mo3d3/2(1T) | 229eV | 229eV | 229.1eV | 229.2eV | 229.1eV |
| Mo3d3/2(2H) | 232eV | 231.8eV | 231.8eV | 232eV | 232.2eV |
| Mo3d5/2(MoVI) | 232.9eV | 233eV | 232.8eV | 233eV | 233.1eV |
| Mo3d3/2(MoVI) | 236.1eV | 236eV | 235.9eV | 235.7eV | 236.1eV |
| Content of 1T phase | 46% | 48% | 55% | 58% | 61% |
| Content of Oxide | 12% | 10% | 13% | 13% | 15% |

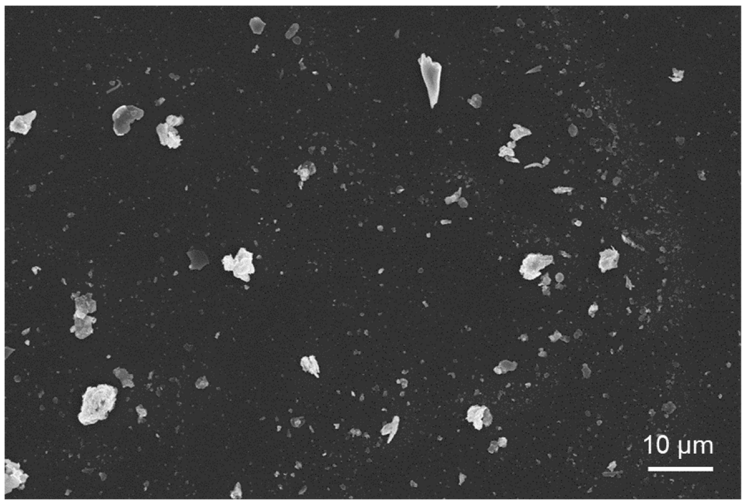


**Figure A4.** SEM image of original $MoSe_2$ powder.

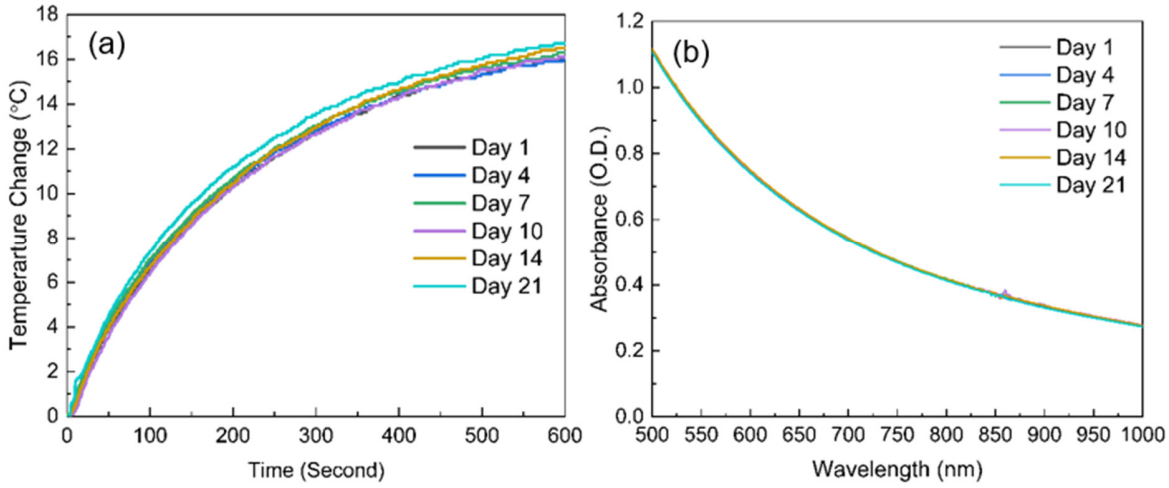


**Figure A5.** (a) Temperature change curves and (b) UV-vis-NIR absorbance spectra of the sample prepared by laser ablation at 1.5 W for 10 min as a function of time. The concentration of the nanoparticles in isopropyl alcohol was 0.2 mg/mL. The nanoparticles were illuminated by an IR continuous-wave laser (808 nm, 0.46 W) for 10 min.

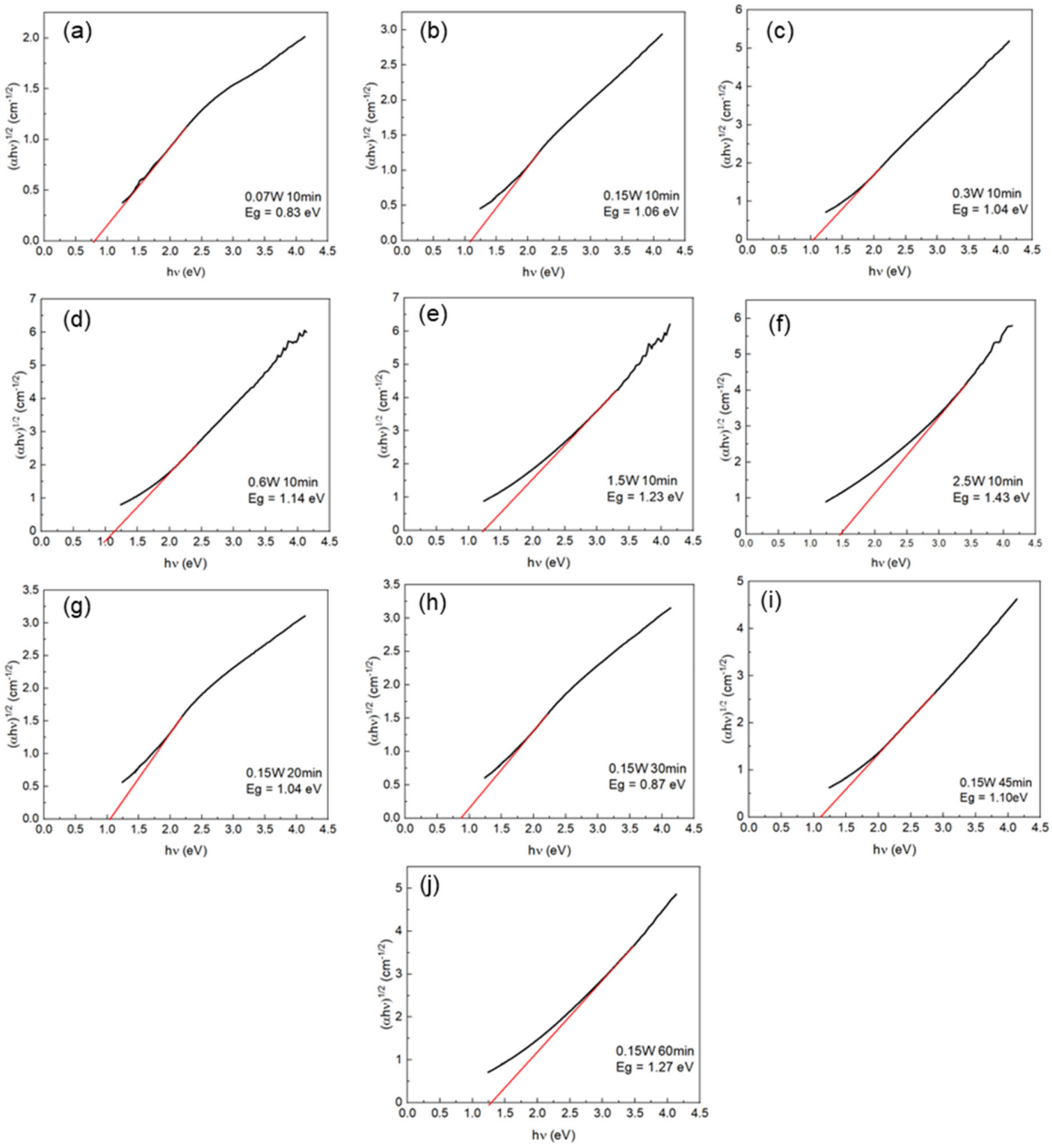


**Figure A6.** Tauc plots of nanoparticles prepared by laser ablation with different powers and ablation times.

**A2: Size Dependence of Bandgaps of Nanoparticles**

To verify the assumption that the increase in bandgap of the nanoparticles that are prepared with high laser powers is caused by the presence of small nanoparticles (size < 10 nm) that display quantum confinement effects, the nanoparticles of the 1.5 W sample were further centrifuged with different speeds of 5,000 rpm, 8,000 rpm and 11,000 rpm consecutively. The 1.5 W sample was first centrifugated at 5,000 rpm for 10min. The sediment was collected and added into 3 mL of IPA as Group A, and the supernatant was centrifugated again at 8,000 rpm for 10 min. The sediment after the second centrifugation was collected and added into 3 mL of IPA as Group B, and the supernatant was collected for the third centrifugation at 11,000 rpm for 10 min. The sediment was collected and added into 3 mL of IPA as Group C and the supernatant was collected as Group D.

The size distributions of the four groups of nanoparticles were measured manually from their TEM images (**Figure A7)**. The average size of nanoparticles was 46 nm for Group A, 27 nm for Group B, 18 nm for Group C and 12 nm for Group D (**Figure A8**). All the samples had 1T phase as shown in Raman spectra (**Figure A9**). The bandgap measured by Tauc plots (**Figure A10**) increased from 0.42 eV for the nanoparticles in Group A to 1.98 eV for the nanoparticles in Group D. As a comparison, the bandgap of $MoSe_2$ quantum dots can be as high as 2.3 eV.[296] Since the prevailing type of laser-synthesized nanoparticle is the onion-structured nanoparticle, which has a shell consisting of multiple layers of {002} planes, the Tauc plots of $MoSe_2$ powder and multilayer nanoflakes prepared by sonication of $MoSe_2$ powder in IPA for 2 hrs are also presented in **Figure A11**. The bandgaps of the $MoSe_2$ powder and the $MoSe_2$ multilayer nanoflakes were measured as 0.98 eV and 1.37 eV, respectively, greater than the bandgap of the nanoparticles in all the groups except Group D, which contained the highest number of small nanoparticles (Size: < 10 nm).

Therefore, it can be concluded that the increase in bandgap of the nanoparticles that were produced by laser ablation with high powers is caused by quantum confinement effects in the small nanoparticles produced (Size: < 10 nm), though the existence of 1T phase in the $MoSe_2$ nanoparticles is expected to lower the bandgap.

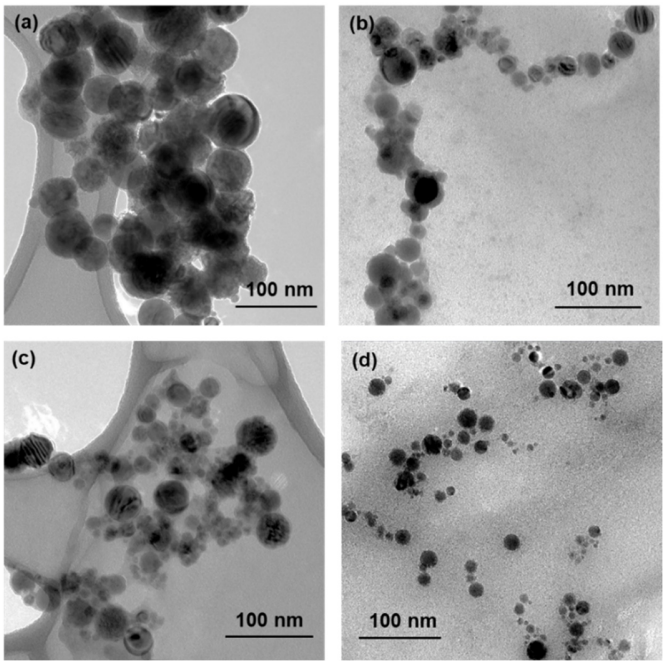


**Figure A7.** TEM images of nanoparticles in (a) Group A, (b) Group B, (c) Group C and (d) Group D.

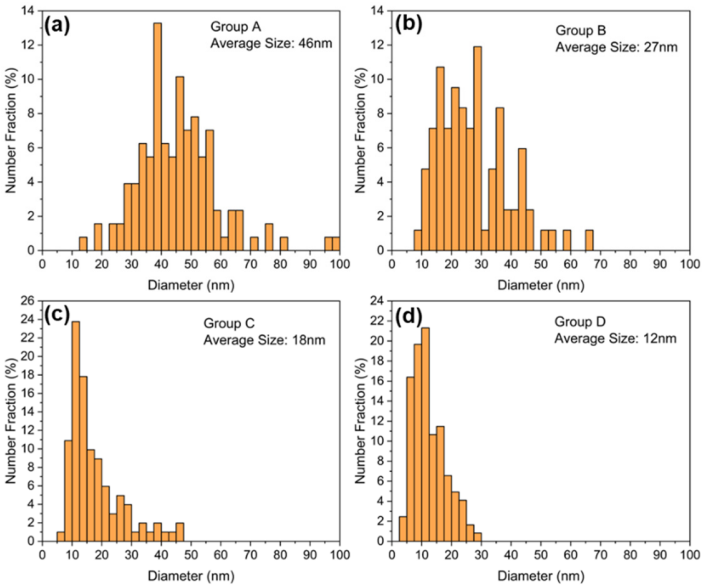


**Figure A8.** Size distributions of nanoparticles in (a) Group A, (b) Group B, (c) Group C and (d) Group D.

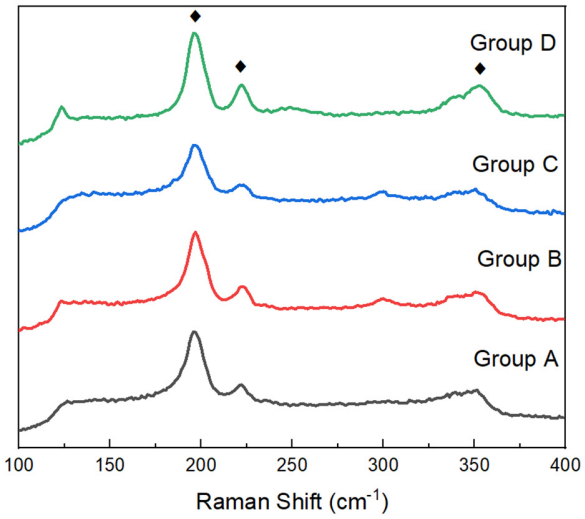


**Figure A9.** Raman spectra of nanoparticles in all the Groups. The peaks marked with diamond symbols are assigned to 1T phase of $MoSe_2$.[109,297]

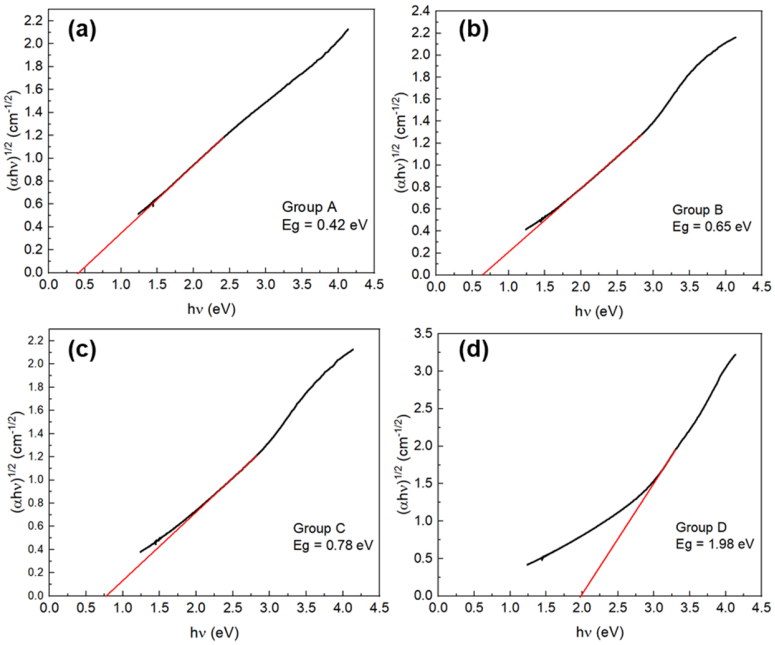


**Figure A10.** Tauc plots of nanoparticles in (a) Group A, (b) Group B, (c) Group C and (d) Group D

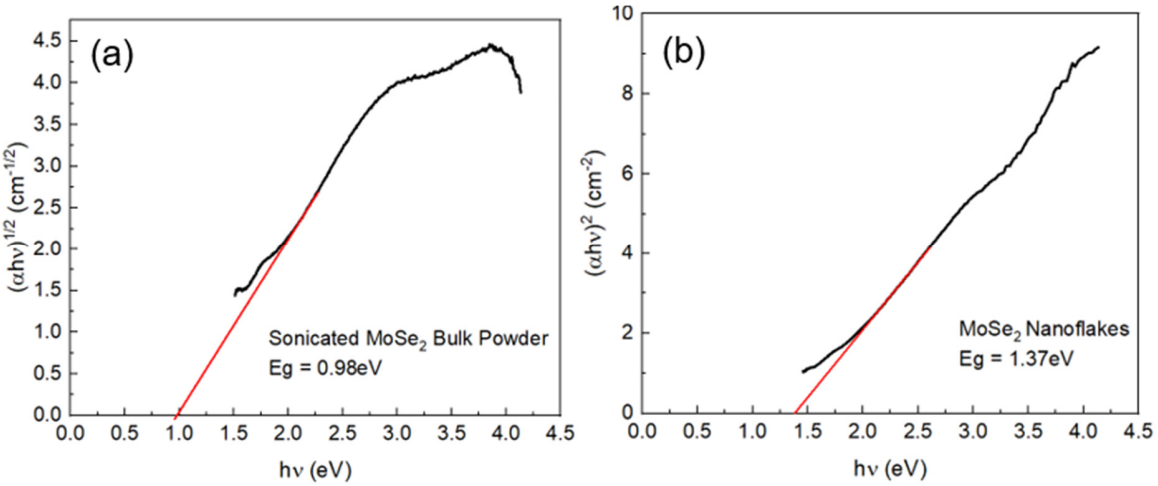


**Figure A11.** Tauc plots of (a) $MoSe_2$ powder sonicated in IPA for 20 min and (b) $MoSe_2$ nanoflakes prepared by sonication of $MoSe_2$ powder in IPA for 2 hrs.

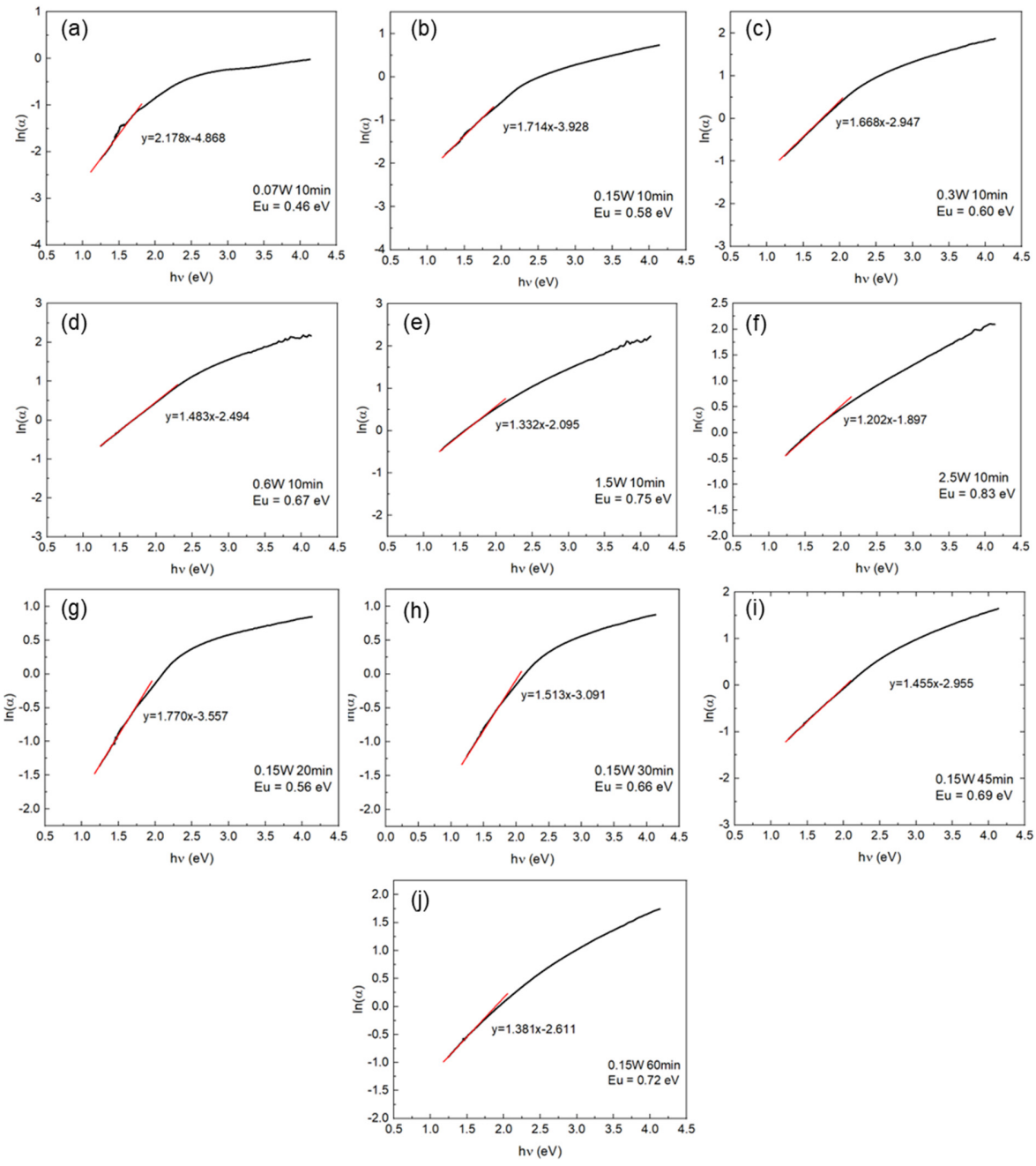


**Figure A12.** Plot of Ln(α) against hν to of nanoparticles prepared by laser ablation with different powers and ablation times to calculate corresponding Urbach energies.

# Appendix B

## Supporting Information for Chapter 7

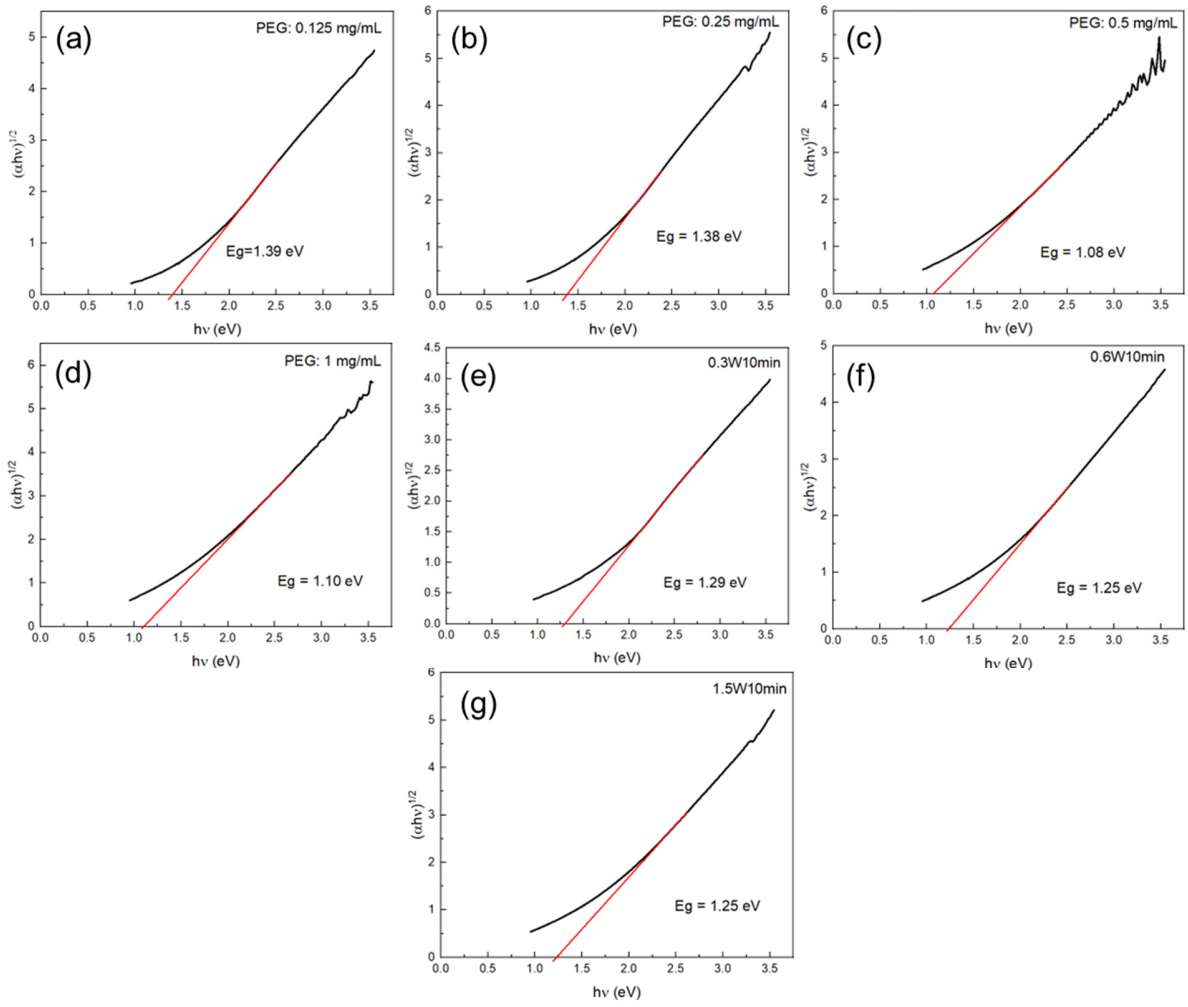


**Figure B1.** Tauc plots of $MoSe_2$ quantum dots prepared by laser ablation (1.5 W, 30 min) in PEG solutions with different concentrations of (a) 0.125 mg/mL, (b) 0.25 mg/mL, (c) 0.5 mg/mL and (d) 1 mg/mL. Tauc plots of $MoSe_2$ spherical nanoparticles prepared by laser ablation for 10 min in the 0.5 mg/mL PEG solution with different powers of (e) 0.3 W, (f) 0.6 W and (g) 1.5 W.

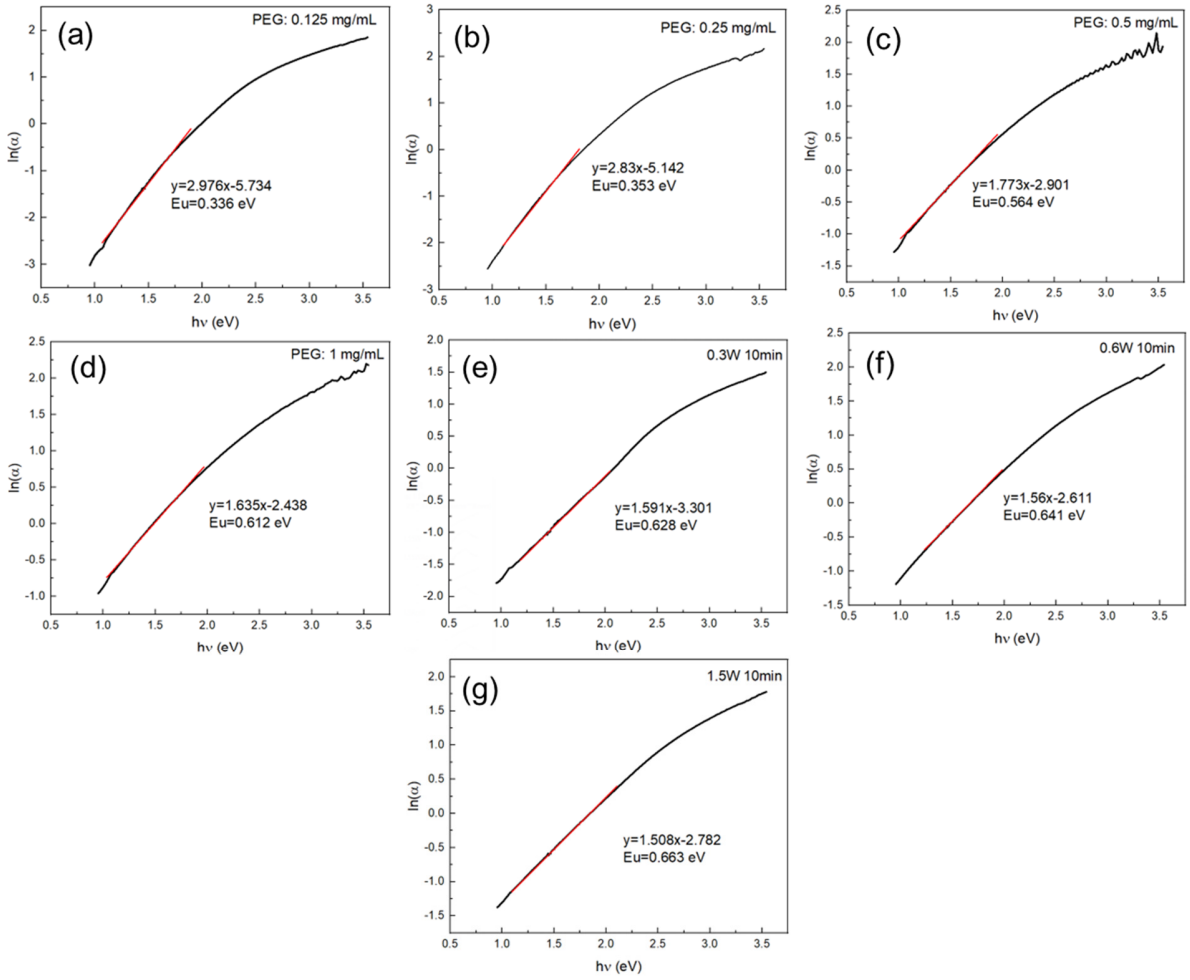


**Figure B2.** Plots of *ln(α)* against *hν* of $MoSe_2$ quantum dots prepared by laser ablation (1.5 W, 30 min) in PEG solutions with different concentrations of (a) 0.125 mg/mL, (b) 0.25 mg/mL, (c) 0.5 mg/mL and (d) 1 mg/mL. Plots of *ln(α)* against *hν* of $MoSe_2$ spherical nanoparticles prepared by laser ablation for 10 min in the 0.5 mg/mL PEG solution with different powers of (e) 0.3 W, (f) 0.6 W and (g) 1.5 W.